

2D Organisation of Complex Organic Molecules

**GEORGE GREEN LIBRARY OF
SCIENCE AND ENGINEERING**

Alexander Saywell, MSci (hons)

Thesis submitted to the University of Nottingham
for the degree of Doctor of Philosophy

August 2010

Abstract

The self-assembly of two-dimensional molecular systems is of significant interest, offering an insight into the fundamental interactions which drive the formation of complex supramolecular structures. A careful choice of the molecular ‘building blocks’ for such self-assembled systems potentially allows the design and production of nanoscale architectures with pre-determined geometries and specific chemical functionalities.

Within this thesis the two-dimensional structures formed by the self-assembly of complex organic molecules, deposited on an Au(111) surface held in an ultra-high vacuum (UHV) environment, are studied using a combination of scanning tunnelling microscopy (STM), photoelectron spectroscopy (PES), molecular dynamics (MD), and density functional theory (DFT) techniques. A UHV electro-spray deposition (UHV-ESD) technique is employed to facilitate the introduction of thermally labile molecules into the UHV environment.

Bi-molecular networks, formed from perylene tetracarboxylic diimide (PTCDI) and melamine, have previously been observed to assemble on the Au(111) surface. Several more complex phases are reported here, as characterised by STM, with the balance between isotropic and anisotropic interactions giving rise to a variety of structures. Chemical functionality may be added to these networks by incorporating functionalised derivatives of PTCDI. Alternative structures produced by altering the shape of the molecular ‘building blocks’ are also discussed.

The UHV-ESD technique is demonstrated here to be compatible with the deposition of the fullerene C₆₀, the single molecule magnet Mn₁₂O₁₂(O₂CCH₃)₁₆(H₂O)₄ (Mn₁₂(acetate)₁₆), and porphyrin based oligomers (**P4** and **P6**) and polymers (**Pn**). The UHV-ESD of C₆₀ on the clean Au(111) surface, and on a surface pre-patterned with a PTCDI/melamine network, results in similar structures to those previously observed to be produced by sublimation.

Mn₁₂(acetate)₁₆ and the porphyrin oligomers and polymers represent complex molecules which are thermally labile and possess, respectively, novel magnetic and electronic properties. Mn₁₂(acetate)₁₆ is observed to form filamentary aggregates due to the anisotropic nature of the molecule-molecule and molecule-substrate interactions, while **P4**, **P6** and **Pn** form highly ordered close-packed domains driven by the interdigitation of the alkyl chains attached to the porphyrin cores.

The findings presented within this thesis demonstrate that self-assembled molecular structures can be understood in terms of intermolecular interactions, and that for systems containing complex molecules the molecule-molecule interaction potential can lead to the formation of novel structures.

List of Publications

- *Vernier templating and synthesis of a 12-porphyrin nanoring*, M. C. O'Sullivan, J. K. Sprafke, D. Kondratuk, C. Rinfray, T. D. W. Claridge, **A. Saywell**, M. O. Blunt, P. H. Beton, M. Malfois, and H. L. Anderson, (*accepted: Nature*)
- *Conformation and packing of porphyrin polymer chains on a gold surface*, **A. Saywell**, J. K. Sprafke, L. J. Esdaile, A. J. Britton, A. Rienzo, H. L. Anderson, J. N. O'Shea, and P.H. Beton, (*accepted: Angew. Chem. Int. Ed. doi:10.1002/anie.201004896*)
- *Self-assembled aggregates formed by single molecule magnets on a gold surface*, **A. Saywell**, G. Magnano, C. J. Satterley, L. M. A. Perdigão, A. J. Britton, N. Taleb, M. Gimenez-Lopez, N. R. Champness, J. N. O'Shea, and P. H. Beton, *Nat. Commun.* 1, 75 (2010).
- *Supramolecular Assemblies Formed on an Epitaxial Graphene Superstructure*, A. J. Pollard, E. W. Perkins, N. A. Smith, **A. Saywell**, G. Goretzki, A. G. Phillips, S. P. Argent, H. Sachdev, F. Muller, S. Hufner, S. Gsell, M. Fischer, M. Schreck, J. Osterwalder, T. Greber, S. Berner, N. R. Champness, and P. H. Beton, *Angew. Chem. Int. Ed.* 49, 1794-1799 (2010).
- *Adsorption of PTCDI on Au(111): photoemission and scanning tunneling microscopy*, J. N. O'Shea, **A. Saywell**, G. Magnano, L. M. A. Perdigão, C. J. Satterley, P. H. Beton, and V. R. Dhanak, *Surf. Sci.* 20, 3094 (2009).
- *Adsorption of a Ru(II) dye complex on the Au(111) surface: photoemission and scanning tunneling microscopy*, L. C. Mayor, **A. Saywell**, G. Magnano, C. J. Satterley, J. Schnadt, and J. N. O'Shea, *J. Chem. Phys* 130, 164704 (2009).
- *Functionalized Supramolecular Nanoporous Arrays for Surface Templating*, L. M. A. Perdigão, **A. Saywell**, G. N. Fontes, P. A. Staniec, G. Goretzki, A. G. Phillips, N. R. Champness, P. H. Beton, *Chemistry - A European Journal* 14, 7600 (2008).
- *Electrospray Deposition of C60 on a Hydrogen-Bonded Supramolecular Network*, **A. Saywell**, G. Magnano, C. J. Satterley, L. M. A. Perdigão, N. R. Champness, P. H. Beton, and James N. O'Shea, *J. Phys. Chem. C* 112, 7706 (2008).
- *Hierarchical Organisation on a Two-Dimensional Supramolecular Network*, P. A. Staniec, L. M. A. Perdigão, **A. Saywell**, N. R. Champness, and P. H. Beton, *ChemPhysChem* 8, 2177 (2007).

- *Electrospray deposition of fullerenes in ultra-high vacuum: in situ scanning tunneling microscopy and photoemission spectroscopy*, C. J. Satterley, L. M. A. Perdigão, **A. Saywell**, G. Magnano, A. Rienzo, L. C. Mayor, V. R. Dhanak, P. H. Beton and J. N. O'Shea, *Nanotechnology* 18, 455304 (2008).
- *Single molecule magnets on a gold surface: in-situ electrospray deposition, X-ray adsorption and photoemission*, **A. Saywell**, A. J. Britton, G. Magnano, C. J. Satterley, L. M. A. Perdigão, N. Taleb, M. Gimenez-Lopez, N. R. Champness, P. H. Beton, and J. N. O'Shea, (*manuscript in preparation*)
- *Electrospray Deposition of the Endohedral Fullerene $N@C_{60}$ on the Au(111) surface*, A. J. Britton, **A. Saywell**, A. Rienzo, and J. N. O'Shea, (*manuscript in preparation*)
- *Electrospray Deposition of Zinc Porphyrins on an Au(111) substrate*, J. N. O'Shea, **A. Saywell**, A. J. Britton, and A. Rienzo, (*manuscript in preparation*)
- *A Haptic-STM interface*, **A. Saywell**, L. M. A. Perdigão, B. Medford, and P. H. Beton, (*manuscript in preparation*)

Acknowledgements

I would like to thank my supervisor Prof. Peter Beton for providing me with the opportunity to participate in a fascinating field of research and for his support and guidance throughout my studies. Dr James O'Shea deserves special mention for introducing me to the joy of synchrotron science and for building the 'electrospray' which has featured so heavily in my work. I am also indebted to Dr Luís Perdigão who has spent numerous hours over the course of my PhD explaining the practical aspects of UHV science.

The Nottingham Nanoscience group as a collective entity should be congratulated for providing an entertaining and productive working environment. Special thanks go to: Adam, Alina, Andy P., Andy S., Claire, Ed, Graziano, James, Karina, Kev, Louise, Luís, Marta L., Marta W., Matt, Pete, Rich F., and Sam. I could double the length of this volume by recounting the adventures we have shared. Thanks to all of you for our many discussions, intellectual and otherwise, my time in Nottingham would have been considerably less enjoyable without you.

I am especially grateful to my family for all the encouragement and support they have given me over the years. Having people who believe in your ability to achieve a goal makes it incalculably easier to do so.

Finally, Maria deserves a huge thank you for sharing all of the experiences I have had during my time in Nottingham. For continuing to be interested in my work, for your unquenchable enjoyment of life, for your smile, for your laugh, and for all of your help, I am eternally grateful. *Ti amo mia bella amica.*

Contents

| | |
|---|-----------|
| Abstract | i |
| List of Publications | ii |
| Acknowledgements | iv |
| 1 Introduction | 1 |
| 1.1 Nanoscale physics - Bottom-up self-assembly | 1 |
| 1.2 Overview of this thesis | 3 |
| 2 The concepts of supramolecular chemistry and two-dimensional self-assembly | 5 |
| 2.1 Supramolecular structures | 5 |
| 2.2 Two-dimensional crystal engineering at surfaces | 8 |
| 2.2.1 Structures formed by hydrogen-bonding interactions | 9 |
| 2.2.2 Structures formed by metal co-ordination | 13 |
| 2.2.3 Non-directional molecule-molecule interactions | 15 |
| 2.2.4 Covalent bonds | 16 |
| 2.2.5 Functionalising supramolecular structures | 18 |
| 2.3 Molecular traps | 18 |
| 2.4 Summary | 20 |
| 3 Experimental techniques and materials | 22 |
| 3.1 Scanning tunnelling microscopy | 22 |
| 3.1.1 Principles of STM - Quantum mechanical tunnelling | 23 |
| 3.1.2 Modes of STM operation | 28 |
| 3.1.3 Controlling tip position | 30 |
| 3.2 Photoelectron spectroscopy | 33 |
| 3.2.1 The electronic levels of atoms and molecules | 33 |
| 3.2.2 Surface sensitivity | 35 |
| 3.2.3 X-ray photoelectron spectroscopy | 36 |
| 3.2.4 Near edge X-ray absorption fine structure | 39 |
| 3.2.5 Synchrotron radiation sources | 43 |

| | | |
|----------|--|-----------|
| 3.3 | Ultra-high vacuum experimental set-up | 44 |
| 3.3.1 | UHV apparatus | 44 |
| 3.3.2 | UHV techniques | 45 |
| 3.4 | Ultra-high vacuum electrospray deposition | 47 |
| 3.4.1 | The electrospray ionisation process | 48 |
| 3.4.2 | The electrospray apparatus | 51 |
| 3.4.3 | The free-jet expansion | 51 |
| 3.4.4 | The concentration gradient produced by UHV-ESD | 54 |
| 3.5 | Surfaces | 54 |
| 3.5.1 | The Au(111) $22\times\sqrt{3}$ reconstruction | 54 |
| 3.5.2 | Preparation of the Au(111) surface | 55 |
| 3.6 | Summary | 56 |
| 4 | Hydrogen-bonded supramolecular networks: PTCDI as a molecular building block | 57 |
| 4.1 | Hydrogen-bonded structures formed from PTCDI and melamine | 57 |
| 4.1.1 | Homo-molecular interactions of PTCDI and melamine | 58 |
| 4.1.2 | The mixed phase of PTCDI and melamine | 61 |
| 4.1.3 | Hexagonal and parallelogram phases of the PTCDI/melamine network | 62 |
| 4.2 | Melamine-rich hydrogen-bonded supramolecular structures | 64 |
| 4.2.1 | Formation of the various PTCDI/melamine phases | 67 |
| 4.3 | Adding chemical functionality to a hydrogen-bonded network | 69 |
| 4.3.1 | DFT calculations of the functionalised R ₂ PTCDI structures | 72 |
| 4.3.2 | Structures formed by Br ₂ PTCDI and melamine on the Au(111) surface | 73 |
| 4.3.3 | Structures formed by S ₂ PTCDI and melamine on the Au(111) surface | 75 |
| 4.4 | Summary | 78 |
| 5 | Electrospray deposition of C₆₀ | 80 |
| 5.1 | The transport of fragile molecules into an UHV environment: C ₆₀ as a test case | 80 |
| 5.1.1 | Experimental set-up | 81 |
| 5.1.2 | UHV-ESD of C ₆₀ on Au(111) | 81 |
| 5.2 | UHV-ESD of molecules on a hydrogen-bonded supramolecular network | 84 |
| 5.2.1 | UHV-ESD of C ₆₀ on a supramolecular network | 86 |
| 5.3 | Summary | 92 |

| | | |
|----------|--|------------|
| 6 | Self-assembled aggregates formed by single molecule magnets on a gold surface | 93 |
| 6.1 | Single molecule magnets as molecular building blocks | 93 |
| 6.2 | Experimental methods | 95 |
| 6.3 | Filamentary aggregates of $\text{Mn}_{12}(\text{acetate})_{16}$ | 97 |
| 6.3.1 | Molecular dynamics simulations of $\text{Mn}_{12}(\text{acetate})_{16}$ | 98 |
| 6.4 | NEXAFS spectra of $\text{Mn}_{12}(\text{acetate})_{16}$ | 103 |
| 6.5 | UHV-ESD of $\text{Mn}_{12}(\text{acetate})_{16}$ on a supramolecular network | 105 |
| 6.6 | Summary | 107 |
| 7 | Conformation and packing of porphyrin oligomers and polymers on a gold surface | 108 |
| 7.1 | Porphyrin polymers as self-assembling molecular wires | 108 |
| 7.2 | Experimental methods | 110 |
| 7.3 | Self-assembly of the porphyrin oligomers P4 and P6 | 111 |
| 7.4 | Synchrotron studies of P4 | 113 |
| 7.5 | Self-assembly and persistence length of the porphyrin polymer Pn | 114 |
| 7.6 | Summary | 118 |
| 8 | Conclusion | 120 |
| 8.1 | Summary of findings | 120 |
| A | Theoretical background to DFT, MM, and MD | 123 |
| A.1 | Background to DFT | 123 |
| A.1.1 | Hartree-Fock approximation | 125 |
| A.1.2 | Limitations of the Hartree-Fock technique | 128 |
| A.2 | Density functional theory | 128 |
| A.2.1 | Basis sets | 131 |
| A.2.2 | Limitations of DFT | 133 |
| A.3 | Implementation of DFT | 133 |
| A.4 | Molecular mechanics simulations | 136 |
| A.4.1 | Introduction to molecular mechanics | 136 |
| A.4.2 | The Forcefield energy | 137 |
| A.4.3 | Forcefield parametrisation - the Universal Forcefield | 139 |
| A.4.4 | Advantages and limitations of MM methods | 139 |
| A.5 | Molecular dynamics simulations | 140 |
| A.5.1 | Phase space and trajectories | 140 |
| A.5.2 | Ensembles | 142 |
| A.6 | Implementation of MM and MD | 142 |
| A.6.1 | MM calculation options | 142 |

| | | |
|----------|--|------------|
| A.6.2 | MD calculation options | 144 |
| B | Details of the DFT and MM simulations | 145 |
| B.1 | DFT calculation details | 145 |
| B.1.1 | HOMO, LUMO, and energy DFT calculations for single molecules | 148 |
| B.1.2 | Homo-molecular binding interactions | 148 |
| B.1.3 | Hetero-molecular interactions | 148 |
| B.2 | MM calculation details for the simulation of $\text{Mn}_{12}(\text{acetate})_{16}$ | 153 |
| B.2.1 | $\text{Mn}_{12}(\text{acetate})_{16}$ on the Au(111) surface | 153 |
| B.2.2 | Two $\text{Mn}_{12}(\text{acetate})_{16}$ molecules on the Au(111) surface | 157 |
| B.2.3 | Five $\text{Mn}_{12}(\text{acetate})_{16}$ on the Au(111) surface | 158 |
| B.2.4 | Note on the magnitude of the calculated BEs | 160 |
| | List of abbreviations and acronyms | 161 |
| | Bibliography | 163 |
| | List of Figures | 182 |
| | List of Tables | 186 |

Chapter 1

Introduction

In this chapter the concept of 'bottom-up' self-assembly is introduced, and an overview of the structure of this thesis is presented.

1.1 Nanoscale physics - Bottom-up self-assembly

Physics provides a framework which enables us to understand and predict the behaviour of the world around us. Nanoscale physics, or nanoscience, is the study of materials on the length scale of nanometres, where it is often appropriate to treat atoms and molecules, which are the component parts of the objects we see around us, as discrete units. This idea of viewing nanoscale systems as groups of interacting discrete units has led to the concept of bottom-up fabrication where individual units are used as 'building blocks' and are positioned relative to each other to produce 'nanoscale' structures. Richard Feynman's talk, "There's plenty of room at the bottom" [1], may be considered as one of the catalysts for the current interest in bottom-up fabrication. Feynman suggested that it could be possible to store vast amounts of information in a very small space (such as writing the contents of the Encyclopaedia Britannica on the head of a pin) by using a block of atoms to represent one bit of data. Feynman also postulated that an ability to manipulate individual atoms would allow for the production of substances with interesting new properties.

One of the earliest examples of a 'bottom up' technique was the manipulation of xenon atoms on a nickel surface, performed by Eigler et al. [2]. The tip of a scanning tunnelling microscope (STM) was used to rearrange the xenon atoms to spell out 'IBM'. Other structures have been created by the mechanical manipulation of atoms, such as the 'quantum corral' shown in Figure 1.1 (a). The 'quantum corral' is constructed from a ring of Fe atoms on a Cu(111) surface, with each Fe atom being mechanically positioned by an STM tip. In this structure the position of the atoms has resulted in a standing wave being set up in the electronic surface states of the metal, providing a visual representation of a quantum mechanical effect. These early attempts at bottom-up self-assembly have given rise to several

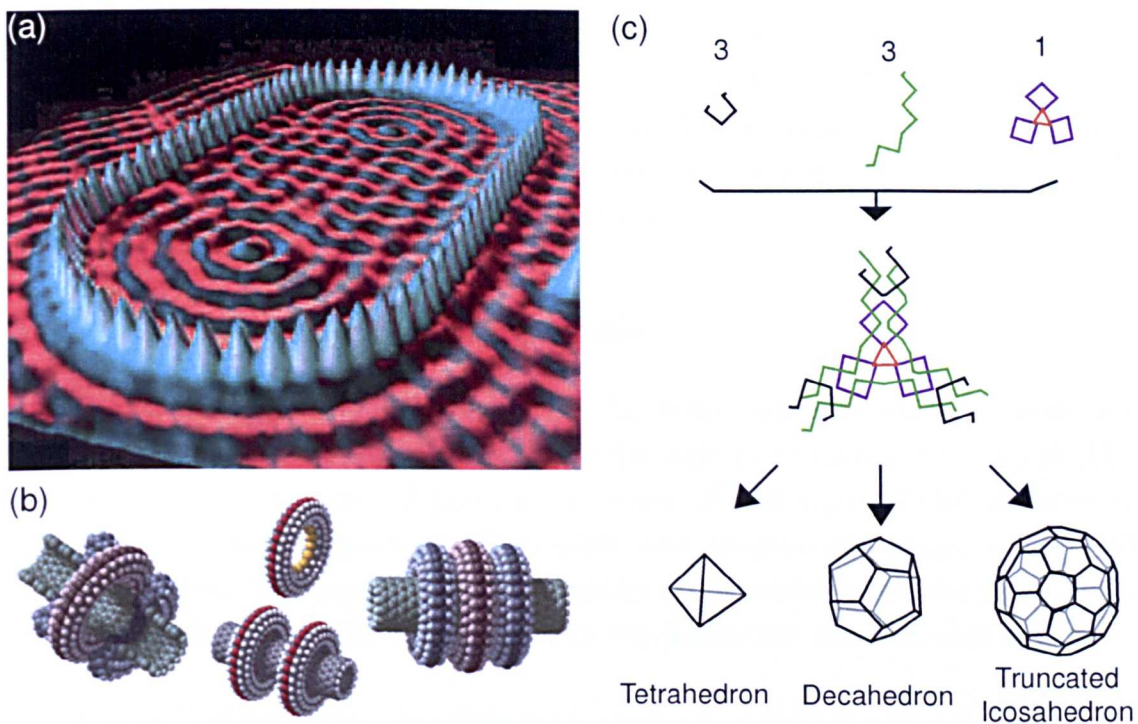


Figure 1.1: (a) Quantum coral formed by the manipulation of iron atoms on a copper surface (taken from [4]). (b) Drexlerian concept of a ‘nanodevice’, where atoms are placed together to produce mechanical objects such as gears and bearings (taken from [5]). (c) The self-assembly of DNA strands into three-dimensional structures (adapted from [6]).

conceptual ideas relating to the production of nanoscale structures.

Figure 1.1 (b) shows several Drexlerian ‘nanomachines’ where atoms are arranged in shapes that resemble traditional mechanical components, such as bearings and gears [3]. These nanomachines are viewed by some as the ultimate step towards miniaturisation, and hold the key to the manipulation of matter on an atomic level. However, many view the construction of such nanomachines as unfeasible. The mechanical manipulation of atoms to produce complex structures would be prohibitively time consuming, and very likely to be impossible due to the nature of the forces governing the interactions between atoms.

A different approach for solving the challenges inherent to bottom-up self-assembly is to use methodologies present in the natural world. The complex structures observed in nature are not created via the slow process of atomic manipulation but are assembled hierarchically, with molecular ‘building blocks’ being allowed to interact and self-assemble to create structures which have length scales several orders of magnitude greater than that of their constituent parts. It is possible to take the concepts of self-assembly exhibited by nature, e.g. the interlocking of base pairs in DNA, and to create structures on the nanometre scale which have pre-designed geometries. Figure 1.1 (c) shows examples of three dimensional shapes which may be formed from the self-assembly of DNA. Small organic molecules are used as ‘building blocks’ to create larger supramolecular structures, such as a tetrahedron and a decahedron. This approach appears to

offer a more realistic paradigm for bottom-up fabrication, as the time scales involved are much shorter than those for the mechanically driven production of structures. The concept of producing structures by designing molecular ‘building blocks’ which interact with each other to produce a supramolecular structure is the basis for the work undertaken in this thesis.

1.2 Overview of this thesis

Within this thesis the complex interactions between molecules which are observed to self-assemble on atomically clean substrates held in ultra-high vacuum (UHV) will be explored. Chapter 2 provides a review of the state of the art in two-dimensional, surface-supported self-assembly, and describes the origins of the field of self-assembly. The principles of supramolecular chemistry are discussed, with reference to the various forces which drive the formation of self-assembled structures.

Chapter 3 details the experimental techniques that are utilised within this work, focusing on the use of STM as a method of characterising supramolecular structures formed on surfaces held in UHV. A discussion of the techniques for depositing molecules on surfaces is given, including a description of the ultra-high vacuum electrospray deposition (UHV-ESD) technique, which has been developed by the Nottingham University Nanoscience group, in order to facilitate the transfer of complex, thermally labile, molecules from solution to UHV. The chapter also covers general aspects of UHV equipment usage, and the use of synchrotron based techniques such as X-ray photoemission spectroscopy (XPS) and near-edge X-ray absorption fine structure (NEXAFS).

Chapter 4 contains work on the investigation of structures formed by the self-assembly of the molecular ‘building blocks’ PTCDI (3,4:9,10- perylenetetracarboxylic diimide) and melamine (1,3,5-triazine-2,4,6-triamine) when deposited on the Au(111) surface. This system gives an insight into the complexity of the structures that are formed due to the balance between van der Waals (vdW) and hydrogen-bonding interactions. Work is also presented where additional chemical functionality is added to these network structures by replacing the PTCDI ‘building block’ with a chemically functionalised derivative of the PTCDI molecule.

In Chapter 5 the fullerene C_{60} is deposited by UHV-ESD on an Au(111) surface. C_{60} has previously been deposited on the Au(111) surface by sublimation and studied by STM, allowing a comparison between the two deposition techniques. The stability of hydrogen-bonded networks under the UHV-ESD of C_{60} is also investigated.

UHV-ESD may also be used to deposit molecules which cannot be sublimed due to their large molecular weights or fragile chemistry. Chapter 6 describes experiments conducted where the single molecule magnet $Mn_{12}O_{12}(O_2CCH_3)_{16}(H_2O)_4$ ($Mn_{12}(\text{acetate})_{16}$) is deposited on an Au(111) surface, and on an Au(111) sur-

face which has been pre-patterned with a PTCDI/melamine hydrogen-bonded supramolecular network. The complex three dimensional shape of the molecule gives rise to the formation of complex filamentary structures. The formation of these structures is investigated using molecular dynamics (MD) simulations, demonstrating that the anisotropic molecule-molecule and molecule-substrate interactions are the driving force behind the observed structures.

In Chapter 7 the UHV-ESD technique is used to deposit large, complex, molecules on an Au(111) surface held in vacuum. The structures formed by sub-monolayer coverages of oligomers and polymers formed from porphyrin sub-units are studied by STM, XPS, and NEXAFS. The porphyrin oligomers are observed to form highly ordered close-packed structures, driven by the interdigitation of alkane chains attached to the cores of the porphyrin sub-units. The polymer molecules show remarkable flexibility and are observed to form a quasi-close-packed arrangement, which is stabilised by a similar molecule-molecule interaction as witnessed for the oligomers.

Finally, Chapter 8 presents an overview of the findings reported on within this work.

Chapter 2

The concepts of supramolecular chemistry and two-dimensional self-assembly

In this chapter a review of the current progress within the field of self-assembly is presented. 'Bottom-up' self-assembly is described with an emphasis on the crystal engineering concepts of supramolecular chemistry, where non-covalent interactions between molecules allow complicated structural patterns to be produced. The ability to incorporate chemical functionality into these structures is also discussed

2.1 Supramolecular structures

Solution based supramolecular chemistry may be viewed as a catalyst for the study of self-assembled systems. Lehn's Nobel lecture described supramolecular chemistry as 'chemistry beyond the molecule' [7], where complex structures are formed from the association of several molecular species held together by non-covalent intermolecular forces. Some structures, like the double helix shown in Figure 2.1 (a), are formed by hydrogen-bond and aromatic stacking interactions. Another example of supramolecular chemistry is the use of metal co-ordination bonds to form two or three-dimensional grid structures (Figure 2.1 (b) [8])

Such supramolecular structures are held together by weak, non-covalent, intermolecular forces. This allows the molecular components of the supramolecular structure to be dissolved in solution where they diffuse, and eventually meet to form the desired structure. By altering the nature of the intermolecular bonding and its directionality, structures with different geometries may be created. Within a given supramolecular structure several distinct forces will compete in order to produce the observed structure. The main forces which we shall consider here are vdW, hydrogen-bonding, and metal co-ordination bonds. It is possible to use several different non-covalent bonding interactions in order to create a supramolecular structure.

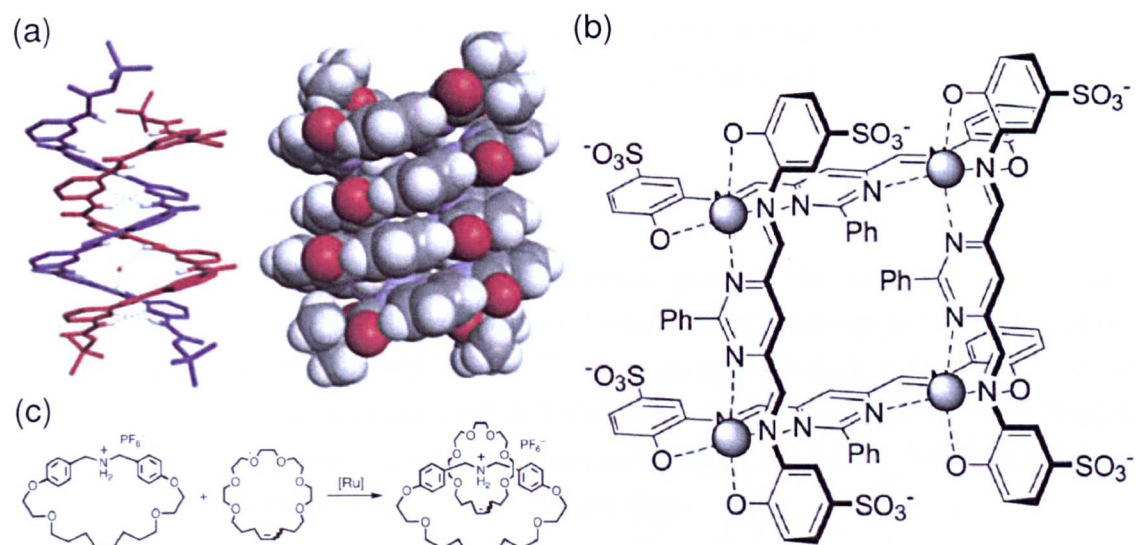


Figure 2.1: Examples of supramolecular chemistry. (a) A double helix structure formed by the hydrogen-bonding and aromatic stacking intermolecular interactions between two oligomers (taken from [9]). (b) [2x2] grid-type metal organic framework, formed by the metal co-ordination interactions between the metallic Zinc atoms and the organic ligands (taken from [8]). (c) ‘Magic ring’ prepared by olefin metathesis, where electrostatic interactions hold the negative oxygenated ring in place over the positive NH₂ group (taken from [10]).

van der Waals interactions

VdW forces are present within all molecular systems, although they are often weaker than hydrogen-bonding or metal co-ordination bonds they can play an important role in the determination of the geometry of supramolecular structures. VdW forces may be split into three contributions: dipole-dipole, dipole-induced dipole, and instantaneous dipole-induced dipole. The first two of these interactions require the molecule to possess a dipole moment. The instantaneous dipole - induced dipole interaction is often known as the London or dispersion force, and is ubiquitous in molecular systems as neither of the participating molecules need to possess a dipole moment. In the case of the dispersion force the motion of the electrons within a molecule gives rise to an instantaneous dipole which in turn induces a dipole in a neighbouring molecule. This leads to an interaction where the energy varies as $1/r^6$ [11], where r is the separation between the two molecules.

Metal co-ordination

Transition metal atoms are known to participate in supramolecular structures where organic ligands are complexed to the metal centre. Metal atoms have ‘d’ type orbitals which are shielded from the effect of the nucleus by the core electrons, allowing these atoms to form a variety of valence electronic configurations. For this reason metal atoms are able to form co-ordinate bonds by sharing valence electrons with neighbouring ligand molecules. By designing ligands for specific metals it is possible to form large supramolecular structures with specified geometry due to

the anisotropic nature of the bonding. These structures have the benefit of strong bonding interactions between the molecules and metal atoms making them very robust [12].

Hydrogen-bonding

The most common hydrogen-bonded system is given in the form $X-H \cdots A$, where X and A are electronegative species such that an interaction is formed between the two polar groups: $X^{-\delta}-H^{+\delta} \cdots A^{-\delta}$. An example of such a bond is given in Figure 2.2, where the cyanuric acid and melamine molecules form three hydrogen-bonds between each other. In this bonding motif there are two $N^{-\delta}-H^{+\delta} \cdots O^{-\delta}=C^{+\delta}$ interactions and one $N^{-\delta}-H^{+\delta} \cdots N^{-\delta}$ interaction.

Three-dimensional crystal engineering

By designing molecules, and producing them via chemical synthesis, it is in theory possible to produce an almost infinite range of ‘building blocks’ which may be used to create complex structures. Supramolecular chemistry has given rise to the field of three-dimensional crystal engineering. An example of a structure created by this methodology is the honeycomb structured cyanuric acid-melamine (CA·M) crystal studied by Ranganathan et al. [13] (the X-ray crystal structure of this system is shown in Figure 2.2 (a)). The structure is formed from two-dimensional sheets of CA·M molecules, which have self-assembled into an open pored hexagonal structure. The hexagonal structure is stabilised by the triple hydrogen-bonding interaction between the cyanuric acid and melamine molecules. The sheets of molecules are held together by $\pi - \pi$ stacking interactions. This combination of interactions leaves channels running through the crystal.

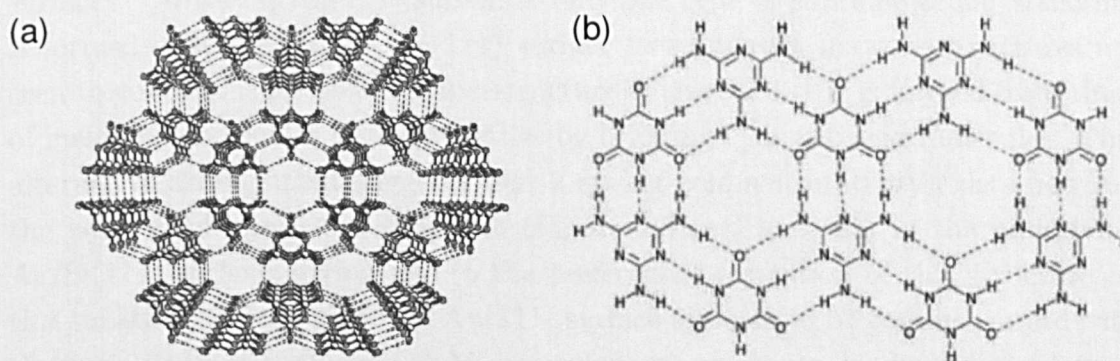


Figure 2.2: Bonding motif of the cyanuric acid - melamine (CA·M) molecular network. (a) Crystal structure of the CA·M network made from sheets of hexagonal network leaving channels running through the crystal (taken from [13]). (b) The alternating ring of cyanuric acid and melamine molecules stabilised by a triple hydrogen-bond interaction (taken from [14]).

A study of the Cambridge structural database (which contains information about the structures of numerous hydrogen-bonded materials) identified the cyanuric acid-melamine bond as the most robust [15], but there are a great many

hydrogen-bond interactions that may be utilised to produce stable crystal structures.

2.2 Two-dimensional crystal engineering at surfaces

Two-dimensional crystal engineering is a term used to describe the self-assembly of molecules on a surface. The same non-covalent interactions described above have been used to produce two-dimensional structures. By confining the molecules to a plane it is easier to design a network structure from the molecular ‘building blocks’. For two-dimensional crystal structures supported by a substrate it is important to consider the interactions between the molecules and the surface. A very strong molecule-substrate interaction may prevent the diffusion of molecules over the surface, and will inhibit the formation of a two-dimensional crystal. For this reason much of the work to date in this field has been performed on relatively inert surfaces such as Au, Cu, and Ag.

Figure 2.3 (a) shows a two-dimensional CA·M crystal formed by depositing the molecules on an Ag/Si(111) surface held in UHV [14]. The triple hydrogen-bond between the cyanuric acid and melamine molecules is identical to that observed in the three-dimensional crystal. This structure may also be produced on the Au(111) surface [16], again with the same triple hydrogen-bond stabilising the structure, and giving rise to the same periodicity of the network. The ability to produce networks on a variety of structures is useful, gold substrates are particularly important due to their ease of manufacture and electrical conductivity. There is however a difference between the structures which may be produced on the two surfaces. On the Ag/Si(111) substrate only one type of supramolecular structure is formed, whereas on the Au(111) surface two different network structures are seen to co-exist. This second superstructure (Figure 2.3 (b)) is formed from rings of melamine molecules bound together by bridging cyanuric acid molecules. This alternative arrangement suggests that a strong commensurability exists between the honeycomb molecular structure (Figure 2.3 (a)) and that of the underlying Ag/Si(111) surface, giving rise to the preferential formation of this structure on this substrate. In contrast, the Au(111) surface appears to be commensurate with the periodicity of both the CA·M molecular arrangements, leading to the formation of the honeycomb and alternative (Figure 2.3 (b)) structures. By changing the substrate from Ag/Si(111) to Au(111) an additional degree of freedom has been introduced, allowing the creation of a molecular network which has a much larger unit cell.

The effect of the substrate on the geometry of structures mediated by hydrogen-bonding interactions is further demonstrated by considering the structures prepared by two different research groups, on two different surfaces, using the same

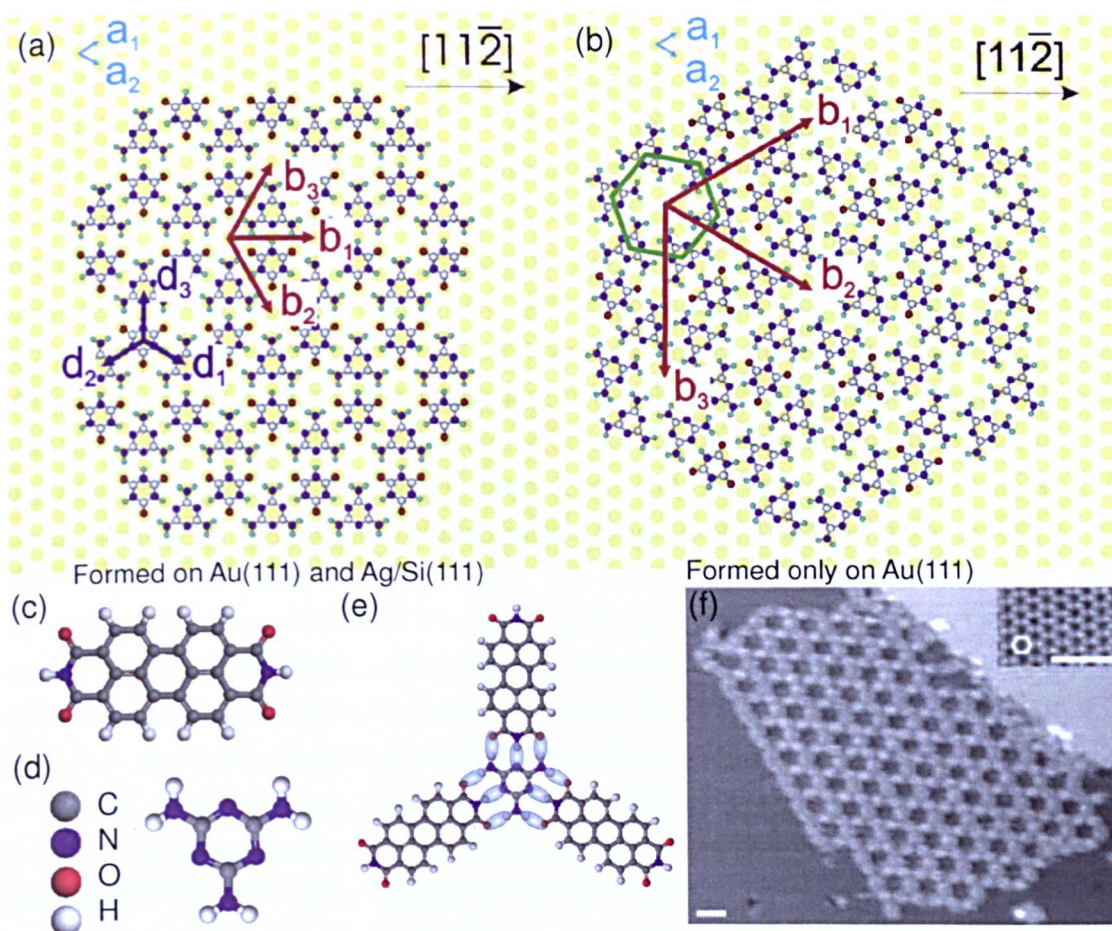


Figure 2.3: CA-M molecular network structure, formed on the Au(111) and Ag/Si(111) surface. (a) Structure of the honeycomb network which is observed to form on both the Au(111) and Ag/Si(111) surface. (b) The CA-M superstructure, which is only observed on the Au(111) surface ((a)-(b) taken from [16]). (c)-(d) The PTCDI-melamine ‘building blocks’ which utilise the same triple hydrogen-bond motif as CA-M to produce the vertex shown in (e). (f) The hexagonal PTCDI/melamine supramolecular network formed on the Ag/Si(111) surface (taken from [19]).

molecule, 4,4'-biphenyl dicarboxylic acid (BDA). When deposited on the Au(111) surface, BDA forms a close-packed structure composed of lines of molecules formed by hydrogen-bonding interactions [17]. However, when deposited on the more reactive Cu(100) surface a ‘herringbone’ pattern was observed [18], with the BDA molecules orientated at right angles to each other. This structure is attributed to the de-protonation of the carboxylic groups, leading to an alternative bonding arrangement. In this particular instance the molecule-substrate interaction is so strong that the chemistry of the BDA molecule is altered, again demonstrating that the choice of substrate plays an important part in the design of a two-dimensional crystal structure.

2.2.1 Structures formed by hydrogen-bonding interactions

As the CA-M bonding motif is so robust much work has been undertaken to see whether it is possible to incorporate the triple hydrogen-bond functionality into

a system containing larger molecules. Several groups, including the Nottingham Nanoscience group, have studied systems based on the CA·M interaction [19–23]. Using the strong triple bond of CA·M, but altering the structure of the cyanuric acid molecule, it is possible to produce two-dimensional crystal structures with nanometer sized pores. Figure 2.3 (c)-(d) shows the molecular ‘building blocks’ for the bi-component PTCDI/melamine network [19] where the PTCDI molecule is a linear rod based on a perylene core functionalised on both ends with imide groups (CO,NH,CO). By combining these molecules on the Ag/Si(111) [19] and Au(111) [24] surfaces, porous hexagonal network structures can be produced. Similar to the CA·M network the hexagonal structure is formed on both substrates, but a second less symmetric network is observed to form on the Au(111) surface [25].

A variety of hydrogen-bonding interactions have been used to produce two-dimensional crystal structures, with the interactions between carboxylic acids gaining particular attention. The carboxylic group is relevant to crystal engineering as it is a highly directional hydrogen acceptor and donor. Lackinger et al. [26] demonstrated that functionalising a benzene ring with carboxylic acid groups at different positions permits a range of two-dimensional structures to be formed at the liquid-solid interface of highly oriented pyrolytic graphite (HOPG). Figures 2.4 (a) and (b) show the structures of two of the molecules investigated, terephthalic acid and isophthalic acid. When the terephthalic acid is adsorbed upon the HOPG surface it forms linear chains which are stabilised by the hydrogen-bonding interactions between the carboxylic acid groups at the ends of the molecule (shown in Figure 2.4 (c)). When the position of the carboxylic acid groups on the benzene ring is altered, as for isophthalic acid, the structure produced on the HOPG surface is altered. Figure 2.4 (d) shows the ‘zig-zag’ chains formed by isophthalic acid. This example serves to demonstrate how the highly directional nature of hydrogen-bonding interactions can be used to govern the geometry of the self-assembled crystal structures.

The carboxylic bonding interaction has also been seen to produce non-crystalline structures, as observed by Blunt et al. [27]. There are two possible hydrogen-bond motifs (Figure 2.4 (e) and (f)) which may be formed, with the directional nature of the hydrogen-bonds giving rise to two distinct molecular orientations. The *p*-terphenyl-3,5,3',5'-tetracarboxylic acid (TPTC) molecule can be seen to form structures on the HOPG surface which have orientational symmetry (i.e. the pore separation is constant), but which lack translational order. This is due to the network pores being formed from several different types of molecular arrangements (shown in Figure 2.4 (h)). The complex nature of the energy landscape for the different pore types means that a non periodic structure is produced on the surface. The formation of this kind of structure implies that thermodynamic considerations are of great importance to the formation of supramolecular structures, and it is often hard to predict an energy minima for the system under study.

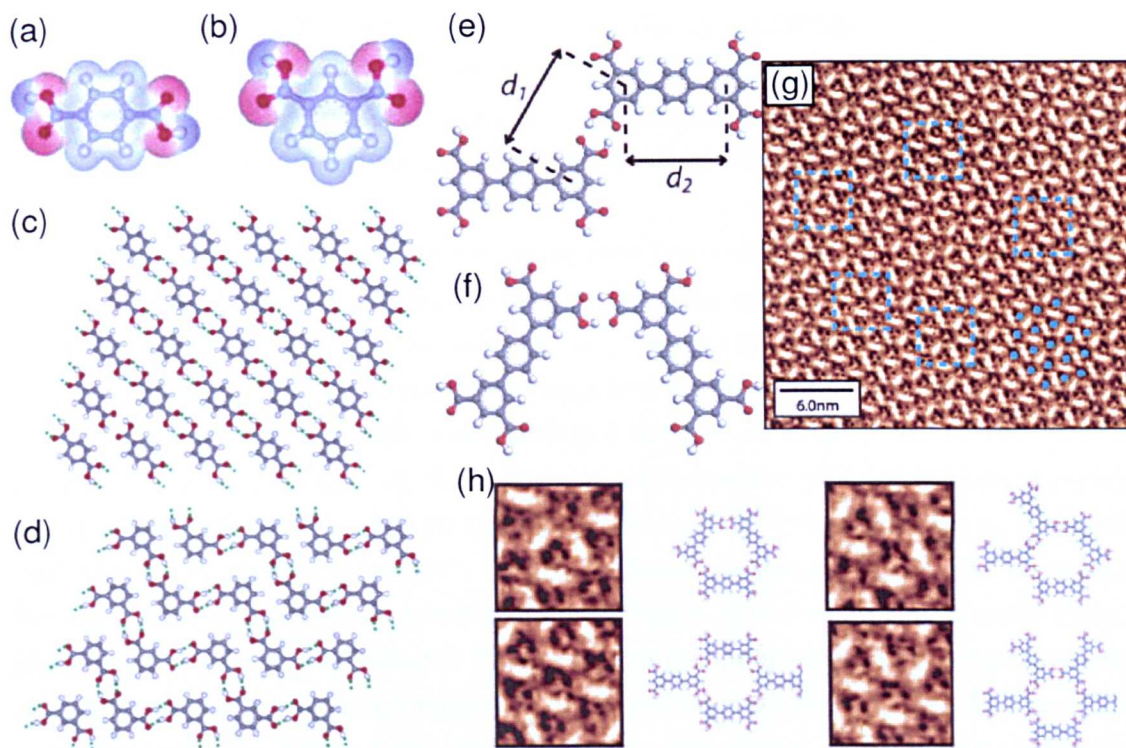


Figure 2.4: Structures formed on the HOPG surface driven by hydrogen-bond interactions between molecules with carboxylic acid functionalities. (a)-(b) Chemical structures of terephthalic acid and isophthalic acid, the negative carbonyl and positive alcohol groups are highlighted in red and blue respectively. (c) and (d) Schematics of the structures formed by terephthalic acid and isophthalic acid when adsorbed on the HOPG surface ((a)-(d) taken from [26]). (e) and (f) The ‘parallel’ and ‘non-parallel’ bonding configurations of two TPTC molecules, with hydrogen-bonds being formed between the carboxylic groups. (g) The network structure formed by the deposited TPTC on the HOPG surface. (h) The four pore types that are observed within the network, each pore type consists of several molecules bonded to each other in a mixture of the ‘parallel’ and ‘non-parallel’ geometries ((e)-(h) taken from [27]).

Two-dimensional crystals can be formed from homo, or hetero-molecular systems and may be open pored or close packed. De Feyter et al. [28] have demonstrated that by altering the structure of a molecule consisting of benzene rings which have been functionalised with carboxylic groups and alkane chains, different close-packed structures can be formed on the HOPG surface at the solid-liquid interface. These molecules combine several non-covalent bonding interactions to arrive at the observed structure, with vdW interactions between the alkyl chains and the surface being the driving force which causes the molecules to aggregate on the surface. Once on the surface the vdW interactions between the alkyl chains result in the self-assembly of the molecules to produce a lamella type structure. This vdW interaction, in combination with additional hydrogen-bonding interactions between the carboxylic groups results in a periodic close-packed structure being formed on the surface.

Homo-molecular close-packed structures formed by a combination of vdW and hydrogen-bonding interactions are also observed on surfaces in UHV, such as those

formed from PTCDA (perylene-tetracarboxylic dianhydride) [20], PTCDI [24], NTCDI (naphthalene-tetracarboxylic diimide) [29], and BDA [17]. These structures are brought into a close-packed arrangement by the vdW forces, but the internal structure of the domains is governed by the intermolecular hydrogen-bonding.

Several homo-molecular porous structures have also been produced, where the balance between the directional hydrogen-bonding interactions and the isotropic vdW interactions needs to be altered to prevent the formation of close-packed arrays. In the case of anthraquinone adsorbed on the Cu(111) surface at 80 K in UHV, a honeycomb network was produced with a periodicity of ~ 5 nm [30] (as shown in Figure 2.5 (a)). In this system a combination of a long range repulsive electrostatic interaction, due to the oxygen atoms on either side of the molecule, and the short range, attractive, hydrogen-bonding gives rise to the structures formed. This competition between the two forces drives the system away from a close-packed phase and towards this open pored structure. The structures produced by the anthraquinone molecule are also coverage dependant. At low coverages the repulsive forces mean that the molecules prefer to orientate themselves into one-dimensional chains, while at higher coverages the hexagonal network is produced. A schematic showing the hydrogen-bonds between anthraquinone molecules is shown in Figure 2.5 (b).

A similar type of behaviour has also been observed by Perdigo et al. when derivatives of PTCDI (functionalised with propylthioether and bromine side groups) are deposited upon the Ag/Si(111) surface [31]. The brominated derivative (Br_2PTCDI , Figure 2.5 (c)) is observed to form one-dimensional row structures when deposited on the Ag/Si(111) surface, with the repulsion between the negatively charged bromine atoms being responsible for the lack of two-dimensional island growth (Figure 2.5 (e)). A PTCDI derivative with propylthioether side chains (di(propylthioether)-PTCDI, labelled hereafter as S_2PTCDI , Figure 2.5 (d)) was also investigated, with the pendant groups seen to disrupt the formation of close-packed structures and actually promote the formation of a porous hexagonal phase. The observed hexagonal phase is rationalised in terms of a trimer vertex where three S_2PTCDI molecules meet, and form a hydrogen-bond structure with each molecule making two hydrogen-bonds. The effect of the pendant chains is therefore two-fold with a destabilisation of the close-packed structure observed for PTCDI, and a secondary interaction whereby the chains are involved in an additional hydrogen-bonded interaction. This example shows that the shape of the molecule plays an important role in the intermolecular forces which ultimately determine the geometry of the structures formed by self-assembly.

Hydrogen-bonding interactions are highly directional and can in theory be used to design molecular ‘building blocks’ which could give rise to structures with predetermined geometries. However, the interaction of the molecules with the substrate and the isotropic vdW forces between the molecules have to be balanced

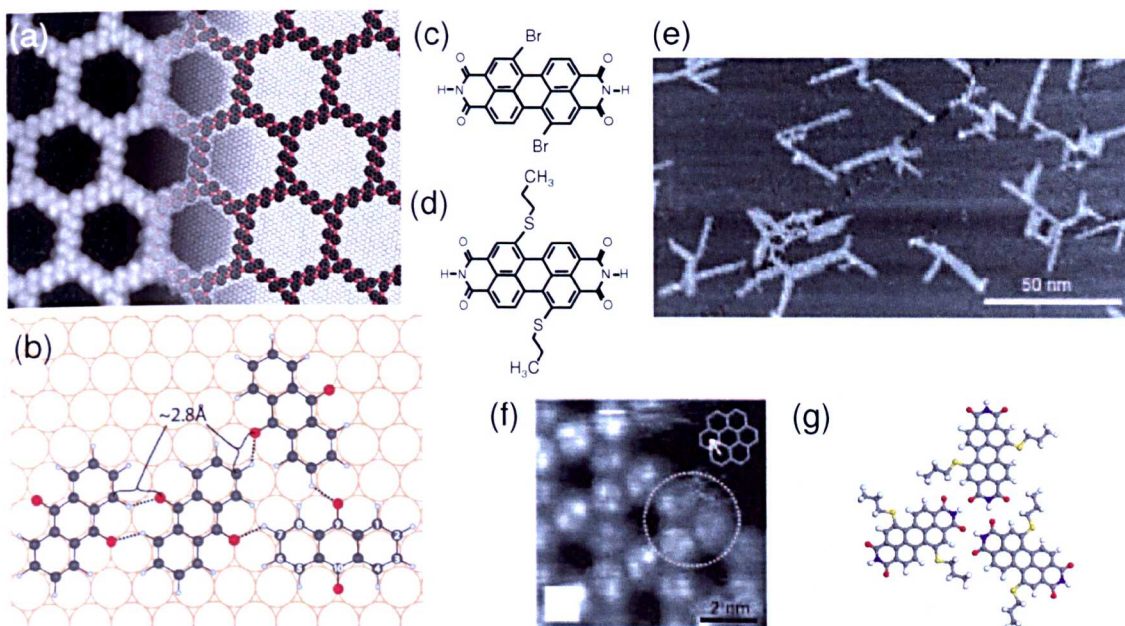


Figure 2.5: Homomolecular interactions leading to open pored and close-packed structures. (a) STM image of the porous homomolecular structure formed by anthraquinone on the Cu(111) surface. (b) Schematic showing the position of the anthraquinone molecules relative to the substrate lattice, and the hydrogen-bonding interactions which stabilise the network. ((a) and (b) taken from [30]). Chemical structures of two derivatives of PTCDI functionalised with (a) bromine atoms (Br_2PTCDI) and (b) propylthioether groups (S_2PTCDI). (e) STM image of Br_2PTCDI on Ag/Si(111), the molecules can be seen to form linear chains. (f) STM image showing an porous homomolecular network composed of S_2PTCDI . (g) Schematic showing the trimer node arrangement which stabilises the hexagonal structure. ((e)-(g) taken from [31]).

in order to prevent the formation of unwanted close-packed structures. Weber et al. [32] have used a kinetic Monte Carlo simulation to model a mixture of PTCDI and melamine molecules on a surface with a hexagonal symmetry. The model shows that if the ratio between the vdW and hydrogen-bonding forces is altered the structures formed undergo a phase transition between a hexagonal network and a close-packed structure. Similar work has been performed by Taylor et al. [33] where a kinetic Monte Carlo model was used to show that the ratio between vdW and hydrogen-bonding interactions of PTCDI molecules could determine the structure of the molecular domains, so that either two-dimensional island growth or one-dimensional chains were formed.

2.2.2 Structures formed by metal co-ordination

Metal co-ordination interactions have also been used to control the molecular assembly of two-dimensional crystals. A study of pyridine and carboxylic ligands co-deposited with Fe atoms on the Cu(111) surface by Langer et al. [34] shows how the dimensions of grid structures may be tuned by altering the size of the ligands. The organic ligands are able to bond with the metal Fe centres (as shown in Figure 2.6 (a)), giving rise to structures based on ‘right angled’ junctions. Fig-

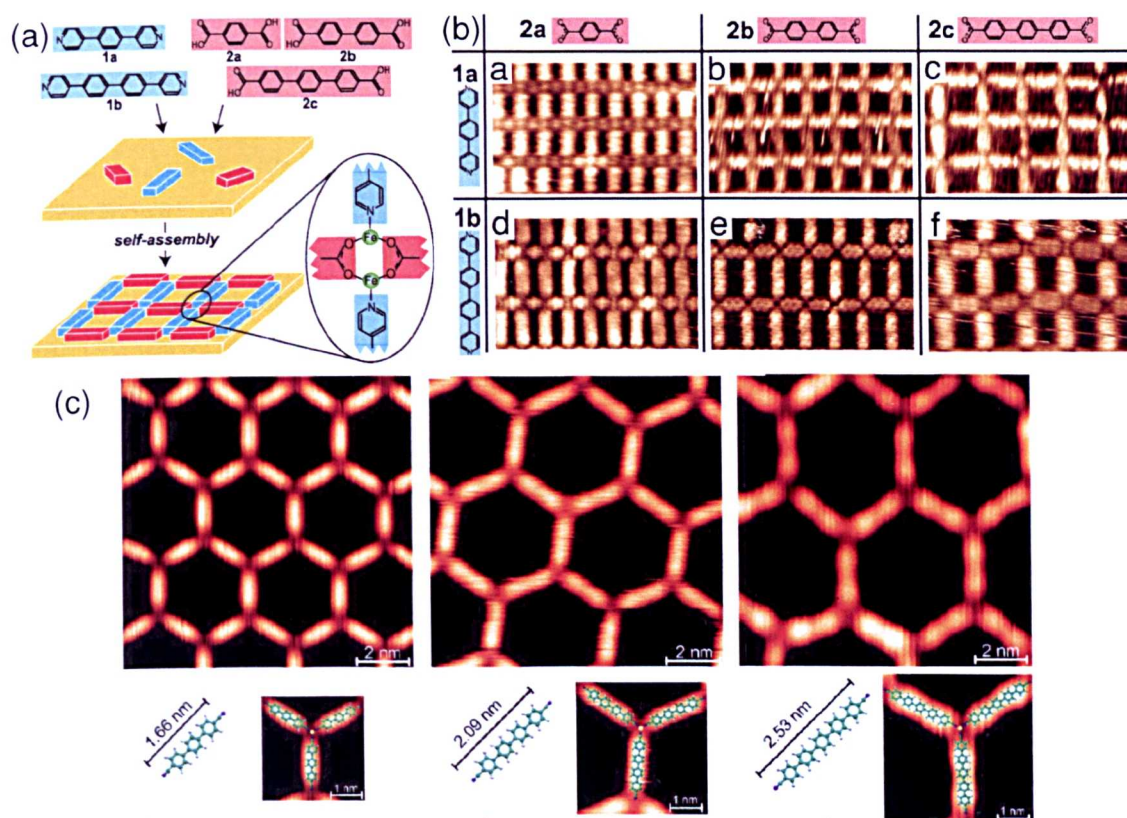


Figure 2.6: (a) Schematic showing the self-assembly process of pyridine and di-carboxylic ligands being co-deposited with Fe atoms on the Cu(111) surface. The deposited moieties are free to diffuse and form a two-dimensional grid. (b) STM images demonstrating how altering the length of the ligands used alters the size of the pores within the grid which forms. ((a) and (b) taken from [34]) (c) STM images showing the metal co-ordinate structures formed from the cobalt to ditopic dicarbonitrile-polyphenyl linkage. The pore size can again be altered by changing the length of the ligand molecules. (taken from [36])

Figure 2.6 (b) shows how using different di-pyridine and di-carboxylic based linkages the pore size of the network may be tuned. This network is of particular interest as it demonstrates ‘self-repair’ where the molecular ‘building-blocks’ can rearrange to form a stable well-ordered structure when a mixture of di-pyridine ligands, with 1 or 2 central benzene rings, are combined with a single length of di-carboxylic ligand and the Fe atoms. The resultant structure undergoes a local phase separation to produce sub-domains with different pore dimensions rather than producing incomplete grid structures with missing ligands. This finding illustrates the desired properties of self-selectivity and self-recognition. The molecules are able to diffuse over the surface and form the desired network structure, even in cases where the molecules could potentially be kinetically trapped in a local energy minima of the system. Further work by Dimitiev et al. [35] shows that the relative stoichiometry of the Fe atoms to the 1,2,4-benzenetricarboxylic acid (TMLA) ligands has an effect upon the structures formed. An increase in the surface coverage of the TMLA molecules results in a complicated structure of alternating porous and close-packed regions.

Schlickum et al. have studied a metal co-ordinated system based on the cobalt - ditopic dicyanitrile-polyphenyl linkage (shown in Figure 2.6 (c)) [36]. These structures are formed on the Ag(111) surface in UHV, and make large domains of $\sim 7 \mu\text{m}^2$. Again, the size of the network pore may be tuned by altering the length of the ligand. An interesting point to note is that the Co atoms form 3 bonds with the ligands at 120° from each other, which is different to the expected co-ordination geometry for cobalt-carbonitrile bonds in bulk complexes. This finding suggests that the underlying Ag(111) structure plays an essential role in the co-ordination stoichiometry.

2.2.3 Non-directional molecule-molecule interactions

Not all supramolecular assemblies require the presence of anisotropic interactions, such as the hydrogen-bonding and metal co-ordination discussed above. A large threefold symmetric molecule, studied by Cnossen et al. [37], has been observed to self-assemble into a honeycomb network when deposited on HOPG. The only intermolecular forces present in this system are the vdW forces, which result in the molecule forming a close-packed structure. However, the shape of the molecule means that the resultant structure is porous.

Another well-studied non-directional interaction is the vdW force between alkyl chains. It has been demonstrated that there is a preference for alkyl chains adsorbed on the HOPG surface, at the liquid solid interface, to lie flat on the surface and to form a lamella structure [38]. This interaction between alkyl chains, and between the alkyl chains and the surface, has been utilised to produce ordered structures. De Feyter et al. have shown that a range of porous and close-packed structures can be produced on the HOPG surface at the liquid solid interface [39, 40]. Synthesising molecules with alkyl chains attached to predetermined positions on a molecule allows kagome, hexagonal, and linear patterns to be formed.

Figures 2.7 (a) and (b) show two planar organic molecules which have been functionalised with alkyl chains consisting of 10 carbon atoms. When the first of these molecules (molecule **A**) is adsorbed on the HOPG surface it forms a hexagonal shaped network, as shown in Figure 2.7 (d). The molecules are adsorbed on the surface due to the substrate-molecule interaction, with the hexagonal structure being stabilised by the interdigitation of the alkyl chains. By changing the shape of the molecule (to that shown in Figure 2.7 (b)) a different structure is formed upon the surface, which has a kagome type motif. This finding demonstrates that by using synthetic chemistry it is possible to design a molecule which will interact in such a way as to produce complex patterns. Further work has demonstrated that the structures formed are concentration and coverage-dependent. Depositing molecules from a high concentration solution onto the HOPG surface results in the formation of network structures with a close-packed linear arrangement, whereas for lower concentration solutions the hexagonal structure dominates.

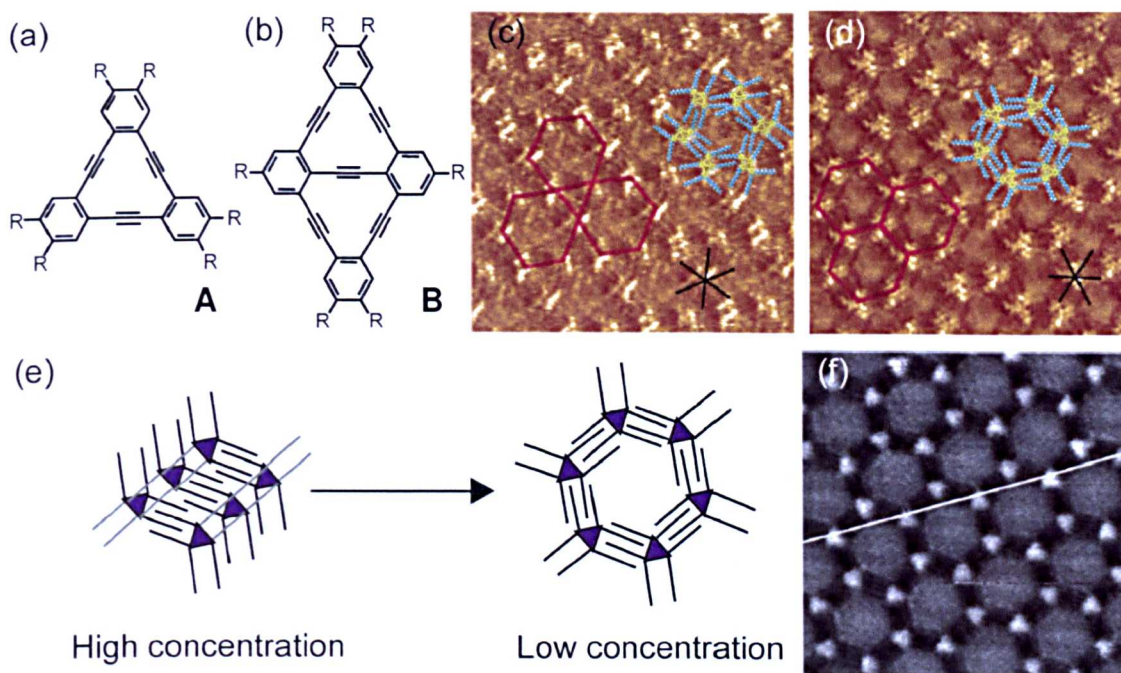


Figure 2.7: (a) and (b) Chemical structures of two planar organic molecules which have been functionalised with alkyl chains. (c) STM image of the kagome structure formed by molecule **A** on the HOPG surface. (d) STM image of the hexagonal structure formed by molecule **B** when deposited on the HOPG surface. ((a)-(d) taken from [39]). (e) Schematic showing how the concentration of molecules on the surface gives rise to different structures. (f) STM image showing the open pored structure formed by molecule **A** at low concentrations on the HOPG surface. ((e) and (f) taken from [40]).

The length of the alkyl chains also have an effect on the structures formed. The work by de Feyter and colleagues has shown that the pore sizes of the hexagonal structures formed above can be altered by varying the length of the alkyl chains attached to the molecules forming the network [41]. Another less predictable effect of the length of alkyl chains on the structures formed has been demonstrated by Wei et al. [42], where having an odd number of carbon atoms produces domains containing a racemic mixture of the two molecules, with even numbered alkyl chains giving rise to enantiomerically pure domains.

2.2.4 Covalent bonds

Supramolecular chemistry is based upon non-covalent interactions, and therefore the structures formed must be by their very nature reversible. This is likely to be problematic for possible technological applications where the structures should be stable under a range of conditions. For this reason there has been much work dedicated to the investigation of how covalent bonds may be formed to produce supramolecular structures. Work by Grill et al. [43] has shown that a protoporphyrin molecule (PP) may be functionalised with bromine atoms on 1,2 or 4 of its ‘legs’ (see Figure 2.8 (a)-(c)). After depositing the molecule on the Au(111)

surface held in UHV, and then heating the sample, the Br atoms are removed from the molecule resulting in the formation of a free radical species. The activated PP may now diffuse over the surface and form a covalent bond when it meets with another PP molecule. By altering the number of Br groups on the PP, different structures may be formed. Whereas one Br group gives rise to covalently bonded dimers (Figure 2.8 (g)), two Br groups allow a covalently bonded one-dimensional chain to be formed (Figure 2.8 (h)).

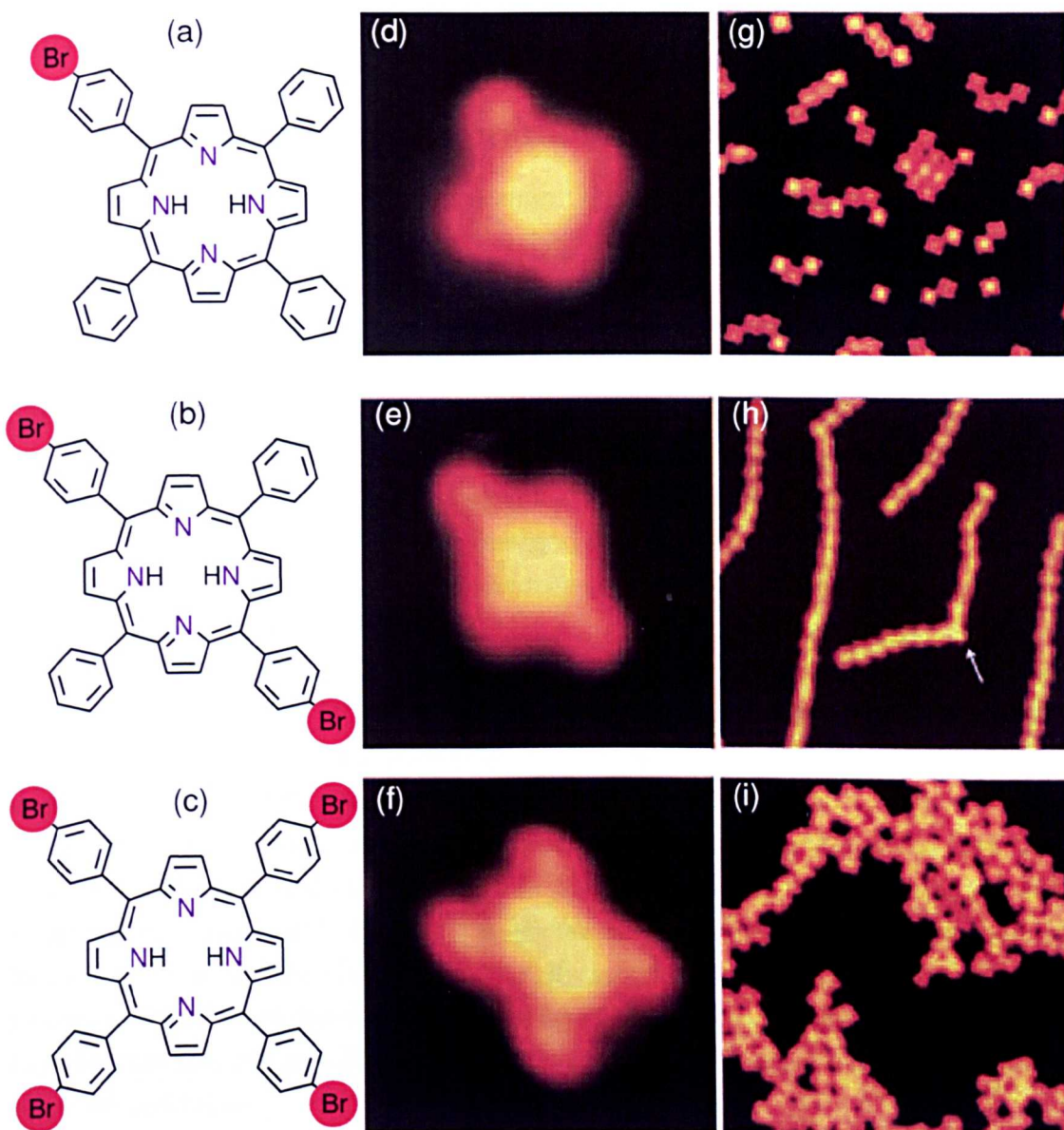


Figure 2.8: (a)-(c) Chemical structures of three proto-porphyrin derivatives, where a bromine atom has been attached to 1, 2, or 4 of the aryl side groups. (d)-(f) STM images of the proto-porphyrin ‘building blocks’, with the bromine atoms imaged as bright protrusions. (g)-(i) Large area STM images showing the covalently bound structures formed by the proto-porphyrins when heated. Dimers, linear chains, and two-dimensional structures are formed depending on the number of bromine groups each molecule possesses (taken from [43]).

Condensation reactions between aldehydes and amines have also been studied as a way of producing covalently bound structures on surfaces held in UHV [44–46]. This method has the advantage that many aldehyde-amine systems (such as PTCDA and 4,4'-diamino-*p*-terphenyl (DATP) [45]) form hydrogen-bonded porous structures. An idealised situation is one where a non-covalently bound network is self-assembled and then covalently linked by a chemical reaction. Unfortunately, while it has been shown that the condensation reaction does produce covalent links between the molecules adsorbed on the surface, the temperatures required to initialise the reaction results in the re-ordering of the network into a covalently bound 'glassy' structure.

2.2.5 Functionalising supramolecular structures

Within this chapter the use of molecular 'building blocks' as a way of creating supramolecular assemblies with predetermined geometries has been discussed. A great deal of progress has been made within this field, and the goal of being able to pick molecules that will self-assemble into a given structure is becoming realistic. A key step in producing nanoscale devices is the ability to incorporate chemical, optical, electronic, and magnetic functionalities into these systems. One potential way of doing this is to add functionality to molecular 'building blocks' which have been previously observed to self-assemble. This approach has been demonstrated by Perdigo et al. [31] where functionalised derivatives of PTCDI have been used to re-create the PTCDI/melamine hydrogen-bonded open hexagonal structures previously discussed (see section 2.2.1).

Figure 2.9 (a) shows the structure of a functionalised R_2 PTCDI/melamine hexagonal pore. The 'R' groups denote the chemical functionality attached to the PTCDI molecule. Two molecules (Br_2 PTCDI and S_2 PTCDI, Figures 2.9 (b) and (c)) were studied, and it was found that on the Ag/Si(111) surface under UHV conditions both derivatives self-assembled into a hexagonal network when co-deposited with melamine (as shown in Figures 2.9 (e)-(g)). This finding demonstrates that it is possible to alter the chemical structure of a molecular 'building block' and to retain its ability to form self-assembled structures. From the experiments it would seem feasible to further functionalise the network by adding more complex groups, potentially allowing porous reactive sites or 'nano test tubes' for selective reactions.

2.3 Molecular traps

One of the more obvious uses for a porous network is to attempt to trap other molecular species within the pores. Being able to trap molecules offers alternative routes towards functionalising the surface, raising the possibility of nanoscale catalysis, and it has even been suggested that such arrays could be used for data

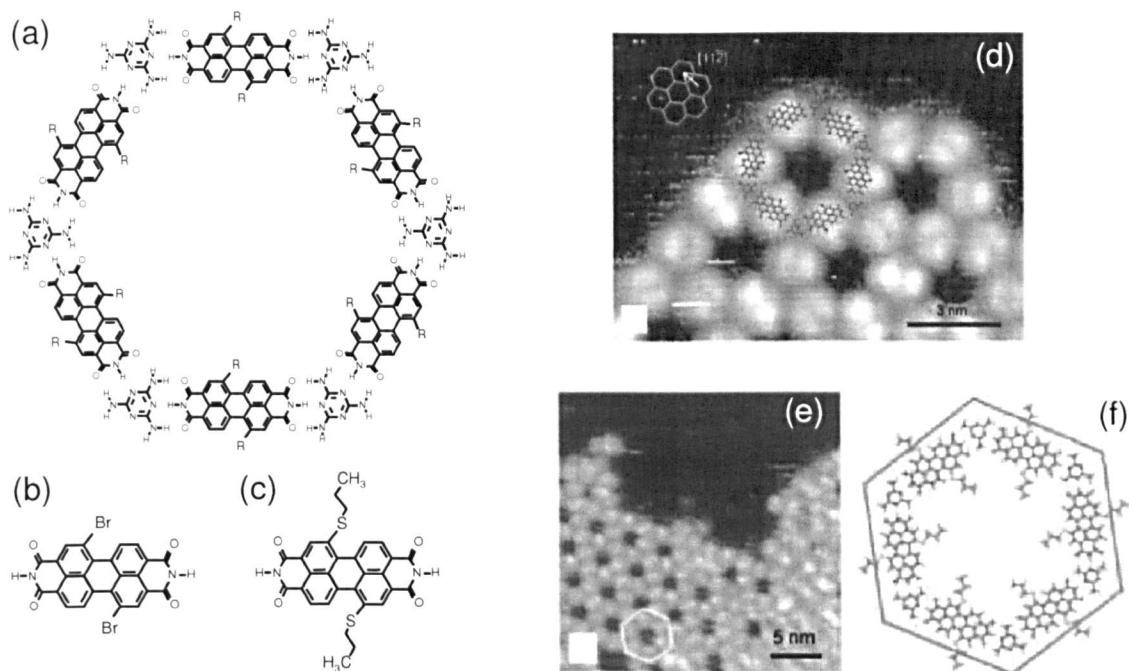


Figure 2.9: (a) Structure of a R_2 PTCDI/melamine hexagonal pore. (b) and (c) Chemical structures of Br_2 PTCDI and S_2 PTCDI. (d) STM image showing the Br_2 PTCDI/melamine network. (e) STM image showing the S_2 PTCDI/melamine network. (f) Schematic of the S_2 PTCDI/melamine network with the alkyl chains of the thioether groups pointing into the centre of the pore. ((d)-(f) taken from [31]).

storage. A wider ranging application of such porous networks however is the ability to utilise them as templates for the further growth of nanostructures. Using a method of sequentially depositing self-assembling layers, it may be possible to build up a hierarchy of order with structural features on a variety of different length scales.

Griessl et al. have investigated the guest-host interactions of the trimisic acid (TMA) honeycomb network formed on a HOPG surface [47]. In Figure 2.10 a TMA molecule has been trapped within a hexagonal pore of the TMA network structure. The trapped molecule is stabilised within the network pore via hydrogen-bonding interactions, these interactions determine the position of the molecule within the pore.

Work by Madueno et al. [48] has shown that a PTCDI/melamine network formed on the Au(111) surface at the solid-liquid interface may be used to trap and latterly organise a variety of thiol species. Thiols are well known to form self-assembled monolayers on the Au(111) surface, but here they have been trapped within the network pores with the thiols adopting a perpendicular orientation relative to the substrate (Figure 2.10). This process allows a surface to potentially be functionalised by a range of chemical groups, as the chemical functionality of the thiols may be transferred to the surface. In UHV the entrapment of thiols within a parallelogram phase of a PTCDI/melamine hydrogen-bonded network results in pairs of thiols occupying each pore with the long axis of the thiols orientated

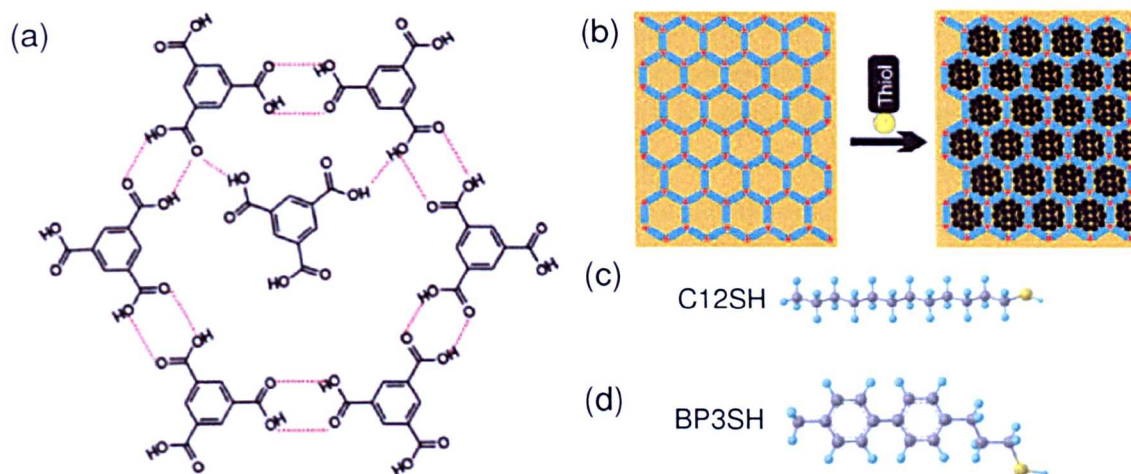


Figure 2.10: (a) Schematic showing how a single TMA molecule may be trapped within a larger TMA hexagonal network structure (taken from [47]). (b) PTCDI/melamine hexagonal network on the Au(111) surface at the solid-liquid interface. A variety of thiol species may be trapped and organised within the network pores, such as those shown in (c) and (d) ((b)-(d) taken from [48]).

parallel to the Au(111) surface [49].

The entrapment of fullerene species within a two-dimensional porous network has also been extensively studied [19,25,50,51]. Theobald et al. demonstrate that a melamine-PTCDI network may be used to selectively trap heptamers of C_{60} molecules [19]. This size selective trapping again demonstrates the possibility of being able to design systems that may self-assemble to produce order on several different length scales. The work done by Staniec et al. [25] has shown that the entrapment of fullerenes in a parallelogram network can lead to a hierarchy of order. The network itself assembles and then selectively traps dimers of C_{60} within its pores. A much larger length scale of ordering is also observed as rows of C_{60} form, where the presence of one dimer increases the probability that a neighbouring pore will be filled in one of the row directions of the network.

The entrapment of endohedral fullerenes within such network pores would add an additional chemical functionality to the surface. Li et al. have shown that a porous template formed on HOPG at the solid-liquid interface may be used to trap endohedral fullerenes [52]. This approach allows a lateral organisation of functionalised fullerene species on a surface.

2.4 Summary

In this chapter an overview of the recent progress with the field of two-dimensional surface-supported self-assembly has been presented. The concept of supramolecular chemistry has been explored, and examples of two-dimensional crystals that may be formed on surfaces both in UHV and ambient conditions have been discussed. It has been shown that from an understanding of the non-covalent inter-

molecular forces between the molecular ‘building blocks’, the production of a wide range of structures is theoretically possible. However, the subtle balance between the forces stabilising these self-assembled structures is hard to predict and control. Steps towards being able to use such templates to organise and trap other molecular species have been shown and will be built upon throughout the rest of this work. The idea of introducing chemical functionality has been discussed, either by functionalising the ‘building blocks’ or by trapping functionalised species, and will form a major focus for the rest of this thesis.

Chapter 3

Experimental techniques and materials

In this chapter the experimental techniques which have been used during the course of this research are described. The principles of scanning tunnelling microscopy and photoelectron spectroscopy (PES) are discussed, together with descriptions of the apparatus used. UHV-ESD is introduced as a method of transferring fragile molecules into UHV. Finally, the surface reconstruction of Au(111) is discussed as well as the techniques used for its preparation.

3.1 Scanning tunnelling microscopy

The development of the STM may be considered a major contributing factor in the birth of nanotechnology. The STM was revolutionary among surface techniques, allowing a real space image of the substrate under study. The STM was pioneered by Binnig and Rohrer [53] and it enabled lateral resolution several orders of magnitude greater than any other technique around at the time.

STM is now one of a large family of scanning probe microscopies (SPMs) such as atomic force microscopy (AFM) [54] and scanning capacitance microscopy (SCM) [55]. All of these techniques produce a real space ‘topography’ of the substrate/adsorbate system under study by measuring the magnitude of the tip-surface interaction. The nature of the interaction provides information about specific physical properties of the material depending on the type of SPM being employed. However, it is important not to interpret the real space image produced by a SPM technique as a simple height topography of the surface. AFM provides information about the force between the tip and the surface, with the magnitude of the interaction determining the apparent ‘height’. An STM measures the flow of electrons between the probe and the surface, with the electrons undergoing a quantum mechanical tunnelling process.

An STM image of a surface is produced by measuring the magnitude of the interaction between the tip and the surface for a grid of points. Each of these

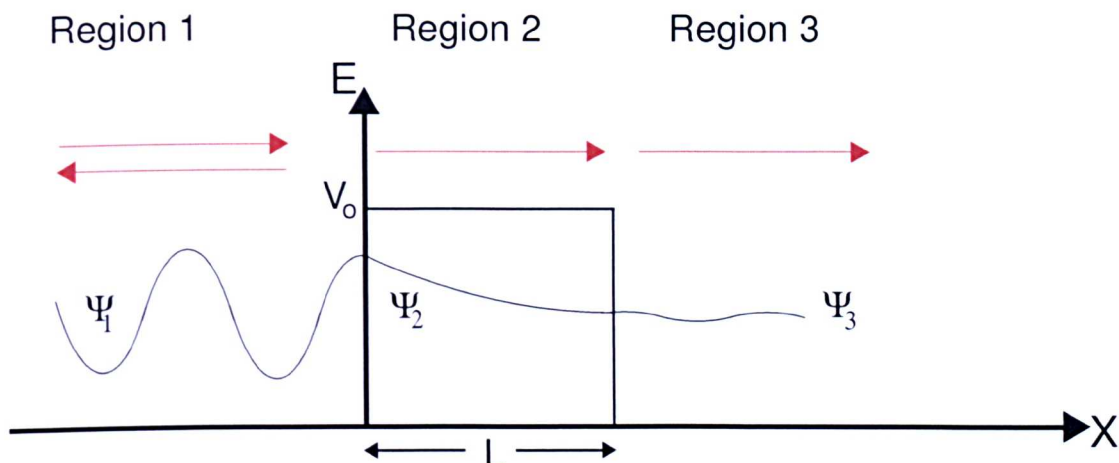


Figure 3.1: Schematic representation of a one-dimensional rectangular potential barrier, illustrating the quantum tunnelling phenomena. Barrier has height V_0 and length L .

points corresponds to a single pixel in the resultant image. The following sections will discuss the principles behind the acquisition of STM images.

3.1.1 Principles of STM - Quantum mechanical tunnelling

The STM apparatus in its simplest form consists of an atomically sharp tip and a scan-tube made from a piezoelectric crystal. The tip is brought close to a surface, a bias voltage is applied between the tip and the surface, and the current flowing between the two is measured. The observed current is a result of the quantum mechanical tunnelling of electrons between the tip and the sample. A one-dimensional rectangular potential barrier may be used to represent the vacuum gap between the tip and the sample, as shown in Figure 3.1 [56]. Assuming that the gap is sufficiently narrow, electrons may tunnel from one side of the potential barrier to the other.

A wave function for an electron of mass, m , and energy, E , incident on a finite potential barrier of height V_0 and length L may be written for each of the three regions shown in Figure 3.1.

$$\Psi_1 = A_0 e^{ikx} + A e^{-ikx} \quad (3.1)$$

$$\Psi_2 = B e^{\alpha x} + C e^{-\alpha x} \quad (3.2)$$

$$\Psi_3 = D e^{ikx} \quad (3.3)$$

where $k = \frac{\sqrt{2mE}}{\hbar}$ and $\alpha = \frac{\sqrt{2m(V_0-E)}}{\hbar}$. It is then possible to calculate a transmission probability for an electron to tunnel through this barrier [56].

$$T = \left| \frac{D}{A_0} \right|^2 \approx 16 \left(\frac{E}{V_0} \right) \left(1 - \frac{E}{V_0} \right) e^{-2\alpha L} \quad (3.4)$$

The tunnel current is proportional to the transmission probability, T , and is therefore exponentially dependent on the width of the potential barrier, L , and the variable α . The width of the barrier is the distance between the sample and the tip and the variable α is dependent on the effective barrier height ($V_0 - E$) and therefore the applied bias. The significance of equation 3.4 is that the tunnel current is exponentially dependent on the tip-sample separation, giving rise to sub-Ångstrom vertical resolution.

Tersoff-Hamman theory

An alternative approach to describe the tunnel current between two metals separated by a vacuum was formulated by Bardeen [57]. In Bardeen's formulation each metal electrode is treated as an independent system, negating the need to solve the Schrodinger equation for the combined system, and allowing the vacuum gap region to be evaluated using perturbation theory. We may apply this model to the tunnelling between the STM tip and the surface, by considering one of the electrodes as the tip and the other as the surface. The tunnel current for such a system has been shown to be given by [57, 58]:

$$I = \frac{2\pi e}{\hbar} \sum_{\mu,\nu} f(E_\mu)[1 - f(E_\nu + eV)] |M_{\mu\nu}|^2 \delta(E_\mu - E_\nu) \quad (3.5)$$

where $f(E)$ is the Fermi function, V is the applied voltage, and $|M_{\mu\nu}|$ is the tunnelling matrix element for transitions between state ψ_μ of the tip and ψ_ν of the surface. E_μ is the energy of an electron in the tip state ψ_μ in the absence of the surface.

The expression may be broken down into its constituent parts with $f(E_\mu)[1 - f(E_\nu + eV)]$ giving the probability of an electron occupying a filled tip state (ψ_μ) and of there being an empty surface state (ψ_ν) with the same energy. This ensures that only tunnelling from filled to empty states is permitted. The delta function in equation 3.5 represents the conservation of energy in the case of elastic tunnelling. The final term in the equation is the 'matrix tunnelling element' which may be interpreted as the probability of the tip and the surface states overlapping, a necessary condition to allow tunnelling to occur.

By making the assumption that the applied bias voltage is small, and that the system is at room temperature, the equation describing the tunnel current may be simplified to:

$$I = \frac{2\pi}{\hbar} e^2 V \sum_{\mu,\nu} |M_{\mu\nu}|^2 \delta(E_\nu - E_F) \delta(E_\mu - E_F) \quad (3.6)$$

where E_F is the Fermi energy. This equation may be further simplified by considering the case where the tip is replaced by a point probe [59] to arrive at:

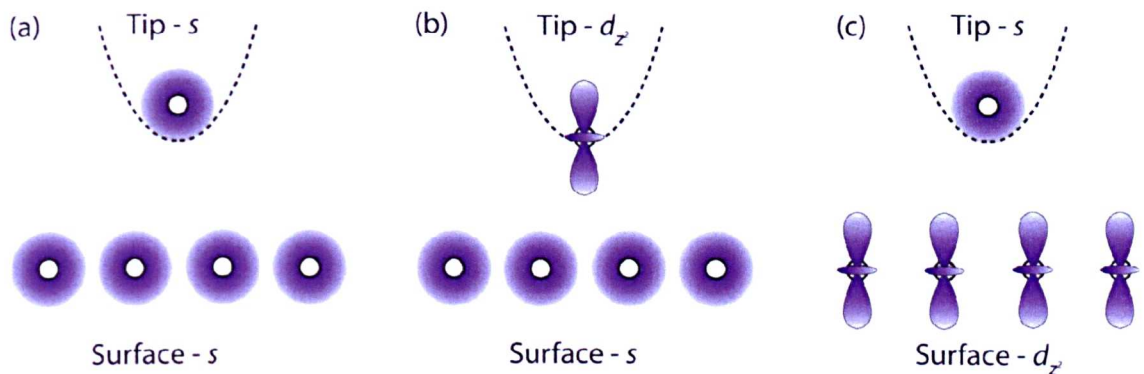


Figure 3.2: Schematic showing the reciprocal nature of the interacting orbitals of the tip and the surface (adapted from [61]).

$$I \propto \sum_{\nu} |\psi_{\nu}(r_o)|^2 \delta(E_{\nu} - E_F) \quad (3.7)$$

where $|\psi_{\nu}(r_o)|^2$ is the probability density of the surface state wavefunction evaluated at the position of the point probe, $r = r_o$. This simple formulation states that the measured current is proportional to the local density of states (LDOS) of the surface, at the Fermi level, at the position of the point probe, r_o .

As an extension to the model where the STM tip is considered a point probe, Tersoff and Hamann [59] have shown that the tip may be modelled as a spherical potential well (corresponding to an s-type electronic orbital at the tip apex). This model led to the prediction that the lateral resolution of an STM would be limited to a value of 6-9 Å. However, experimentally determined values for the lateral resolution of STM images acquired of metallic substrates are significantly better than this (2.5-3 Å [60]). This is due to the tip states used to image the surface having a higher angular momentum, p_z or d_z², than the s-type orbitals assumed above [61].

The reciprocity principle states that interchanging the tip state and the surface state should result in the predicted STM images being identical [61]. An STM topograph produced by imaging a series of s orbitals using a tip with a protruding d_z² orbital will be identical to that produced by imaging a series of d_z² orbitals on the surface with a s orbital at the tip apex (the tip and surface orbitals for such configurations are shown in Figure 3.2). Figure 3.2 (c) shows the second of these situations illustrating that the observed periodicity of the surface will be resolved on a much smaller length scale than if both the tip and the sample possessed purely s-type orbitals. Chen [61] has re-evaluated the Tersoff-Hamann tunnelling matrix for a tip with a d_z² orbital. A tip terminated with a d_z² orbital will follow the derivatives of the surface wavefunctions which will have a much stronger corrugation than the Fermi level LDOS.

In summary, the tunnelling current measured using an STM contains information about the LDOS at the position of the tip. For tips terminated with an

atom possessing a dominant s state a constant current STM image will represent a contour map of the LDOS. However, greater corrugation may be achieved when a sharper orbital is present on the terminating atom of the tip, and for this reason the tips most suitable for producing high resolution STM images are those made from d-band metals (e.g. Pt, Ir, W) and semiconductors which form dangling p_z bonds (e.g. Si).

Sample bias and the direction of current flow

Figure 3.3 shows the tunnelling of electrons between the sample and the tip, demonstrating how applying a bias affects the direction that they travel and the energy of the states that they may occupy. When zero bias is applied the Fermi levels of the sample and the tip are equal (Figure 3.3(a)). If a positive bias is applied to the sample then the Fermi level of the tip is raised relative to that of the sample, by an amount eV , where V is the applied bias. This allows the tunnelling of electrons from the filled states in the tip to the empty states in the sample, as shown in Figure 3.3(b), and provides information about the empty states of the sample. Alternatively we may apply a negative bias to the sample, Figure 3.3(c), allowing tunnelling from the filled states in the sample to the empty states of the tip.

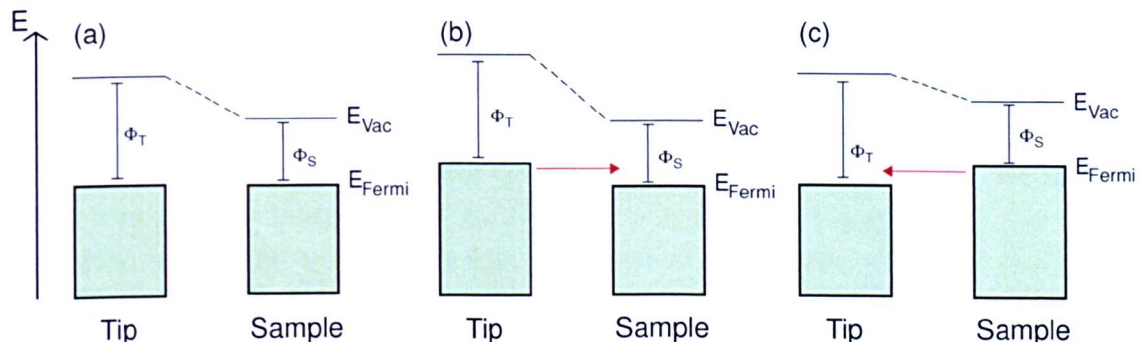


Figure 3.3: Schematic showing how electrons may tunnel between the filled and empty states of the tip and sample. (a) Zero applied sample bias. (b) Positive sample bias. (c) Negative sample bias.

For an applied bias of approximately zero the tunnel current is proportional to the LDOS at the Fermi level, as stated in equation 3.7. For finite voltages, such as those commonly used during STM operation, the current may be approximated by summing the contributions of the LDOS across a range of energies where tunnelling is possible. The current is therefore given by:

$$I \propto \int_{E_F}^{E_F+eV} |\psi(E, r_o)|^2 \delta(E - E_F) T(E, eV) dE \quad (3.8)$$

where $T(E, eV)$ is the transmission co-efficient (defined in equation 3.4). The variations in $T(E, eV)$ with V can be large, but for small biases we may assume that $T(E, eV)$ remains constant.

$$I \propto \int_{E_F}^{E_F+eV} |\psi(E, r_o)|^2 \delta(E - E_F) dE \quad (3.9)$$

It is interesting to note that taking dI/dV results in an expression for the density of states. This is the basis for scanning tunnelling spectroscopy where I is measured as a function of V at a given point on the sample, and the derivative of this data shows information about the energy of LDOS at that point.

Tunnelling through adsorbed molecular species

STM may be used to image molecular species which have been adsorbed on a surface. The electronic structure of a molecule is often expressed in terms of a set of molecular orbitals, all of which have well defined energies, and which may be filled or empty. The highest occupied molecular orbital is labelled the HOMO with all other filled orbitals labelled as the HOMO-1, HOMO-2, etc. Similarly, the lowest unoccupied molecular orbital is labelled the LUMO, with subsequent empty orbitals labelled as the LUMO+1, LUMO+2, etc. In the limit of the weak coupling regime the transfer of the electrons from the tip to the surface could be treated as two separate tunnelling steps, with the electrons tunnelling between the tip and the molecule and then between the molecule and the surface. However, the molecule is in close-proximity to the surface and so is likely to be strongly coupled to the surface states, meaning that the energies of the molecular orbitals will be pinned relative to the Fermi energy of the surface [62]. This is demonstrated in Figure 3.4 where electrons are shown tunnelling to the molecular orbitals of an adsorbed molecular species. Figure 3.4(a) shows electrons moving from a negatively biased tip to LUMO of the molecule. Figure 3.4(b) shows the situation where the tip polarity has been inverted, allowing electrons in the the HOMO of the molecule to tunnel into unoccupied tip states.

In terms of the tunnelling model outlined above the HOMO and LUMO of a molecule will be imaged in STM there is a non-zero probability density for the wave function describing the orbital present at the position of the STM tip, and there is a non-zero transmission co-efficient:

$$I \propto \int_{E_F}^{E_F+eV} |\psi(E, r_o)|^2 \delta(E - E_F) T(E, V) dE \approx \int_{E_F}^{E_F+eV} |\psi_{mol}(r_o)|^2 T(E_{mol}, V) \quad (3.10)$$

where $|\psi_{mol}(r_o)|^2$ is the probability density for the wave function of the molecule at position r_o , and $T(E_{mol})$ is the transmission co-efficient. The states are summed over the energies E_F to $E_F + eV$, and if the HOMOs or LUMOs of the molecule lie within this range they will be imaged during the STM scan.

For substrate-molecule systems a positive sample bias will result in the LUMO being imaged, and for a negative sample bias the HOMO of the molecule will be imaged. It has also been shown that the molecular orbitals of molecules adsorbed

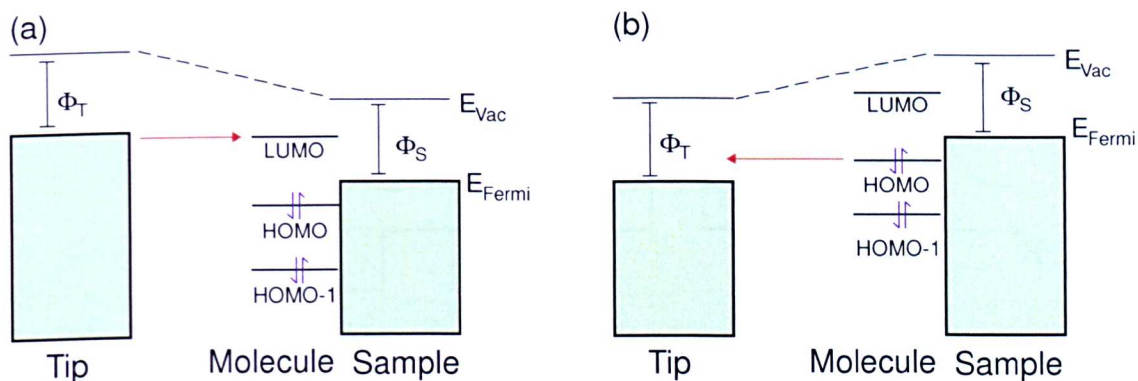


Figure 3.4: Schematic showing the energetic states of an STM tip, an adsorbed molecule, and a sample. Strong coupling between the molecule and the sample pins the HOMO and LUMO relative to the Fermi level of the sample. (a) For a positive sample bias, tunnelling from the tip to the LUMO is observed. (b) For a negative sample bias, tunnelling from the molecular HOMO is observed.

on inert metal surfaces such as Ag will be imaged with little contribution from the surface states [63].

3.1.2 Modes of STM operation

An STM may be operated in one of two main modes, constant height or constant current. In both modes the tip is raster scanned over the surface with a series of parallel linescans being acquired. For each linescan the current is recorded at a number of points (256 points per linescan for the STM used for this work), with each point corresponding to a single pixel in the final STM image. The individual linescans are combined over the course of the scanning procedure to produce a complete STM image. In constant height mode, Figure 3.5(a), the vertical position of the tip, Z , is not altered. This particular scan mode presents problems as sudden variations in surface height will result in the tip crashing into the surface, destroying the atomically sharp tip and prevent further high resolution scanning. In constant current mode the vertical position of the tip is continuously altered so as to keep the tunnel current constant, and the variation in vertical tip position, Z , is recorded, as shown in Figure 3.5(b).

If we assume the simple relationship between the tunnel current and the tip sample separation, the variation in Z could be seen as a description of the topography of the surface. Figure 3.5 (c) demonstrates the effect of an insulating defect on the path of the tip, during operating in constant current mode. As the tip passes over the defect it will move closer to the surface in order to maintain constant current. This change in Z will be observed as depression on the surface, whereas in reality the surface has a small protrusion at this point. The example illustrates the dangers of interpreting STM data as a simple height profile of the surface.

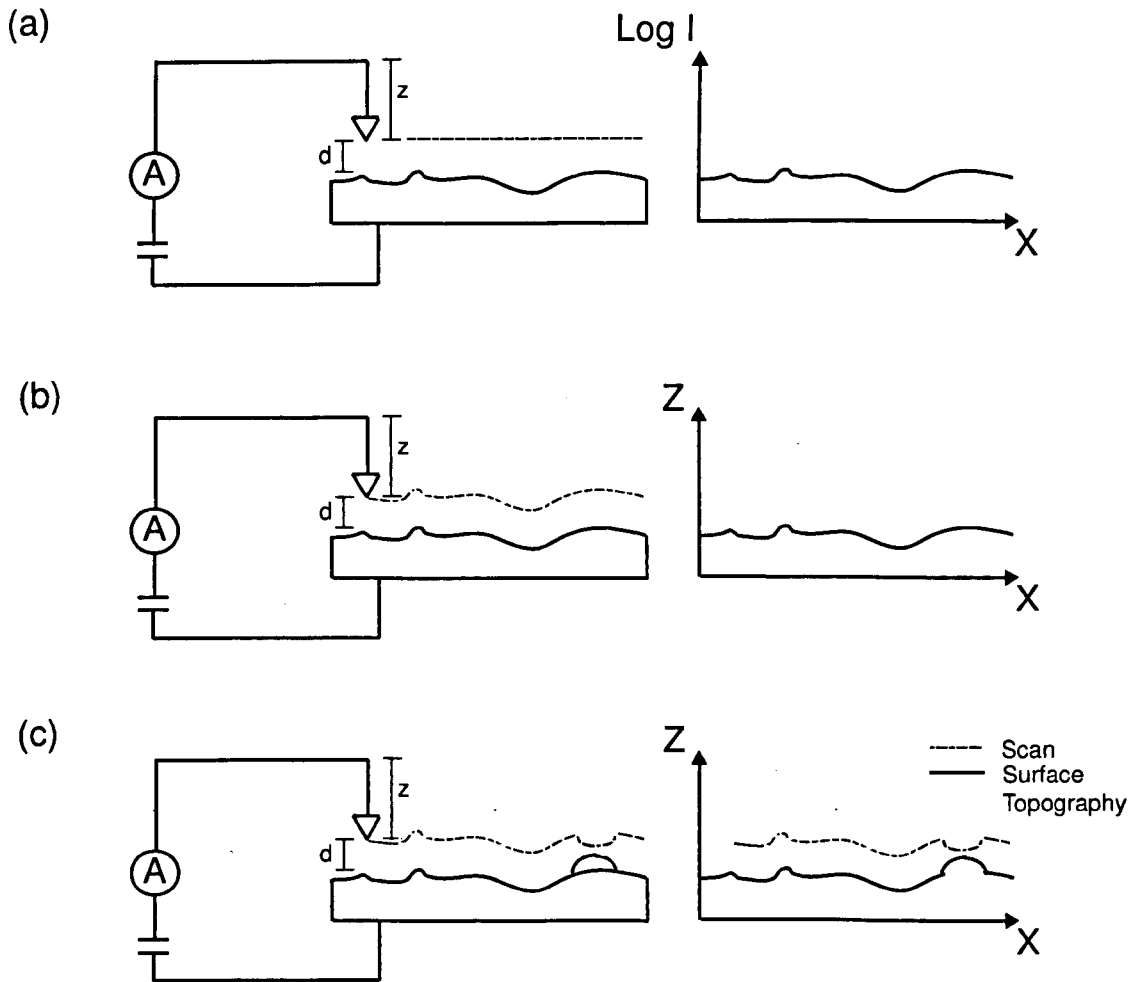


Figure 3.5: Diagram showing the different imaging modes of STM. (a) Constant height mode. (b) Constant current mode. (c) The effect of insulating surface features on a STM linescan.

Feedback control in constant current mode

A PI (proportional, integral) feedback system is used to obtain a given value for the tunnel current, I_{set} . During STM operation the current is recorded, $I_{meas}(t)$, and the difference between these two values gives the error signal, $\Delta I(t)$, which can then be used to calculate the distance the tip needs to move in order to maintain I_{set} . This process is iterative and does not immediately result in the tip returning to a position where I_{set} is obtained. For each iteration the change in the vertical position of the tip is given by $\Delta Z(t)$:

$$\Delta Z(t) = \alpha \Delta I(t) + \beta \int_0^t \Delta I dt \quad (3.11)$$

where the first term is the proportional contribution to the change in Z and the second term is the integral contribution to the change in Z . α and β are respectively the proportional and integral gain constants, which may be tuned in order to improve the response of the system.

Figure 3.6 shows how the measured current changes over time for various values

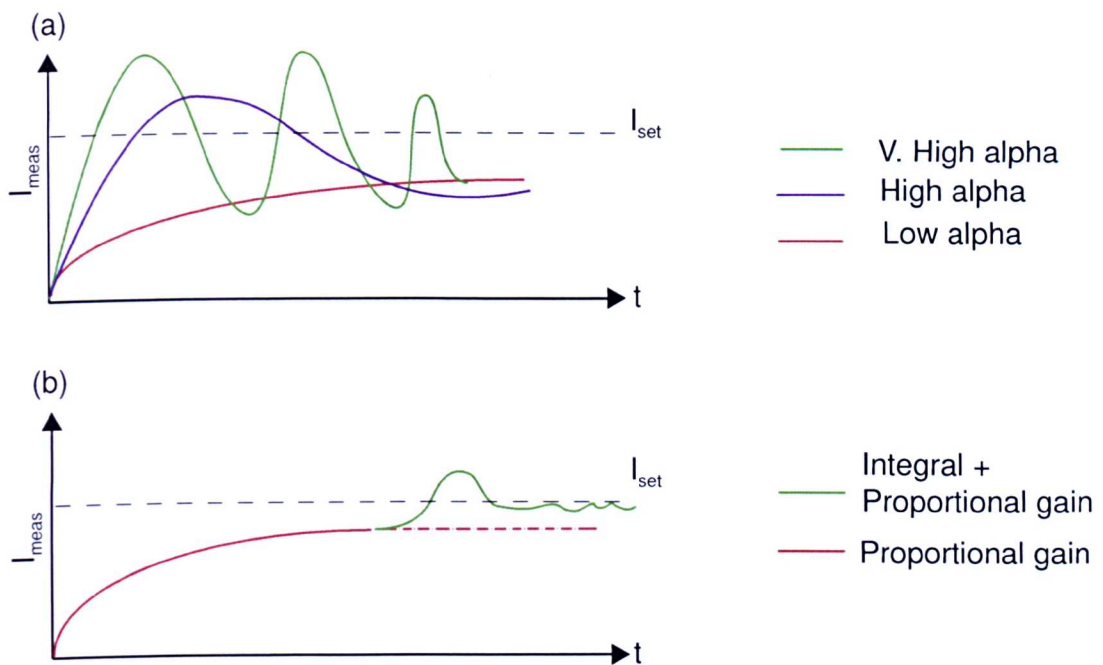


Figure 3.6: Diagram demonstrating the effect of different feedback parameters. (a) How variation in α affects the approach to the set point. (b) How integral and proportional gains are combined to arrive at the set point.

of the proportional and integral gain constants. A feedback loop responding only to the proportional gain will never reach I_{set} , and so the integral gain must also be incorporated. The values for α and β must be chosen with care. If α is too high the response of the tip will be too great when it encounters an object adsorbed on the surface, leading to instability. Conversely a small value of α will lead to the tip not responding quickly enough to changes in surface height, resulting in a tip crash. If the value for the integral gain constant, β , is too high, a resonance is introduced into the current signal. The ideal β value is just before the onset of this resonance.

During the acquisition of an STM image it is important that the PI feedback loop is given sufficient time to ensure that current at each pixel in the scan is equal to I_{set} . For this reason the STM tip ‘dwells’ for a set time at each pixel where the current is allowed to stabilise to a value of I_{set} . For each pixel several measurements of the tip position are acquired, with an average value being used in the final STM image.

3.1.3 Controlling tip position

The STM tip positioning system requires both fine and coarse movements. Coarse movement is required to allow the tip to be positioned at a variety of locations on the surface, as well as to retract the tip from the surface by a macroscopic distance to allow sample transfer. These movements are on the length scale of several millimetres, and for this a slipstick inertial motor is used [64, 65]. The

operation of the motor is shown schematically in Figure 3.7. The stage holding the piezoelectric scan-tube and the tip is mounted atop a piezoelectric plate with a shear motion. A voltage is applied to the piezoelectric plate with a sawtooth-type wavefunction, producing two types of motion. Firstly, the slow increase in voltage causes a slow shear movement in the piezoelectric plate, pushing the scan-tube stage forward, shown in Figure 3.7(b). Secondly, the rapid decrease in voltage causes the plate to return to its original position leaving the scan-tube stage in its forward position 3.7(c). The continued repetition of this slipstick motion allows the scan-tube stage to move forward rapidly over distances of mm, while moving in discrete steps with each step being on the order of a few nanometers.

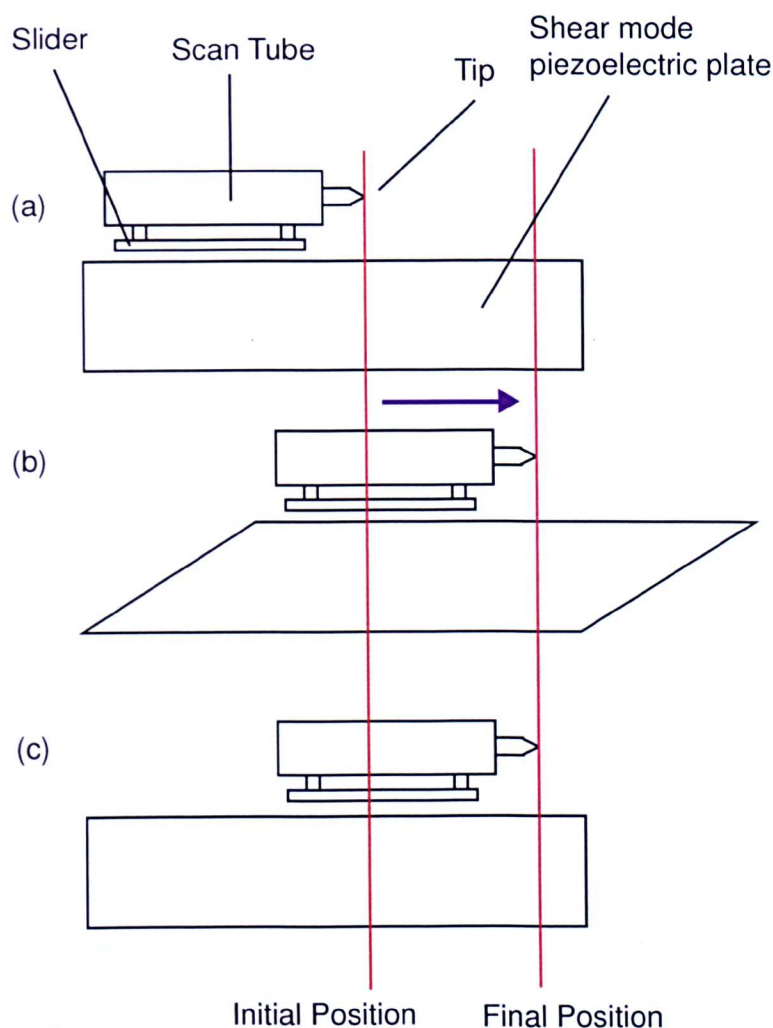


Figure 3.7: Schematic showing the motion of a slipstick inertial motor. (a) Initial position of scan-tube. Voltage to the shear mode piezoelectric crystal is slowly increased. (b) Scan-tube is moved forward as piezoelectric crystal shears. (c) By rapidly removing the voltage the piezoelectric crystal returns to its original position leaving the scan-tube in its new location (adapted from [66]).

The scan-tube is constructed from PZT ($\text{Pb}(\text{Zr}, \text{Ti})\text{O}_3$) [58], with the STM tip attached to one end of the tube. The tube is split into four quadrants, each sharing a common ground at the centre of the tube. When a voltage is applied to one of

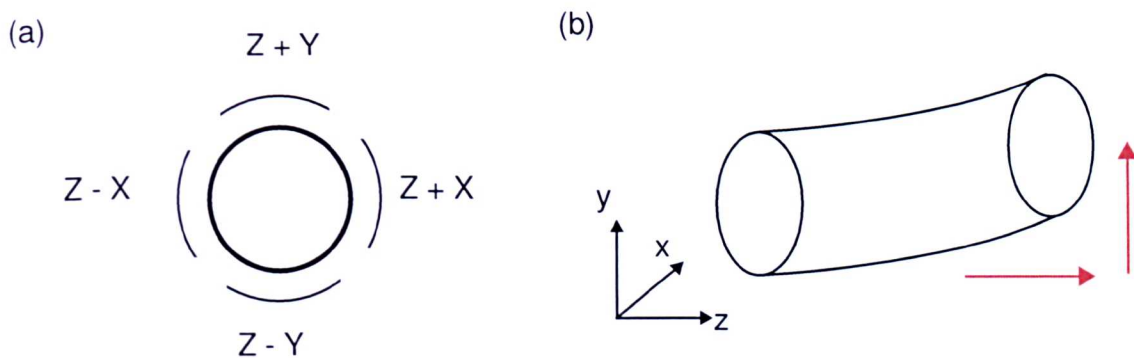


Figure 3.8: Illustration of the motion of the piezoelectric scan-tube. (a) End on view showing the four quadrants of the scan-tube. (b) Schematic showing motion of scan-tube due to an applied voltage.

the quadrants it extends or contracts depending on the sign of the applied voltage. This results in a change in Z direction and induces a bending motion in either the X or Y direction depending on the restrictions implied by the stationary quadrants. Figure 3.8 shows how these quadrants are set-up. By varying the voltage applied to each of the quadrants it is possible to move the scan-tube, and hence the tip, very precisely in all three dimensions. These motions are used for varying the tip height above the surface in the feedback loop and for controlling the rastering of the tip across the surface during scanning.

Experimental limits of STM

The resolution of an STM is limited by vibrational noise, tip geometry, and the piezoelectric controlled movement of the tip. The tunnel current is highly sensitive to the tip-surface separation, and as such it is important that vibrational motion is removed from the system. In order to avoid the images acquired being dominated by the oscillation of the tip due to external mechanical vibrations being coupled with the system, STMs are decoupled from their surrounding environment by damping the STM ‘stage’, which contains the tip and the sample, and by the vibrational isolation of the STM system by use of a pneumatic table.

The tip geometry is of obvious importance, and although in the ideal situation the tip will be perfectly symmetric and terminated by a single protruding atom (preferably with a d_{z^2} orbital present), in reality this is unlikely to be the case. A tip will have several protruding atoms, all of which will facilitate tunnelling between the tip and the sample. Depending on the distance between these protrusions, features such as step edges may appear blurry or even as two distinct features (known as ‘tip doubling’). Another observed effect due to the tip apex structure is that the surface may ‘image’ the tip and the shape of the tip may appear as a topographic feature within the acquired STM image. The shape of the tip may be altered by applying short high voltage pulses to it, facilitating the re-ordering of the atoms at the tip apex. Repeated pulsing results a variety of

tip geometries to be sampled, allowing the STM operator to obtain a tip which provides ‘good’ resolution.

The movement of the scan-tube over the surface can also introduce artefacts into the acquired STM images. Piezoelectric creep is an effect observed when the STM tip is moved from one surface site to another, resulting in the tip continuing to move relative to the surface after the desired movement has finished [67]. This problem can be overcome by allowing the scan-tube to settle in the new position before commencing imaging.

A major experimental limitation of STM imaging is due to thermal drift, and is of particular relevance to the work undertaken here as all the experiments are conducted at room temperature. Thermal drift introduces an uncertainty in the relative positions of the tip and the surface. With no thermal drift the path of the STM tip should map out a square section of the surface, but with thermal drift present the tip will map out a section of the surface with a parallelogram shape. Thermal drift may be reduced by allowing the tip-sample stage to thermally equilibrate with the rest of the UHV-system, but it is also possible to compensate for the effects of drift via image processing. Applying skew and stretch operations to a thermally drifted image will result in regaining the correct dimensions of the acquired data.

3.2 Photoelectron spectroscopy

PES is a term which covers a range of techniques that utilise the photoelectric effect to gain information about surfaces and molecular systems [60]. For isolated atomic elements there are several discrete electronic states that may be populated with electrons. The energies of these states are determined by the combination of protons, neutrons and electrons that make up the individual chemical element, and as such may be used as a unique ‘finger print’ to identify the presence of a particular atomic species within a sample.

3.2.1 The electronic levels of atoms and molecules

The electronic orbitals of an atom may be split into two categories; those which participate in the bonding and interaction with other atomic species are the valence orbitals, while those which are tightly bound to the nucleus are the core orbitals. The core orbitals are associated specifically with one atom, whereas the valence orbitals of two chemically bonded atoms overlap and delocalise over the area of the interaction. These overlapping valence orbitals produce new molecular orbitals based on a linear combination of the atomic orbitals (LCAO) and are then associated with the molecule as a whole rather than a particular atom. The filled valence states of a molecule are termed the HOMOs, with the filled orbital closest to the Fermi level being labeled the HOMO, and the subsequent filled orbitals

known as the HOMO-1, HOMO-2, etc. Similarly the empty valence states are termed the LUMOs, with the empty orbital closet to the Fermi level being labeled the LUMO, and the subsequent empty orbitals being defined as the LUMO+1, LUMO+2, etc. The core states are labelled by the quantum numbers required to describe the orbitals and are written as nl , where n is the number of the orbital shell and l is the angular momentum. Figure 3.9 shows the electronic states of an organic molecule.

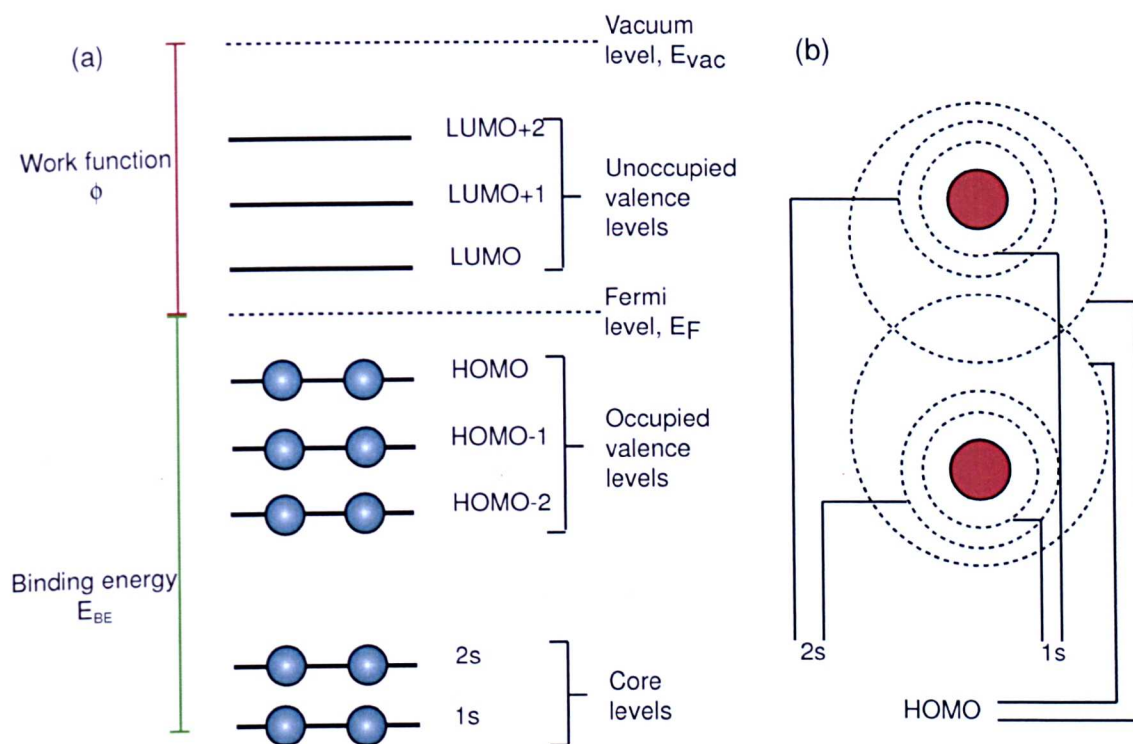


Figure 3.9: (a) Schematic of the electronic energy levels for a molecule. (b) Schematic showing the overlap of atomic orbitals to give rise to the molecular HOMO.

To allow a comparison of binding energies between different atomic species a definition of a zero energy level is required. A conventional reference point is the Fermi level of the system under study. The Fermi level is defined as the energy where the probability of an electron being present is $\frac{1}{2}$, which for a metal (at low temperatures) lies just above the highest occupied electronic level. For intrinsic semiconductors the Fermi level is positioned in the centre of the band gap, and for molecules the Fermi level should be halfway between the HOMO and the LUMO.

The photoelectric effect is observed when a beam of monoenergetic photons, with energy $h\nu$, are incident on a sample. Photoelectrons will be ejected with kinetic energy E_{KE} (providing the energy of the incident photons is greater than the work function of the material). From a knowledge of the kinetic energy of the ejected photoelectron and the energy of the incident photon, the binding energy (BE) of the electronic state from which the photoelectron was removed may be determined using equation 3.12.

$$E_{BE} = h\nu - E_{KE} - \phi \quad (3.12)$$

where ϕ is the workfunction of the material.

3.2.2 Surface sensitivity

One of the many benefits of PES techniques is their inherent surface sensitivity. X-rays incident on the surface have a penetration depth of several microns [68], although due to the inelastic scattering process undergone by the photoelectrons, only photoelectrons produced near the surface will have sufficient kinetic energy to leave the sample. Photoelectrons produced deep within the bulk will undergo so many inelastic scattering events that they will have insufficient kinetic energy to reach the surface. Photoelectrons produced a few atomic layers below the surface will escape with a greatly reduced kinetic energy and will be registered as a broad background signal to any measurements taken.

The inelastic scattering processes may include energy transfer to other electrons, or the excitement of phonons and/or plasmons, within the surface bulk. All of these interactions will reduce the kinetic energy of the photoelectrons. A measure of how far the electron may travel through a particular medium is given by the inelastic mean free path, $\lambda(E)$. Equation 3.13 shows the relationship between the initial and final intensities for a flux of electrons travelling a distance d through a material [69].

$$I(d) = I_0 \exp\left(-\frac{d}{\lambda(E)}\right) \quad (3.13)$$

where $I(d)$ is the intensity of an electron beam after travelling a distance d through a material with an initial intensity of I_0 . The inelastic mean free path of an electron is defined as the distance an electron beam travels before its intensity is reduced by $\frac{1}{e}$ (~ 0.37) of its initial value [69].

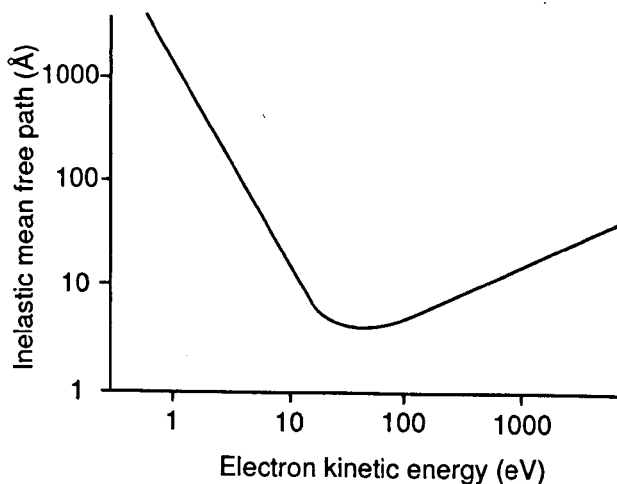


Figure 3.10: Universal curve showing how the inelastic mean free path of electrons varies with their kinetic energy (adapted from [69]).

The inelastic mean free path is highly dependent on the kinetic energy of the electrons. The empirically derived ‘universal curve’ [69] is depicted in Figure 3.10 and shows that the shortest mean free path ($< 10 \text{ \AA}$) is given for electrons with kinetic energies of between 40-100 eV. A short mean free path gives rise to a high surface sensitivity, therefore it is ideal to produce photoelectrons with kinetic energy of the order of 50 eV. To achieve this an incident photon energy 50 eV greater than the BE of the electron energy level being probed is required.

3.2.3 X-ray photoelectron spectroscopy

Isolated atoms have orbitals with unique energies and when, as discussed above, two atoms are brought together the atomic orbitals combine to form molecular orbitals. However, the core-orbitals of the atom remain largely unchanged and it is these core-orbitals that may be investigated using XPS to identify the type of atoms present.

The fundamental concept of XPS is that the sample of interest is illuminated with X-ray photons of energy $h\nu$, liberating electrons from the core orbital levels of the atomic elements within the sample. The kinetic energy of the emitted electrons may be measured, and by applying knowledge of the photoelectric effect (equation 3.12), the BE of the orbital from which the electron was removed may be obtained. By comparing the BE obtained from XPS analysis of a sample to a reference table [70], it is a simple matter to determine the types of material which are present within the sample.

The ability to identify the types of elements within a given sample makes XPS a powerful tool for chemical analysis. By illuminating a sample with high frequency X-rays it is possible to obtain BEs for all the elements within the sample, and hence determine the chemical composition of the sample. Although XPS can identify different elements, it may also be used to identify the specific chemical environments that these atoms are in. To understand how this works a consideration of the ‘initial state’ is required.

Initial state effects - Chemical shifts

XPS is highly sensitive to the energy levels of the initial system. The core-levels act as a way of determining the type of atom present, but these core-levels are perturbed by the presence of neighbouring atoms. This effect may be demonstrated by considering the C 1s core-level of a carbon atom, which would be expected to have a BE of $\sim 294 \text{ eV}$. Figure 3.11 (a) shows the chemical structure of a fluorinated ethyl acetate molecule, whose XPS spectra is shown in Figure 3.11 (b) [71]. The XPS spectra clearly shows four peaks which have different BEs corresponding to four distinct chemical environments.

The positions of these peaks are described in terms of a chemical shift i.e. how much the environment of a given atom is changed from a reference value

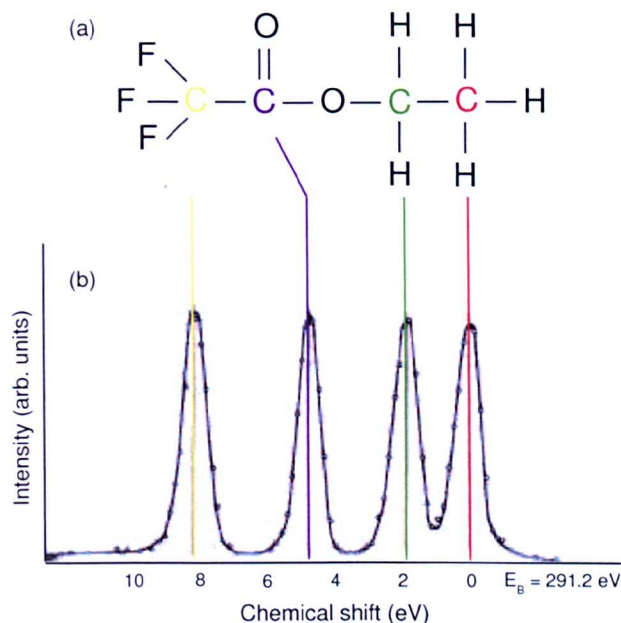


Figure 3.11: XPS spectra illustrating the ‘initial state effects’ on BE. (a) Chemical structure for a fluorinated ethyl acetate molecule, (b) XPS Spectra showing the C 1s peaks and their corresponding chemical environments (adapted from [71]).

due to its interaction with the neighbouring atoms. The peak corresponding to the CH₃ group is labelled with a chemical shift of 0, with the CH₂ group being shifted by ~ 2 eV due to the presence of a neighbouring oxygen atom. The effect of neighbouring atoms on the chemical shift may be understood in terms of the electronegativity of the neighbouring atoms. Oxygen has a greater electronegativity than carbon and so will withdraw electronic character away from the carbon atom (CH₂) resulting in an increase in the BE of the C 1s core-level, and hence a chemical shift. The same is true for the CF₃ carbon with the chemical shift being more pronounced due to the high electronegativity of the three fluorine atoms.

Final state effects

In the formulation of the photoelectric process it is assumed that the electrons within an atom, and their corresponding energy levels, are unperturbed by the removal of the core electron during an XPS experiment. This is known as Koopmans’ theory [72] where the final state is assumed to be equivalent to the initial state minus an electron. However, the formation of the core-hole is unstable and the electrons within the atomic levels may re-arrange, giving rise to a difference between the final and initial states and hence the kinetic energy of the outgoing electron will be lowered. This in turn will lead to a value for the BE of the electron which is artificially inflated.

Two examples of commonly observed re-arrangements are shown in Figure 3.12

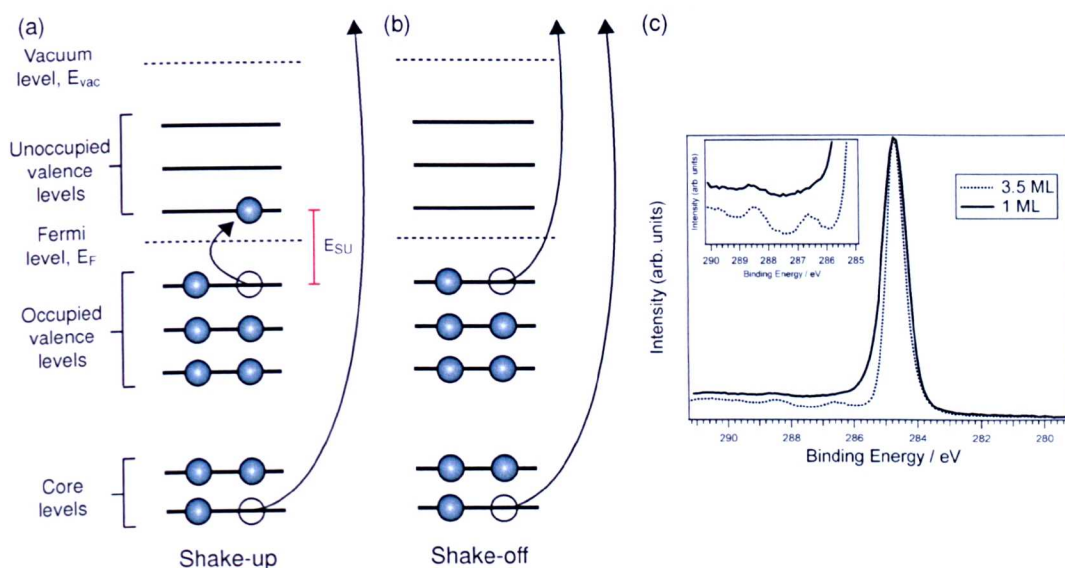


Figure 3.12: Schematic depicting shake-up and shake-off of electrons as a result of the removal of a core-electron. (a) Shake-up process, (b) shake-off process, (c) C 1s XPS spectra from C_{60} deposited on the Au(111) surface. Inset shows peaks that correspond to shake-up features (C 1s XPS spectra taken from [73]).

where electrons may move from the HOMO to the LUMO or even be ejected from the molecule/atom. These re-arrangements are known as shake-up and shake-off effects. For a shake-up effect (Figure 3.12 (a)) the outgoing electron will lose kinetic energy equal to the difference between the initial and final energies of the shake-up electron E_{SU} , which manifests itself as a chemical shift in the XPS spectrum. Figure 3.12 (c) shows the C 1s XPS spectrum for C_{60} deposited on an Au(111) surface, with the small peaks to the high BE side of the main peak being due to a shake-up feature. Shake-up features are well defined for multi-layer coverages with the shake-up in the monolayer being quenched by the presence of the surface. This quenching is due to a disruption of the LUMO by the surface. Shake-off features (Figure 3.12 (b)) are not commonly observed due to the high energy cost involved.

Spin-orbit coupling

Electron spin plays an important role in the structure of XPS spectra. In section 3.2.1 electronic orbitals were described in terms of the quantum numbers n and l . Electrons also possess a spin ($s = +1/2, -1/2$, up or down) and the electrons within an orbital will form ‘up-down’ pairs. Electrons in an electronic orbital interact amongst themselves so as to conserve total angular momentum, j ($j = l + s$). The removal of an electron from an orbital during XPS leaves a now un-paired electron in either the up or the down state. Depending on the value of s adopted by the unpaired electron, two different j states will be produced, which will have two different energies [68]. The relative intensities of these two states are determined by the degeneracy, i.e. the number of electrons in each state, which is

given by $2j + 1$ (NB for s-type states which have $l=0$ there is no splitting).

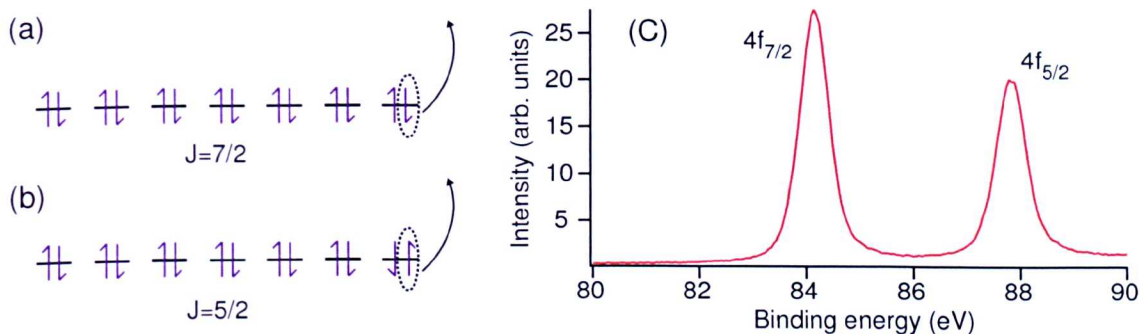


Figure 3.13: Schematic showing how the removal of an electron from a high angular momentum orbital will result in a splitting of energy levels. (a) Removal of a ‘down’ electron from the 4f to leave the 4f_{7/2} electronic state. (b) Removal of an ‘up’ electron from the 4f to leave the 4f_{5/2} electronic state. (c) XPS Au 4f spectra showing the splitting of the states.

Figure 3.13 (a) and (b) shows the electron structure for the Au 4f state ($n=4$, $l=3$) which gives rise to j values of $7/2$ and $5/2$. This will produce a relative intensity of 4:3 for the two peaks, and an energy splitting of 3.7 eV, which is shown in the XPS spectra in Figure 3.13 (c). As an aside, the electron states may be described in terms of the $j-j$ coupling or $l-s$ coupling and may be expressed as nl_j or ^{2s+1}L respectively. Within this work $j-j$ coupling notation is used and hence the two Au peaks are labelled as Au 4f_{7/2} and 4f_{5/2}.

Line shape and experimental accuracy

In an ideal view the peaks would be observed as δ -functions at fixed binding energies. However, experimentally obtained data shows the broadening of the peaks, which may be explained due to two distinct effects. Firstly, the core-hole created by the removal of an electron has a finite life time, and the relaxation of the electrons in the atom gives rise to a Lorentzian broadening of the signal [68]. Secondly, the peak will be broadened due to experimental uncertainty in the energy of the incident X-ray, and in the detection of the emitted electrons (producing a Gaussian broadening of the peak). Therefore XPS data needs to be fitted with a combination of Gaussian and Lorentzian line shapes to accurately model the peak shapes.

3.2.4 Near edge X-ray absorption fine structure

The previous section described how XPS may be used to obtain information about the core-levels of atoms to identify the element and its chemical state. This section discusses the NEXAFS technique and details how it may be used to probe the unoccupied levels of both atoms and molecules. Probing the unoccupied states provides information about the oxidation state of the material and even the orien-

tation of the molecular orbitals relative to the plane of the surface. Both of these applications are investigated as part of the later chapters of this work.

X-ray absorption and the relaxation of atoms

The incident X-rays used in XPS are chosen so that they have sufficient energy to remove a core-electron from an atom. NEXAFS measurements are acquired using X-rays with energies tuned so that a core-electron may be excited into an unoccupied state. Figure 3.14 (a) shows the absorption of an X-ray photon which has been tuned to excite an electron from an occupied core-level to an unoccupied valence-level. The absorption of X-rays may be calculated by measuring the intensity of the X-rays before and after they are incident on the sample, but it is more common to measure the effect of the absorption indirectly.

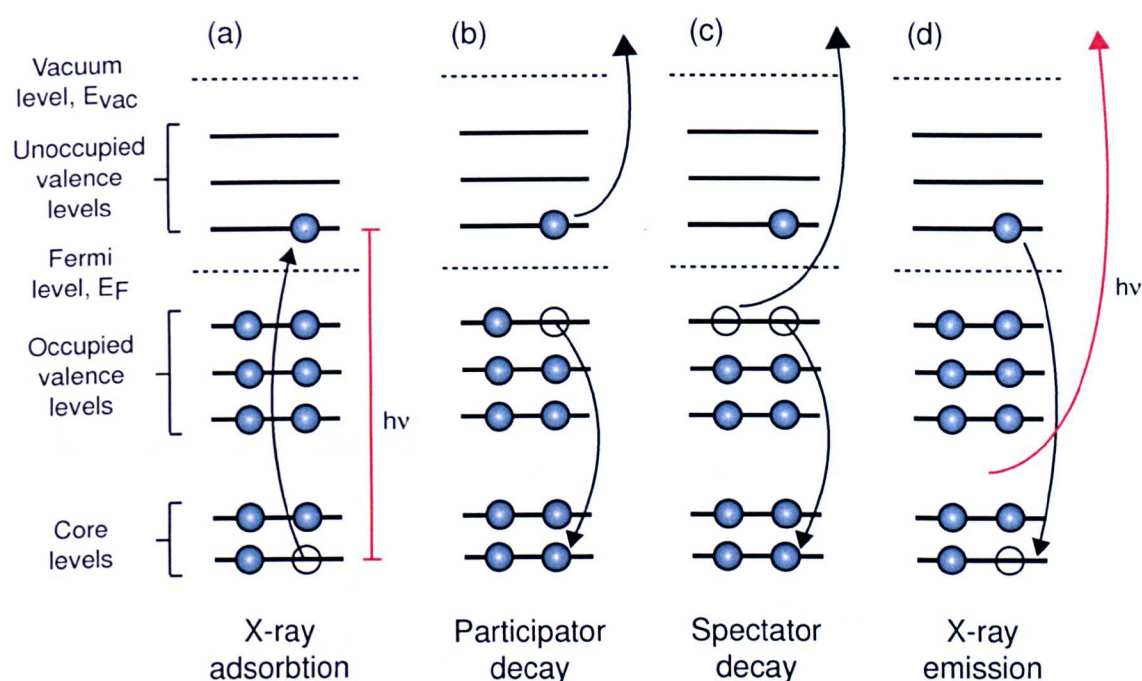


Figure 3.14: Schematic showing the re-arrangement of electrons during (a) X-ray absorption ($h\nu$ tuned to excite electron to the LUMO), (b) participator Auger decay, (c) spectator Auger decay, (d) X-ray emission.

Figure 3.14 (b)-(d) shows three possible routes for the relaxation of the excited atoms. The first two routes are Auger processes, with an electron dropping down to fill the empty core-hole state resulting in the emission of an Auger electron. The Auger electron may be the original excited electron (participator decay) or a valence electron (spectator decay). The final process (Figure 3.14 (d)) is X-ray emission where the excited electron drops back into the core-hole and gives out energy as a photon. This process is more common for heavier elements and therefore for light elements the flux of Auger electrons is proportional to the X-ray absorption.

The NEXAFS spectrum

A NEXAFS spectrum is obtained by scanning over a range of X-ray energies, starting at a point below resonance (i.e. the energy required to excite a core-electron to the lowest unoccupied orbital). An ideal system containing an isolated atom, as shown in Figure 3.15 (a), will have valence and core-levels which are occupied with electrons as well as unoccupied states. From this simple picture it is possible to predict the expected NEXAFS spectra. Figure 3.15 (b) shows a schematic of a NEXAFS spectrum for an isolated atom. Peaks are observed where the photon energy is tuned so that a core-level electron is excited into one of the unoccupied states. The feature to the right of the spectra demonstrates excitation into the continuum of states, which do not have resolvable discrete energy levels.

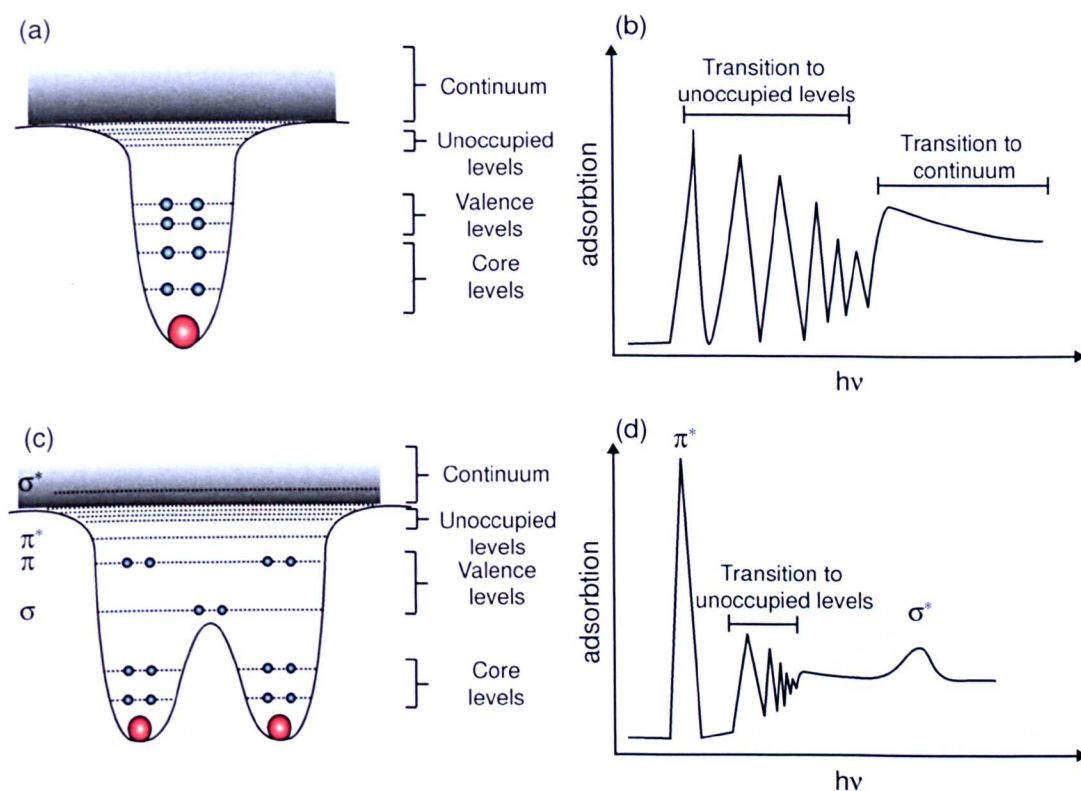


Figure 3.15: Schematic showing the predicted NEXAFS spectra for single atoms and diatomic pairs. (a) Energy levels for a single isolated atom. (b) Predicted NEXAFS spectra for an isolated atom. (c) Energy levels of a diatomic pair with σ and π bonds. (d) Predicted NEXAFS spectra for a diatomic pair (image after [74]).

In the situation where two atoms are bonded together, so that π and σ bonds are formed, the NEXAFS spectrum alters dramatically. Figure 3.15 (c) shows the energy levels formed from the combination of the orbitals of two atoms, where the LCAO results in the formation of π and σ bonding orbitals as well as the π^* and σ^* anti-bonding states. The predicted NEXAFS spectra for a pair of bonded atoms is given in Figure 3.15 (d), with two new features being depicted. The peak corresponding to a transition to the π^* state is seen to appear, and the broad peak which appears among the continuum levels is due to a transition to the σ^* state.

The NEXAFS technique has been utilised in two ways during this work. First, by considering the transitions to unoccupied levels we may determine which states are filled and which are empty, allowing a determination of the oxidation states of transition metals. Second, we use angle resolved NEXAFS to investigate the molecules orientation on the surface. This technique is described within the next section.

Angle resolved NEXAFS

A useful property of NEXAFS is the relationship between the orientation of the orbitals to which an electron is excited and the polarisation of the X-ray that is used to excite the transition. X-rays produced by a synchrotron are linearly polarised, allowing a range of angles between the E-vector of the incident X-rays and the substrate to be investigated.

As the polarisation of the σ^* orbitals runs along the direction of the bond and the polarisation of the π^* orbitals runs perpendicular to the σ^* polarisation vector, the maximum transition probabilities are 90° out of phase with each other [75]. The π^* and σ^* have a $\sin^2\theta$ and a $\cos^2\theta$ dependence, respectively (where θ is the angle between the vector of a sigma bond and the polarisation vector of the incident X-ray), on the absorption probability and so by applying a knowledge of the orientation of the E-vector relative to the surface plane the orientation of the molecular bonds can be determined.

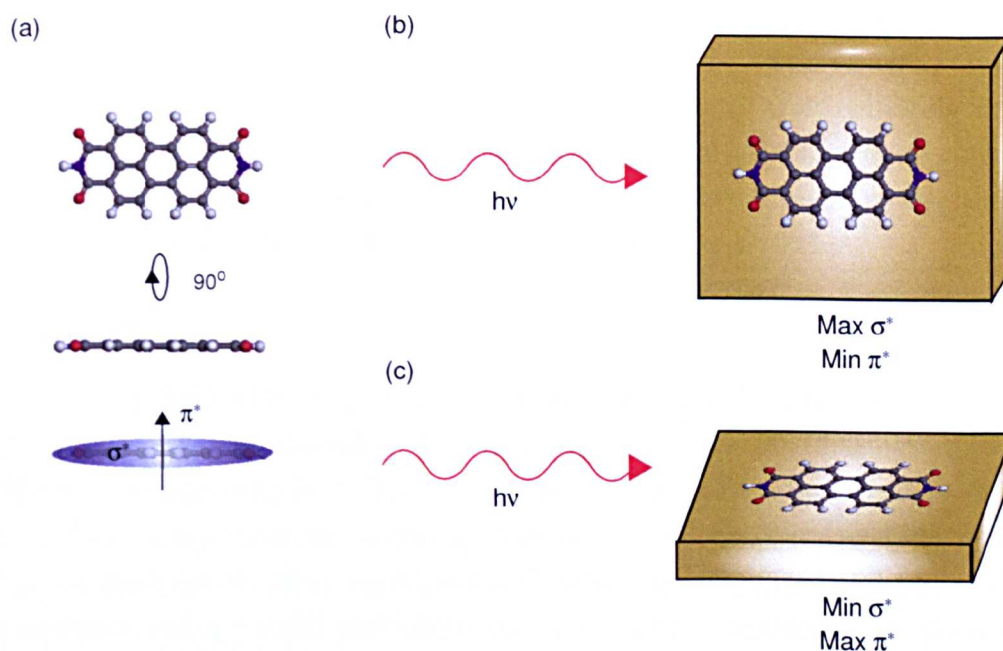


Figure 3.16: Schematic showing the angular dependence of the NEXAFS technique. (a) Chemical structure of the PTCDI molecule, with the polarisation directions of the π^* and σ^* orbitals highlighted. (b) PTCDI molecule lying parallel to the Au(111) surface with the E-vector of the incident X-rays being parallel to the surface plane. (c) PTCDI molecule lying parallel to the Au(111) surface with the E-vector of the incident X-rays being perpendicular to the surface plane (after [66]).

Figure 3.16 (a) shows a PTCDI molecule (a planar molecule with σ^* and π^* orbitals), which we may consider to be lying parallel to the plane of the substrate. When the polarised E-vector of the incident photons is parallel to the σ^* plane of the molecule, as in Figure 3.16 (b), the σ^* transition signal is maximised and the transition to the π^* orbital is minimised. If the sample is rotated by 90° so that the E-vector is now parallel to the π^* orbital vector, as in Figure 3.16 (c), the transition to the π^* orbital is now maximised. This angular dependence allows the orientation of the molecules orbitals relative to the surface to be determined.

3.2.5 Synchrotron radiation sources

Synchrotrons are large scale facilities which are able to produce a range of polarised electromagnetic radiation with frequencies ranging from the infra-red to hard X-rays. A monochromator may be used to select a narrow band of photon energies synchrotron radiation can be utilised to perform a range of experiments, including XPS and NEXAFS [76].

At the start of the process, electrons from an electron gun are accelerated using a linear accelerator (LINAC). The electrons are transferred to a booster ring where they undergo further acceleration and are finally released into the storage ring where they will have an energy of several GeV (~ 1.5 GeV at Max II). The storage ring is a polygon with a number of straight sections linked by vertices where a bending magnet is used to alter the direction of the electrons. At each bending magnet vertex, the velocity of the electrons is altered, producing photons which are used as the source of X-rays for the experiments conducted at the synchrotron's beamlines. Synchrotron radiation is approximately linearly polarised with the E-vector being parallel to the plane of the storage ring. The synchrotron experiments discussed within this work were undertaken at the Max II synchrotron facility in Lund, Sweden, using beamline D1011.

Beamline D1011

The XPS and NEXAFS experiments reported here were conducted at beamline D1011 at Max-II. The beamline has an energy range of 20-1500 eV and uses a SX-700 monochromator [77]. The end station consists of a preparation chamber with facilities for annealing, argon sputtering of the sample, and UHV-ESD, as well as an analysis chamber equipped with a Scienta SES200 hemispherical electron analyser and a partial yield detector. Both of the chambers are pumped by separate ion pumps allowing pressures of $\sim 10^{-10}$ Torr to be maintained.

A partial yield detector is used to record the flux of emitted electrons during the NEXAFS experiments. In its simplest form (total yield) the current on a metal plate, or collector, is recorded, but by biasing a grid of gold wire (situated between the sample and the collector) with a retardation voltage the signal from the low

kinetic energy background electrons can be removed. The NEXAFS experiments detailed in Chapters 6 and 7 use a retardation voltage of 100 V.

The hemispherical electron analyser is used to determine the kinetic energy of electrons emitted from the sample during the XPS experiments [68]. The analyser consists of two hemispheres, with the outer hemisphere being biased so as to be positive relative to the inner hemisphere. Due to the electric field within the analyser only electrons with a certain kinetic energy will be able to pass through the detector. By varying the electric field the relative fluxes of electrons with different kinetic energies may be measured, this information may then be converted into an XPS spectra.

3.3 Ultra-high vacuum experimental set-up

The aim of this thesis is to study the formation of supramolecular assemblies on the Au(111) surface. To ensure that the system under study remains free of contaminants, experiments are carried out under UHV conditions. UHV is defined is a vacuum with a pressure of 10^{-8} Torr or lower. Under ambient conditions a monolayer of contaminant molecules will cover a surface in less than a second (~ 3.5 ns).. At UHV pressures of 10^{-10} Torr the surface will remain clean for at least several hours [60], allowing study by XPS, NEXAFS, and STM.

3.3.1 UHV apparatus

The UHV system with which this research has been conducted has a base pressure of $\sim 5 \times 10^{-11}$ Torr. This pressure is maintained by the continuous pumping of the system with ion pumps and titanium sublimation pumps (TSP) [78]. The system is split into three main chambers with one subsidiary chamber, all of which are separated by gate valves. Figure 3.17 shows the system set-up.

Chamber 1 is primarily used as a sample preparation chamber with several Knudsen cells (K-cells) attached to allow sublimation of organic molecules. A quartz crystal microbalance is positioned in line with the flux emitted from the K-cells, allowing the rate of deposition to be measured. The chamber has a manipulation arm allowing the sample to be moved between chambers 1 and 2. The yoke attached to the manipulation arm also has the facility to apply a voltage across the sample holder and hence allows resistive heating.

The STM is housed within chamber 2 which does not contain deposition or heating apparatus in order to avoid contamination of the STM head. Above chamber 2 is a subsidiary chamber, chamber 2b, which is connected via a gate valve. This chamber is used for Ar ion sputtering of samples, and for cleaning STM tips by electron bombardment. Due to the pressures required for Ar sputtering chamber 2b is equipped with a turbo-molecular pump (TMP).

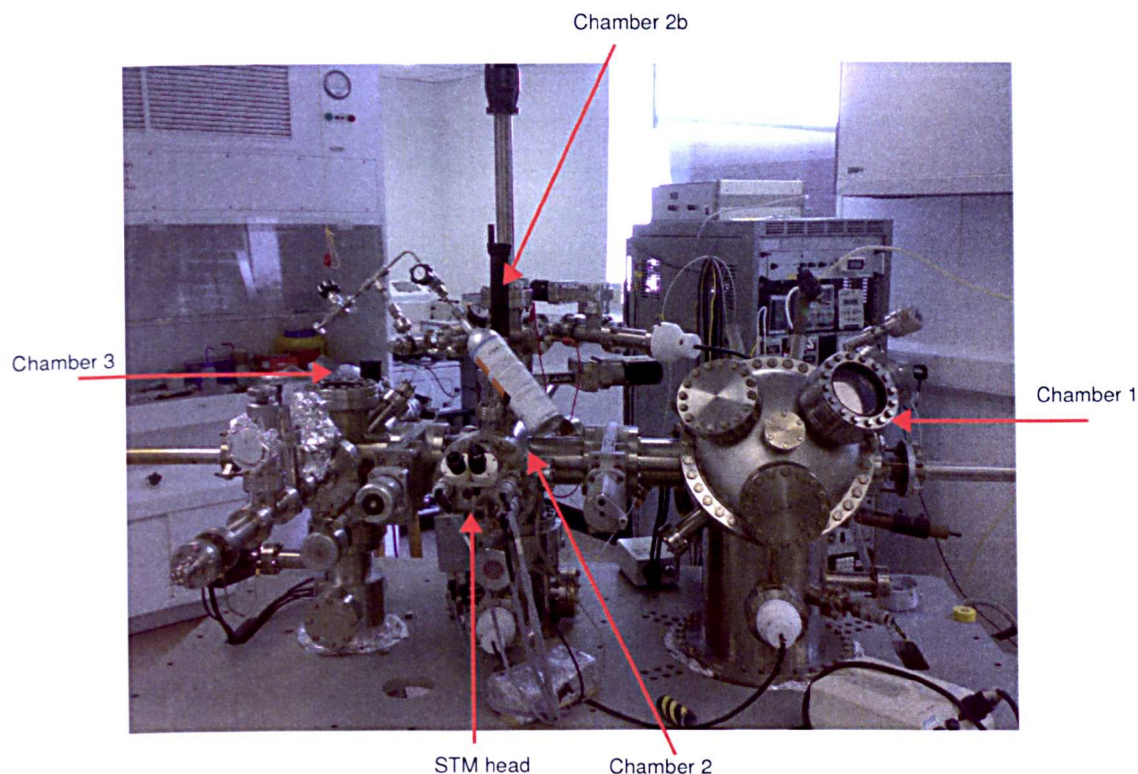


Figure 3.17: Image of the Nottingham STM/UHV chamber.

Chamber 3 is used for the deposition of volatile materials, either by sublimation or UHV-ESD. The manipulator arm for sample transfer into chamber two has a filament attached to it to allow indirect annealing of samples by radiative heating. The chamber contains a residual gas analyser (RGA) which provides information about the molecular species present within the vacuum system.

Attached to chamber 3 is a fast entry load lock (LL) which allows the insertion, or removal, of samples. In order to pump the LL down from atmospheric pressure a TMP is attached to this section of the chamber. The LL may be exchanged with the UHV-ESD apparatus.

3.3.2 UHV techniques

As all the experimental work reported on within this thesis takes place under UHV the techniques which are specific to this environment are discussed here.

Achieving UHV - Pumping and baking

In order to obtain a UHV environment, molecular species must be removed from the system. To do this the UHV chamber must be sequentially pumped down. At atmospheric pressure air may be regarded as a fluid and so displacement pumps, such as rotary vane and scroll, are used to ‘shovel’ air from inside the system to the outside. At lower pressures the gasses in the UHV system are better modelled as individual ballistic particles and it is no longer efficient to use displacement

pumps. At this stage TMPs are efficient at reducing the pressure to $\sim 10^{-8}$ Torr, and from there Ion pumps are used to produce pressures of $\sim 10^{-10}$ Torr.

The thin layer of water that covers all objects in ambient conditions is detrimental to achieving UHV. Without removing this layer of water the pressure in the system would not be able to drop below $\sim 10^{-8}$ Torr, as the water molecules slowly degas from the walls of the chamber. This problem is overcome by baking the system at temperatures over 100°C thus removing water from the chamber walls, and allowing it to be pumped away.

Sublimation using Knudsen cells

Molecules may be deposited on a surface in UHV by sublimation from a K-cell. The K-cells used for this work consist of a tantalum crucible, containing the molecules to be sublimed, surrounded by a heating element. The crucible is heated until a flux of molecules is detected by the quartz crystal micro-balance allowing a deposition temperature to be determined. With knowledge of the deposition temperature for each molecule, and the flux for this temperature, it is possible to expose a sample for a given period of time to produce the required monolayer coverage.

Tip preparation

In order to obtain atomic resolution of a sample an atomically sharp tip needs to be prepared. The ideal STM tip should be sharp with a single atom at its apex, but due to the exponential dependence of the tunnelling current on the tip-sample distance any atoms a few angstroms further back than the tip atom will have a negligible effect. For UHV-STM a common method of preparing tips is by electrochemical etching.

The tips used for this work are made from 0.5 mm diameter tungsten wire. The tip is held within a tantalum 'tip nut' which is screwed into the piezoelectric scan-tube. The tips are etched by suspending them in a solution of aqueous NaOH (~ 3 molar concentration). The experimental set-up for this process is shown in Figure 3.18. An electrochemical reaction occurs with the submerged part of the wire being oxidised to produce WO_4^{2-} [79]. A much greater rate of etching is present at the meniscus formed around the wire, with the wire thinning and eventually breaking under its own weight. At this point the tip must be removed from the NaOH solution and plunged into water to prevent further etching. This method produces an atomically sharp tip that is covered with a non conductive oxide layer. The oxide layer is removed by electron bombardment under UHV conditions before the tip is inserted in the STM.

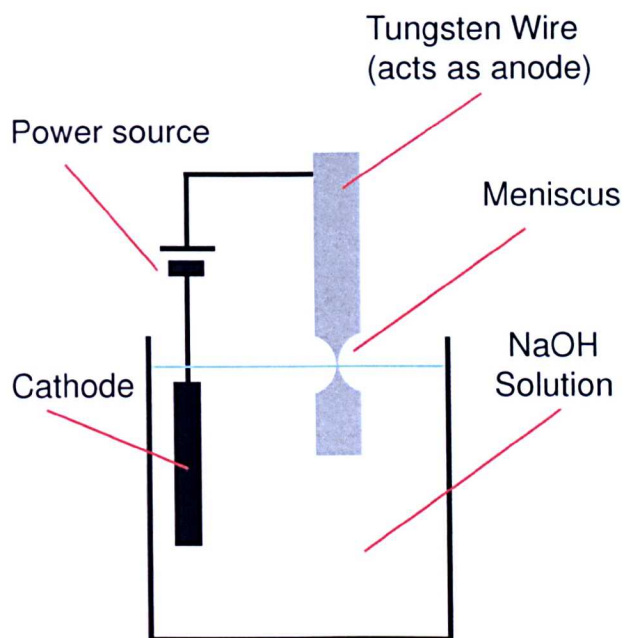


Figure 3.18: Diagram showing the set up for electrochemical tip etching.

3.4 Ultra-high vacuum electrospray deposition

Studying the self-assembly of molecules adsorbed on surfaces requires a method for transferring them onto the substrate. For small molecules (such as PTCDI and melamine) it is possible to sublime them using a K-cell. The deposition of larger molecules is problematic as the energy of sublimation is often greater than the intramolecular binding energies within the molecule and hence dissociation occurs. In order to facilitate the production of thin films of large molecules for study under UHV conditions, an alternative method of deposition is required. One such method is a ‘rapid heating’ technique where the sample is heated very quickly and operates on the principle that the rate of molecular desorption and molecular fragmentation are not the same. Thus by heating the sample quickly molecules may be sublimed before fragmentation occurs [80]. Pulsed valve techniques have also been employed to study large molecules [81], where the molecule of interest is dissolved in a solution and this solution is introduced into the UHV chamber by means of a small aperture valve ($\sim 50 \mu\text{m}$) which is opened and closed quickly (on the time scale of milliseconds) to allow solvent and solute molecules to enter the UHV chamber. For this work an electrospray ionisation technique has been chosen to deposit molecules.

Electrospray ionisation is a technique that has been pioneered by Fenn and colleagues [82, 83], to introduce fragile, thermally labile, or non-volatile species into vacuum for analysis by mass spectroscopy [84]. The technique has been utilised within the Nottingham Nanoscience group to transfer molecules, dissolved or suspended in solution, onto a sample held in UHV conditions. The technique of UHV-ESD allows fragile molecules to be deposited onto surfaces to be analysed by

high sensitivity UHV techniques such as STM and synchrotron based studies. The Nottingham Nanoscience group has previously used the electrospray technique to deposit carbon nanotubes [85], dye molecules [86, 87], and porphyrins [88]. Other groups have also demonstrated that UHV-ESD is a promising method for depositing polymers and biomolecules [89, 90] into vacuum. Within this work UHV-ESD has been combined with STM, XPS, and NEXAFS to allow an investigation of the chemical, electronic, and structural properties of large complex molecules deposited on a surface. This section describes the theoretical and practical aspects of UHV-ESD.

3.4.1 The electrospray ionisation process

The electrospray ionisation process may be considered as having three distinct stages [91]. The first stage is the formation of charged droplets which carry the molecule to be deposited; in the second stage the droplets shrink due to solvent evaporation and undergo fissions leading to very small highly charged droplets; finally gas-phase ions are produced. Charged droplets are formed by the electrospray ionisation event, which is central to UHV-ESD, and allows molecules which have been suspended or dissolved in a solvent to be volatilised. The solvent containing the solute is passed through a metal emitter (a hollow capillary), with a flow rate of $\sim 1 \mu\text{L}$ per minute, leading to a droplet of liquid forming at the end of the tip. Under conditions where no bias is applied to the emitter, the droplet will detach itself from the capillary and form a small sphere of solvent and solute.

If a high voltage (HV) is applied to the metal emitter then it is possible to alter the way the system behaves. Figures 3.19(a) and (b) shows the effect of a positive bias being applied to the emitter. If the counter-electrode is large and planar compared to the emitter, the value for the electric field, E_c , in the air at the capillary tip can be approximated from the following equation [92, 93]:

$$E_c = \frac{2V_c}{r_c \ln(4d/r_c)} \quad (3.14)$$

where V_c is the applied bias, r_c is the outer radius of the emitter, and d is the distance between the counter-electrode and the emitter. This leads to a very strong electric field being present at the tip of the emitter. As ionic species emerge from the emitter they undergo electrophoretic movement due to the electric field. In the situation where the emitter is positively biased, this results in the migration of any positive ions in solution away from emitter, and any negative ions will be drawn into the emitter. The positive ions move to the surface of the liquid at the end of the emitter, which has the effect of destabilising the liquid surface as the charge wishes to move away from the emitter but cannot escape from the liquid [91]. The repulsion between the positive charges at the surface of the liquid results in the formation of a ‘Taylor cone’ at the end of the emitter to enable the solvent molecules to reduce their repulsive interaction [94].

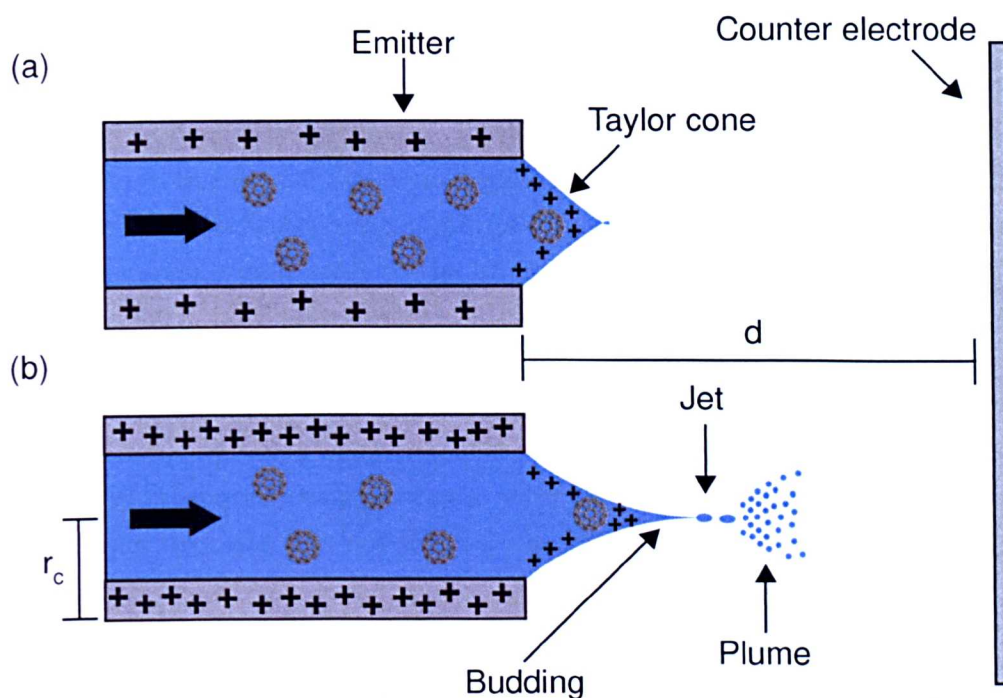


Figure 3.19: Diagram showing the formation of an electro spray event whereby a solvent containing C_{60} is converted from a liquid into a plume of droplets.

At a critical value for the applied HV, resulting in a sufficiently high electric field E_c , the repulsive force of the positive charges within the solvent overcomes the surface tension of the liquid, and a liquid filament with a diameter of a few micrometres is emitted from the tip of the Taylor cone [91]. This filament is unstable and breaks up into separate droplets each of which carry an excess of positive charge, solvent ions and the solute of interest. It is these small droplets that are eventually transferred into UHV, with the initial radius of these droplets increasing approximately in proportion to $(\text{flow-rate})^{2/3}$ [95]. The radius of the emitted droplets also increases with decreasing conductivity, implying that the smallest droplets will be obtained for operating conditions with low flow rates and high conductivity solutions [93].

Solvent evaporation and droplet fission

The droplets produced by the electro spray event are unstable due to the high number of positively charged species that are contained within them. As the droplets travel forward, solvent molecules will evaporate from the droplets, reducing their size but maintaining their original charge. This will result in an increase in the stress at the surface of the droplet, due to the coulomb repulsion, and after several evaporation events the force of the electrostatic repulsion between the charges will become equal to the surface tension holding the droplet together. This is the ‘Rayleigh stability limit’ and is defined by the Rayleigh equation [96]:

$$q_R = 8\pi(\epsilon_0\gamma D^3)^{1/2} \quad (3.15)$$

where q_R is the total charge within the droplet, ϵ_0 is the permittivity of vacuum, γ is the surface tension of the liquid and D is the droplet diameter. Before the Rayleigh limit is reached the droplets undergo a ‘Coloumb fission’ (or ‘Coloumb explosion’) process which leads to the production of several smaller droplets. This fission is ‘uneven’ with the ‘parent’ droplet emitting a tail of much smaller droplets, with the stream of droplets carrying off $\sim 2\%$ of the mass of the parent droplet and $\sim 15\%$ of the charge [97]. The ‘offspring’ droplets are much smaller than the parent droplet and have a much higher charge-to-mass ratio. These smaller droplets may then undergo subsequent fission events, with the droplets further reducing in size, but for smaller droplets it is not known whether the fission is even or uneven [91].

CRM and IEM models of ion formation

The electrospray process will produce gas phase ions, but the pathway by which this occurs is still debated. The principal mechanisms for the formation of the gas phase ions are the charged residual model (CRM) and the ion evaporation model (IEM). In the CRM [98], the droplets undergo successive fission events until droplets (with single or multiple charges) containing only one solute molecule remain. The solvent molecules in these drops will evaporate leaving the solute molecule which will retain the ‘residual’ charge of the droplet. In the IEM [99] the droplets are assumed to reduce in size by solvent evaporation and fission processes, until the charge density is high enough for ions to be emitted from the droplet.

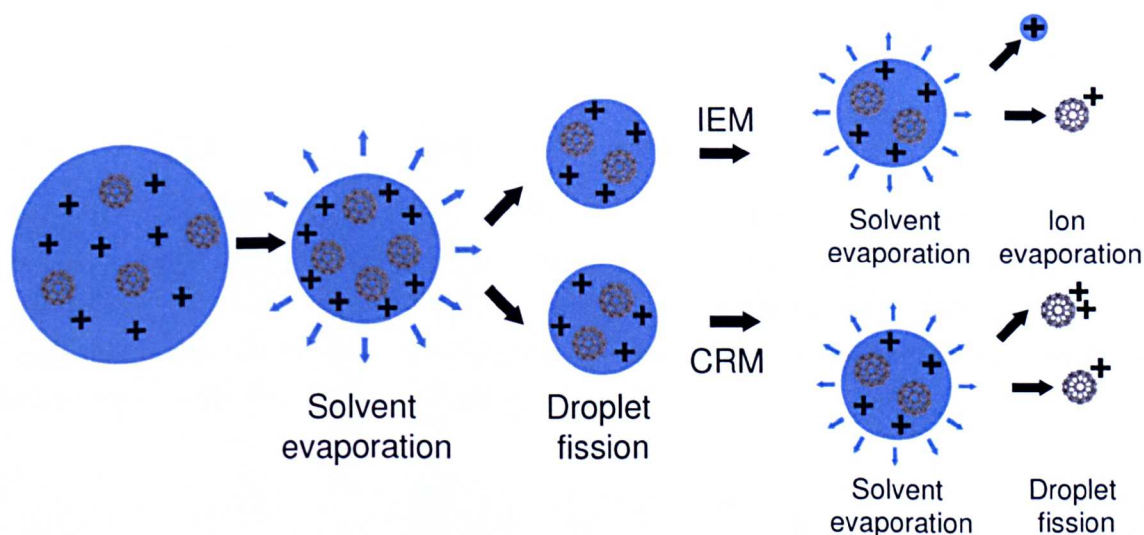


Figure 3.20: Schematic representation of the IEM and CRM pathways for the formation of gas-phase ions.

Figure 3.20 shows a schematic representation of both the IEM and CRM pathways. Both processes are initiated by solvent evaporation and droplet fission, with the CRM mechanism droplets undergoing further solvent evaporation and droplet

fission until single molecule with a residual charge remain. In the IEM mechanism, droplets undergo solvent evaporation and then ion evaporation to displace charged solvent molecules and solute molecules from the droplet.

3.4.2 The electrospray apparatus

The set-up for the UHV-ESD apparatus is shown in Figure 3.21. The solvent is forced from the syringe through a metal emitter (with an internal diameter of 100 μm) using a constant backing pressure to obtain a flow rate of $\sim 1 \mu\text{L}$ per min. Applying a bias of between +1.5 kV and +2 kV to the emitter, with the grounded entrance capillary acting as the counter electrode, gives rise to the formation of the electrospray event at atmospheric pressure. The resultant spray then enters the system through the metal entrance capillary (internal diameter 0.25 mm) into the first differentially pumped chamber (DPC-1) which is at a pressure of ~ 1 mbar, maintained by constant pumping with a scroll pump.

The molecular beam then passes through a skimmer cone (S1, aperture diameter, 0.4 mm) into DPC-2 which is held at a pressure of $\sim 10^{-2}$ mbar, and passes through the second skimmer cone (S2, aperture diameter, 0.6 mm) into a chamber which is pumped by a TMP and has a background pressure of $\sim 10^{-5}$ mbar. Finally the beam passes through a pin hole (PH, aperture diameter, 1 mm) and into a UHV where the sample is mounted. In the Nottingham UHV system the sample preparation chamber (chamber 3) has a base pressure of $\sim 10^{-11}$ mbar.

With the sample preparation chamber open to the differential pumping system, but in the absence of spray, the pressure is of the order 6×10^{-9} mbar. When the spray is in operation the pressure in the sample preparation chamber rises to 2×10^{-7} mbar indicating that solvent molecules (detected by a RGA) are present.

3.4.3 The free-jet expansion

In order to enable the transfer of molecules from ambient conditions to a UHV environment the electrospray apparatus incorporates a series of differentially pumped chambers. When gas moves from one chamber to another it may undergo a free-jet expansion depending upon the magnitude of the change in pressure, and the ratio of specific heats for the expanding gas [100, 101]:

$$\frac{P_0}{P_1} \geq \left(\frac{\gamma + 1}{2} \right)^{\frac{\gamma}{\gamma - 1}} \quad (3.16)$$

where γ is the ratio of specific heats (C_P/C_V), P_0 is the pressure of the low pressure chamber, and P_1 is the pressure of the chamber which the gas is expanding into. If the inequality in equation 3.16 is met, and the gas is initially in the continuum flow regime, then a free-jet expansion occurs. For the apparatus used for these experiments the transition from atmospheric pressure to DPC-1 results in the

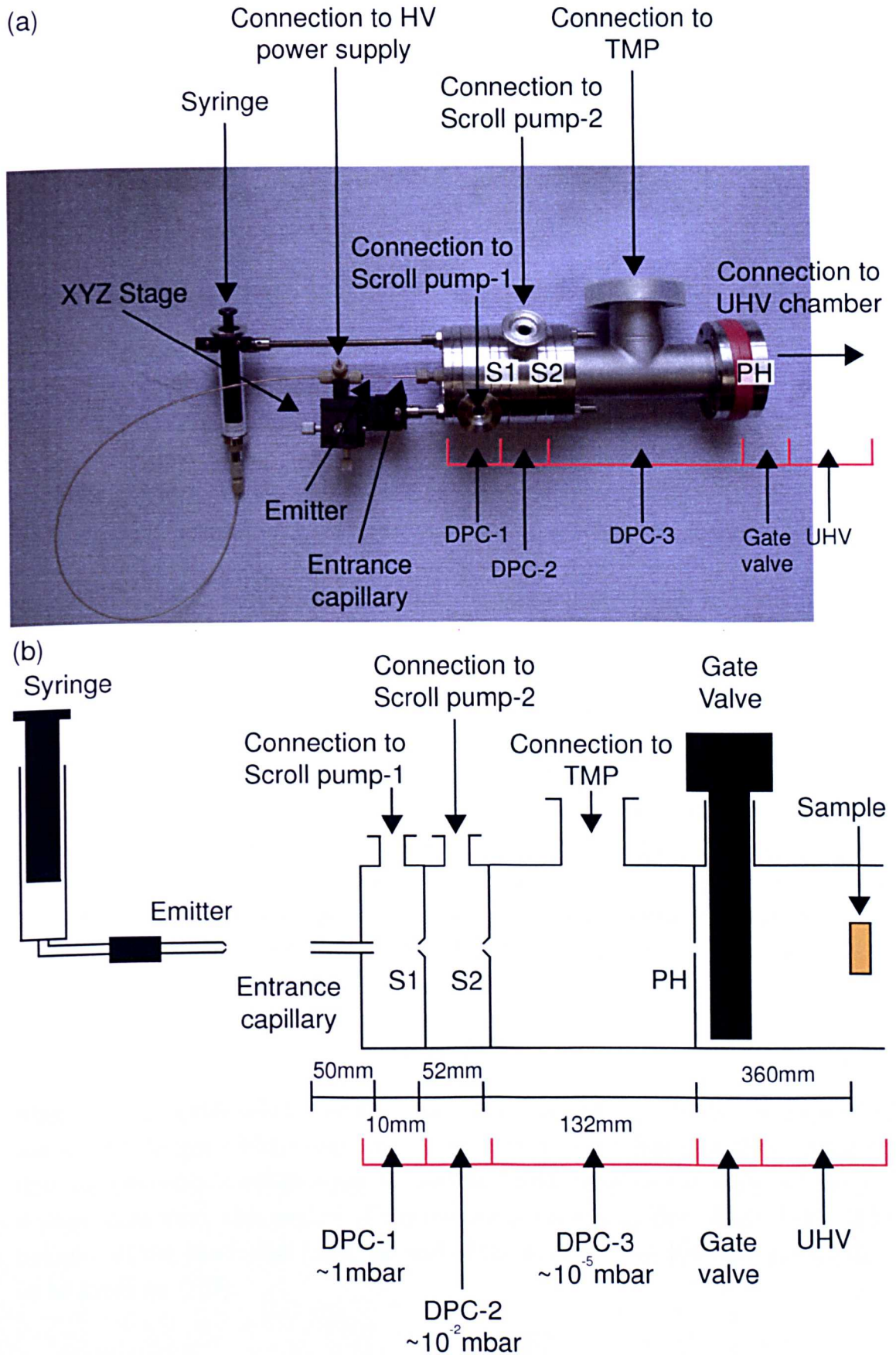


Figure 3.21: The electro spray experimental set-up. (a) Photograph showing the electro spray apparatus before attachment to a UHV system. (b) Schematic representation of the electro spray apparatus.

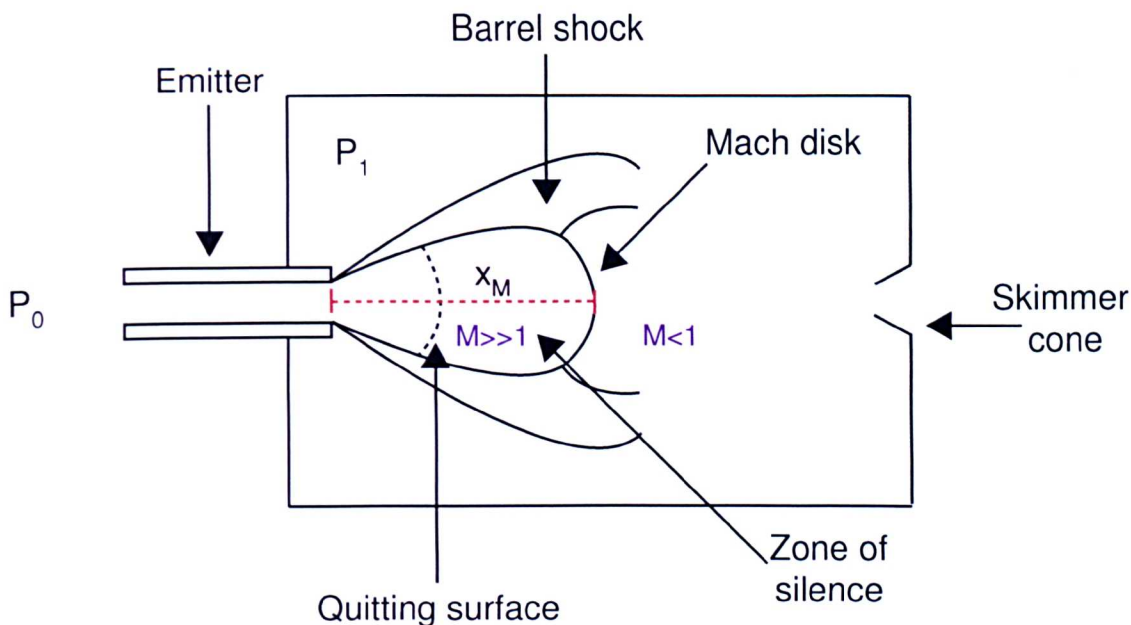


Figure 3.22: Schematic showing the free-jet expansion.

formation of a free-jet expansion as the gas moves from a high to a low pressure (γ is taken to be 7/5 - the value diatomic molecules, such as nitrogen, which is the major component of air).

Figure 3.22 shows a schematic of the expansion of a gas from a low pressure region to a high pressure region where a free-jet expansion is formed. The pressure to the left of the emitter is P_0 and the pressure in the chamber is P_1 . If the pressure differential is sufficient to allow the free-jet expansion, then gas moving through the emitter is accelerated as it moves into the lower pressure chamber, and will expand and reach supersonic speeds. The expansion causes the formation of a cone known as the ‘zone of silence’, where the velocity of the gas is supersonic i.e. it has a Mach number greater than 1. The Mach number of an expanding gas is given by:

$$M = \frac{v_{expand}}{v_{local}} \quad (3.17)$$

where v_{expand} is the velocity of the expanding gas and v_{local} is the local speed of sound. As the gas continues to expand it becomes turbulent and slows down, so that the pressure conditions can be matched with those of the chamber the gas is expanding into, this region of turbulence is known as the ‘Mach disk’. The distance of the Mach disk from the end of the emitter, x_M , has been determined to be given by [102]:

$$x_M = 0.67D \sqrt{\frac{P_0}{P_1}} \quad (3.18)$$

where D is the internal diameter of the emitter. For the UHV-ESD system used for the experiments presented within this thesis the skimmer cones are always po-

sitioned after the Mach disk of the expanding gas. This allows for a determination of an upper limit for the velocity of the expanding gas. After the Mach disk the velocity of the expanding gas takes a value of M less than 1. This means that the velocity of the expanding gas is equal to or less than the local speed of sound (which for an ideal diatomic gas at room temperature is 344 ms^{-1} [101]). It is therefore possible to estimate an upper limit on the kinetic energy of any solute molecule, with mass m , travelling through the differentially pumped electrospray apparatus (and hence the kinetic energy when they impinge on the sample) by assuming that they are travelling at the local speed of sound and applying:

$$KE = \frac{1}{2}mv^2 \quad (3.19)$$

3.4.4 The concentration gradient produced by UHV-ESD

The UHV-ESD apparatus described here produces a non-uniform coverage of molecules over the surface during deposition. This non-uniform coverage is due to the fact that the flux of molecules impinging on the surface will be greater at the centre of the molecular beam and will decrease with radial distance from the centre. This is due to the diffusion of molecules as the beam travels from the entrance to the UHV chamber to the sample. This distribution of coverage, as a function of distance from the centre of the beam, is expected to lead to a concentration gradient of deposited molecules across the surface. This concentration gradient could be problematic in terms of producing uniform films of deposited molecules, but it also allows the investigation of a range of surface coverages on a single sample. Therefore, a single sample can be used to study the coverage dependence of XPS and NEXAFS due to sub-monolayer, multi-layers, and even thick films.

3.5 Surfaces

The Au(111) substrate is used during this work as a support for the supramolecular assemblies that are studied. Within the context of these experiments an ideal surface should allow molecular diffusion. Although the substrate will play a role in the orientation and morphologies of the structures produced, the Au(111) surface has been chosen as it has previously been shown that molecular diffusion is not inhibited, allowing the self-assembly of structures which are non-covalently bound.

3.5.1 The Au(111) $22x\sqrt{3}$ reconstruction

In the bulk, gold has a face centred cubic (FCC) structure. However, the (111) plane of the surface reconstructs to give a 'herringbone' structure with a unit cell $22 \times \sqrt{3}$ times larger than that of the bulk [103]. This 'herringbone' pattern is

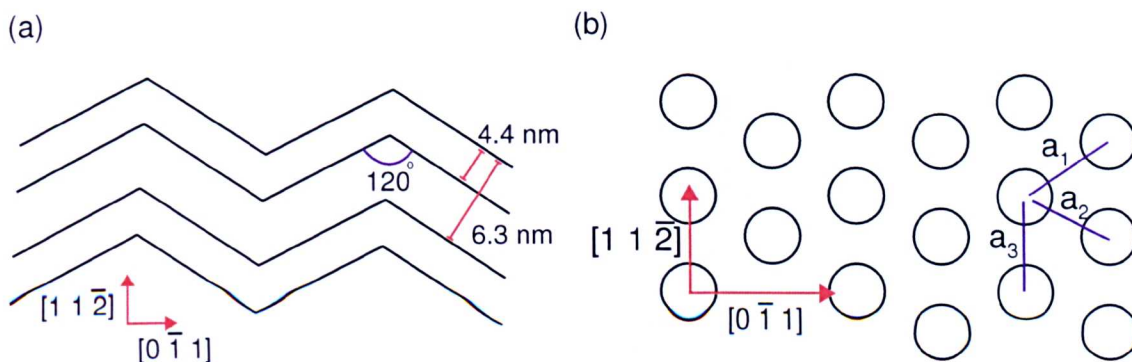


Figure 3.23: Schematic showing the herringbone reconstruction of the Au(111) surface. (a) Spacing and directions of the double bright lines of the herringbone reconstruction. (b) Atomic position of the Au atoms on the surface $a_1=a_2=2.85 \text{ \AA}$ $a_3=2.75 \text{ \AA}$ which corresponds to a lateral compressions of 4.55% in the $[0 \bar{1} 1]$ direction compared with the bulk.

observed in STM as pairs of bright, parallel lines which ‘zig zag’ their way across the surface. The reconstruction of the Au(111) surface is unusual as gold is the only coinage metal to undergo this process.

The top layer of atoms in the Au(111) plane are laterally compressed along the $[0 \bar{1} 1]$ direction which allows 23 rows of atoms to fit into the space normally occupied by only 22 rows in the bulk configuration. This compression leads to alternate domains of FCC and hexagonal close-packed (HCP) structure. Atoms which reside on the boundaries between these domains sit in an energetically unfavourable position and appear brighter in an STM scan by approximately 0.2 \AA [103]. Due to the three-fold rotation symmetry of the (111) surface these domain boundaries, represented by rows of raised atoms, may change direction with an angle of 120° relative to one another. This results in the classic herringbone pattern, illustrated in Figure 3.23.

The herringbone reconstruction has been extensively studied using STM [103–105], and it has been seen that the atoms at the boundary of the HCP and FCC domains appear as bright features (Figure 3.24). These pairs of lines are observed to bend through $\pm 120^\circ$ every 250 \AA due to long range elastic lattice strain.

3.5.2 Preparation of the Au(111) surface

This section briefly describes the processes that are required to obtain the surface reconstruction of the Au(111) surface. The gold on mica samples were purchased from Agilent as 10 mm^2 pieces (thickness 1500 \AA). They are formed by the epitaxial growth of Au on a mica substrate and are then flame annealed in H_2 to produce a flat, clean surface. The samples are trimmed to $4 \text{ mm} \times 10 \text{ mm}$ strips to be inserted into the sample holder, with a strip of low resistivity Si placed behind it to allow resistive heating of the sample.

Samples introduced to UHV will be covered in a thin layer of water, which may be removed by annealing. Contaminants are then removed from the surface

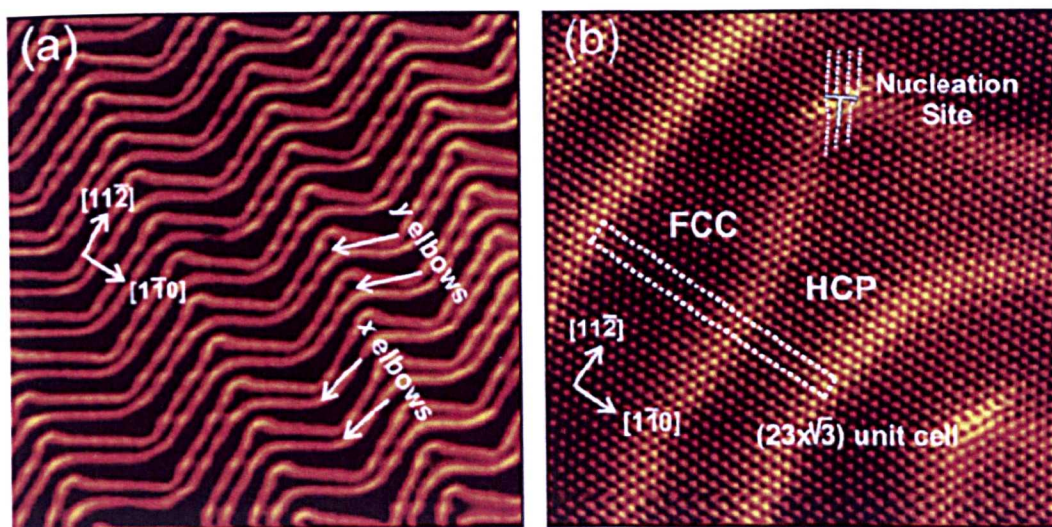


Figure 3.24: STM images showing the Au(111) herringbone reconstruction. (a) Large scale image ($800 \text{ \AA} \times 800 \text{ \AA}$) showing the herringbone pattern with crystallographic directions indicated. (b) Close up image ($140 \text{ \AA} \times 140 \text{ \AA}$) with atomic resolution showing the FCC and HCP regions. Atoms on boundary between these regions appear brighter due to their energetically unfavourable position (images from [105]).

by bombarding it with Ar ions. Argon is introduced to chamber 2b of the UHV system via a leak valve to give a background pressure of 6×10^{-6} Torr. The argon atoms are then ionised, accelerated over a potential difference of ~ 1 keV, and then impinge on the Au(111) sample. A drain current is measured from the sample, with a typical current of $\sim 3 \mu\text{A}$ being obtained. The sample is sputtered for 20 minutes, and then subjected to an anneal at 500°C for 20 minutes before slowly reducing the temperature to allow the reconstruction to form. Images of the surface taken after the sputter-anneal cycle show the characteristic $(22 \times \sqrt{3})$ herringbone reconstruction of the Au(111) surface [103].

3.6 Summary

Within this chapter the experimental techniques (STM, XPS, NEXAFS, and UHV-ESD) that will be utilised throughout this work have been described. A description of the operating methodology has been given along with an overview of the underlying theory. The general topic of UHV science has been introduced, and details of the equipment needed to obtain and maintain a UHV environment have been given. Finally, the Au(111) surface, which is used as a support for the molecular assemblies studied in this work, has been described.

Chapter 4

Hydrogen-bonded supramolecular networks: PTCDI as a molecular building block

In this chapter the PTCDI molecule is studied as a potential molecular 'building block' for use in the formation of hydrogen-bonded supramolecular structures. Previous studies of the use of the PTCDI-melamine synthon to create hexagonal and parallelogram network structures on the Au(111) surface are reviewed. In addition to these structures two new phases are discussed, where an excess of melamine leads to the formation of an alternative hydrogen-bonding junction. Following this, the ability to functionalise these molecular networks using derivatives of PTCDI is explored.

4.1 Hydrogen-bonded structures formed from PTCDI and melamine

Hydrogen-bonded structures based on the interaction between PTCDI and melamine have been extensively studied by the Nottingham Nanoscience group. This chapter provides an introduction to previous work undertaken in this area, as well as detailing further work conducted as part of this thesis. The results presented here demonstrate that the complex nature of interactions between PTCDI and melamine gives rise to a variety of complex structural arrangements. Initially work within the group was focused upon the investigation of planar organic molecules such as PTCDI, PTCDA, NTCDI, melamine, and cyanuric acid [14, 19, 20, 106, 107]. The molecules were sublimed onto an Ag/Si(111) surface held in a UHV environment and studied by in situ STM. These experiments revealed that the deposited molecules are free to diffuse on the surface and are able to form hydrogen-bonded supramolecular structures commensurate with the high symmetry Ag/Si(111) surface.

The Ag/Si(111) surface is not stable under ambient conditions and hence is of limited use for many potential technological applications. For this reason experiments have been conducted where these supramolecular structures have been prepared on the Au(111) surface. There are two main benefits in using the Au(111) substrate: Firstly it allows the effect of altering the surface chemistry on the structures formed to be studied. Secondly, we may determine whether it is possible to produce networks on a more robust substrate. Previous experimental work within the group has shown that the cyanuric acid/melamine structures formed on the Ag/Si(111) can also be formed on the Au(111) surface (see Chapter 2). The next section of this chapter discusses the structures formed from PTCDI and melamine molecules which have been deposited onto the Au(111) surface.

Methods

All of the supramolecular structures discussed within this chapter have been formed under UHV conditions and are supported on either Ag/Si(111) or Au(111) substrates and then imaged using an STM operating in constant current mode using electrochemically etched tungsten tips. Work which has been performed as part of this thesis has been carried out exclusively on the Au(111) surface. Gold on mica substrates were prepared by Ar ion sputtering ($\sim 6 \times 10^{-6}$ Torr, ~ 0.7 keV, ~ 2 A) and annealing (500°C) as described in Chapter 3. STM was used to check the surface quality, ensuring that the characteristic herringbone reconstruction was observed [103].

The materials used as molecular ‘building blocks’ have relatively low molecular weights, and as such may be deposited by sublimation from K-cells. The molecules were deposited at the following temperatures: PTCDI (435°C), melamine (95°C), Br_2PTCDI (362°C), and S_2PTCDI (292°C). These temperatures were recorded with a thermocouple attached to the K-cell, and the flux of the molecules was detected using a quartz crystal micro-balance.

After the deposition of molecules the sample may be annealed using a Si back-heater incorporated within the sample-holder. Annealing and deposition of the PTCDI based molecules were conducted in chamber 1 of the Nottingham UHV system, with the STM measurements being acquired in an adjoining isolated chamber (chamber 2) to avoid contamination. Deposition of the more volatile melamine molecule was carried out in another isolated chamber (chamber 3).

4.1.1 Homo-molecular interactions of PTCDI and melamine

The chemical structures of PTCDI and melamine are shown in Figure 4.1 (a). Both molecules contain sp^2 hybridised carbon atoms, with the atoms being confined to a plane. These molecules have previously been observed to form homo-molecular

interactions governed by hydrogen-bonding. These interactions are highly directional and give rise to the well defined dimer bonding arrangements shown in Figure 4.1 (b). Close-packed structures, such as those in Figure 4.1 (c), have been previously observed on both the Ag/Si(111) [20] and Au(111) [14] surfaces. Chains of molecules, stabilised by the double hydrogen-bonded arrangement (see Figure 4.1 (b)), are observed for low coverages (<0.02 ML) of PTCDI deposited on the Ag/Si(111) surface. The centre to centre spacing of the molecules along the hydrogen-bond chain is measured to be $14.1 \text{ \AA} \pm 0.2 \text{ \AA}$ [20]. The molecules within the chain are canted by $8 \pm 2^\circ$ within the row in order to facilitate the hydrogen-bonding interaction. When the molecular coverage is increased (>0.02 ML) two-dimensional islands are formed on the Ag/Si(111) surface. For the Au(111) surface only two-dimensional islands are observed irrespective of the molecular coverage [14].

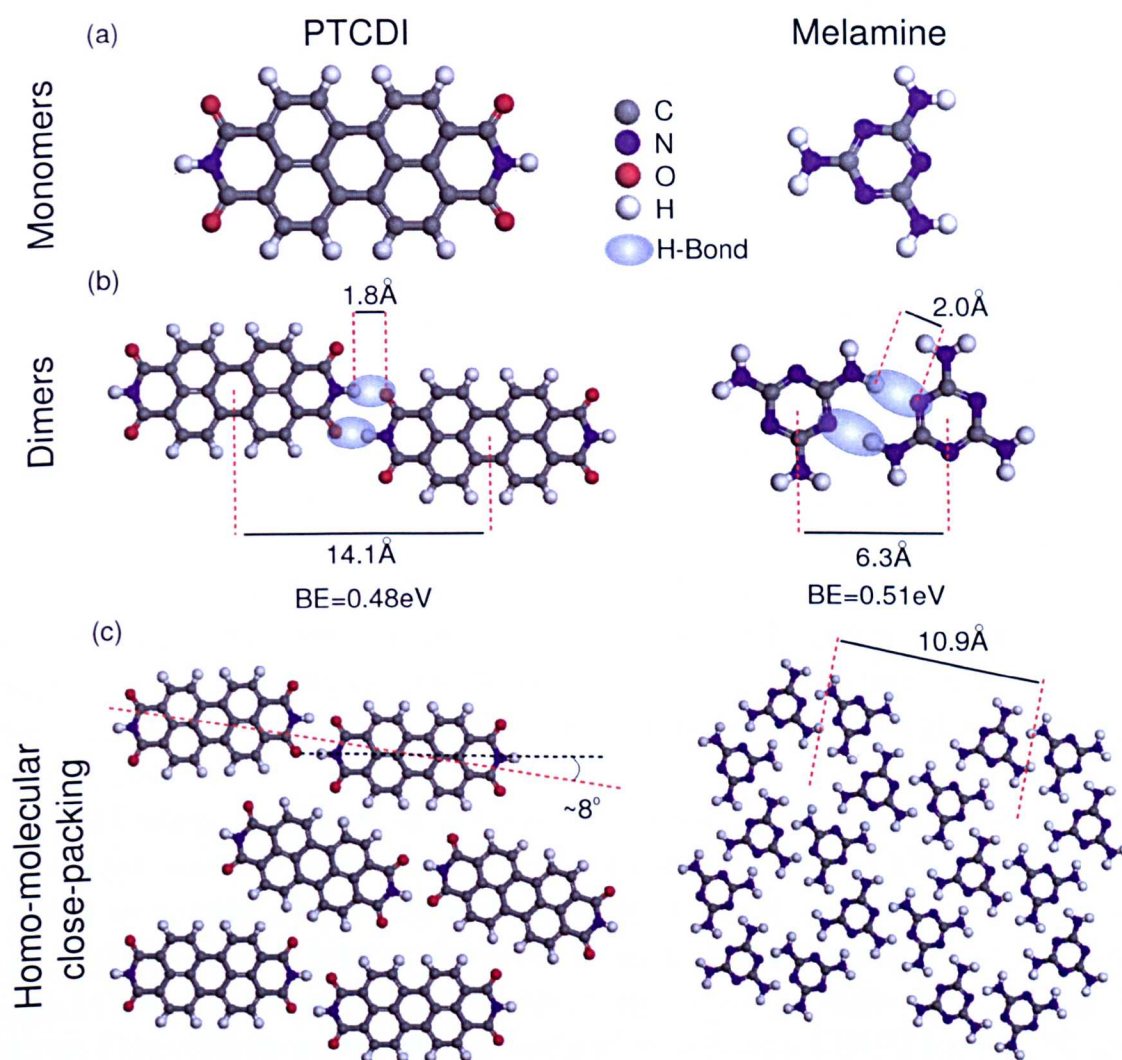


Figure 4.1: (a) Chemical structures of PTCDI and melamine. (b) Double hydrogen-bond interactions between dimers of PTCDI and melamine. The experimentally observed centre to centre spacings [16,20] are shown as well as the hydrogen-bond separation and binding energies obtained from DFT (see appendices A and B for details). (c) Homo-molecular close-packed structures of PTCDI and melamine, with the experimentally observed dimensions [16, 20].

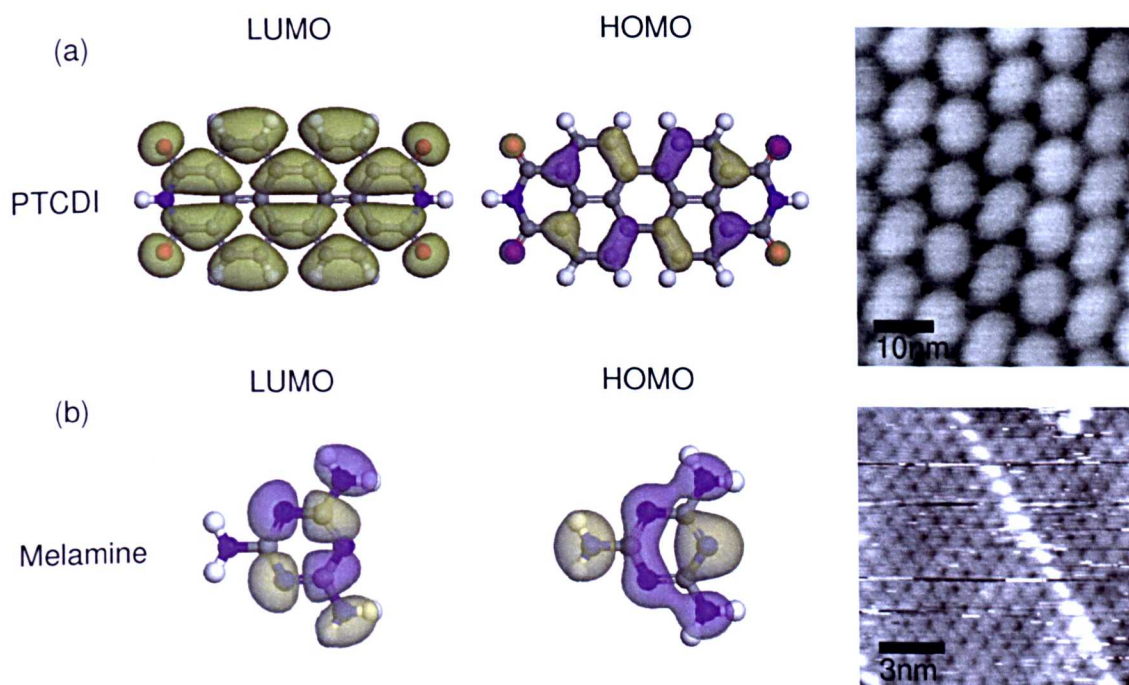


Figure 4.2: (a) Structure of the PTCDI molecule overlaid with the DFT calculated HOMO and LUMO, STM image to the right shows a region of close-packed PTCDI on the Au(111) surface showing tunnelling from the HOMO ($V_{sample} = -0.70$ V, $I_{tunnel} = 0.03$ nA). (b) Structure of the melamine molecule overlaid with the DFT calculated HOMO and LUMO, STM image to the right shows a region of close-packed melamine on the Au(111) surface showing tunnelling from the HOMO ($V_{sample} = -1.70$ V, $I_{tunnel} = 0.03$ nA). [STM images provided by L.M.A. Perdigao]

Domains consisting exclusively of melamine molecules are not observed to form on the Ag/Si(111) substrate in the absence of PTCDI, possibly due to the low sticking co-efficient of melamine on this surface. However, experiments performed on the Au(111) surface show the formation of domains of porous, honeycomb, melamine networks [16]. These honeycomb networks have a periodicity of $10.9 \text{ \AA} \pm 0.2 \text{ \AA}$, with the structure stabilised by the double hydrogen-bonds formed between pairs of molecules. The centre to centre spacing of these molecules has been found to be $6.3 \text{ \AA} \pm 0.1 \text{ \AA}$ which is close to the DFT calculated separation (6.1 \AA) [16].

STM offers a method of accurately determining the dimensions of self-assembled molecular structures. However, in order to utilise STM to its full potential we require information about how the molecule is expected to appear in an STM image. To a good approximation (see Chapter 3) the molecule's HOMO and LUMO can be used to predict the shape of the molecule when imaged in STM. Figure 4.2 shows the DFT calculated HOMO and LUMO for PTCDI and melamine, as well as STM images showing tunnelling from the HOMO to the tip. These calculations allow us to better understand the structures observed in STM. PTCDI molecules are imaged as bright lozenges, whereas melamine molecules may be observed as darker triangular features.

4.1.2 The mixed phase of PTCDI and melamine

When PTCDI and melamine are co-deposited on Au(111) and annealed at $\sim 50^\circ\text{C}$, they combine to produce a ‘mixed phase’ structure, consisting of alternating rows of PTCDI and melamine. Such structures are stabilised by a triple hydrogen-bond between the PTCDI and melamine molecules (shown in Figure 4.3 (a)). An STM image of the highly ordered mixed phase is shown in Figure 4.2 (b). The white lozenge features correspond to rows of PTCDI molecules, with the dark contrast regions corresponding to the positions of the melamine molecules. A less ordered type of the mixed phase has previously been reported [14], but this structure has not been analysed before now. A high resolution image of the structure is shown in Figure 4.3 (d). The separation between the parallel rows of the PTCDI molecules varies across the structure, indicating that the regions of melamine have different structures. A spacing of $21.9 \text{ \AA} \pm 0.5 \text{ \AA}$ is indicated on the STM image as well as a much large separation of $31.5 \text{ \AA} \pm 0.5 \text{ \AA}$.

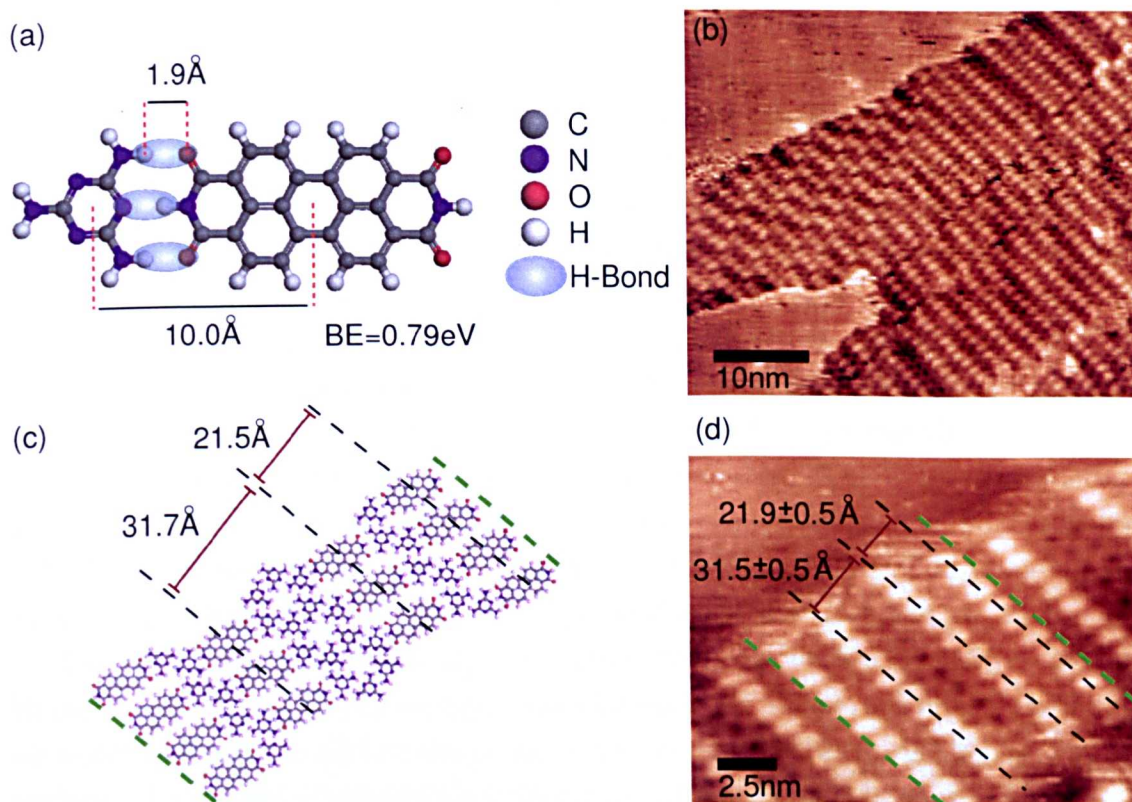


Figure 4.3: Mixed phase structure formed by PTCDI and melamine. (a) Structure of the PTCDI-melamine triple hydrogen-bond, with the DFT calculated distances and BE shown. (b) STM image of the PTCDI/melamine mixed phase on the Au(111) surface ($V_{sample} = -2.50 \text{ V}$, $I_{tunnel} = 0.03 \text{ nA}$). (c) Schematic showing the structure of the mixed phase, distances shown are obtained from DFT calculations. (d) STM image of the mixed phase, with the internal structure of the alternating rows of PTCDI and melamine being shown ($V_{sample} = -2.50 \text{ V}$, $I_{tunnel} = 0.03 \text{ nA}$).

The structure of the mixed phase may be modelled using the molecular sep-

arations obtained from the DFT calculated PTCDI-melamine and melamine-melamine hydrogen-bonding distances. Figure 4.3 (c) shows the proposed model for the structure of the mixed phase. A separation of 21.5 Å for the small spacing between PTCDI rows is in good agreement with the experimentally determined distance and corresponds to a single ‘ribbon’ of melamine molecules. This ‘ribbon’ is able to form double hydrogen-bonds between the melamine molecules while further stabilising the structure by forming triple hydrogen-bonds between themselves and the neighbouring PTCDI molecule. The larger separation (31.7 Å) is congruent with the experimental data, and corresponds to a domain of melamine arranged in a ‘honeycomb’ structure positioned between the rows of PTCDI. This larger structure allows the formation of both melamine-melamine and PTCDI-melamine hydrogen-bonds.

4.1.3 Hexagonal and parallelogram phases of the PTCDI/melamine network

By annealing the mixed phase of PTCDI/melamine at $\sim 50\text{-}80^\circ\text{C}$, a hexagonal network structure may be produced on both the Ag/Si(111) [19] and the Au(111) [24] surfaces. The pore-pore separation of the hexagonal network has previously been determined to be 34.6 Å and 35.0 Å for the Ag/Si(111) and the Au(111) surfaces, respectively. Figure 4.4 (a) shows a schematic of the hexagonal network structure. Melamine molecules are positioned at the vertices of the network, with each molecule forming three triple hydrogen-bonds with the neighbouring PTCDI molecules. The directionality of the hydrogen-bonds, and the three fold symmetry of the melamine molecule, gives rise to an angle of 120° between the long axes of the PTCDI molecules attached to the melamine vertex. This hydrogen-bonding determines the large scale hexagonal structure of the network. The stoichiometric PTCDI:melamine ratio for the hexagonal structure is 3:2. An STM image of the hexagonal network formed on the Au(111) surface is shown in Figure 4.4 (b).

Further annealing of the hexagonal phase formed on the Au(111) surface results in the production of an additional, more complex ‘parallelogram phase’ (it should be noted that the parallelogram phase is not observed to form on the Ag/Si(111) surface). Figure 4.4 (c) shows a schematic of the parallelogram phase. The experimentally determined dimensions of the structure were found to be $30.7 \text{ \AA} \pm 0.4 \text{ \AA}$ and $19.4 \text{ \AA} \pm 0.3 \text{ \AA}$ with an angle of $87 \pm 2^\circ$ [25]. This structure is stabilised by a mixture of hydrogen-bonding arrangements. The PTCDI molecules running in the approximately horizontal direction in Figure 4.4 (c) are involved in triple-hydrogen-bonds with the two melamine molecules at either end. The vertical double rows of PTCDI are stabilised by each PTCDI molecule being bound to a melamine molecule (via a triple hydrogen-bond) at one end and to a PTCDI molecule (via a double hydrogen-bond) at the other end. The stoichiometric ratio for the parallelogram structure is identical to that of the hexagonal network (3:2 in

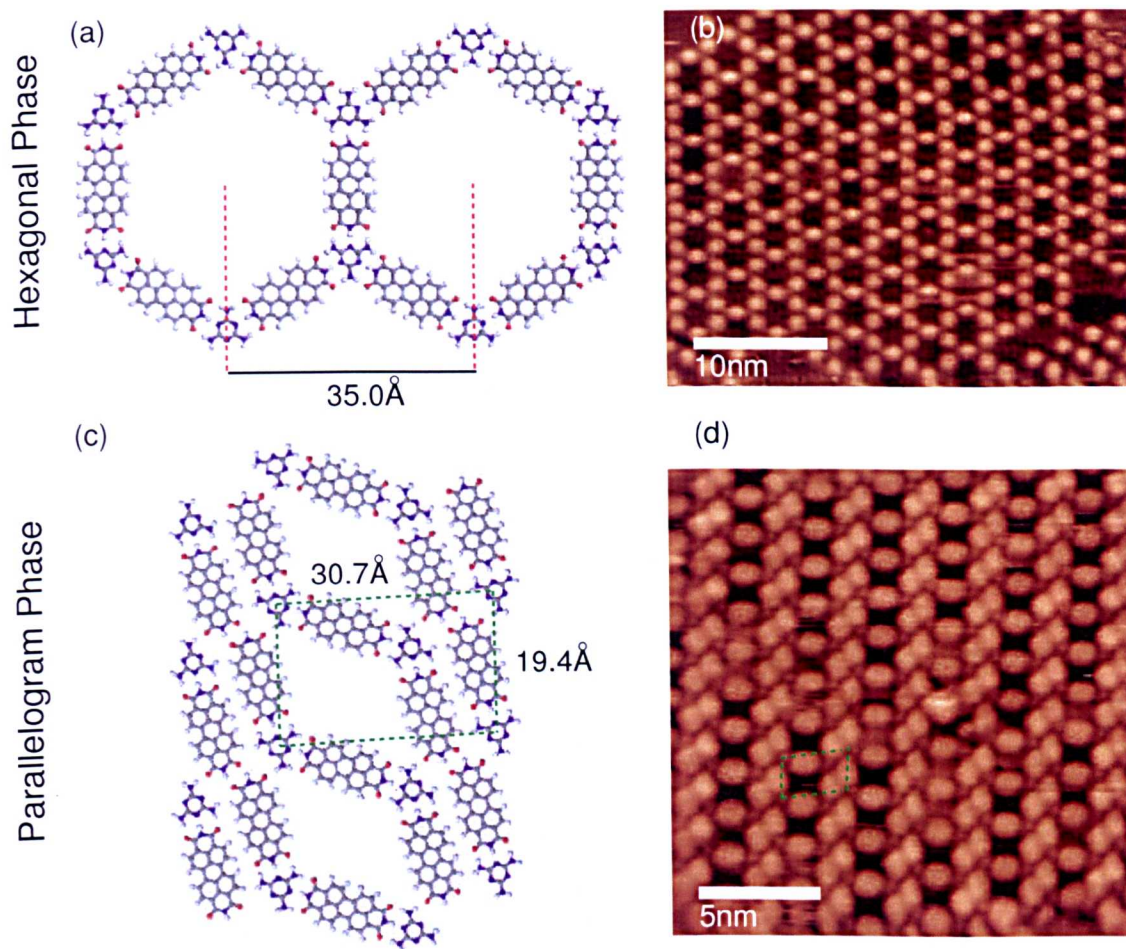


Figure 4.4: (a) Schematic of the hexagonal network structure with each vertex consisting of three PTCDI/melamine triple hydrogen-bonds. (b) STM image of the hexagonal phase formed on the Au(111) surface ($V_{sample} = +2.50$ V, $I_{tunnel} = 0.03$ nA). (c) Schematic of the parallelogram network structure, the unit cell is highlighted with a green dotted line. (d) STM image of the parallelogram network formed on the Au(111) surface ($V_{sample} = -2.30$ V, $I_{tunnel} = 0.03$ nA).

both cases). Figure 4.4 (d) shows an STM image of a region of the parallelogram network formed on the Au(111) surface.

Although both network structures have the same stoichiometric ratio, the fact that the parallelogram network forms at a higher temperature implies that there is a difference in the energy required to produce the two structures. It is possible to estimate an energy per unit area based on the unit cell of these structures and the number of hydrogen-bonds that they contain. The unit cell of the hexagonal network contains 6 PTCDI-melamine hydrogen-bonds (0.80 eV per bond), and the unit cell of the parallelogram structure contains 4 PTCDI-melamine bonds and 1 PTCDI-PTCDI bond (0.48 eV per bond). This gives an energy per unit area value of $4 \times 10^{-3} \text{ eV}\text{\AA}^{-2}$ for the hexagonal network and $6 \times 10^{-3} \text{ eV}\text{\AA}^{-2}$ for the parallelogram structure. These findings indicate that we would expect the parallelogram structure to be the more stable. This simple argument for the energetics of the two structures does not include the vdW interactions between molecules or the interaction between the molecules and the surface. However,

due to the close-packed nature of the parallelogram phase, the vdW contribution would be expected to increase the stabilisation of the parallelogram phase relative to the hexagonal phase.

4.2 Melamine-rich hydrogen-bonded supramolecular structures

The hexagonal and parallelogram network structures have the same PTCDI:melamine ratio. Structures can also form which have a larger proportion of melamine than either the parallelogram or hexagonal phase. Such structures are created by increasing the amount of melamine on the surface during the annealing stage of network production. As part of this work two melamine-rich supramolecular structures have been characterised. The STM image shown in Figure 4.5 (a) shows a PTCDI/melamine network structure which has approximately square shaped pores. The experimentally measured distances for the periodicity of the ‘square’ phase structure were determined to be $24 \text{ \AA} \pm 1 \text{ \AA}$ and $27 \text{ \AA} \pm 1 \text{ \AA}$, with the angle between the unit cell vectors measured as $99^\circ \pm 4^\circ$. The square phase is seen to exist alongside the hexagonal phase, which allows for an easy identification of the features corresponding to PTCDI and melamine molecules. A model for the proposed structure of the square network is given in Figure 4.5 (b). This structure is based on a melamine-rich node (shown in Figure 4.6) and is discussed in more detail below.

Another network structure is also observed to co-exist with the square and hexagonal phases. Figure 4.5 (c) shows an STM image of a network structure consisting of hexagonal and triangular pores, reminiscent of a kagome lattice structure. The dimensions of the unit cell for this structure are measured to be $50 \text{ \AA} \pm 1 \text{ \AA}$ by $50 \text{ \AA} \pm 1 \text{ \AA}$, with an angle of $59^\circ \pm 4^\circ$. As with the square phase, the hexagonal shaped pores may be used to identify the features which correspond to the PTCDI and melamine molecules. A proposed model for this ‘super-hex’ structure is shown in Figure 4.5 (d). Similar to the square phase the super-hex phase may be constructed by combining several melamine-rich vertices together. Both of the melamine-rich structures have the same PTCDI:melamine ratio of 1:2.

The melamine-rich vertex (shown in Figure 4.6 (a)) is composed of 4 melamine molecules and 4 PTCDI molecules. The two melamine molecules at the top right and bottom left of the central cluster each form two triple hydrogen-bonds with two PTCDI molecules (highlighted in blue in the Figure). The cluster of melamine molecules are bound together by two different hydrogen-bonding interactions. The top and bottom pairs of molecules interact via the same double hydrogen-bond as discussed for melamine dimers (highlighted in red). Within the melamine-rich junction there are also two new hydrogen-bonding interactions (highlighted in green).

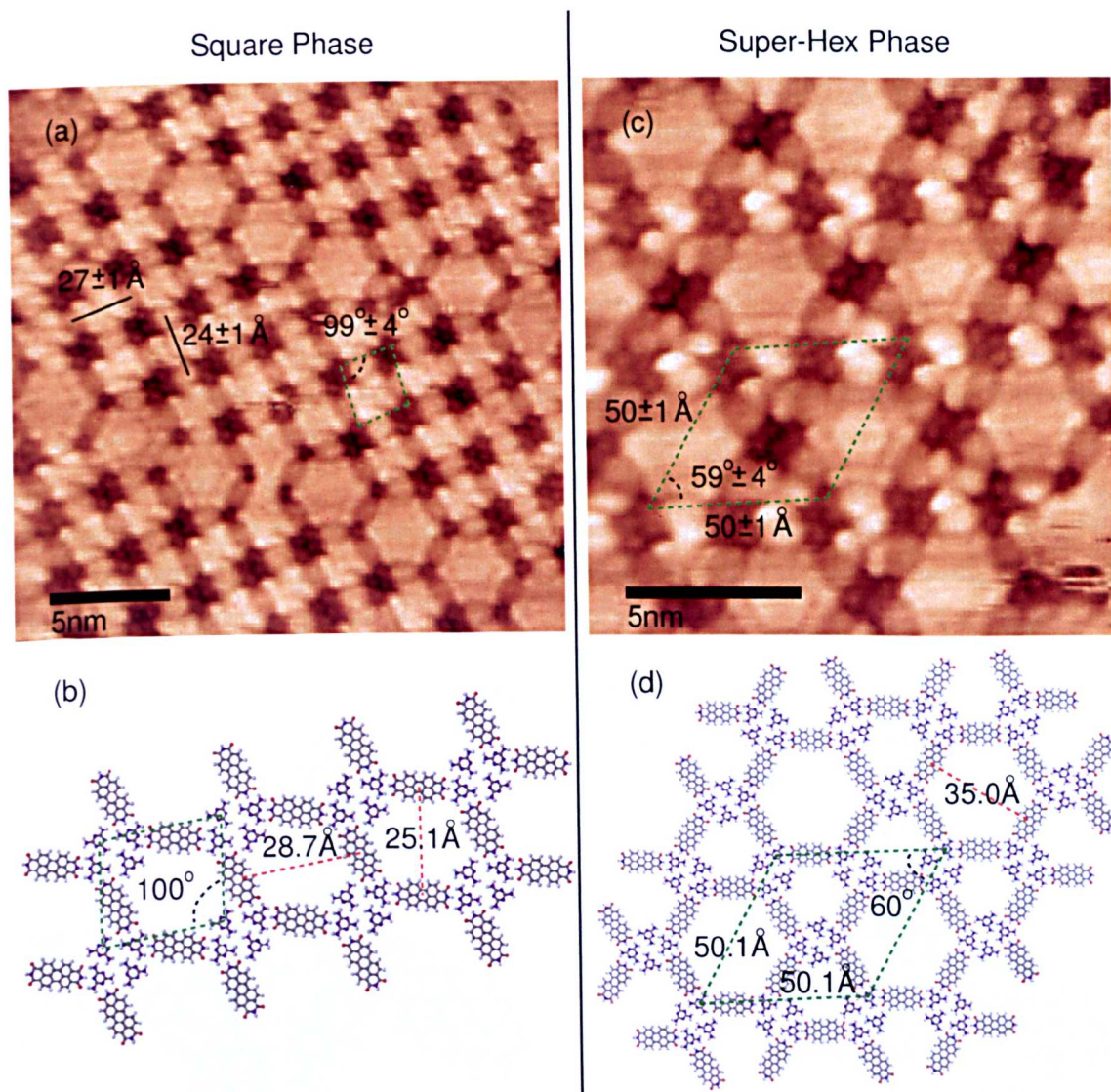


Figure 4.5: (a) STM image of the square phase formed on the Au(111) surface ($V_{sample} = +2.50 \text{ V}$, $I_{tunnel} = 0.03 \text{ nA}$). (b) Schematic showing the proposed structure of the melamine-rich square phase. The unit cell is highlighted by a green dotted line. (c) STM image of the super-hexagonal phase formed on the Au(111) surface ($V_{sample} = +2.50 \text{ V}$, $I_{tunnel} = 0.03 \text{ nA}$). (d) Schematic showing the proposed structure for the melamine-rich super-hexagonal phase, the unit cell is highlighted by a green dotted line.

The stability of the melamine-rich vertex structure has been investigated using DFT calculations. The dimensions of the geometry optimised structure are shown in Figure 4.6 (b). The total BE of the structure has been calculated to be 5.75 eV. By breaking the junction down into its component hydrogen-bond interactions (2 melamine-melamine, 4 melamine-PTCDI, 2 melamine-rich) an estimate of the BE of the additional melamine-rich interactions can be obtained. These additional interactions provide 1.53 eV of energy to the structure.

The melamine-rich junction can be extended in two different ways to give rise to the square and super-hex network phases. Figures 4.5 (b) and (d) show the structures created by using the melamine-rich node (as calculated by DFT) and then extending the network structure. The dimensions obtained from the DFT calculations are in good agreement with the experimentally determined values. The melamine-rich structures appear to be meta-stable as annealing the sample at 100°C gives rise to the complete conversion of the mixed and hexagonal phases to the parallelogram phase. By comparing the PTCDI:melamine stoichiometric ratio for all the structures we can see that annealing has reduced the 1:2 ratio for the melamine rich phases to a 3:2 ratio for the parallelogram phase. This demonstrates that the excess melamine involved in the melamine-rich vertex has been removed from the surface during the annealing process allowing the more stable parallelogram phase to form.

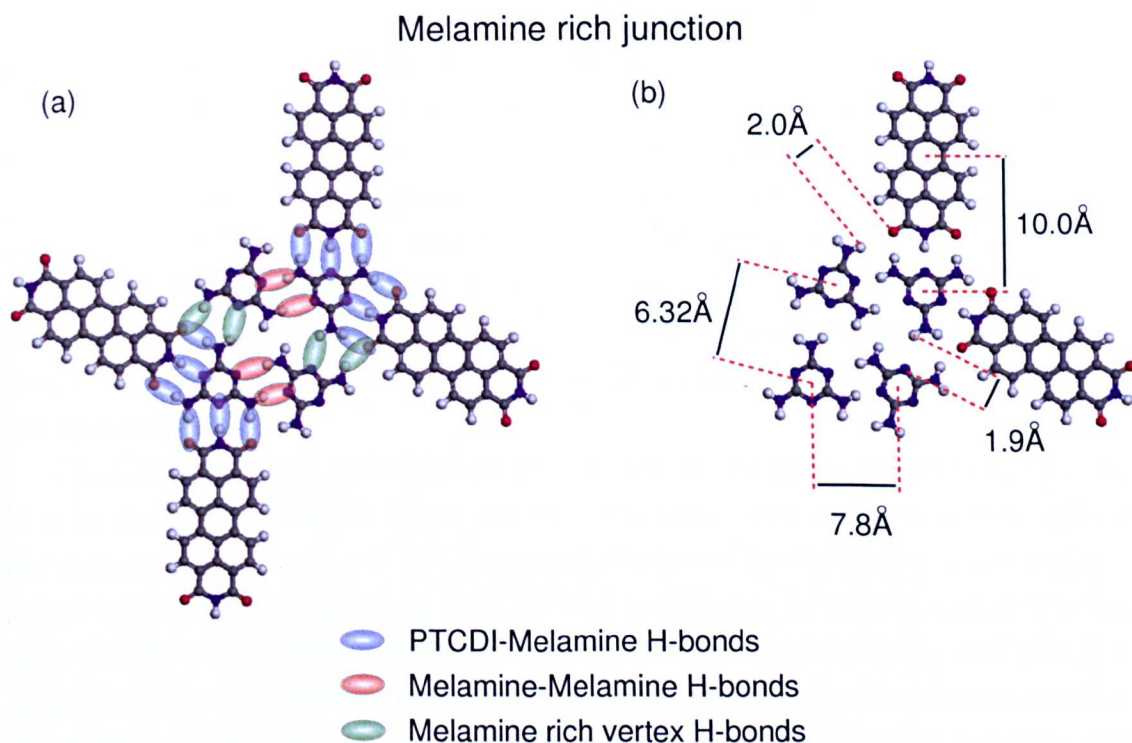


Figure 4.6: (a) Structure of the proposed melamine-rich hydrogen-bonded junction. Previously observed PTCDI-melamine and melamine-melamine hydrogen-bonds are present as well as additional hydrogen-bond interactions. (b) Schematic showing the DFT calculated dimensions of the melamine-rich junction.

4.2.1 Formation of the various PTCDI/melamine phases

In order to understand the methodology for the creation of the various phases of the PTCDI/melamine molecule networks on the Au(111) surface, a flow diagram of the processes involved is illustrated in Figure 4.7. Starting from a clean Au(111) substrate the deposition of PTCDI by sublimation results in the formation of the homo-molecular close-packed PTCDI structure. The subsequent deposition of melamine allows the mixed phase to self-assemble on the surface. Consequently the mixed phase will have an excess of melamine, and stoichiometric ratio of at least 1:2. Depending upon the PTCDI:melamine ratio at the surface, annealing the sample at $\sim 50^\circ\text{C}$ gives rise to the formation of either an exclusively hexagonal phase, or a co-existing mixture of hexagonal and melamine-rich phases. It is interesting to note that a similar procedure performed on the Ag/Si(111) surface only produces the hexagonal phases. This may be due to a mismatch in the commensurability between the network structure and the underlying periodicity of the substrate. If the periodicity of the Ag/Si(111) surface is incommensurate with that of the melamine-rich structure then the formation of such structures may be inhibited, whilst the hexagonal network (with a commensurate periodicity) is able to form. Finally, annealing the sample at $\sim 100^\circ\text{C}$ removes excess melamine from the surface so that the PTCDI:melamine ratio is reduced to 3:2, allowing for the re-arrangement of the molecules into the more stable parallelogram phase.

Another way of looking at the structures formed is to consider a phase diagram for the system, where the variables are the sample anneal temperature and the PTCDI:melamine ratio. Figure 4.8 shows a schematic representation of such a phase diagram, illustrating the complex nature of a bi-component system. The homo-molecular phases can be understood in terms of the molecules adopting their lowest energy structures, which are driven by the formation of the highly directional, anisotropic, hydrogen-bonds. The molecules are also able to close-pack so as to maximise the vdW interactions between the molecules. By forming close-packed structures both the vdW and hydrogen-bonding interactions are maximised.

Combining the two molecules on the surface results in the possibility of a range of structures being formed. Some of these structures, such as the hexagonal phase, are easy to understand and could arguably be predicted by simply considering of triple hydrogen-bond between PTCDI and melamine. However, the subtle balance between the highly directional hydrogen-bonding interactions and the more general isotropic attraction of the vdW forces between the molecules means that, in practice, it is difficult to predict whether structures such as the melamine-rich and parallelogram phases will form on the surface.

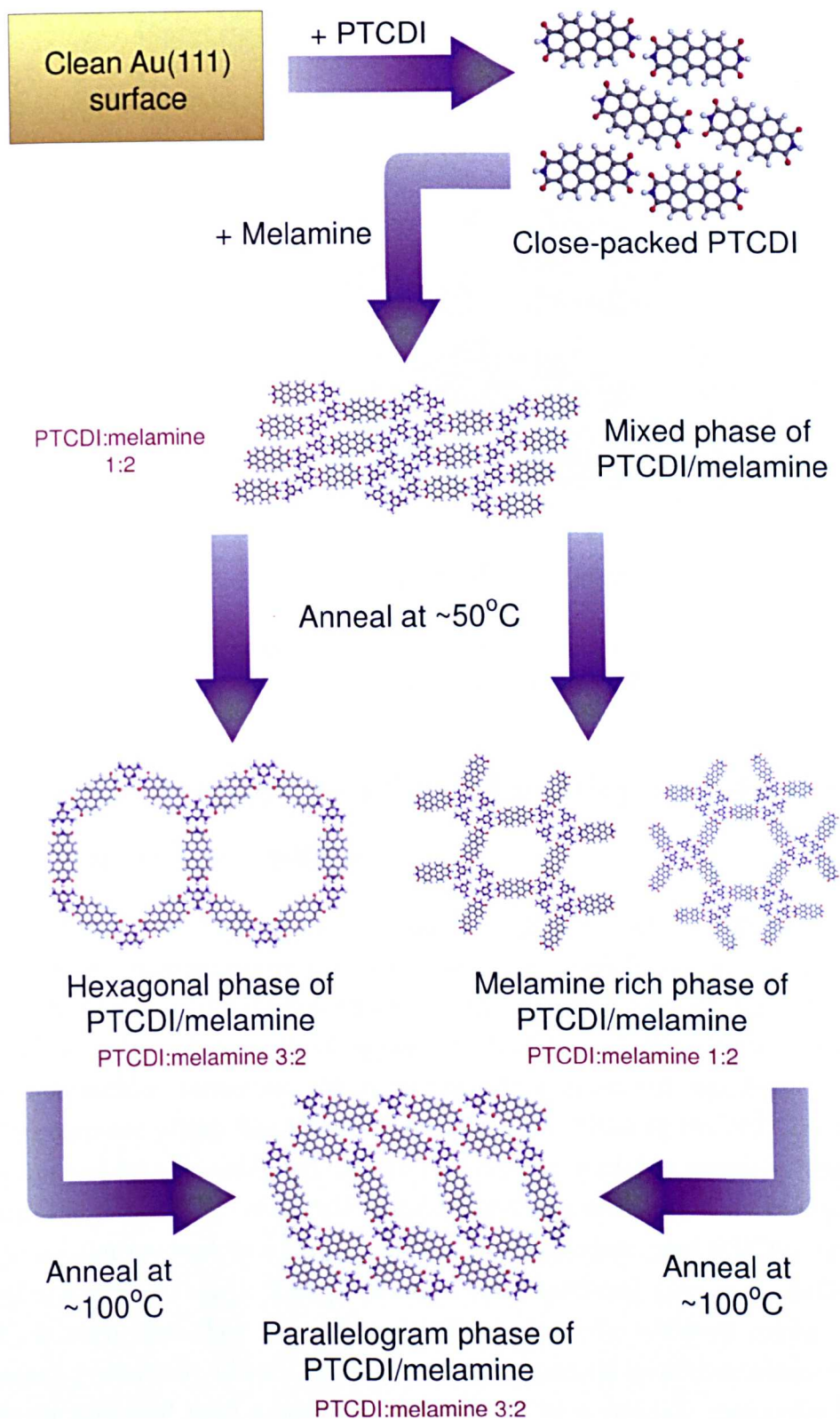


Figure 4.7: Flow diagram demonstrating the methodology for forming the various PTCDI/melamine hydrogen-bonded network phases on the Au(111) surface.

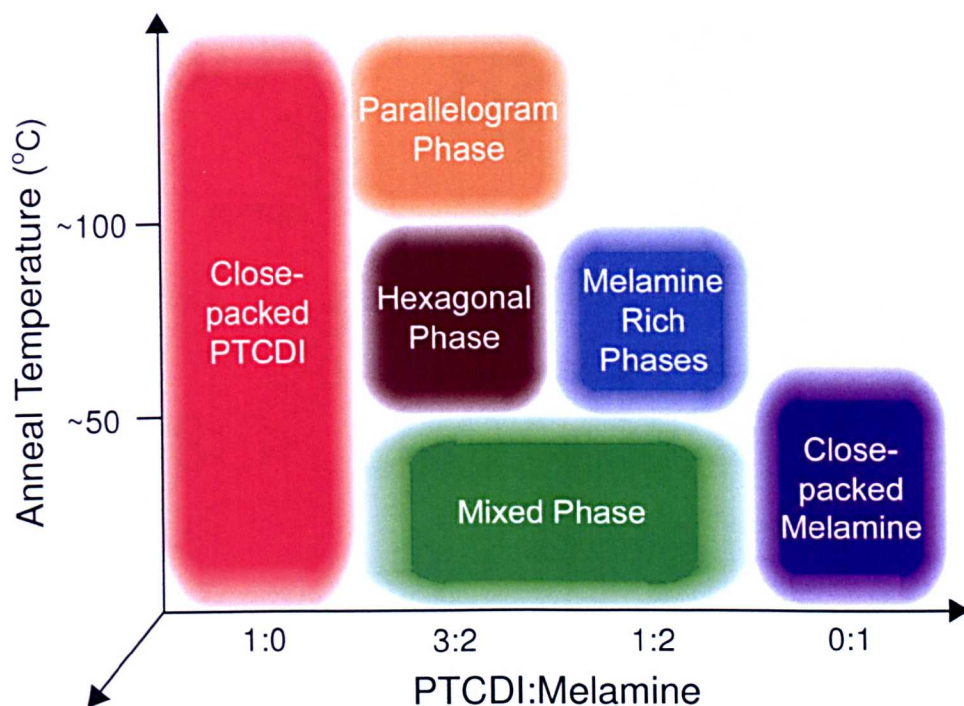


Figure 4.8: Schematic showing the conditions required to form the various PTCDI/melamine structures. By altering the PTCDI:melamine stoichiometric ratio and the anneal temperature a wide range of structures may be formed.

4.3 Adding chemical functionality to a hydrogen-bonded network

It is desirable to be able to create surface supported self-assembled structures which incorporate predetermined chemical, optical, electronic, or magnetic functionality within the structures formed. One possible way of achieving this is to use chemically functionalised molecular ‘building blocks’ as the components of a self-assembled structure. Work previously carried out within the Nottingham Nanoscience group has focused on using derivatives of the PTCDI molecule with chemical groups attached to the bay positions of the perylene core. This functionalised R_2 PTCDI molecule could be incorporated into a hydrogen-bonded supramolecular network in a similar fashion to unfunctionalised PTCDI (as demonstrated in Figure 4.9 (a)). The position of the functional groups, as indicated by an ‘**R**’, is such that they are able to protrude into the network pores. This arrangement potentially allows the formation of a porous structure where the pores have been prepared with a specific chemistry. Two candidate molecules for these experiments are shown in Figure 4.9 (b) and (c), where the molecule in (b) has had two Br atoms attached to its sides (Br_2 PTCDI) and molecule (c) has been functionalised with propyl-thioether side groups (S_2 PTCDI). Both of these molecules have been previously studied on the Ag/Si(111) surface, and have been observed

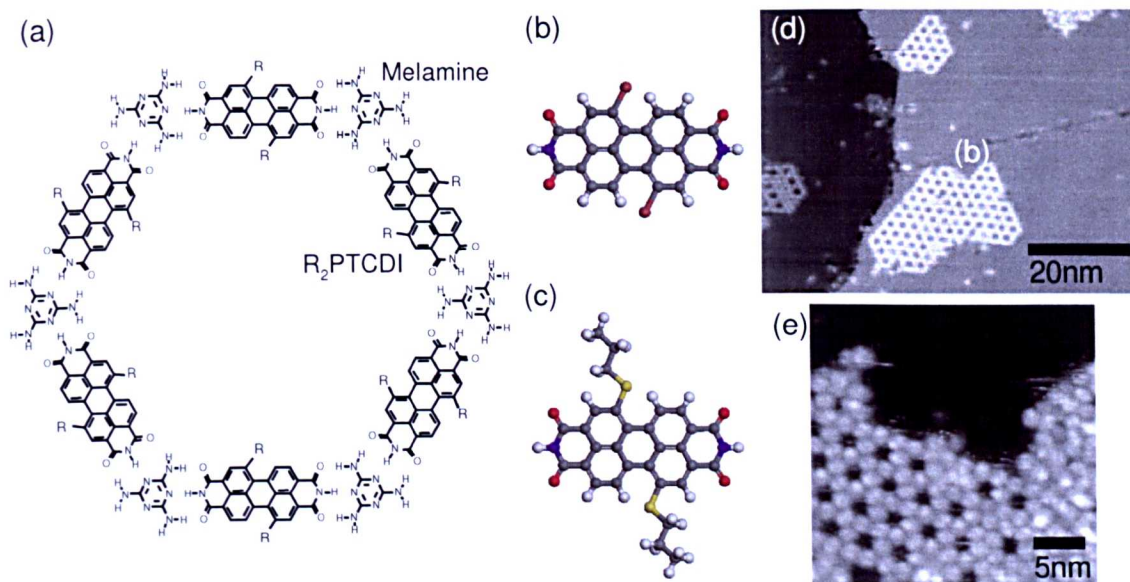


Figure 4.9: (a) Schematic showing how a chemically functionalised R_2 PTCDI molecule could be incorporated into the hexagonal network [adapted from [31]]. (b) and (c), chemical structures of Br_2 PTCDI and S_2 PTCDI. (d) and (e) STM images of Br_2 PTCDI/melamine, and S_2 PTCDI/melamine, networks formed on the Ag/Si(111) surface ($V_{sample} = +2.10$ V, $I_{tunnel} = 0.05$ nA, and $V_{sample} = -2.50$ V, $I_{tunnel} = 0.03$ nA) [images courtesy of L.M.A. Perdigo].

to form hetero-molecular hexagonal structures when mixed with melamine [31]. STM images of the structures formed from Br_2 PTCDI and S_2 PTCDI are shown in Figure 4.9 (d) and (e).

The shape of the S_2 PTCDI molecules allows for an alternative homo-molecular structure to be formed on the Ag/Si(111) surface. When the molecule is sublimed onto the substrate, regions of an open porous network are observed in the STM images. Figure 4.10 (a) is an STM image showing a region of the hexagonal network formed in the absence of melamine. The periodicity of the network is smaller than that of the PTCDI/melamine hexagonal structure and is measured to be $28.3 \text{ \AA} \pm 1 \text{ \AA}$ [31].

The formation of this homo-molecular hexagonal structure is driven by an alternative hydrogen-bonding arrangement involving three S_2 PTCDI molecules at each vertex of the network. This type of hydrogen-bonding motif has previously been observed for the cyanuric acid molecule when deposited onto both the Ag/Si(111) [14] and the Au(111) [16] surfaces. Figure 4.10 (b) shows a schematic of the hydrogen-bonding arrangement for 3 cyanuric acid molecules at a trimer junction, with Figure 4.10 (c) showing how the S_2 PTCDI molecules can be arranged on the Ag/Si(111) surface using this type of trimer bonding arrangement to give rise to the open pored hexagonal structure. The hexagonal network was found to be commensurate with the underlying surface lattice, with the network running $16^\circ \pm 2^\circ$ off the $[1 \ 1 \ \bar{2}]$ major surface axis [31].

This type of bonding arrangement has not been observed for either the PTCDI or Br_2 PTCDI molecules deposited on the Ag/Si(111) or the Au(111) surfaces. The

arrangement is therefore attributed to an effect mediated by the thioether pendant groups. The most obvious effect that the pendant groups will have, is to destabilise the homo-molecular close-packed structure exhibited by non-functionalised PTCDI. The second, less obvious effect, is that the addition of the alkyl side-chains allows for the formation of secondary hydrogen-bond interactions adding further to the stability of the trimer node.

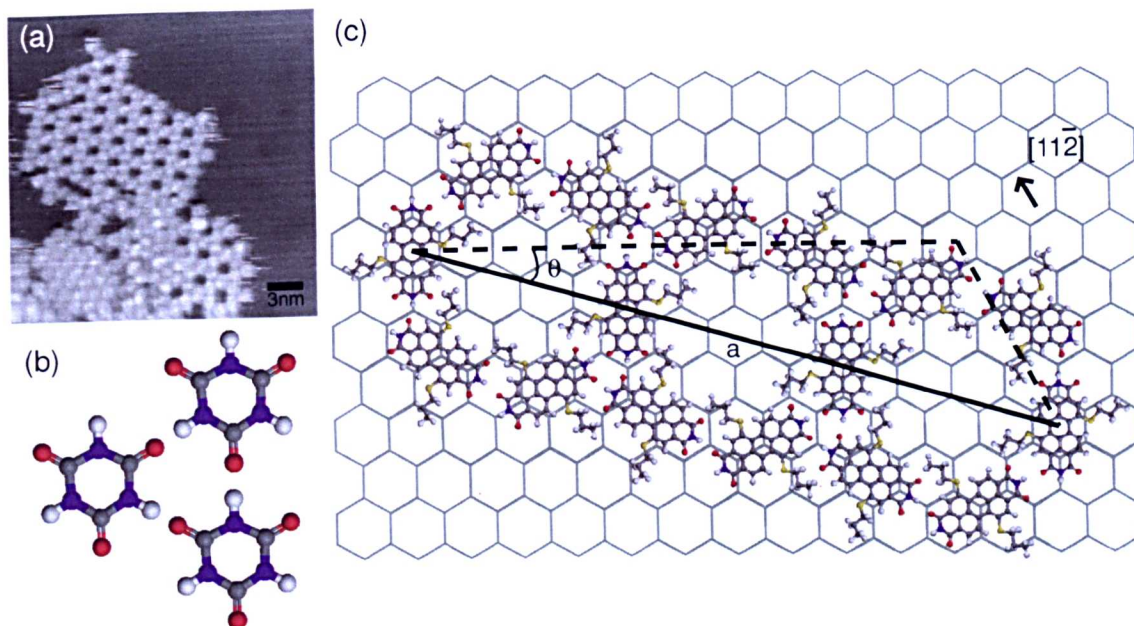


Figure 4.10: (a) STM image showing the homo-molecular hydrogen-bonded hexagonal structure formed by S_2 PTCDI on the Ag/Si(111) surface ($V_{sample} = -2.50$ V, $I_{tunnel} = 0.03$ nA). (b) Schematic showing the trimer node of three hydrogen-bonded cyanuric acid molecules. (c) Schematic showing the homo-molecular hexagonal network formed by S_2 PTCDI on the Ag/Si(111) surface. [STM image courtesy of L.M.A. Perdigao, (c) adapted from [31]]

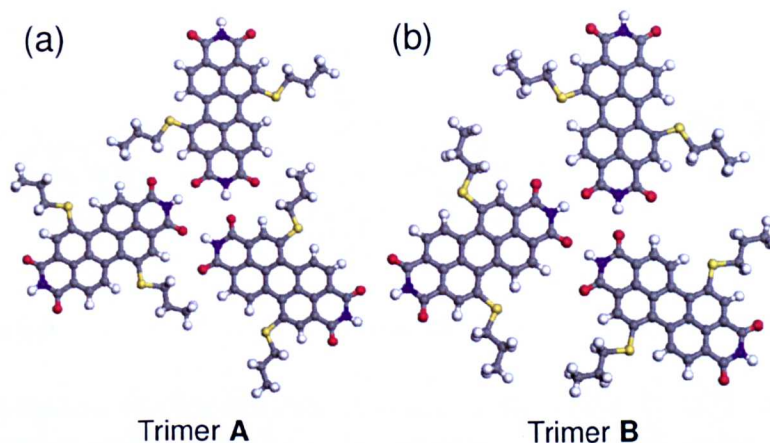


Figure 4.11: Two possible arrangements for the trimer node formed from S_2 PTCDI molecules. The pendant thioether groups may be in bonding, (a), or non-bonding, (b), positions giving rise to additional hydrogen-bonding interactions.

Figure 4.11 shows two possible models for the arrangement of the side chains of the S_2 PTCDI molecules involved in a trimer bonding node. Trimer A shows a con-

figuration where the side chains of one molecule are brought into close proximity with the carboxyl (C=O) group of a neighbouring molecule within the junction, allowing for a potential secondary hydrogen-bond interaction. Trimer **B** shows a different bonding set-up where the side chains are positioned so that there is no interaction with the carboxyl groups.

4.3.1 DFT calculations of the functionalised R_2 PTCDI structures

In order to investigate the effect of these chemical groups on the hydrogen-bonding interaction between molecules, DFT calculations have been performed as part of this work. Figure 4.12 shows schematics of the different hydrogen-bonding arrangements that have been modelled using DFT. The ‘**R**’ group represents either H, Br, or $SCH_2CH_2CH_3$ for PTCDI, Br_2 PTCDI, and S_2 PTCDI respectively. For the dimer bonding arrangements (Figure 4.12 (a) - (c)) three distinct structural arrangements are possible, labelled **A**, **B**, and **C**. Table 4.1 shows the BE between the two molecules, with all the calculated BEs being in the range 0.47-0.49 eV. These calculations demonstrate that the addition of the chemical side groups does not effect the strength of the hydrogen-bond interaction between the two molecules.

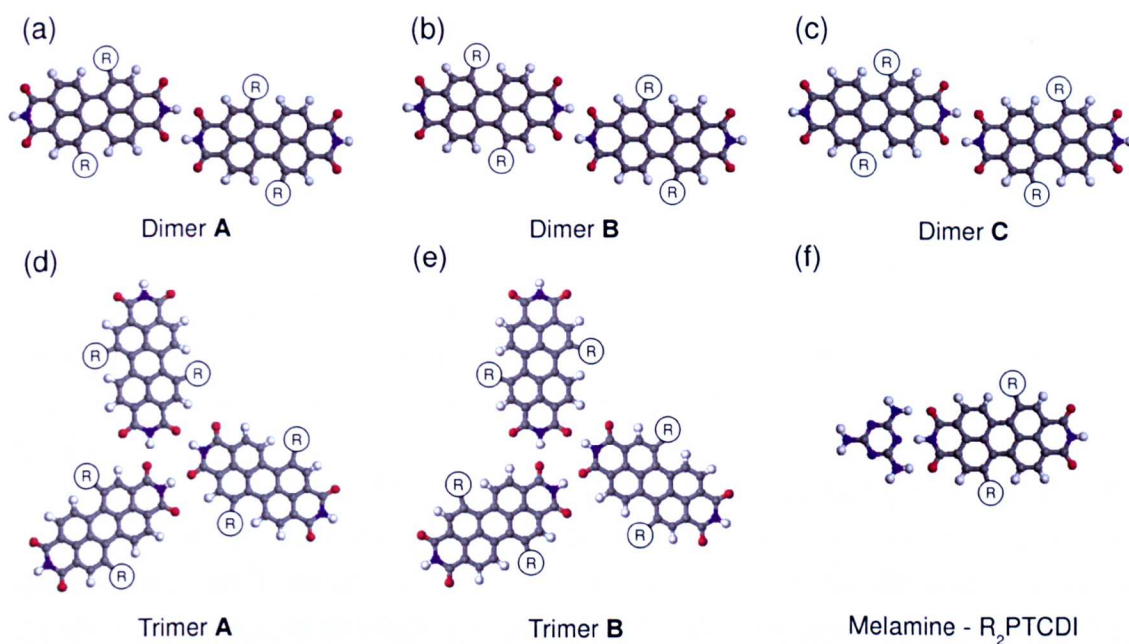


Figure 4.12: Schematic showing the structures used to determine the DFT calculated binding energies for homo-molecular dimers ((a)-(c)), and trimer ((d) and (e)) arrangements, as well as the R_2 PTCDI/melamine hetero-molecular interactions.

As discussed previously there are two possible orientations for the molecules involved in the trimer bonding junction (labelled trimer **A** and **B** in Figure 4.12 (d) and (e)). Table 4.1 shows that for the S_2 PTCDI trimer junction, trimer **A** is more stable than trimer **B** by 0.16 eV. This additional stabilisation may be attributed

to the secondary hydrogen-bonding interaction between the alkyl chains and the carboxyl group. Compared to the other trimer nodes which have been modelled, trimer A is the most stable. Even though all of the trimer junctions modelled by DFT are predicted to be stable structures, only the S₂PTCDI trimer is observed experimentally. This may be attributed to the fact that the close-packed structure, which is the observed structure for PTCDI and Br₂PTCDI, is de-stabilised by the presence of the alkyl chains.

| Molecule | Dimer Arrangement | Dimer BE (eV) | Trimer Arrangement | Trimer BE (eV) | R ₂ PTCDI + melamine BE (eV) |
|-----------------------|-------------------|---------------|--------------------|----------------|---|
| PTCDI | - | 0.48 | - | 0.78 | 0.80 |
| Br ₂ PTCDI | A | 0.48 | A | 0.73 | 0.87 |
| | B | 0.47 | B | 0.78 | |
| | C | 0.47 | | | |
| S ₂ PTCDI | A | 0.48 | A | 0.86 | 0.87 |
| | B | 0.49 | B | 0.70 | |
| | C | 0.48 | | | |

Table 4.1: Binding energies for various R₂PTCDI interactions.

4.3.2 Structures formed by Br₂PTCDI and melamine on the Au(111) surface

The R₂PTCDI derivatives of PTCDI have been investigated further as part of this thesis. The Br₂PTCDI molecule has been sublimed onto an Au(111) surface held in UHV conditions, with the resultant self-assembled structures being characterised by STM. These experiments were performed in order to ascertain whether functionalised network structures could be formed on both the Ag/Si(111) and Au(111) surfaces.

Figure 4.13 shows the DFT calculated HOMO and LUMO for the Br₂PTCDI molecule. Both the HOMO and the LUMO have part of their orbital structure positioned over the Br atoms and it is therefore expected that the Br atoms should be visible in STM images as bright protrusions. The STM image shown in Figure 4.13 (c) shows a domain of close-packed Br₂PTCDI deposited on the Au(111) surface, with the pairs of bright features on each molecule corresponding to the Br atoms. The molecules have adopted a close-packed structure similar to that observed for PTCDI, with rows of molecules forming double hydrogen-bonds at both ends. The separation between the molecules along the row is found to be 15 Å ± 1 Å, which is in excellent agreement with the measured values obtained for the PTCDI close-packed structure. The formation of close-packed Br₂PTCDI is unexpected, as a repulsive interaction between the bromine atoms of the molecules in adjacent

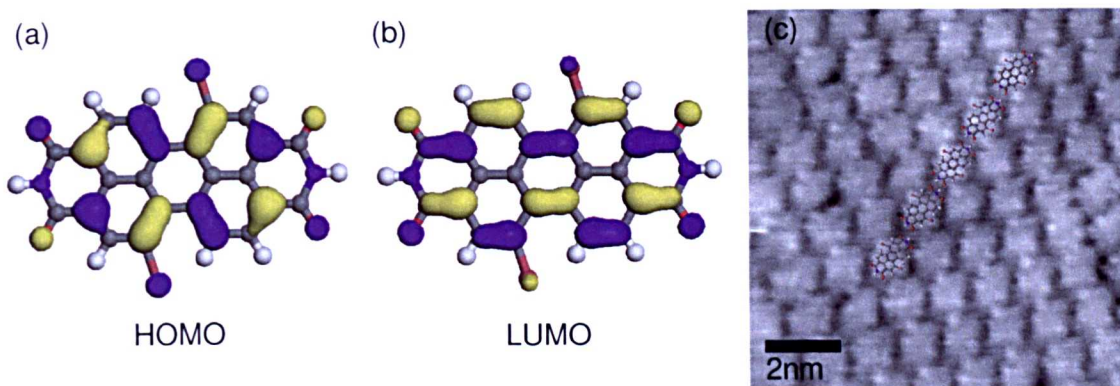


Figure 4.13: Structure of the Br_2PTCDI molecule overlaid with the DFT calculated LUMO, (a), and HOMO, (b). (c) STM image showing a close-packed domain of Br_2PTCDI on the Au(111) surface. The bright features correspond to the position of the Br atoms ($V_{\text{sample}} = -0.30$ V, $I_{\text{tunnel}} = 0.03$ nA).

rows (due to the electronegativity of the bromine atoms) is anticipated to destabilise the close-packed structure. Similar to the PTCDI close-packed structure, the Br_2PTCDI close-packed domains show that there is a balance between the vdW and hydrogen-bonding forces both of which are maximised by the close-packed arrangement.

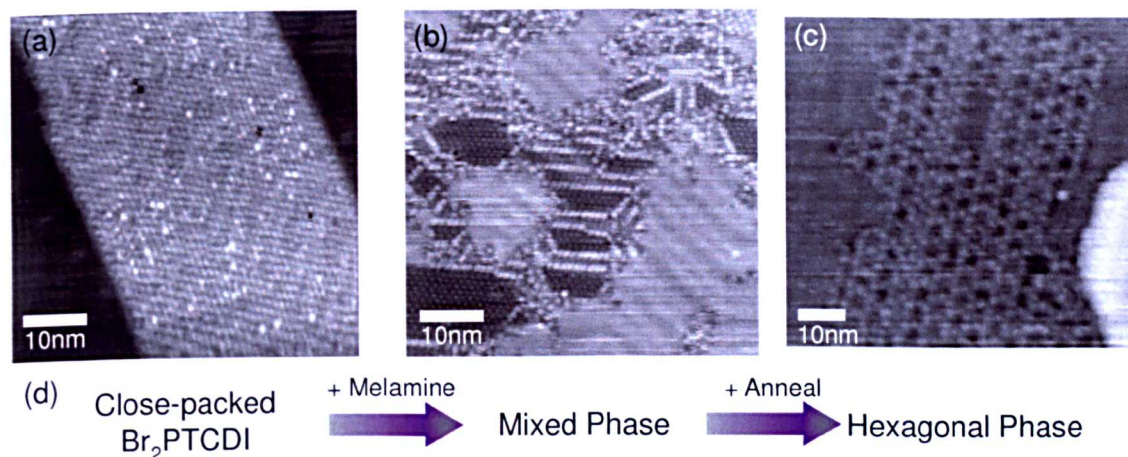


Figure 4.14: STM images showing: (a) A domain of close-packed Br_2PTCDI ($V_{\text{sample}} = -1.80$ V, $I_{\text{tunnel}} = 0.03$ nA). (b) Mixed phase of Br_2PTCDI and melamine ($V_{\text{sample}} = -2.25$ V, $I_{\text{tunnel}} = 0.03$ nA). (c) Hexagonal network structure ($V_{\text{sample}} = -2.50$ V, $I_{\text{tunnel}} = 0.03$ nA). All structures are formed on the Au(111) surface.

Following a similar methodology to that described for PTCDI it is possible to form a hexagonal phase incorporating the Br_2PTCDI molecules. Figure 4.14 shows STM images of the Au(111) surface at various stages throughout the network production. Figure 4.14 (a) shows a region of close-packed Br_2PTCDI , while (b) shows the mixed phase produced after the deposition of melamine. This structure is identical to the mixed phase structure observed for PTCDI and melamine. The bright lozenge features correspond to Br_2PTCDI molecules, and the darker features correspond to the position of melamine. Annealing the sample at $\sim 80^\circ\text{C}$ results in the

formation of domains of hexagonal network such as those shown in Figure 4.14 (c). The measured periodicity of the hexagonal structure is $34 \text{ \AA} \pm 1 \text{ \AA}$, in agreement with the previously measured PTCDI/melamine hexagonal structure.

4.3.3 Structures formed by S₂PTCDI and melamine on the Au(111) surface

Following the deposition of a low molecular coverage of S₂PTCDI on the Au(111) surface, the formation of one-dimensional chains of hexagonal structures are seen to run along the $[1\ 1\ \bar{2}]$ direction of the reconstructed Au surface. Figure 4.15 (a) shows a large scale STM image where several one-dimensional hexagonal chains are seen to run along the $[1\ 1\ \bar{2}]$ direction, which corresponds to the bright lines of the herringbone reconstruction. The chains alter direction with an angle of $\sim 120^\circ$ (as shown at the top of Figure 4.15) in order to maintain their orientation relative to the herringbone structure. The periodicity of the structure is measured to be $26.5 \text{ \AA} \pm 1 \text{ \AA}$ for the centre to centre spacing of the hexagonal pores. This distance is in agreement with the periodicity measured for the hexagonal structures formed on the Ag/Si(111) surface [31]. Increasing the coverage of molecules on the surface results in the formation of small regions of two-dimensional hexagonal structures such as that labelled in STM image Figure 4.15 (b). The higher coverage results in ‘noisy’ STM images indicating that there a great deal of molecular species diffusing over the surface. Figure 4.15 (c) shows a schematic of the hexagonal structure with the experimentally determined periodicity highlighted.

The structure of the hexagonal chains can be confirmed by investigating the internal structure of the S₂PTCDI molecule as it appears in STM images. Figures 4.15 (d) and (e) show the DFT calculated HOMO and LUMO for the S₂PTCDI molecule. The calculations reveal that part of the molecular orbital structure for both the HOMO and LUMO is located over the sulphur atoms within the molecule, and hence it is expected that the S atoms will appear as bright features in the STM images. Figure 4.15 (f) shows a close-up STM image of a region of the hexagonal network where pairs of bright protrusions can clearly be resolved for each S₂PTCDI molecule (highlighted with open circles). By overlaying the S₂PTCDI molecules onto this STM image (Figure 4.15 (g)), it can be seen that the bright features correspond to the positions of the S atoms for three molecules arranged in a trimer node structure. The position of the bright protrusions also allows us to distinguish between the two trimer types (A and B). As the structure shown in the image is a trimer of type A conformation, where the alkyl chains are in a position to participate in the secondary hydrogen-bonding interaction discussed previously in this chapter. Analysis of several STM images shows that only trimer A structures are observed on the Au(111) surface following deposition.

Surfaces prepared with a coverage of ~ 1 ML produce different molecular structures. Figure 4.16 (a) shows an STM image acquired from an Au(111) surface after

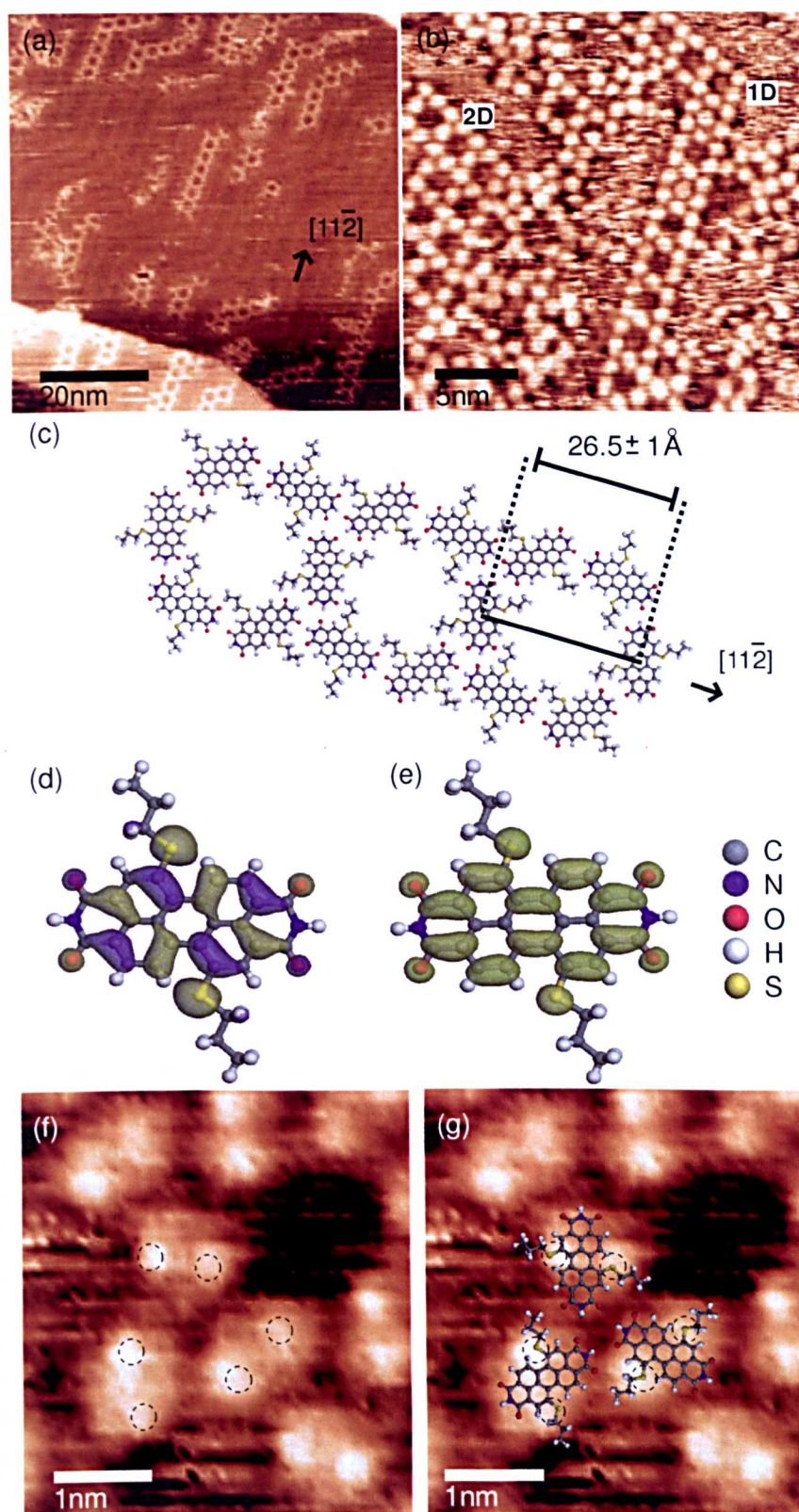


Figure 4.15: (a) STM image showing chains of the hexagonal network, formed from S_2 PTCDI, running along the $[1\bar{1}2]$ direction of the Au(111) surface ($V_{sample} = -1.20 \text{ V}$, $I_{tunnel} = 0.03 \text{ nA}$). (b) STM image showing the Au(111) surface with a higher molecular coverage, two-dimensional hexagonal structures are observed to form ($V_{sample} = +2.00 \text{ V}$, $I_{tunnel} = 0.03 \text{ nA}$). (c) Schematic of the hexagonal chain structure, with the experimentally observed periodicity indicated. DFT calculated (d) HOMO and (e) LUMO, for S_2 PTCDI. (f) STM image of a trimer node, the bright features correspond to the positions of the S atoms ($V_{sample} = +1.25 \text{ V}$, $I_{tunnel} = 0.03 \text{ nA}$). (g) STM image with the position of the S_2 PTCDI molecules.

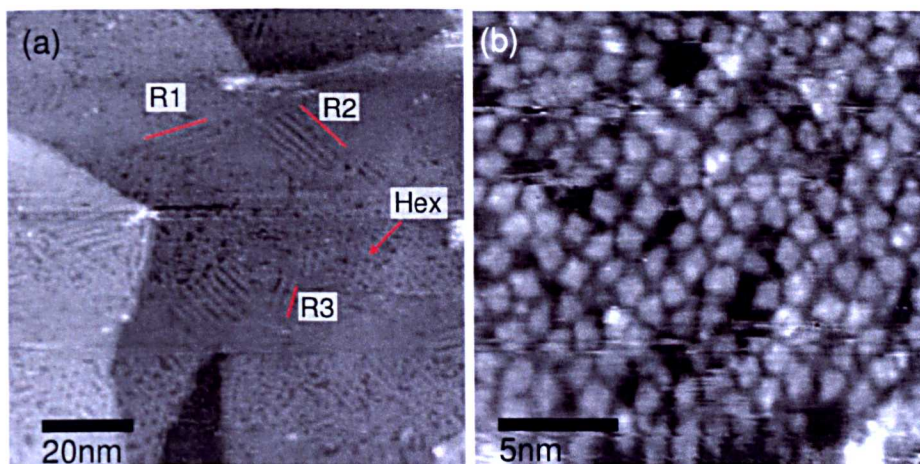


Figure 4.16: STM image showing a high coverage of S_2 PTCDI on the Au(111) surface. Three direction of the row phase are indicated (R1-R3), running at 60° to one another. A region of the two-dimensional hexagonal structure is also highlighted ($V_{sample} = -2.00$ V, $I_{tunnel} = 0.03$ nA). (b) Close-up STM image showing the row phase and a region of the amorphous phase ($V_{sample} = -1.80$ V, $I_{tunnel} = 0.03$ nA).

the deposition of ~ 1 ML of S_2 PTCDI. Regions of the two-dimensional hexagonal structure are still present, but co-exist alongside regions of a ‘row’ phase. The row phase is seen to run in three different directions on the surface, labelled **R1-R3**, with each row domain being rotated by 120° relative to each other. These rotations suggest that the three-fold symmetry of the underlying gold surface (possibly the herringbone reconstruction) is playing a role in the direction of these molecular domains. The separation between the rows of molecules varies between 15 \AA and 27 \AA , with the larger separation indicating that the molecules are unlikely to be interacting with each other through vdW or hydrogen-bonding forces. The spacing between the molecules along the row direction is $14 \text{ \AA} \pm 1 \text{ \AA}$ which is in agreement with the separation expected for a structure stabilised by a double hydrogen-bond between the molecules, similar to that observed for PTCDI and Br_2 PTCDI.

As well as the well ordered row and two-dimensional hexagonal phases a large proportion of the surface is covered in an amorphous structure (shown in Figure 4.16 (b)). There appears to be no order to the molecular domains. This type of structure may be formed as the alkyl chains inhibit the formation of a close-packed structure and the high surface density of molecules prevent diffusion to form the two-dimensional hexagonal structure.

Finally, an attempt was made to form the S_2 PTCDI/melamine hexagonal network structure by depositing S_2 PTCDI, then melamine, and annealing the sample at $\sim 80^\circ\text{C}$. In contrast to the same experiment previously carried out on the Ag/Si(111) surface, the hexagonal phase is not readily formed on the Au(111) surface. Some small regions of the hexagonal network were observed, such as that shown in the STM image in Figure 4.17 (a). The bottom right corner of the image

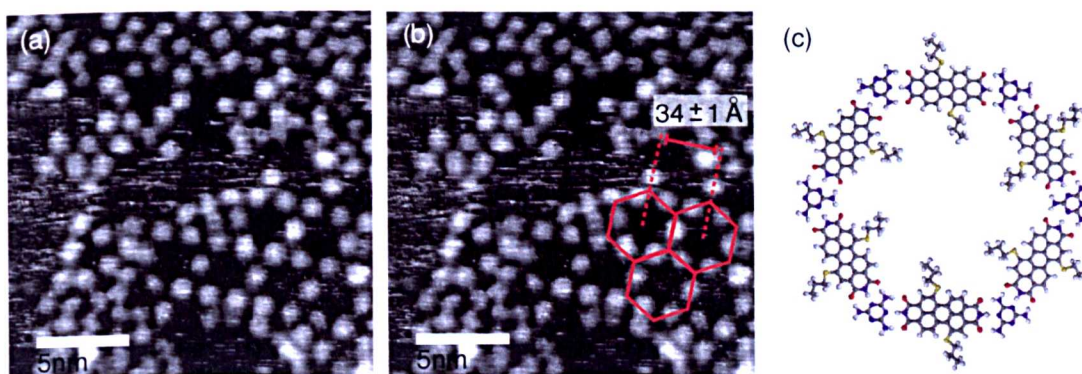


Figure 4.17: (a) STM images showing a small region of the S_2 PTCDI/melamine hexagonal structure ($V_{sample} = +1.50$ V, $I_{tunnel} = 0.03$ nA). (b) The same STM image with an overlay of the hexagonal network structure, the centre to centre spacing of the pores is indicated. (c) Schematic showing the structure of the S_2 PTCDI/melamine hexagonal network.

is a small section of the hexagonal network, where the centre to centre spacing is measured to be $34 \text{ \AA} \pm 1 \text{ \AA}$. Figure 4.17 (b) shows the same STM image with the structure of the hexagonal network overlaid, with a schematic of the molecular structure shown in Figure 4.17 (c).

4.4 Summary

Within this chapter the hydrogen-bonded structures formed by PTCDI and R_2 PTCDI have been discussed. An overview of the previous work conducted on the Ag/Si(111) surface has been given, and new results have been presented describing previously unobserved structures formed on the Au(111) surface. The complexity of the PTCDI/melamine structures has been detailed, highlighting the delicate balance between the anisotropic hydrogen-bonding interactions, which should drive the system to form highly symmetric ordered networks such as the hexagonal phase, and the vdW forces which drive the formation of complex close-packed structures like the parallelogram phase.

The ability to produce chemically functionalised supramolecular structures has also been investigated. The addition of Br atoms to the core of the PTCDI molecule does not inhibit the formation of the hexagonal phase on either the Ag/Si(111) or Au(111) surfaces. However, the addition of the thioether chains of the S_2 PTCDI molecule radically alters the shape of the molecule and hinders the formation of the close-packed molecular structures observed for PTCDI and Br_2 PTCDI whilst promoting the formation of a new hydrogen-bond stabilised structure.

The work discussed in this chapter shows that hydrogen-bond mediated self-assembly is a promising way to produce a range of structures and that it is possible to add chemical functionality to these structures. However, it is not easy to predict which structures will form without a complete understanding of the molecule-

molecule and molecule-substrate interactions. These interactions become even more unpredictable for more complex three-dimensional molecules (examples of which are discussed in Chapters 6 and 7 of this thesis). However, such complex molecules are thermally labile and hence may not be sublimed. The next chapter investigates the use of the UHV-ESD technique as a way of transferring molecules from solution to substrates held in UHV.

Chapter 5

Electrospray deposition of C_{60}

In this chapter an alternative technique for transferring fragile molecules into a UHV environment for analysis by STM and XPS measurements is described. The fullerene C_{60} is investigated as a test case, allowing comparisons to be made between UHV-ESD and thermal deposition techniques as a way of producing thin films of C_{60} on an Au(111) substrate. Step-edge decoration and hexagonally close-packed islands are observed at low and multilayer coverages respectively. It is also demonstrated that the deposition of molecules by UHV-ESD can be used in conjunction with a surface which has been prepared with a hydrogen-bonded supramolecular template.

5.1 The transport of fragile molecules into an UHV environment: C_{60} as a test case

The concept of bottom-up fabrication of nanoscale devices relies on the ability to accurately position molecular and atomic species, which possess well defined optical, electronic, and magnetic properties. Unfortunately many of the molecules that display these interesting physical properties (e.g. functionalised/endothedral fullerenes, porphyrins, single molecule magnets, etc.) are fragile and hence may not be sublimed. Electrospray ionisation provides a highly promising route for the deposition of non-volatile molecules onto surfaces held in UHV (as discussed in Chapter 3). The Nottingham Nanoscience group have previously demonstrated that carbon nanotubes can be deposited from a liquid suspension onto a surface held in high vacuum using an in-vacuo implementation of electrospray ionization [85]. It should be possible to deposit fragile molecules on a surface held in UHV using UHV-ESD and to then characterise the surface using high sensitivity UHV techniques such as STM and XPS.

C_{60} is known to be a highly stable molecule which may be sublimed, and has been chosen to illustrate the potential of UHV-ESD. The behaviour of fullerenes on noble metal surfaces has been extensively studied and allows us to compare

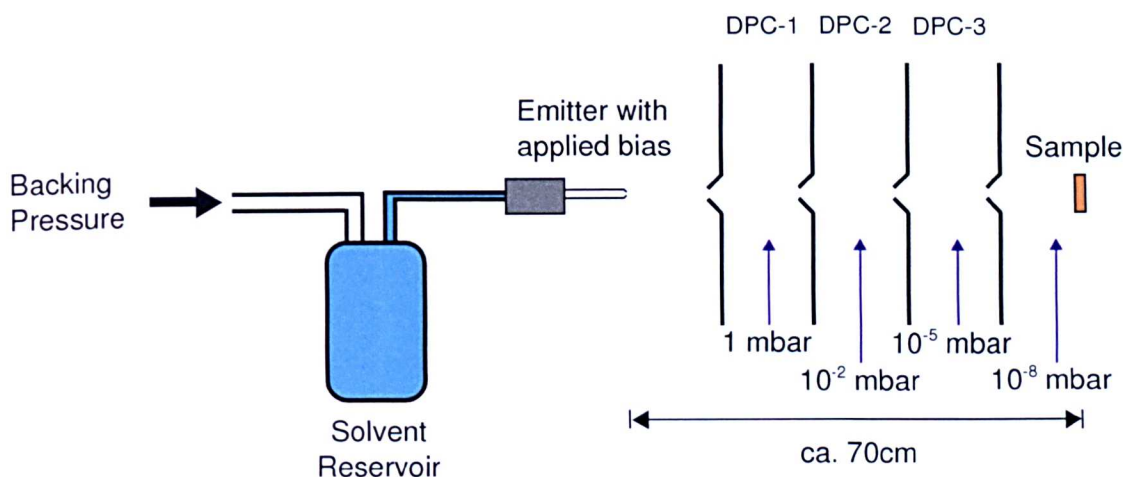


Figure 5.1: Schematic of the electro spray apparatus.

the results obtained from the UHV-ESD of C_{60} with previous STM and XPS data. Within this chapter the adsorption of C_{60} on an Au(111) substrate and a hydrogen-bonded supramolecular network will be described.

5.1.1 Experimental set-up

The electro spray apparatus used for this experiment is described in Chapter 3. In this version of the apparatus (shown in Figure 5.1) the solvent containing the dissolved fullerenes is forced from a reservoir and through an emitter due to a backing pressure of Ar gas. The volatilised spray enters the differentially pumped chambers of the apparatus via a skimmer cone with a 0.5 mm aperture (replaced by an entrance capillary in later versions). The remaining three apertures are skimmer cones, each with an aperture of 0.5 mm. The electro spray molecular beam was aligned with an Au(111) sample held in chamber 3 of the Nottingham UHV system. The Au(111) sample was prepared by Ar sputtering and annealing cycles (as described in Chapter 3) until a clean surface was observed in STM. A dilute solution of C_{60} in toluene/acetonitrile was prepared by ultrasonication (concentration typically less than 1 mg ml^{-1} of C_{60} , purity 99.9 %), with the mixture of toluene and acetonitrile in a 4:1 ratio by volume.

During deposition a pressure rise from 5×10^{-9} Torr to 2×10^{-7} Torr was observed, indicating the introduction of solvent molecules to the chamber. Toluene and acetonitrile molecular species were identified by a RGA. After UHV-ESD of C_{60} the Au(111) sample was characterised by an STM housed within an adjoining UHV chamber (chamber 2).

5.1.2 UHV-ESD of C_{60} on Au(111)

Initially the Au(111) sample was positioned below the direct line of sight of the electro spray beam and the sample was exposed to a flux of C_{60} for 1 hour. Subse-

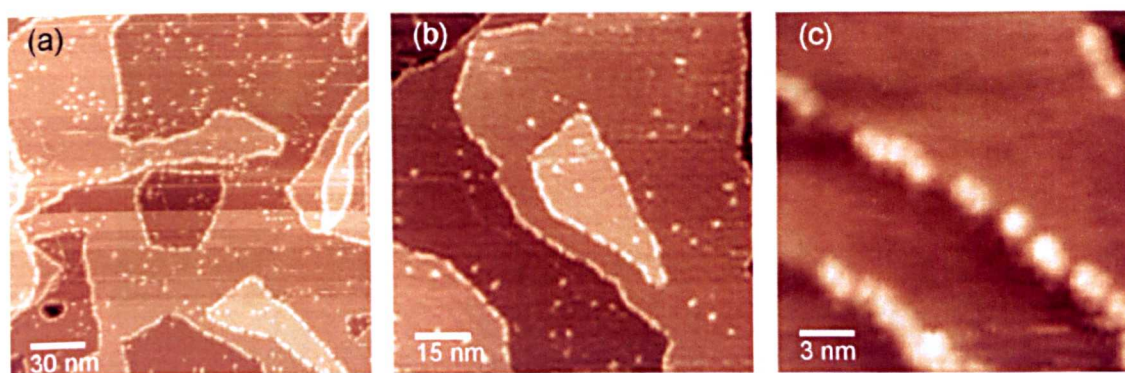


Figure 5.2: STM images of an Au(111) surface after electro spray deposition of C_{60} . Images show that at low coverages C_{60} is preferentially adsorbed at step edges. (a) $V_{sample} = +2$ V, $I_{tunnel} = 0.03$ nA. (b) $V_{sample} = -0.7$ V, $I_{tunnel} = 0.03$ nA. (c) $V_{sample} = -0.7$ V, $I_{tunnel} = 0.03$ nA.

quent STM characterisation of this surface showed that the monatomic step edges of the Au(111) substrate were decorated with C_{60} molecules. Figure 5.2 shows STM topographs where bright features, corresponding to C_{60} , cluster at step edges. A high resolution image (Figure 5.2 (c)) shows individual C_{60} molecules trapped at a step edge. The structures observed here are in good agreement with those expected for a low coverage of C_{60} on Au(111) produced by sublimation [108]. This finding demonstrates that C_{60} molecules deposited by UHV-ESD are able to diffuse from the centre of the Au(111) terraces and become pinned at the step edges, in a similar way to C_{60} deposited by sublimation.

As a test to ensure that the surface features observed after UHV-ESD are not due to a contaminant present within the solvent, a blank solution was sprayed onto a clean Au(111) substrate. The resulting surface morphology, after 1 hour of spray deposition, is shown in Figure 5.3 and shows no step edge decoration. This calibration experiment confirms that the structures observed in Figure 5.2 are due to the presence of C_{60} on the Au(111) surface.

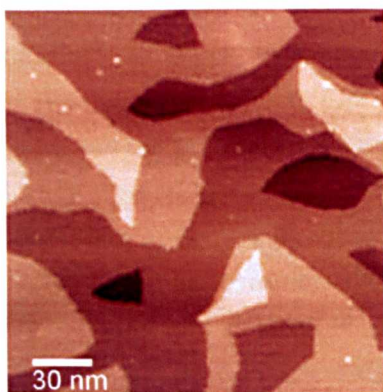


Figure 5.3: STM images of an Au(111) surface after electro spray of blank solvent, no decoration of the step edges is observed ($V_{sample} = -1.8$ V, $I_{tunnel} = 0.03$ nA).

The experiment was then repeated with the sample directly in-line with the electro spray beam, allowing a greater flux of molecules to impinge upon the sur-

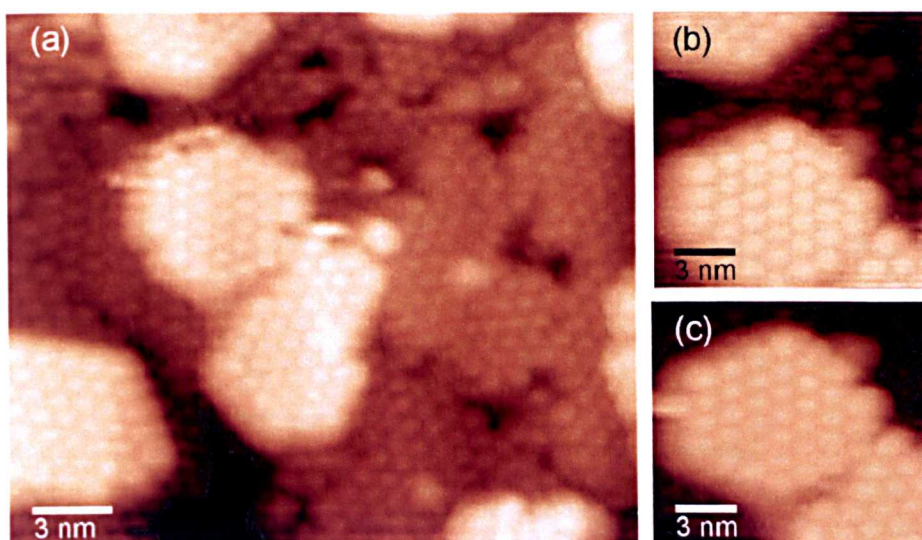


Figure 5.4: STM images of an Au(111) surface after UHV-ESD of multilayer C_{60} coverage. Multilayers of hexagonally close-packed C_{60} islands are observed. (a) $V_{sample} = +2$ V, $I_{tunnel} = 0.03$ nA (b) $V_{sample} = +2$ V, $I_{tunnel} = 0.03$ nA (c) $V_{sample} = +2$ V, $I_{tunnel} = 0.03$ nA

face. The sample was subjected to a 30 minute deposition, resulting in different surface structures to those discussed above. Characterisation of the surface by STM after the deposition of C_{60} shows that faceted islands have been formed (Figure 5.4). The internal structure of the islands may be resolved as hexagonally close-packed features with a diameter of $10 \text{ \AA} \pm 1 \text{ \AA}$ (Figures 5.4(b) and (c)), in good agreement with the structures produced by sublimation [108]. The formation of close-packed structures again demonstrates that the UHV-ESD deposited molecules are free to diffuse across the surface in a similar way to sublimed C_{60} .

XPS data and analysis

In a separate experimental run at the UK synchrotron radiation source (SRS) facility in Daresbury, XPS measurements for electrospray deposited C_{60} on an Au(111) substrate were acquired. The experimental set-up is identical to that described in the previous section (section 5.1.1). The experiments were conducted on beamline 5U.1 using a concentric hemisphere electron energy analyser (VG-CLAM). The experimental data was collected by C. J. Satterley, G. Magnano, A. Rienzo, and L. C. Mayor, and was analysed by C. J. Satterley and published in reference [73]. The findings from this experimental run are included here as they clarify the amount of solvent arriving at the sample as well as demonstrating that the expected electronic properties of C_{60} are maintained.

A 10 mm by 10 mm gold single crystal was used as the substrate for these measurements. The sample surface was cleaned by argon ion sputtering and annealing cycles. The cleanliness of the sample, prior to UHV-ESD of C_{60} , was verified by a negligible C1s signal ($h\nu=390$ eV) and by a wide-scan survey spectra showing that no contaminants were present.

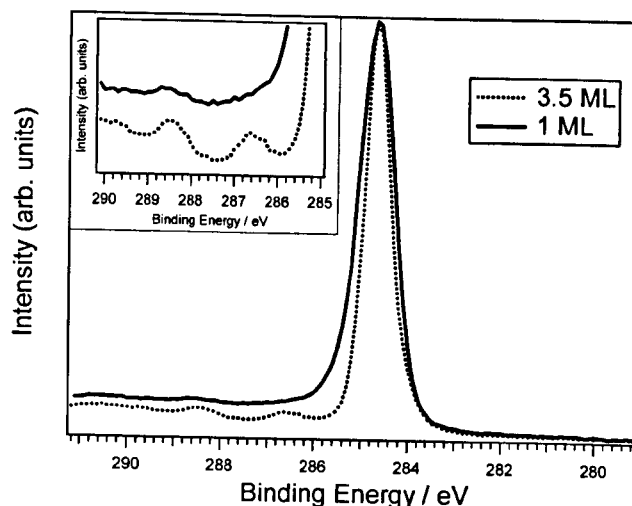


Figure 5.5: C 1s spectra for 3.5 ML and 1 ML of C_{60} on Au(111). Spectra have been normalised to the top of the peak. The inset shows the shake-up features on the high BE side of the C 1s peak (taken from [73]).

Initially 3.5 monolayers (ML) of C_{60} were deposited onto the Au(111) substrate using UHV-ESD (coverages obtained by comparing the ratio of the C 1s peak to the Au $4f_{7/2}$ using the Seah and Dench method [69]). A monolayer of C_{60} was then produced by annealing the sample at ~ 670 K until the ratio of the peaks remained constant and there were no further changes to the line-shape of the spectrum, indicating that the monolayer with its higher BE to the Au(111) surface was left with the loosely bound multilayers being desorbed.

The C 1s spectra (Figure 5.5) shows a single peak which may be attributed to C_{60} . A single broad peak is expected as the carbon atoms in C_{60} are in approximately equivalent chemical environments. There is no evidence of a peak at higher BE in the region that would indicate the presence of the CN group found in acetonitrile. This indicates that there is no solvent on the surface which agrees with the lack of features in the N1s region of the spectrum (not shown here). For the monolayer coverage a single ‘shake-up’ feature is observed at higher BE with increasing coverage giving rise to more pronounced ‘shake-up’ features. The line-shape and shake-up features of the C1s peak closely matched core-level spectra from thermally deposited C_{60} [109] suggesting that the deposited molecules have not been damaged by the electrospray process.

5.2 UHV-ESD of molecules on a hydrogen-bonded supramolecular network

Following the successful UHV-ESD of C_{60} on to an Au(111) substrate, the question as to whether UHV-ESD is compatible with surfaces that have been templated with a hydrogen-bonded supramolecular network is addressed. The formation

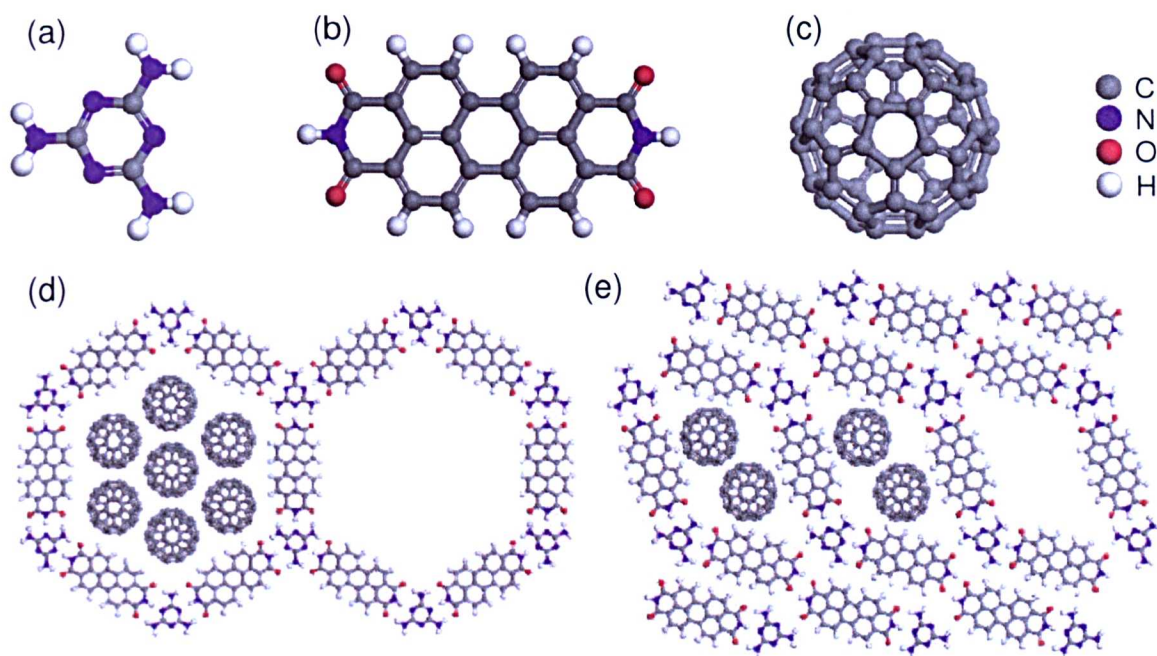


Figure 5.6: Chemical structure for (a) melamine (b) PTCDI and (c) C_{60} . (d) and (e) show the proposed structural models for the hexagonal and parallelogram hydrogen-bonded networks. The position of trapped dimers and heptamers of C_{60} are shown within the network pores.

of two-dimensional supramolecular structures has been extensively studied (work in this field has been discussed in Chapter 2) and it has been shown that such structures may be used as ordered templates containing pores with dimensions on the order of nanometres. Such nanoscale templates are ideally suited to the capture of additional moieties which may be used to further functionalise the surface. Here the potentially destructive nature of UHV-ESD is addressed by studying the PTCDI/melamine bi-molecular network as a test system for the UHV-ESD of C_{60} . The combination of these two techniques potentially allows the lateral organisation of the deposited moieties.

Melamine and PTCDI molecular ‘building blocks’ (molecular structures shown in Figure 5.6, (a) and (b)) are known to self-assemble into open pored hexagonal [24], and parallelogram [25], networks when co-deposited on an Au(111) substrate and subjected to the appropriate annealing conditions. The structures for the hexagonal and parallelogram networks are shown in Figures 5.6 (d) and (e). Sublimation of fullerenes, from a K-cell in UHV, onto such a network results in the size selective trapping of heptamers and dimers of C_{60} in the hexagonal and parallelogram network pores respectively. In this section it is demonstrated that the UHV-ESD of C_{60} on a bimolecular PTCDI/melamine network produces structures that are comparable to those produced by sublimation.

5.2.1 UHV-ESD of C_{60} on a supramolecular network

Network structure before UHV-ESD of C_{60}

The experimental set-up of the electrospray apparatus, preparation of the C_{60} solution and preparation of the Au(111) substrate are identical to that described above in section 5.1.1. Co-existing bi-molecular networks with hexagonal and parallelogram shaped pores were produced on the surface using the procedures detailed in Chapter 4. Figure 5.7 (a), (b) and (c) show STM images of the network produced prior to the UHV-ESD of C_{60} . Figure 5.7 (a) is a STM topograph showing several small domains of the parallelogram network (labelled A). Regions of the parallelogram network with dimensions of $200 \text{ \AA} \times 200 \text{ \AA}$ were typically observed. Islands of close-packed PTCDI [20] (labelled B) which have not been converted into the network arrangement are seen to co-exist with the hydrogen-bonded networks, as well as with regions of the clean gold substrate (labelled C). Although the majority of the ordered structures are composed of the parallelogram network, under the annealing conditions used for this experiment, small regions of the hexagonal network are also observed (shown in Figure 5.7 (c)).

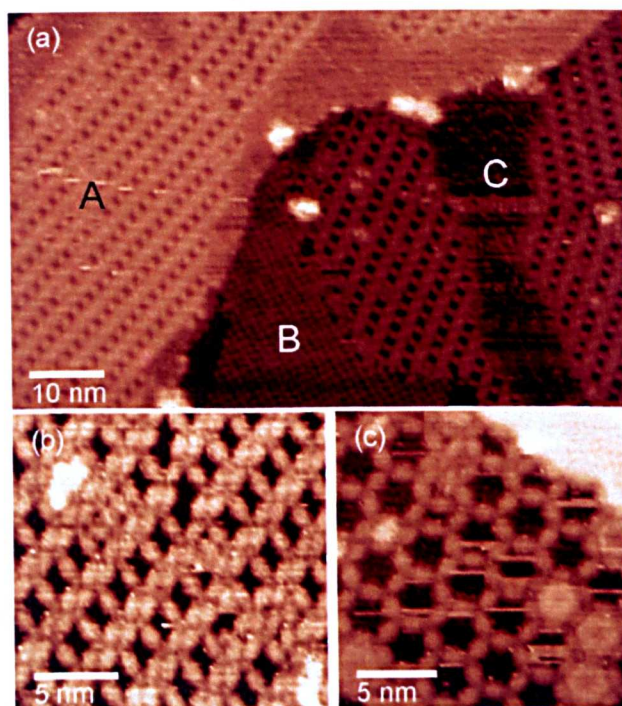


Figure 5.7: STM images showing the network structures prior to UHV-ESD of C_{60} . (a) STM image showing the types of structure formed upon the Au(111) surface ($V_{sample} = -2.00 \text{ V}$, $I_{tunnel} = 0.03 \text{ nA}$). Area A shows a large domain of the parallelogram network, B is a region of close-packed PTCDI, and region C is an area of gold which is free from adsorbed molecules. (b) STM image showing the internal structure of the parallelogram network ($V_{sample} = -1.80 \text{ V}$, $I_{tunnel} = 0.03 \text{ nA}$). (c) STM image of the internal structure of the hexagonal network which exists alongside the parallelogram network ($V_{sample} = -1.80 \text{ V}$, $I_{tunnel} = 0.03 \text{ nA}$).

Network structure after UHV-ESD of C₆₀

The series of STM images shown in Figure 5.8 provide insight into the effect of energetic C₆₀ and solvent molecules colliding with the network structure during UHV-ESD. Figure 5.8 (a) shows an image of the surface morphology after a two minute UHV-ESD of C₆₀. From the image it is possible to identify several areas of interest. The dashed box labelled A shows a region of parallelogram network with a row of C₆₀ dimers trapped within the pores. Area B is a region of hexagonal network with C₆₀ heptamers filling the pores, while C shows an area of network which appears to have been re-ordered during the UHV-ESD. The area to the right of the image is a large island of close-packed PTCDI and is free of adsorbed C₆₀.

Figure 5.8 (b) shows an area with a similar structure to region B, where a regular array of trapped C₆₀ clusters, with each cluster being formed from seven molecules in a hexagonal arrangement, are identified as heptamers trapped in the hexagonal shaped pores of the network. Second layer growth of C₆₀ is also observed, with the extra layer of molecules filling the spaces in between the trapped heptamers, leading to the ‘bright’ open pored structure seen in the centre of the image. The ‘streaky’ scan-lines observed in the top section of the image are indicative of the presence of diffusive molecules, suggesting that some molecules are not completely immobilised by the presence of the network. Trapped C₆₀ dimers mixed in among the heptameric structure demonstrate that defects, of the type reported in previous work [24] (where domain boundaries between regions of hexagonal network lead to the formation of pores which may trap C₆₀ dimers), are also present on the surface.

Due to their size and shape, the parallelogram network pores provide trap sites for dimers of C₆₀ [25]. The bright rectangular features present in the central region of the image shown in Figure 5.8 (c) have a periodicity and an apparent height, which agrees with that previously measured for the thermally deposited C₆₀ trapped within the parallelogram network pores (dimensions of $30.7 \text{ \AA} \pm 0.4 \text{ \AA}$ by $19.4 \text{ \AA} \pm 0.3 \text{ \AA}$ [25] and an apparent height of $\sim 6 \text{ \AA}$) allowing us to attribute these features to trapped C₆₀ dimers.

In addition to the trapped molecules, there are several islands of close-packed C₆₀ visible in the image. These islands have the same apparent height as the dimers, indicating that the close-packed domains are formed on the clean Au(111) surface and not on top of the PTCDI regions. Areas of close-packed PTCDI (e.g. the region to the right of the image in Figure 5.8(a)) are free from C₆₀ providing further evidence that the adsorption of C₆₀ onto PTCDI is unfavourable.

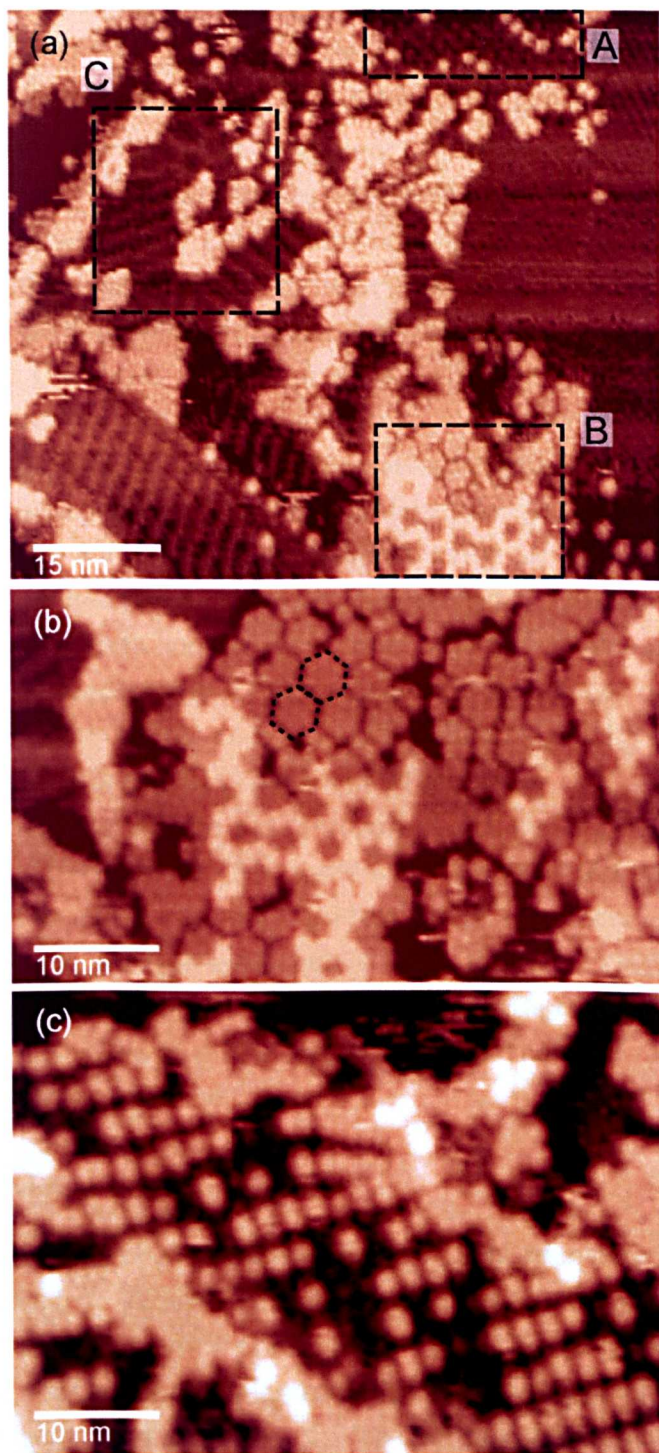


Figure 5.8: STM images of the surface after UHV-ESD of C_{60} . (a) The surface after being subjected to 2 minutes of electrospray deposition of C_{60} from a solution of toluene:acetonitrile (1 mg/ml of C_{60} dissolved in a 4:1 solution, by volume). The areas marked A, B and C demonstrate the three different surface morphologies observed ($V_{sample} = +1.80$ V, $I_{tunnel} = 0.03$ nA). (b) Area of hexagonal network pores filled with heptamers of C_{60} (similar morphology to area C highlighted in (a)). In the bottom part of the image a second layer of C_{60} growth is observed, forming a bright, open pored, hexagonal array ($V_{sample} = +1.80$ V, $I_{tunnel} = 0.03$ nA). (c) Region of parallelogram network which has trapped several C_{60} dimers (similar morphology to area A highlighted in (a)). ($V_{sample} = +1.80$ V, $I_{tunnel} = 0.03$ nA).

Comparison between structures produced by UHV-ESD and thermal deposition

The observed structures of trapped C₆₀ dimers and heptamers formed by UHV-ESD and sublimation are in excellent agreement [24,25]. Figure 5.9 compares STM images of the structures formed by the two techniques. Figures 5.9, (a) and (b), show trapped heptamers of C₆₀ held within a hexagonal PTCDI/melamine network pore. The individual molecules within the heptamer form a hexagonal close-packed arrangement and have an intermolecular separation of $\sim 10 \text{ \AA}$ which is similar to the structure that C₆₀ forms on clean Au(111). This result demonstrates that any solvent molecules deposited on the sample have no effect upon the trapping of molecules within pores, implying that any solvent contamination present does not effect the diffusion or packing of the deposited molecules.

In regions of the surface with a higher coverage of C₆₀ second layer growth over the regions of hexagonal network is observed. This second layer growth manifests itself as a ‘bright’ porous hexagonal structure which exactly reproduces the geometry of the underlying PTCDI/melamine hexagonal network. The STM images shown in Figure 5.9, (c) and (d), again demonstrate the agreement between the structures produced by UHV-ESD and sublimation.

The STM images in Figure 5.9, (e) and (f), show regions of parallelogram network that have been filled with dimers of C₆₀. It is interesting to note that the parallelogram network does not preferentially form second layer growth of C₆₀; areas of parallelogram network remain with only one layer while surrounding hexagonal networks exhibit multilayer growth. The reluctance of the parallelogram phase to form a second layer of C₆₀ again confirms that the molecules deposited by UHV-ESD are free to diffuse.

Network Re-ordering

Some areas of the supramolecular network have been re-ordered during the UHV-ESD of C₆₀. Figure 5.10 shows STM images of surface domains that have different morphologies to those observed prior to the UHV-ESD. Figure 5.10 (a) shows a ‘mixed’ phase of PTCDI and melamine where rows of PTCDI are stacked side by side and are separated by rows of close-packed melamine (labelled as A, a domain of close-packed C₆₀ is labelled as B). This structure has been observed previously and is produced after the co-deposition of melamine and PTCDI, prior to the further annealing stage which is required to form the network (discussed in Chapter 4). It is similar to, but more ordered than, one of the mixed phases identified in reference [24]. In Figure 5.10 (b) it can be seen that there are three distinct layers of close-packed PTCDI islands (labelled 1-3), with a difference in apparent height between the layers of $\sim 1.5 \text{ \AA}$ which agrees with the expected value for the measured ‘thickness’ of a PTCDI molecule.

As this ‘mixed’ structure is not present on the surface before UHV-ESD (and

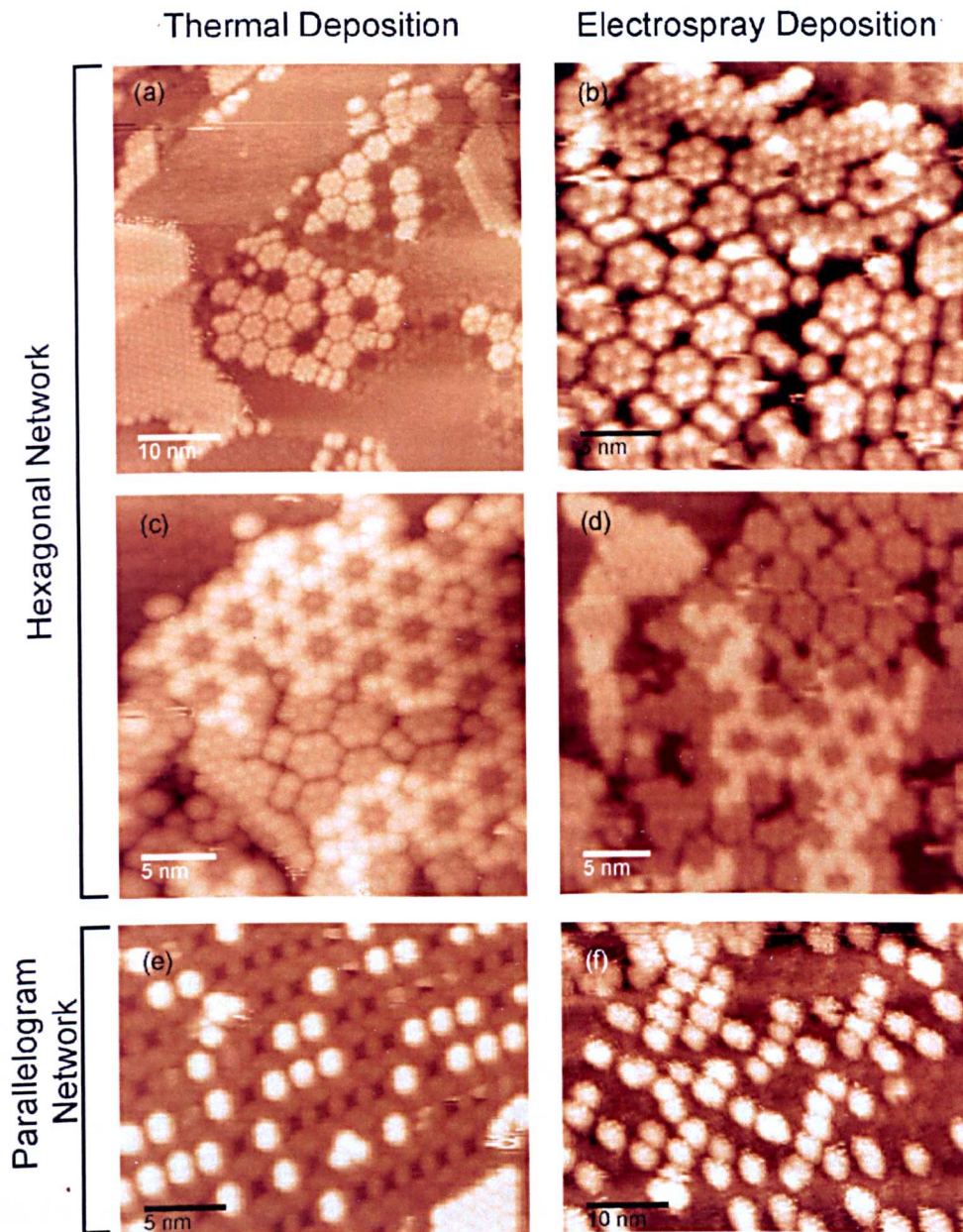


Figure 5.9: STM images showing the similarities between electro sprayed and thermally deposited C_{60} . (a) Thermally deposited C_{60} trapped as heptamers within hexagonal network pores ($V_{sample} = -2.00$ V, $I_{tunnel} = 0.03$ nA). (b) STM image showing electro spray deposited C_{60} trapped in hexagonal network pores ($V_{sample} = -2.00$ V, $I_{tunnel} = 0.03$ nA). (c) and (d) show second layer growth of C_{60} over a region of hexagonal network ($V_{sample} = +1.80$ V, $I_{tunnel} = 0.03$ nA) and ($V_{sample} = +1.80$ V, $I_{tunnel} = 0.03$ nA). (d) and (e) are STM images of trapped dimers of C_{60} held within the pores of the parallelogram network ($V_{sample} = -1.0$ V, $I_{tunnel} = 0.03$ nA) and ($V_{sample} = +1.8$ V, $I_{tunnel} = 0.03$ nA). Images (a) and (c) acquired by L. M. A. Perdigão.

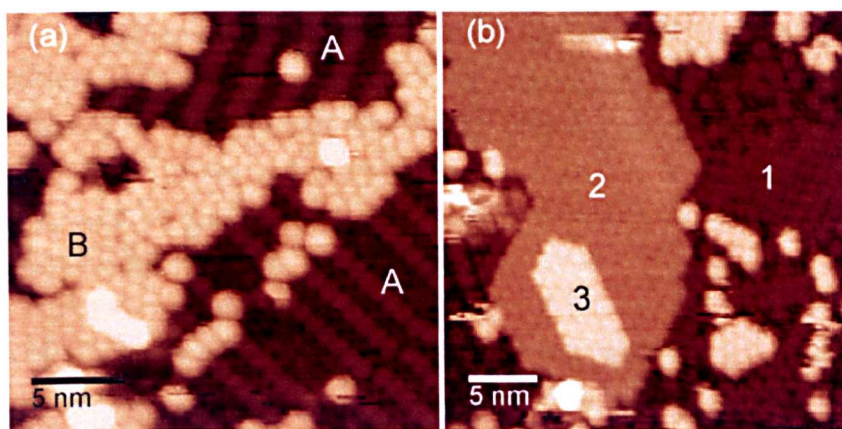


Figure 5.10: (a) STM image showing an area of network that has been re-ordered. The regular hydrogen-bonding structure of the network has been altered leading to a ‘mixed’ phase of melamine and PTCDI ($V_{sample} = +1.80$ V, $I_{tunnel} = 0.03$ nA). (b) Multiple layers of close-packed PTCDI have been produced as a by-product of the network re-organisation ($V_{sample} = +1.80$ V, $I_{tunnel} = 0.03$ nA).

is not observed as an effect of thermal sublimation) we conclude that the network re-ordering is associated with the UHV-ESD process. The PTCDI:melamine ratio for this ‘mixed’ structure is approximately 1:2, and is different to the equivalent ratio for the hexagonal and parallelogram networks, both 3:2. Therefore if re-ordering were to occur during UHV-ESD, areas with an excess of PTCDI would be expected on the surface. The result of this re-ordering is shown in Figure 5.10 (b) where, by analysing the apparent height of the PTCDI islands, it can be seen that three distinct layers of close-packed PTCDI have been formed. All PTCDI islands before UHV-ESD were measured to have an apparent height corresponding to a height of one molecule, therefore the resulting multilayered structure of islands following deposition provides evidence for the removal of PTCDI molecules from the bi-molecular network during the creation of the ‘mixed’ phase.

Image analysis of the STM data allows a quantitative picture to be obtained of the differences between the surface coverage of the supramolecular structures before and after UHV-ESD of C_{60} . The overall ratio of PTCDI to melamine, 2:1, is unaffected by exposure to electrospray deposition, but the relative abundance of the various phases does change. The coverage of the parallelogram network is reduced from $48\% \pm 9\%$ before UHV-ESD to $15\% \pm 8\%$ afterwards. Conversely, the coverage of both the close-packed PTCDI and ‘mixed’ phases increase from $\sim 10\%$ to $\sim 20\%$ and from 0% to $\sim 20\%$, respectively, suggesting the conversion of the parallelogram network into other phases.

The conversion of the network structure is unlikely to be a direct result of the impact of the deposited C_{60} molecules. An upper limit for the kinetic energy of a single C_{60} molecule may be calculated by treating it as a ballistic object with $KE = 1/2mv^2$ and assuming that the maximum velocity is equal to the speed of sound at 298 K (as discussed in Chapter 3). This analysis gives a value of 440 meV,

which is lower than the DFT calculated value for the PTCDI/melamine synthon BE of ~ 750 meV. This comparison of energies confirms that the supramolecular framework should be stable under the electrospray beam, but it does not preclude the possibility that clusters of molecules, or the impact of multiple molecules upon the same site, may be responsible for the change in network structure.

It is possible that network re-ordering is mediated by solvent droplets arriving at the surface. Subsequent evaporation of the solvent may lead to a phase separation of the melamine and PTCDI molecules producing the ‘mixed’ phase observed. It may be possible to characterise and reduce this effect, and also investigate whether it is due to nanoscale solvation in droplets, by increasing the desolvation of the electrospray beam; this is a design feature which will be included in future models of the UHV-ESD apparatus. Chapters 6 and 7 discuss experiments which use a modified UHV-ESD set-up which should reduce the amount of solvent introduced into the UHV system.

The results discussed above show that it is possible to deposit molecules on a hydrogen-bonded supramolecular network in UHV using electrospray deposition. The structures observed in the STM images provide clear evidence that C₆₀ dimers, and heptamers, may be trapped within the network pores in a similar fashion to molecules which have been sublimed. The similarities in the structures produced by the two deposition techniques show that the organisation of the guest C₆₀ molecules, i.e. the size selective trapping of molecules, is driven by similar microscopic processes, confirming UHV-ESD as a highly promising method for introducing guest moieties onto a pre-prepared (potentially fragile) nanostructured surface.

5.3 Summary

The results contained within this chapter demonstrate that UHV-ESD is a technique that produces similar structures to those obtained by sublimation when used to transfer C₆₀ into vacuum and onto an Au(111) substrate and Au(111) pre-patterned with a hydrogen-bonded supramolecular network. Fullerenes themselves are neither fragile nor thermally labile but are extremely useful in showing the possibilities of UHV-ESD. This work is an important stepping stone on the way to using UHV-ESD to deposit fragile molecules which will be discussed in the next chapter. In the next two chapters the use of UHV-ESD to deposit single molecule magnets and porphyrin based molecular wires will be discussed.

Chapter 6

Self-assembled aggregates formed by single molecule magnets on a gold surface

In this chapter the use of UHV-ESD to deposit a molecule which is thermally labile is investigated. The single molecule magnet (SMM), $Mn_{12}O_{12}(O_2CCH_3)_{16}(H_2O)_4$ ($Mn_{12}(\text{acetate})_{16}$) has been transferred from solution, using UHV-ESD, onto an Au(111) substrate held in UHV. The deposited $Mn_{12}(\text{acetate})_{16}$ molecules form filamentary aggregates due to the anisotropic nature of the molecule-molecule and molecule-substrate interactions. The spontaneous ordering of molecules into two-dimensional self-assembled arrays is commonly stabilised by directional intermolecular interactions which may be promoted by the addition of specific chemical side-groups to a molecule. Here the self-assembly observed is driven by anisotropic interactions which arise from the three-dimensional shape of the molecule. The interactions are modelled using MD simulations. The fragile $Mn_{12}O_{12}$ core of the $Mn_{12}(\text{acetate})_{16}$ molecule is found to be compatible with the UHV-ESD process, as confirmed by NEXAFS spectroscopy. UHV-ESD of SMMs onto a surface that has been pre-patterned with a hydrogen-bonded supramolecular network is shown to provide additional control of lateral organisation.

6.1 Single molecule magnets as molecular building blocks

The focus of the work within this thesis is the investigation of the intermolecular forces which drive the bottom-up self-assembly of large organic molecules. An understanding of these forces may potentially lead to the production of nanoscale structures with pre-designed optical, chemical, structural and magnetic functionalities [110–117]. The formation of such devices requires a detailed knowledge and control of the forces which drive the ordering of molecular arrays [81, 118–122].

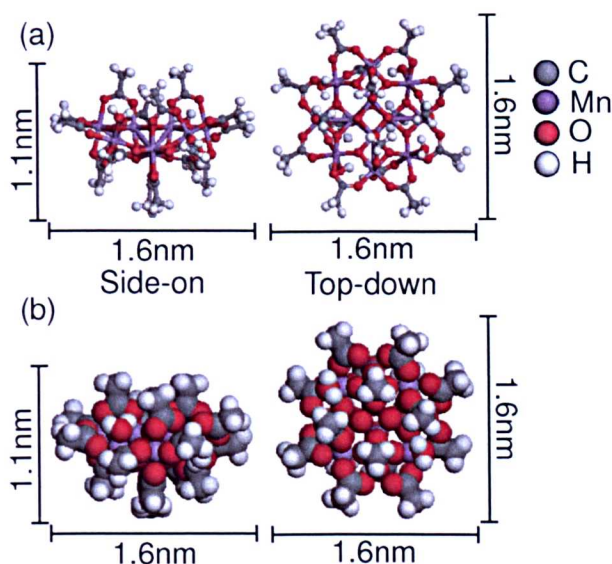


Figure 6.1: (a) Chemical structure of $\text{Mn}_{12}\text{O}_{12}(\text{O}_2\text{CCH}_3)_{16}(\text{H}_2\text{O})_4$ ($\text{Mn}_{12}(\text{acetate})_{16}$), (b) Structure of $\text{Mn}_{12}(\text{acetate})_{16}$ shown as a space filling CPK model. The dimensions of the molecule are indicated.

Research within the area of self-assembly has largely focused on the investigation of systems which use highly directional anisotropic interactions such as hydrogen bonding, or metal co-ordination, to promote the formation of arrays with controlled structural characteristics. There have been great successes in this approach, particularly when applied to relatively simple molecules with high symmetry (such as the PTCDI/melamine structures discussed in Chapter 4). For larger, more complex moieties, the influence of intermolecular interactions is much more difficult to predict, since anisotropies result from the balance between the three-dimensional shape of a molecule and its surface chemistry. The SMM $\text{Mn}_{12}(\text{acetate})_{16}$ (structure shown in Figure 6.1) provides an interesting and well studied example of a large, complex molecule and has attracted great interest due to its intrinsic magnetic functionality. Of particular interest to this thesis is the complex three-dimensional molecular shape which leads directly to the spontaneous formation of filamentary structures through the aggregation of diffusing $\text{Mn}_{12}(\text{acetate})_{16}$ molecules. In this context $\text{Mn}_{12}(\text{acetate})_{16}$ provides an exemplar of a nanoscale object with a complex intermolecular potential in which anisotropies arise from the asymmetric shape of the molecule rather than through interactions which are intrinsically anisotropic.

SMMs exhibit magnetic properties, such as hysteresis cycles and magnetic anisotropy, originating from a purely molecular basis [123, 124], in contrast to classical systems which derive their magnetic properties from the bulk material. SMMs have been shown to exhibit quantum magnetic tunnelling effects [125, 126] which demonstrate their potential to be used as components in molecular information storage devices [127, 128]. Lateral organisation is highly relevant to these applications, although so far there have been relatively few high resolution studies

to determine the influence of intermolecular interactions on the packing and ordering of these molecules. This is due in part to the fragile nature of $\text{Mn}_{12}(\text{acetate})_{16}$ and other SMMs which makes them unsuitable for sublimation and largely precludes the investigation of derived thin films using techniques such as UHV-STM and XPS.

The molecule investigated here is based on the mixed valence dodecamanganese (III, IV) cluster which contains four Mn^{+4} ions within the core and eight Mn^{+3} ions around the periphery. The magnetic core is protected by an organic shell which may be altered by conventional wet chemistry techniques such as ligand exchange [129–131] and direct synthesis from the appropriate carboxylate reagents [132]. Recently there have been successful attempts to deposit various SMM moieties onto surfaces using solution based deposition methods. This can be achieved either by functionalising the cluster so that it may be grafted onto an Au(111) surface [130, 131, 133–137], or by pre-functionalising both the substrate and the SMM to encourage the formation of adsorbed layers [138–140]. Deposition in UHV using pulsed laser deposition [141], matrix assisted pulsed laser evaporation [142], a pulsed vacuum spray technique [143], and a local mechanical method [144] have also been demonstrated. However, when applied to the formation of thin films, these techniques may result in fragmentation and damage to the manganese core [143, 145].

In this chapter UHV-ESD is discussed as a way of depositing sub-monolayer to multilayer coverages of $\text{Mn}_{12}(\text{acetate})_{16}$. It has recently been shown that UHV-ESD, and related spray techniques, provide a viable method for the transfer of non-volatile/thermally labile species such as dye molecules, and polymers from solution onto surfaces held in UHV [73, 86, 90, 146–149] and the development and application of these techniques is crucial for the deposition of $\text{Mn}_{12}(\text{acetate})_{16}$. The complex molecule-molecule and molecule-substrate interactions of $\text{Mn}_{12}(\text{acetate})_{16}$ show the challenges in utilising such molecules as molecular ‘building blocks’.

6.2 Experimental methods

Deposition of $\text{Mn}_{12}(\text{acetate})_{16}$ and subsequent characterisation by STM were carried out in the Nottingham UHV system with a base pressure of $\sim 5 \times 10^{-11}$ Torr. A gold on mica substrate was loaded into the UHV system and cleaned by Ar ion sputtering (6×10^{-6} Torr, 0.7 keV, 2 μA) and annealing (500°C). Images of the surface were acquired using an STM, housed within the UHV system, using electrochemically etched tungsten tips, and operating in constant current mode at room temperature. Images of the surface taken after the sputter-anneal cycle show the characteristic ($22 \times \sqrt{3}$) herringbone reconstruction of the Au(111) surface [103].

The SMM $\text{Mn}_{12}(\text{acetate})_{16}$ (shown in Figure 6.1) was transferred, using UHV-ESD, from a solution of methanol (MeOH) onto the Au(111) substrate. The

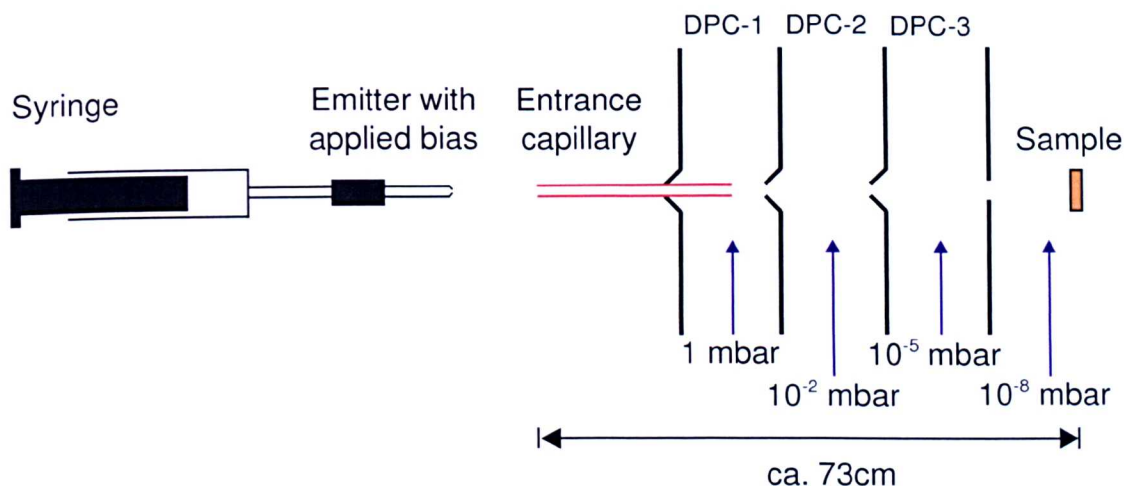


Figure 6.2: Schematic of the modified UHV-ESD set-up where the initial skimmer cone at the entrance to the differential pumping section has been replaced by a capillary to reduce the volume of solvent entering the system.

UHV-ESD experimental set-up, described in Chapter 3, has been modified in light of the results from the C_{60} deposition experiment. In order to reduce the amount of solvent being introduced into the UHV chamber the first skimmer cone has been replaced by a capillary with an aperture diameter of ~ 0.2 mm, increasing the effective path length that the emitted drops have to travel before impinging on the sample. This increases the probability that molecules arriving at the surface will be completely desolvated. The new experimental set-up is shown in Figure 6.2. The length of the capillary may be varied in order to maximise the desolvation, and heat may be applied to further increase the removal of solvent. In the experiment reported here, a capillary is used which increases the path length by ~ 3 cm compared to the previous set-up, with no heating applied due to the fragile nature of the molecules. The backing pressure applied to the solvent reservoir has been reduced (a syringe is now used to force the solvent through the emitter), which provides a decreased flow-rate, allowing greater control for the rate of deposition.

The operation of the UHV-ESD apparatus is identical to that described in the previous C_{60} deposition experiment (Chapter 5), with the only difference being a smaller pressure rise in the preparation chamber during deposition ($\sim 2 \times 10^{-8}$ Torr to $\sim 4 \times 10^{-8}$ Torr) due to the decreased volume of solvent entering the system.

XPS and NEXAFS experiments were conducted at the bending magnet beamline D1011 at Max II, MAX-lab in Lund. The D1011 end station is equipped with a SCIENIA SES200 electron analyser, with the base pressure within the analysis and preparation chambers being 2×10^{-10} mbar and 5×10^{-10} mbar respectively. For these experiments the sample was orientated at normal emission relative to the analyser. The sample used was a single crystal Au(111) substrate with a 10 mm diameter (2.5 mm thickness) purchased from Metal Crystals and Oxides Ltd.

UK. A loop of tungsten wire was passed through the crystal in order to mount it and to provide resistive heating, with a thermocouple wire attached within a small cavity to monitor the temperature. The sample was cleaned using cycles of argon sputtering (1 keV) and annealing (600°C) until it showed a negligible C 1s core-level signal. C 1s core-level spectra were measured using $h\nu=340$ eV. Mn NEXAFS data were recorded at the Mn 2*p* adsorption edge (Mn L-edge) with the emitted electrons collected by a partial yield detector, with a retardation potential of 100 V. The photon energy was calibrated by taking the energy separation of the Au 4*f* core-level photoemission peaks excited by X-rays in 1st and 2nd order. Coverages were calibrated by comparing the attenuation of the Au 4*f* substrate peak to that of the clean Au(111) sample with the mean free path through the SMMs calculated using the Seah and Dench method [69].

6.3 Filamentary aggregates of Mn₁₂(acetate)₁₆

A sub-monolayer coverage (~ 0.35 ML) of the SMM Mn₁₂(acetate)₁₆ has been prepared on an Au(111) surface using UHV-ESD. Figure 6.3(a) shows a large area STM image typical of the surface following deposition. It is immediately clear from the image that the molecules are mobile and diffuse on the surface following adsorption as they form complex aggregates in which meandering filamentary structures coexist with small disordered clusters. These features are somewhat reminiscent of the filamentary networks reported for planar organic molecules [150, 151], which have been described as two-dimensional glasses. From a consideration of the hard sphere radius of the molecule (Figure 6.1(b)) it might be expected that the Mn₁₂(acetate)₁₆ molecule would be orientated so as to maximise contact area, potentially maximising the vdW interactions with the substrate, giving rise to a circular cross section in STM images. However, as shown in the STM image of an isolated Mn₁₂(acetate)₁₆ (Figure 6.3(b)) the orthogonal dimensions of the molecule, labelled r_1 and r_2 , are not equal and the molecule is imaged with an ellipsoidal cross section. The average values of r_1 (short axis) and r_2 (long axis) for isolated molecules have been experimentally measured to be $1.6 \text{ nm} \pm 0.3 \text{ nm}$ and $2.2 \pm 0.4 \text{ nm}$ respectively, with an aspect ratio of 1.4 ± 0.2 . The lateral dimensions of the Mn₁₂(acetate)₁₆ appear to be approximately 30% larger than the hard-sphere radius values due to STM tip convolution (two different STM tips were used for these measurements). The average apparent-height of the molecules is found to be $0.45 \text{ nm} \pm 0.08 \text{ nm}$, lower than the hard-sphere dimension. This difference is attributed to a lower LDOS associated with the Mn₁₂(acetate)₁₆ as compared to the metallic Au surface.

A striking feature of the molecular assemblies observed using STM is the propensity of the Mn₁₂(acetate)₁₆ molecules to self-assemble into meandering filamentary structures as depicted in Figure 6.3(c). These structures are observed to run over step edges, giving rise to the large scale surface structure seen in Fig-

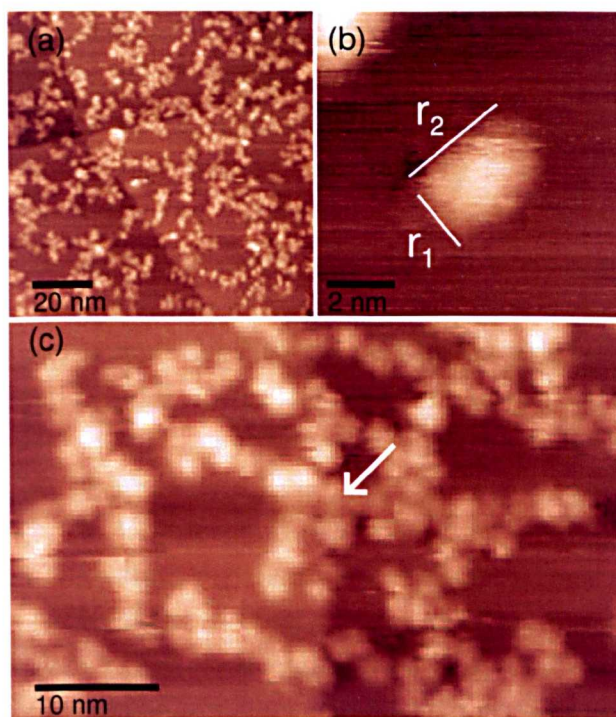


Figure 6.3: (a) Large scale STM image of the Au(111) surface after the UHV-ESD of ~ 0.35 ML of $\text{Mn}_{12}(\text{acetate})_{16}$ ($V_{\text{sample}} = +1.80$ V, $I_{\text{tunnel}} = 0.03$ nA). Filamentary structures are observed to run over the surface and are contiguous at step edges. (b) Close-up STM image of an isolated $\text{Mn}_{12}(\text{acetate})_{16}$ molecule ($V_{\text{sample}} = +2.00$ V, $I_{\text{tunnel}} = 0.03$ nA). The molecule displays an elliptical cross-section ($r_2 > r_1$). (c) STM image showing the internal structure of a molecular aggregate comprised of individual SMMs ($V_{\text{sample}} = +2.00$ V, $I_{\text{tunnel}} = 0.05$ nA).

ure 6.3(a). The formation of these structures is not associated with, and does not follow, the underlying herringbone reconstruction of the Au(111) surface. In the previous chapter (Chapter 5) it was shown that the UHV-ESD of C_{60} onto an Au(111) surface results in the formation of close-packed two-dimensional domains, indicating that the vdW forces that cause the molecules to close-pack are isotropic. However, in contrast to C_{60} , the vdW interactions between the $\text{Mn}_{12}(\text{acetate})_{16}$ molecules leads to the formation of filamentary structures which indicates an anisotropy within the molecule-molecule interactions. These interactions may be investigated using MD simulations, and are discussed in the next section.

6.3.1 Molecular dynamics simulations of $\text{Mn}_{12}(\text{acetate})_{16}$

The STM images raises questions as to how the $\text{Mn}_{12}(\text{acetate})_{16}$ molecules orientate themselves relative to the surface, and about the nature of the mechanism which drives the self-assembly of these complex aggregates. Semi-empirical MD simulations have been used to obtain information about the energetic states that an individual molecule deposited onto the Au(111) substrate may occupy. A simple schematic of the molecule, shown in Figure 6.4(a) (with the majority of the

$\text{Mn}_{12}(\text{acetate})_{16}$ depicted as a red ellipsoid and with the protruding CH_3 groups shown as grey circles), is used to analyse the MD results.

There are 16 CH_3 groups in total, eight of which lie around the circumference of the ellipsoid (labelled 1 to 8), and four on both the top and bottom of the molecule (labelled A to D and E to H respectively). MD quench simulations were performed on a single $\text{Mn}_{12}(\text{acetate})_{16}$ molecule on the Au(111) substrate (see appendix B for details of the MD simulations). The quench simulation allows geometry optimisation calculations to be performed using a variety of starting geometries determined by MD. From the geometry optimised structures it is possible to identify several distinct local energy minima, each of which may be defined by the orientation of the molecules CH_3 groups relative to the surface. The left hand column of Figure 6.4(b) shows a top-down view of the geometry-optimised energy minima with the values for their aspect ratios. The middle column shows schematic representations of the molecule, with the CH_3 groups in contact with the Au(111) surface for each orientation highlighted in blue. The edge-on view of the molecule in the right hand column shows how the molecules are orientated relative to the surface with the CH_3 groups in contact with the surface highlighted. States **M1** and **M2** (identified in Figure 6.4) are energy minima where the molecule is positioned perpendicular to the gold surface, while in state **M3b** the molecule lies almost flat on the surface. In the lowest energy state (state **M4b**), the molecule is canted so that four CH_3 groups are in contact with the surface.

The energies of the states have been plotted as a function of the number of CH_3 groups in contact with the surface (Figure 6.4(c)). The graph shows a linear trend which demonstrates that the BE of the molecule to the surface, and hence the molecular orientation, is determined by the number of CH_3 groups in contact with the Au(111) surface. State **M4b** has the greatest BE (0.31 ± 0.02 eV), and the geometry of this state gives a top-down aspect ratio of 1.3 ± 0.1 which is in agreement with the value obtained from the STM images. Within error, states **M3c**, **M4a** and **M4b** fit the experimentally measured aspect ratio (states **M1** and **M2** may be discounted due to their low BE to the Au(111) surface), in these states the molecule is canted relative to the plane of the Au(111) surface. The MD simulations show that the structures observed in STM are driven by the maximisation of the number of CH_3 groups in contact with the Au(111) surface. This anisotropic interaction between the molecule and the substrate, due to the anisotropic shape of the molecule, is the first step in understanding the structures observed in STM.

The simulations also provide insight into the formation of the complex aggregates of $\text{Mn}_{12}(\text{acetate})_{16}$ molecules on the Au(111) surface. A similar approach to that described above is taken with a quench simulation being performed to determine the energy minima for a system containing two $\text{Mn}_{12}(\text{acetate})_{16}$ molecules absorbed on an Au(111) surface. Figure 6.5(a)-(d) shows the geometry of the four local energy minima states for two molecules. For each state the BE between

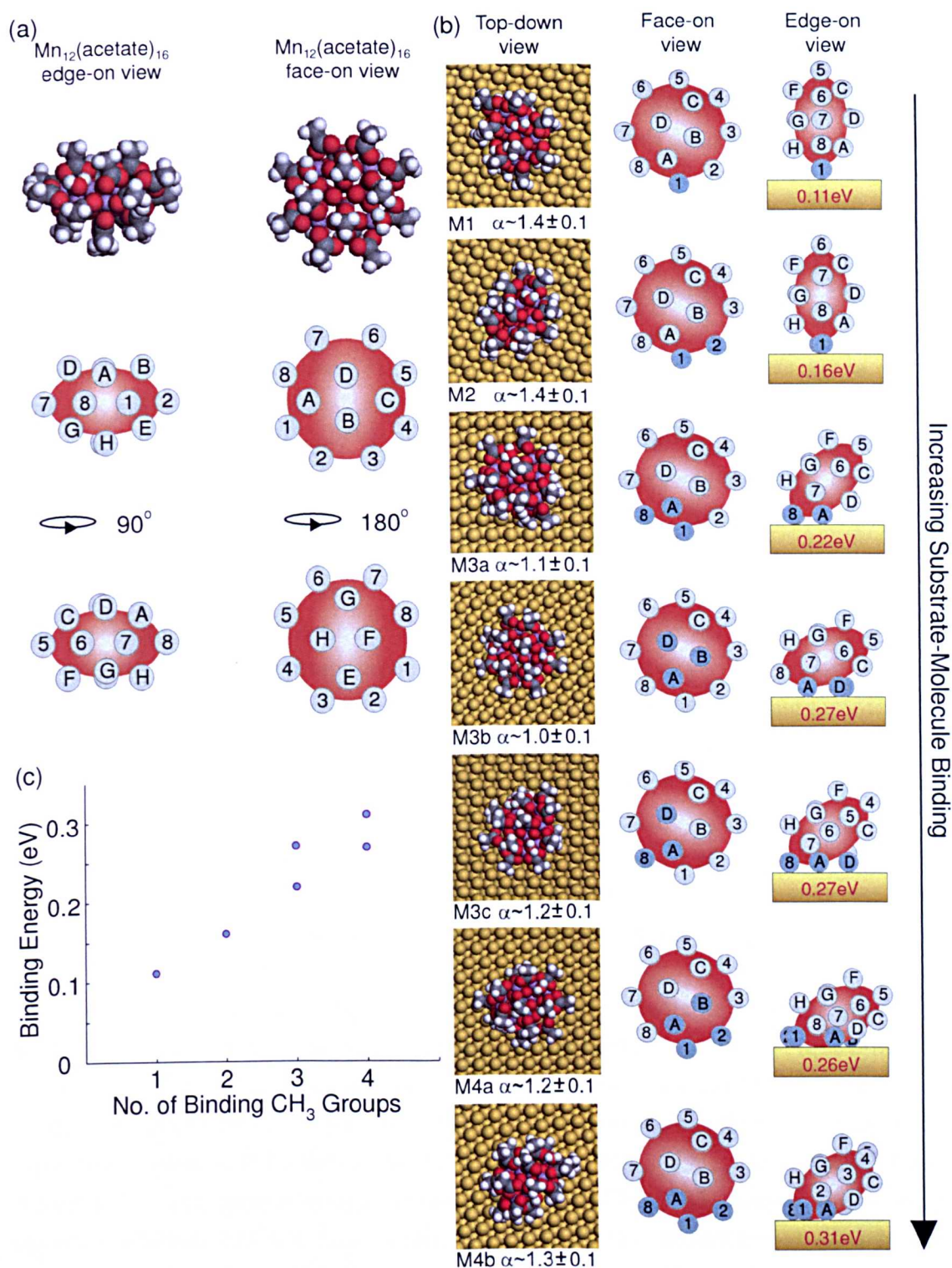


Figure 6.4: MD calculated configuration of $\text{Mn}_{12}(\text{acetate})_{16}$ on Au(111). (a) CPK hard-sphere model of $\text{Mn}_{12}(\text{acetate})_{16}$ and schematic of the molecule with the CH_3 groups of the organic shell labelled 1-8 and A-H (grey circles) and the core represented as a red ellipsoid. (c) The left hand column shows a top-down view of the states α determined to be energy minima of the system (1 $\text{Mn}_{12}(\text{acetate})_{16}$ on the Au(111) surface) by the MD quench simulation. The aspect ratio of each state is shown (α). The middle column is a schematic of a face-on view, with the CH_3 groups in contact with the Au surface highlighted as blue circles. The right hand column shows an edge-on view rotated by 90° compared to that of side 1, with the CH_3 groups in contact with the Au surface highlighted as blue circles. The states are shown in order of increasing BE, **M1** to **M4b**. (c) Graph showing the BE of the SMM to the Au surface as a function of the number of CH_3 groups in contact with the surface.

the two molecules has been calculated, with state **D1** defined as a non-bonding configuration where the molecules are not in contact with each other. State **D2** shows an edge-to-edge configuration, while states **D3** and **D4** show face-to-face configurations where the surface area between the two interacting molecules is maximised (the substrate interaction is included in the calculation but is approximately equal for all pair configurations and has been subtracted from the quoted values which thus correspond to intermolecular interactions - see appendix B). Importantly, the BE of state **D4** is considerably greater than that of state **D3** due to the interdigitation of the methyl groups.

The determination of these states allows us to identify the anisotropy in the BE between pairs of molecules which manifests itself in the formation of the filamentary structures. Interestingly the two molecules in the most strongly bound pair arrangement (**D4**) adopt inequivalent surface configurations with, for example, a difference in tilt angle of $\sim 15^\circ$ as illustrated in Figure 6.5. One consequence of this is that a given molecule cannot maximise its pair-wise intermolecular interactions with more than one of its nearest neighbours. We may therefore expect a competition and interdependency between interactions with multiple nearest-neighbours. Overall we may expect the molecular shape asymmetry to lead to a complex intermolecular potential, which promotes an overall anisotropy through the face-to-face configuration but also possesses several local minima. This leads to a large multiplicity of quasi-degenerate configurations for an arrangement of many molecules. From this perspective the $\text{Mn}_{12}(\text{acetate})_{16}$ morphology may be seen as analogous to the networks described recently as glasses [150, 151]. These findings again show the differences between the regular two-dimensional island growth observed for C_{60} (see Chapter 5), which is driven by isotropic interactions, and the filamentary structures presented in this chapter.

In order to further investigate the nature of the anisotropic forces between the molecules, a larger simulation containing several $\text{Mn}_{12}(\text{acetate})_{16}$ molecules was performed. Figure 6.5(e) shows the results of a MD simulation where the positions of five $\text{Mn}_{12}(\text{acetate})_{16}$ on an Au(111) substrate have been allowed to evolve over time (see appendix B for details of the MD simulations). The resultant structure is a molecular aggregate similar to those observed in the STM images. Figure 6.5(f) shows a schematic of the final configuration, with the molecules labelled 1 and 2 clearly adopting the state **D2** type of bonding configuration, while molecules 3, 4, and 5 adopt conformations similar to states **D3** and **D4**.

It is important to note that the magnetic properties of $\text{Mn}_{12}(\text{acetate})_{16}$ are unlikely to be the driving force behind the formation of the observed structures. The MD simulations do not include any information about the magnetic interactions between the molecules and therefore is not responsible for the predicted structures. It would be unphysical to include magnetic interactions within the simulations as the blocking temperature of $\text{Mn}_{12}(\text{acetate})_{16}$ (the temperature at which the magnetic spin will not relax back to its ground state) is 4 K [152] and

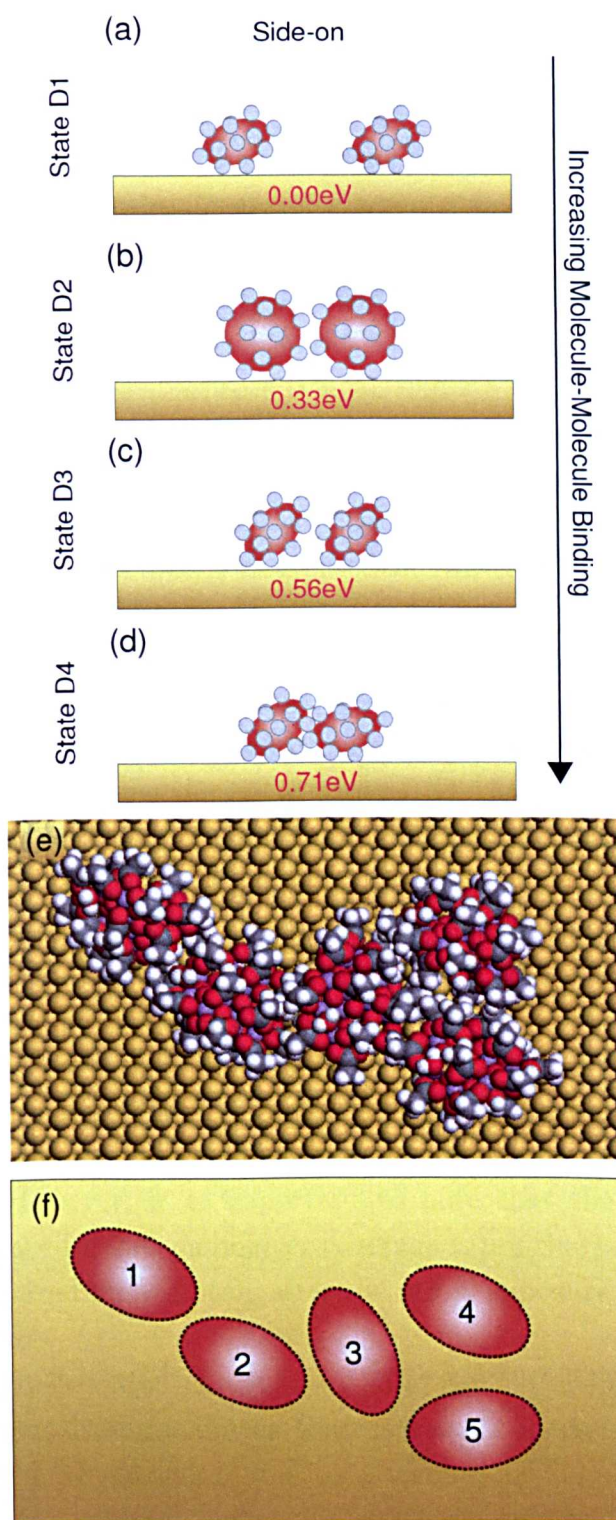


Figure 6.5: Schematic showing the bonding states (corresponding to local energy minima obtained by a MD quench simulation) available to a pairs of $\text{Mn}_{12}(\text{acetate})_{16}$ molecules adsorbed on the Au(111) surface. (a)-(d) Schematics showing the energy minima of the molecule-molecule interaction between two $\text{Mn}_{12}(\text{acetate})_{16}$ molecules. (e) Final structure from a MD simulation of five $\text{Mn}_{12}(\text{acetate})_{16}$ molecules on an Au(111) surface showing the formation of a filamentary structure. (f) Schematic showing the positions of the five SMMs at the end of the MD simulation.

therefore magnetic ordering is not expected at room temperature.

6.4 NEXAFS spectra of $\text{Mn}_{12}(\text{acetate})_{16}$

The combination of STM and MD simulations has allowed us to characterise the structures formed by the $\text{Mn}_{12}(\text{acetate})_{16}$ when deposited on the Au(111) surface. The stability of the SMMs undergoing the deposition process is confirmed by NEXAFS measurements acquired at beamline D10111 of the MAX-Lab synchrotron radiation facility. Figure 6.6 shows NEXAFS spectra taken at the Mn 2*p* adsorption edge for coverages between 0.2 ML and 2.5 ML, from which the oxidation state of the manganese atoms in the core of the molecule may be identified. For multi-layer coverages, the NEXAFS spectra are consistent with a mixture of Mn^{3+} and Mn^{4+} oxidation states, similar to those previously observed [153] for an undamaged $\text{Mn}_{12}(\text{acetate})_{16}$ molecule (the $\text{Mn}_{12}(\text{acetate})_{16}$ molecule should contain 4 Mn^{4+} and 8 Mn^{3+} atoms [152]).

However, for the sub-monolayer coverages (0.2ML, 0.5ML, and 0.6ML) the spectra observed is consistent with that of a sample consisting predominantly of the Mn^{2+} oxidation state. This analysis is based on a comparison with NEXAFS data acquired for a reference sample of MnO [153, 154], which contains only the Mn^{2+} oxidation state and is characterised by a large peak in the NEXAFS spectra at ~ 640 eV (labelled as Mn^{2+} in Figure 6.6). From this comparison we may assert that for sub-monolayer coverages of $\text{Mn}_{12}(\text{acetate})_{16}$ deposited by UHV-ESD the majority oxidation state for the Mn atoms is 2+. This finding bears similarities to beam damage studies where several single crystal samples of SMMs, based on the $\text{Mn}_{12}(\text{acetate})_{16}$ core, were investigated by measuring NEXAFS spectra over the course of several hours [155]. The continued exposure of the sample to the synchrotron beam resulted in the growth of the peak corresponding to the Mn^{2+} oxidation state. However, it is important to note that the observation of the Mn^{2+} oxidation state for sub-monolayer coverage is not due to beam damage and all spectra are acquired immediately after the initial exposure to the beam, before beam damage occurs.

The features labelled Mn^{3+} (~ 642.0 eV) and Mn^{4+} (~ 643.5 eV) in Figure 6.6 can be seen to grow dramatically as the coverage is increased, confirming that the reduction of the Mn atoms is due to a surface mediated effect. The mechanism for reduction may be due to a direct charge transfer from the surface or may arise from internal changes to the bonding within the $\text{Mn}_{12}\text{O}_{12}$ core, possibly due to surface-induced modification or even loss of the attached H_2O or acetate ligands. A simple charge transfer from the surface would likely be associated with strong surface-core bonding which is unlikely to be compatible with the observed diffusivity of the $\text{Mn}_{12}(\text{acetate})_{16}$ and therefore the second possibility is more probable. Modification of the shell ligands would naturally lead to corrections to the simple numerical model, but the overall hypothesis that the shape

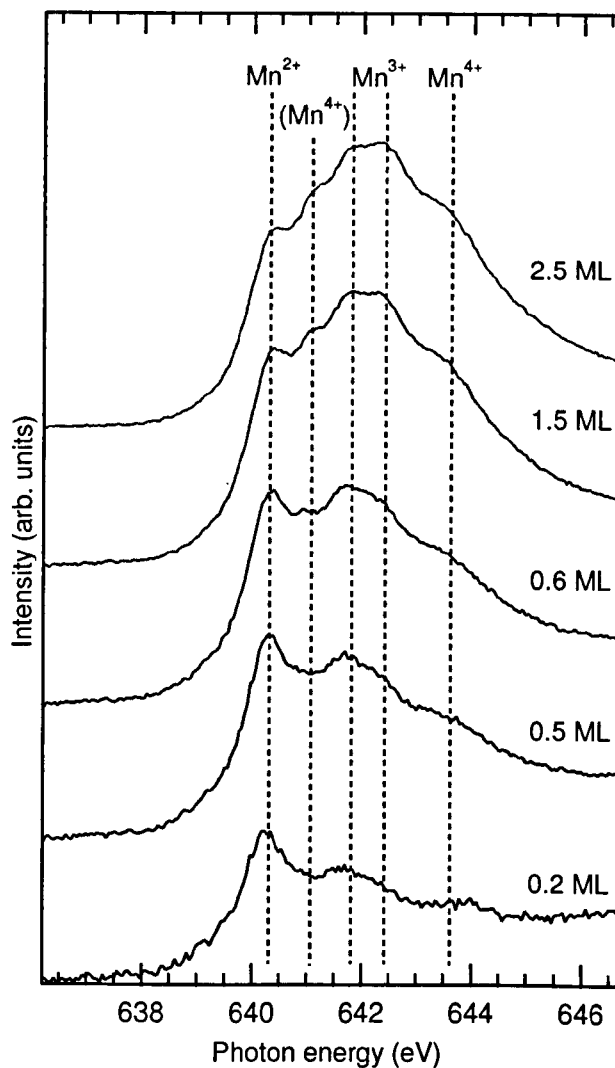


Figure 6.6: NEXAFS spectra measured at the Mn 2p adsorption edge (Mn L-edge) for a range of coverages (0.2 ML - 2.5 ML) of the Mn₁₂(acetate)₁₆ deposited on the Au(111) surface. The photon energy was calibrated by measuring the energy separation of the Au 4f core-level photoemission peaks excited by 1st and 2nd order X-rays. The positions of the peaks corresponding to the presence of Mn²⁺, Mn³⁺, and Mn⁴⁺ are labelled.

asymmetry of the molecule leads to the observed structures is expected to remain valid. However, it must be noted that the exact nature of the surface-molecule and molecule-molecule interactions in this situation are undefined within the context of our current model. Overall the expected oxidation states for an intact molecule are observed for multilayer coverage, confirming that the chemical properties of $\text{Mn}_{12}(\text{acetate})_{16}$ are unaffected by the UHV-ESD process.

6.5 UHV-ESD of $\text{Mn}_{12}(\text{acetate})_{16}$ on a supramolecular network

The previous sections have demonstrated that UHV-ESD of $\text{Mn}_{12}(\text{acetate})_{16}$ can be used to produce sub-monolayer and multilayer films on the Au(111) surface. The compatibility between PTCDI/melamine hydrogen-bonded supramolecular networks and UHV-ESD has been demonstrated in the previous chapter (Chapter 5). Here it is shown that $\text{Mn}_{12}(\text{acetate})_{16}$ may be induced to form structures with a different order to those reported on above, when deposited on a surface on which a hydrogen-bonded nanoporous network has been prepared. In Chapter 4 the various phases of PTCDI/melamine structures were discussed: in this experiment the hexagonal phase was prepared on the Au(111) surface. The pores within such a network have been shown to act as nanoscale traps for diffusing molecules [47,50,51,118], including (for low coverage) molecular species deposited by UHV-ESD (i.e. UHV-ESD of C_{60} - Chapter 5). Figure 6.7((a), (b), and (c)) shows the structure of melamine, PTCDI and the structure of the hexagonal network respectively. From a comparison of the dimensions of the hexagonal network pores and the $\text{Mn}_{12}(\text{acetate})_{16}$ molecule it is expected that each pore will have the capacity for one molecule. Figure 6.7(d) shows an Au(111) substrate which has been pre-patterned with a PTCDI/melamine hexagonal network and has been exposed to a deposition of ~ 0.05 ML of $\text{Mn}_{12}(\text{acetate})_{16}$ via UHV-ESD. The positions of $\text{Mn}_{12}(\text{acetate})_{16}$ trapped within a pore of this host/guest architecture are highlighted (in addition some, non-highlighted, $\text{Mn}_{12}(\text{acetate})_{16}$ molecules are adsorbed at other sites on the surface), and it can be seen that the resultant structure demonstrates a trapping of the molecules within the pores. This result shows that hydrogen-bonded supramolecular networks have the potential to trap $\text{Mn}_{12}(\text{acetate})_{16}$ deposited by UHV-ESD and locally inhibit the formation of filaments, such as those discussed above, or other molecular aggregates. Figures 6.7(e) and 6.7(f) show close-up STM images of the hexagonal network containing two trapped $\text{Mn}_{12}(\text{acetate})_{16}$ molecules, with the overlay in Figure 6.7(f) highlighting the positions of the network pores. A line profile of a trapped $\text{Mn}_{12}(\text{acetate})_{16}$ is shown in Figure 6.7(g) (the path of the line profile is depicted in 6.7(f)) from which the periodicity of the hexagonal network, labelled P , and the position of the trapped $\text{Mn}_{12}(\text{acetate})_{16}$ may be determined.

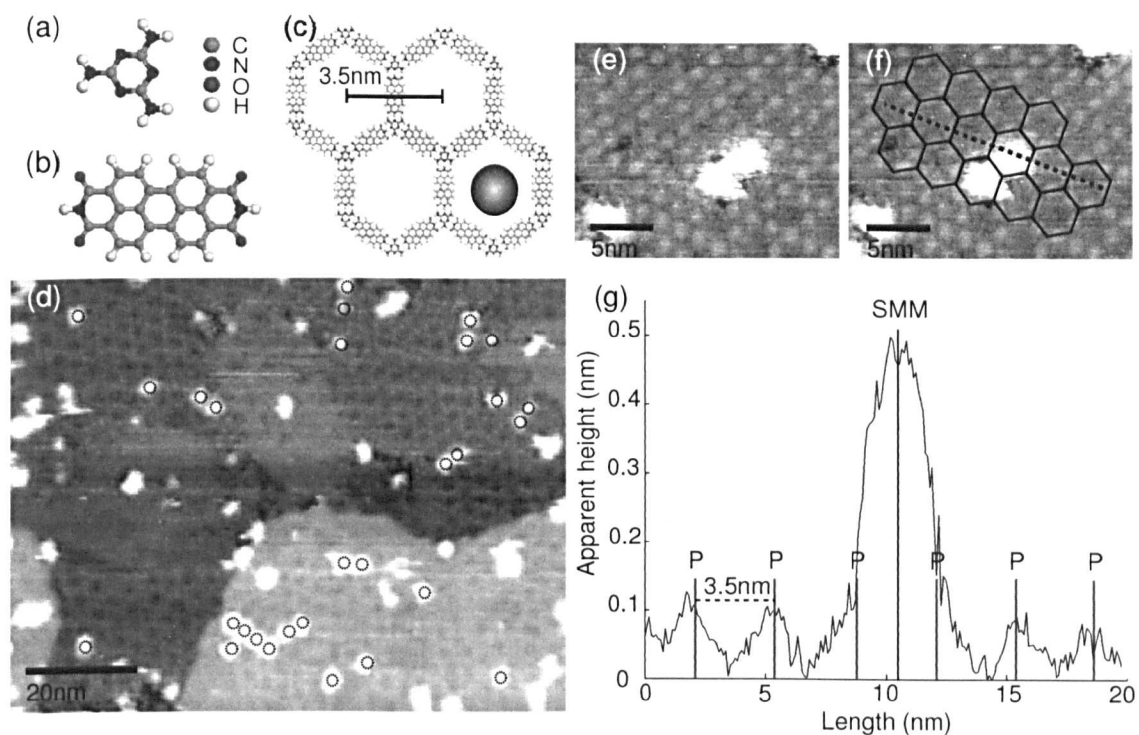


Figure 6.7: $\text{Mn}_{12}(\text{acetate})_{16}$ adsorbed on a supramolecular network. Chemical structures of (a) melamine, and (b) PTCDI. (c) Structure of the self-assembled hexagonal network formed by the hydrogen-bonding interaction between melamine and PTCDI. The grey circle represents the size of a $\text{Mn}_{12}(\text{acetate})_{16}$ relative to the dimensions of the network. From geometric considerations, one $\text{Mn}_{12}(\text{acetate})_{16}$ may be trapped within each pore. (d) STM image of the Au(111) surface which has been pre-patterned with a PTCDI/melamine network prior to the UHV-ESD of $\text{Mn}_{12}(\text{acetate})_{16}$ ($V_{\text{sample}} = +1.80$ V, $I_{\text{tunnel}} = 0.03$ nA). The dashed black circles highlight $\text{Mn}_{12}(\text{acetate})_{16}$ molecules trapped within a network pore. (e) Close-up STM image showing two $\text{Mn}_{12}(\text{acetate})_{16}$ molecules trapped within neighbouring network pores ($V_{\text{sample}} = +1.80$ V, $I_{\text{tunnel}} = 0.03$ nA). (f) STM image, from (e), with an overlay highlighting the position of the hexagonal network. (g) Line profile taken over a region of network containing one trapped $\text{Mn}_{12}(\text{acetate})_{16}$. The path of the line profile is shown in (f) and the periodicity of the hexagonal network is labelled P . The location of the trapped $\text{Mn}_{12}(\text{acetate})_{16}$ in the centre of the pore is marked.

Interestingly there is an indication in this image that the occupancy of the neighbouring host sites is slightly correlated, with the presence of a trapped $\text{Mn}_{12}(\text{acetate})_{16}$ increasing the likelihood of a neighbouring pore also containing a trapped $\text{Mn}_{12}(\text{acetate})_{16}$. This finding bears similarities to the observed correlation between occupancy of C_{60} dimers trapped with a PTCDI/melamine parallelogram network and the probability of a neighbouring pore being occupied [25]. For the C_{60} dimers the correlation was attributed to a kinetic effect, although for the $\text{Mn}_{12}(\text{acetate})_{16}$ molecule an energetic origin is also possible. In this instance no statistical analysis has been performed to determine the extent of any correlation which may be present.

6.6 Summary

In this chapter the UHV-ESD of $\text{Mn}_{12}(\text{acetate})_{16}$ on an Au(111) substrate, producing both sub-monolayer and multilayer coverages, has been demonstrated. These findings show that large three-dimensional molecules, such as $\text{Mn}_{12}(\text{acetate})_{16}$, can form complex aggregate structures, with the growth of the filamentary structures being due to anisotropic intermolecular interactions. In this case the anisotropy is a direct consequence of the vdW interactions between the acetate ligands which are asymmetrically arranged around the Mn_{12} core and does not arise from chemically specific interactions (i.e. hydrogen-bonding, metal-organic co-ordination). The interlocking of these groups may be considered as a three-dimensional analogue of the alkyl chain interdigitation as observed for planar molecules [156]. These results show that the growth of materials from the vapour deposition of large molecules which lack a high degree of symmetry can give rise to highly complex structures, and that such aggregated structures can be modelled using MD simulations.

NEXAFS analysis of the samples show that the expected oxidation states for the Mn atoms is maintained for coverages of two mono-layers or more and hence it is expected that the molecules will maintain their magnetic properties. Finally it has been shown that supramolecular templating can influence the lateral organisation of large three-dimensional molecules. These new insights into the combination of UHV-ESD and the surface adsorption of complex organic molecules should find relevance for the controlled formation of nano-structured surfaces based not only on $\text{Mn}_{12}(\text{acetate})_{16}$ but with many other large molecules. In the following chapter a porphyrin based molecular wire is investigated, providing further information about the complexities of the self-assembly of complex organic molecules.

Chapter 7

Conformation and packing of porphyrin oligomers and polymers on a gold surface

In this chapter porphyrin oligomers and polymers are studied as an example of a complex molecule which possesses novel optical and electronic properties. Here UHV-ESD has been utilised to deposit the thermally labile, porphyrin based molecules on the Au(111) surface. The porphyrin oligomers (consisting of 4 and 6 porphyrin units) are observed to self-assemble into highly ordered close-packed domains, stabilised by the interdigitation of alkyl chains attached to the porphyrin cores of the molecules. A combination of STM, XPS, and NEXAFS techniques are used to investigate the structure and chemistry of the oligomers. The porphyrin polymer, consisting of approximately 40 porphyrin units (~ 54 nm in length), is observed to form domains of quasi-close-packed structures stabilised by the interdigitation of alkyl chains. A measure for the persistence length of the polymer has been obtained (~ 25 nm), demonstrating that despite the flexibility of the polymer chains, localised ordering on the surface is present due to the chain-chain interactions.

7.1 Porphyrin polymers as self-assembling molecular wires

The production of nanoscale electronic devices may potentially be realised by a bottom-up self-assembly process, utilising electronic components which have been produced via chemical synthesis. Many systems have been studied where the electronic components of a circuit are pre-designed 'molecular components' with the desired opto-electronic properties such as light emitting diodes [157], photo-voltaic diodes [158], and field-effect transistors [159]. In order to join these components together to produce a truly nano-electronic circuit, molecular wires will be required.

Major candidates for molecular wires include materials like carbon nano tubes (both single [160] and multi-walled [161]) and π -conjugate organic polymers [162].

Conjugated organic polymers have stimulated great interest due to their potential applications in nonlinear optics [163], light harvesting [164,165], and nano-scale charge transport [166–168]. As with many other organic materials, interfacial properties are likely to play an important role in their applications in molecular electronics [169]. However, it has not so far been possible to study these effects due to the difficulty in preparing suitable monolayers, since these polymers cannot be sublimed. A question of particular interest relates to the influence of the flexibility of such large molecules on the ordering within interfacial regions.

On a more fundamental level, the interactions between such molecular wires has the potential to give rise to the formation of self-assembled structures. In the previous chapter (Chapter 6) it was demonstrated that the $\text{Mn}_{12}(\text{acetate})_{16}$ molecule forms filamentary structures on the Au(111) surface due to its complex three-dimensional shape, therefore the porphyrin oligomers and polymers may also be expected to exhibit complex interaction potentials. The chemical structure of the porphyrin sub-units is of particular relevance with respect to the self-assembly of supramolecular structures. Each porphyrin core has been functionalised with four octyl chains (see Figure 7.1), providing an alternative method of stabilising supramolecular structures via the interdigitation of alkyl chains. Alkyl chains have been previously shown to form self-assembled structures directed by vdW interactions at the liquid-substrate interface on Au(111) [170] and HOPG [171,172] surfaces. This interdigitation of the alkyl chains leads to the formation of close-packed structures, and it is this intermolecular interaction that has been utilised to order molecules functionalised with alkane chains, leading to the formation of close-packed [173–175] and porous [40,176–178] supramolecular structures.

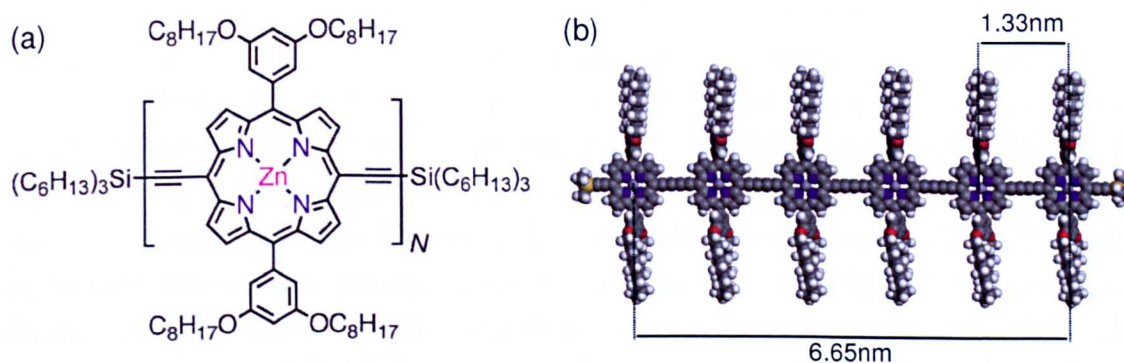


Figure 7.1: (a) Chemical structures of the porphyrin oligomers **P4** ($N = 4$) and **P6** ($N = 6$) and porphyrin polymer **P n** ($N \approx 30$ -50, polydisperse, endgroups H rather than $\text{Si}(\text{C}_6\text{H}_{13})_3$). (b) The structure of the porphyrin hexamer **P6**. The separation between the centres of the porphyrin sub-units is indicated.

In this chapter the adsorption of two oligomers, a tetramer (**P4**, $N = 4$) and a hexamer (**P6**, $N = 6$), and a porphyrin polymer (**P n** , $N \approx 30$ -50), formed from a

monomer unit with alkyl side chains (chemical structure shown in Figures 7.1 (a)), has been investigated. Due to the fragile nature of these molecular species it is not possible to deposit these molecules on a substrate held in UHV by sublimation, therefore UHV-ESD is utilised to deposit **P4**, **P6** and **P n** on an Au(111) surface for characterisation via STM and synchrotron based studies (XPS and NEXAFS).

7.2 Experimental methods

The UHV-ESD of the porphyrin polymers and oligomers was performed within the Nottingham UHV system with a base pressure of 5×10^{-11} Torr. The electrospray apparatus and operation is identical to that described in the previous chapter (Chapter 6). **P4** was dissolved in a toluene/methanol mixture (1:1 by volume). **P6** and **P n** were dissolved in a toluene/methanol solution (2:1 and 3:1 by volume respectively) with the addition of $\sim 5\%$ of pyridine to prevent the molecules from aggregating and precipitating out of solution. All of the compounds were dissolved to give a concentration of ~ 50 μg per ml of solvent mixture. A bias of ~ 2 kV (relative to the grounded entrance capillary) was applied to the emitter in order to produce the electrospray event, with the pressure rise in the preparation chamber (due to the introduction of the molecular beam) measured to be of the order 5×10^{-8} Torr. A drain current of 50-100 μA was measured at the entrance capillary to the UHV system.

The preparation of the Au(111) substrate, and the details of the STM are identical to that described in the previous chapter. XPS and NEXAFS experiments were conducted at the bending magnet beamline D1011 at Max II, MAX-lab in Lund. The D1011 end station is equipped with a SCIENTA SES200 electron analyser. For the XPS experiments the sample was orientated at normal emission relative to the analyser, for NEXAFS experiments this angle was varied. The sample, and the preparation methodology, for this experiment are identical to that described in Chapter 6. A single crystal substrate was prepared by cycles of argon sputtering (1 keV) and annealing (600°C) until it showed a negligible C 1s core-level signal (measured using $h\nu=340$ eV). N 1s and Zn 2p core-level spectra were measured using $h\nu=500$ eV and $h\nu=1250$ eV respectively. N 1s NEXAFS data were recorded at normal incidence, 30° and 60° with the emitted electrons being collected with a partial yield detector (100 V retardation potential). All XPS spectra were calibrated to the Au4f substrate peak at 84.0 eV. The photon energy for the NEXAFS spectra was calibrated from the energy separation of the Au 4f photoemission peaks excited by X-rays in 1st and 2nd order.

7.3 Self-assembly of the porphyrin oligomers P4 and P6

Images acquired after the deposition of a sub-monolayer coverage of **P6** show that, despite their large size, the porphyrin oligomers diffuse on the surface and form highly ordered islands composed of parallel molecular rows (see Figure 7.2 (a)). The porphyrin sub-units are clearly resolved in the STM images as bright features, with six porphyrin units being observed for each **P6** molecule, and the intramolecular separation of porphyrins determined to be $1.33 \text{ nm} \pm 0.07 \text{ nm}$. The measured porphyrin separation is found to be in good agreement with the value obtained by X-ray crystallography (1.353 nm) [179]. There appears to be no preferred orientation between the molecular domains and the crystallographic axes of the substrate.

Annealing the sample at $\sim 100^\circ\text{C}$ causes the **P6** islands to grow and become more ordered (shown in Figure 7.2 (b)). The predominant feature of these domains is the formation of columns, with molecules stacked above one another. The heavily faceted edge of the molecular domain at the top of the STM image shown in Figure 7.2 (b), compared to the smooth side on the right of the domain, indicates a preference for molecules to join at the ends of the molecular columns. Figure 7.2 (c) is a high resolution STM image showing the molecular structure of the close-packed domains, from which the distance between porphyrins in neighbouring molecules ($a = 2.6 \text{ nm} \pm 0.2 \text{ nm}$) and the canting angle between the long axis of the molecule and the row axis ($\phi = 15^\circ \pm 3^\circ$) can be measured. Within the close-packed array there are a small number of molecules with a different number of porphyrin units, the region D in Figure 7.2 (c) shows a porphyrin oligomer with only 5 monomer units. The presence of a small proportion of shorter oligomers is consistent with the sample purity.

The offset between porphyrin groups in neighbouring molecules (as defined in Figure 7.2 (d)), $\Delta \approx 0.7 \text{ nm} \pm 0.1 \text{ nm}$, is equal within experimental error to half the porphyrin spacing, 1.33 nm . This offset is suggestive of an interdigitated arrangement in which the octyl sidechains lie perpendicular to the long axis of the molecule and parallel to the gold surface (a schematic of this structure is shown in Figure 7.2 (d)). This chain conformation would allow the alkyl chains of adjacent molecules to interdigitate within the close-packed structure facilitating the maximisation of both the amount of surface covered by the ‘footprint’ of molecules and the vdW interaction between the interdigitating chains which has previously been shown to be the driving force behind many self-assembled systems containing alkyl chains [40, 118, 170, 173, 174, 176–178, 180].

In order to gain further information about the nature of the interaction a shorter porphyrin oligomer (**P4**) has been studied. The **P4** oligomer was deposited on the Au(111) substrate, resulting in the production of an analogous structure to that described for the **P6** molecule. Figure 7.3 (a) shows an STM image of a

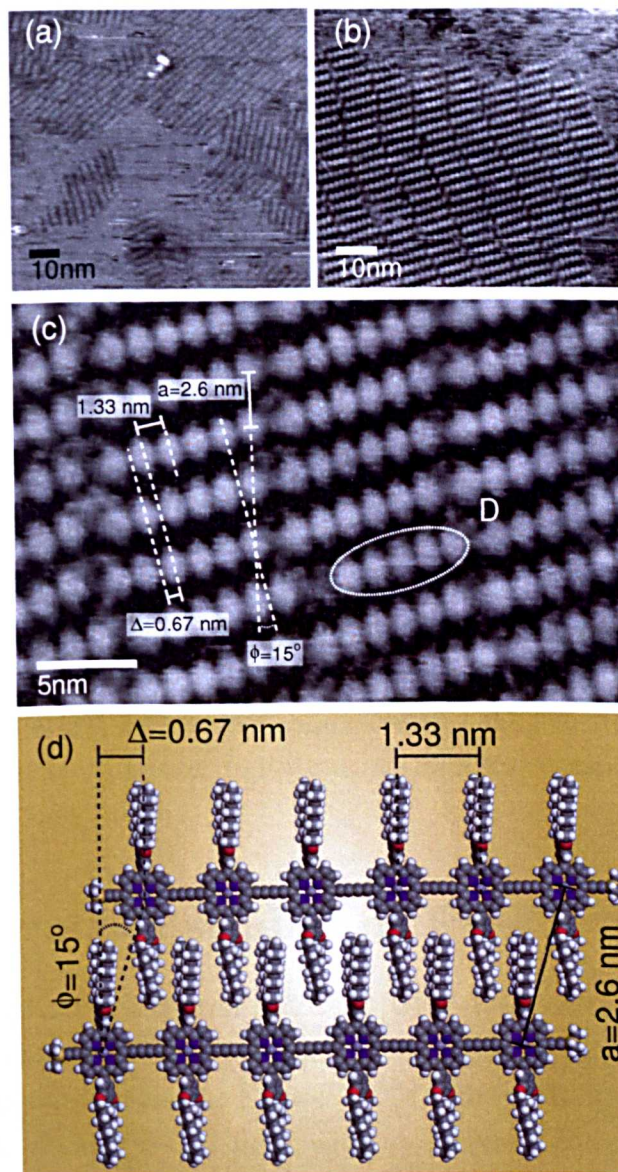


Figure 7.2: (a) STM image of close-packed domains of **P6** adsorbed on the Au(111) surface after UHV-ESD ($V_{sample} = -1.80$ V, $I_{tunnel} = 0.03$ nA). (b) Close-packed domains of **P6** imaged after annealing the sample at $\sim 100^\circ\text{C}$ ($V_{sample} = -1.80$ V, $I_{tunnel} = 0.03$ nA). Annealing facilitates formation of highly ordered molecular domains (typically 50 nm x 50 nm in area). (c) High resolution STM image of a close-packed domain of **P6**, the separation of the bright features corresponding to the positions of the porphyrins is indicated ($V_{sample} = -1.80$ V, $I_{tunnel} = 0.03$ nA). The region labelled D highlights a porphyrin oligomer with only five monomer units. (d) The proposed model for the **P6** molecules in the close-packed structure.

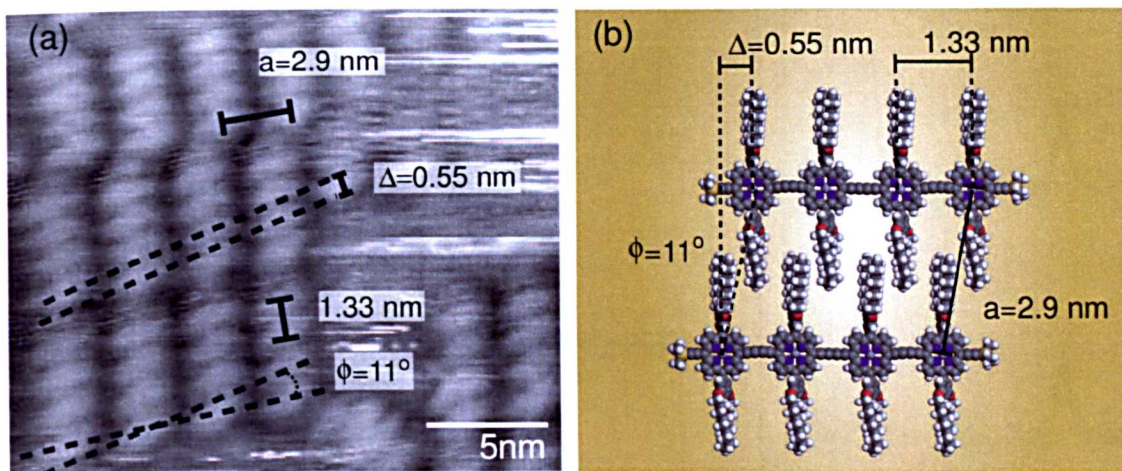


Figure 7.3: (a) STM image showing the **P4** molecules within a close-packed domain ($V_{\text{sample}} = -1.80 \text{ V}$, $I_{\text{tunnel}} = 0.03 \text{ nA}$). (b) Schematic showing the molecular orientations of the **P4** molecule, and the experimentally determined dimensions of the close-packed domain.

region of close-packed molecules, the dimensions of the structure are indicated on the image. Similar to the **P6** structure the separation between the molecules is determined to be $a = 2.9 \text{ nm} \pm 0.2 \text{ nm}$, with an average canting angle $\phi = 11^\circ$. The offset value, Δ , is smaller than that observed for **P6** but is still consistent with the interdigitation of the alkyl chains. The similarities between the structures of **P6** and **P4** close-packed molecules demonstrates that the self-assembly of these structures is driven by the interdigitation of the alkyl chain sidegroups and the conformation that they adopt.

7.4 Synchrotron studies of P4

Angle resolved NEXAFS acquired following UHV-ESD of the **P4** oligomer show that the porphyrin cores of the molecules are lying flat relative to the Au(111) surface. This is demonstrated in Figure 7.4 (a) where the nitrogen $1s$ NEXAFS shows the growth of the $1s \rightarrow \pi^*$ peak with an increasingly grazing angle of incidence, with negligible intensity at normal incidence. This is consistent with the nitrogen π^* bond being parallel to the surface, as described in Chapter 3. Further to this, XPS data was collected which demonstrates that the Zn atoms within the porphyrin are not displaced when the molecule is deposited. Figure 7.4 (b) shows N $1s$ XPS data for a range of molecular coverages, where in all cases there is only one chemical environment indicating that all 4 nitrogen atoms within the porphyrin core are bonded to the zinc (if the Zn atoms were removed to form the porphyrin free base then two chemical environments for the N atoms would be expected). Zn $2p$ spectra are shown in Figure 7.4 (c) for a range of coverages, again only showing one chemical environment. This finding is in contrast to other work on more reactive surfaces where the Zn atom is removed from the porphyrin [88]. This additional information confirms the structural model determined by STM

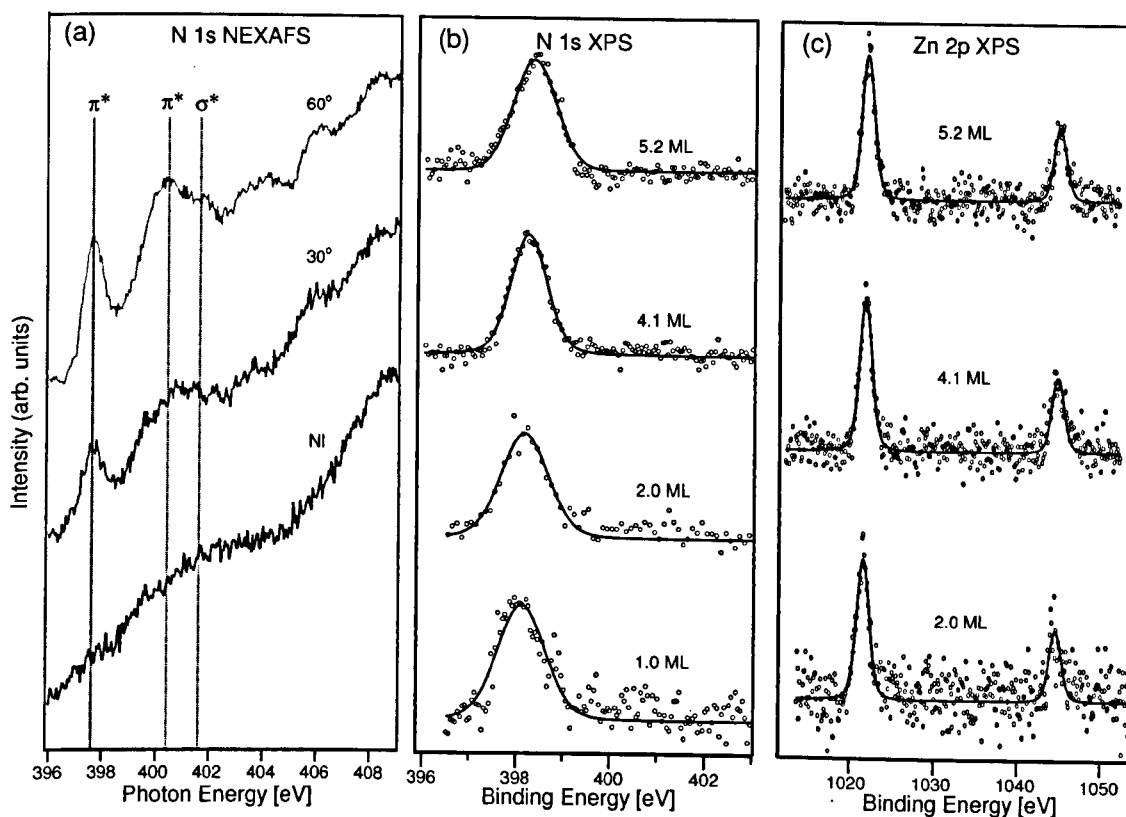


Figure 7.4: (a) N 1s NEXAFS spectra (5.2 ML). The growth of the $1s \rightarrow \pi^*$ transition with increased grazing angle shows that the porphyrin sub-units are lying flat relative to the Au(111) plane. (b) N 1s, and (c) Zn 2p, core-level photoemission spectrum measured using $h\nu = 500$ eV and $h\nu = 1250$ eV respectively. One chemical environment is observed in all cases.

and allows additional chemical information to be obtained. The ability to combine the techniques of STM, XPS and NEXAFS by producing samples that can be investigated in situ makes UHV-ESD a powerful experimental tool.

7.5 Self-assembly and persistence length of the porphyrin polymer P_n

Deposition of the porphyrin polymer (P_n , consisting of ~ 40 porphyrin subunits - determined by gel permeation chromatography [181]) on the Au(111) surface results in long chains being observed to run along the surface. Quasi-close-packed regions where chains are aligned (similar to, but smaller than, the lamella structures formed by polythiophene [90, 182, 183]), and more disordered regions where bends and kinks occur, together with points where the polymer chains cross (see Figure 7.5) are seen to co-exist on the surface. As with the porphyrin oligomers it is possible to identify the porphyrin sub-units as bright features within the molecules. The intramolecular separation between porphyrin units is in good agreement with both the X-ray diffraction data and the measured values for the oligomers with a value of $1.34 \text{ nm} \pm 0.07 \text{ nm}$ being found for P_n .

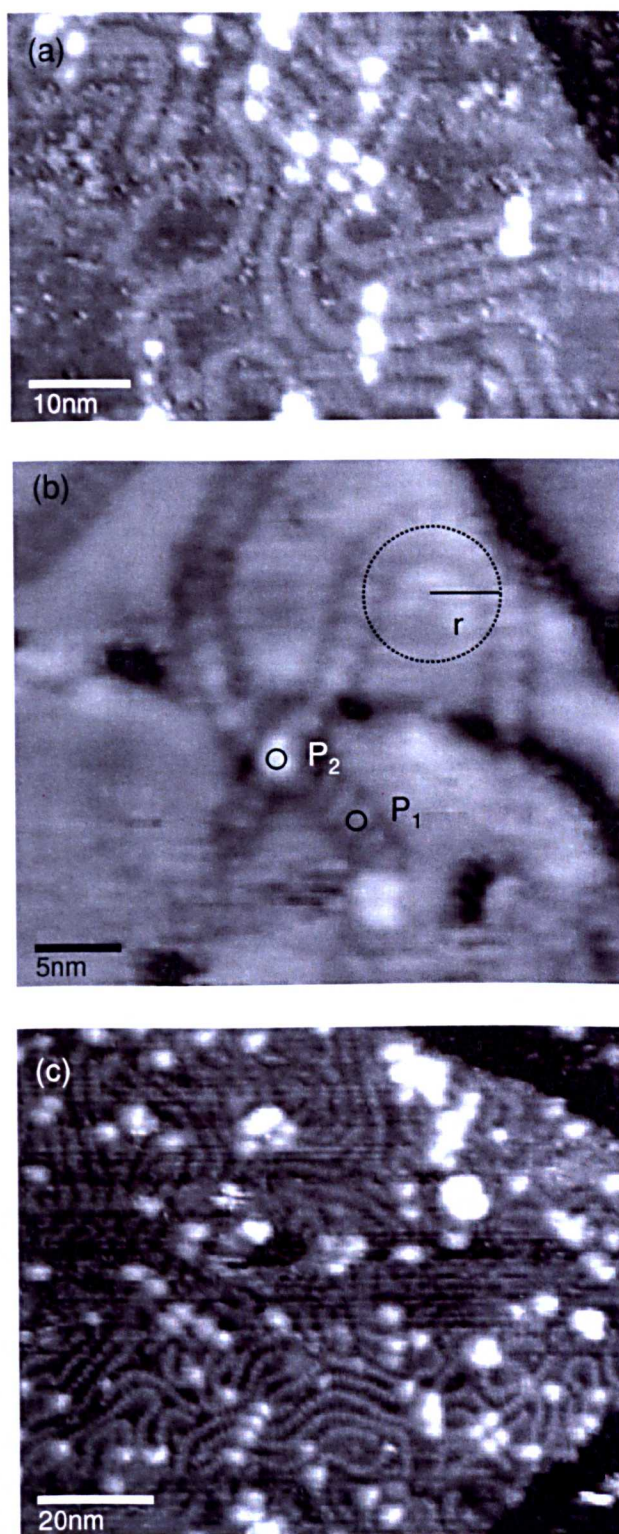


Figure 7.5: (a) STM image of the porphyrin polymer \mathbf{Pn} after UHV-ESD on the Au(111) surface ($V_{sample} = -1.80$ V, $I_{tunnel} = 0.03$ nA). (b) STM image showing a close-up of two \mathbf{Pn} molecules ($V_{sample} = -1.80$ V, $I_{tunnel} = 0.03$ nA). The individual porphyrin units can be distinguished, and the \mathbf{Pn} molecules can be observed to travel over a step edge. The two \mathbf{Pn} polymers can be seen to cross over at the point labelled P_2 resulting in a bright contrast feature twice the height of a single \mathbf{Pn} (measured at P_1). A \mathbf{Pn} chain which has a nonlinear backbone is shown with its radius of curvature labelled r . (c) Large area STM image showing a high density region of \mathbf{Pn} ($V_{sample} = -1.80$ V, $I_{tunnel} = 0.03$ nA). The bottom third of the image shows a region where the tip state allows imaging of individual porphyrins within the \mathbf{Pn} to be resolved. Bright contrast points show where two \mathbf{Pns} cross over, and several ‘hair-pin bends’ are observed.

The average length of the polymer chains is measured to be 54 nm with a standard deviation of 12 nm, consistent with the expected length of ~ 54 nm for a 40 unit porphyrin chain. This demonstrates that the **Pn** molecules are not damaged by the UHV-ESD process. In quasi-close-packed areas, prior to annealing, there is a small variation in the separation of the neighbouring segments of the aligned chains, but after annealing ($\sim 100^\circ\text{C}$) the polymers show a separation of $2.8 \text{ nm} \pm 0.3 \text{ nm}$. This value is close to the separation of the porphyrin oligomers, indicating that the quasi-close-packing of the polymers may also be driven by the interdigitation of the alkyl chain sidegroups.

In regions of the surface with a low molecular coverage, such as that shown in Figure 7.5 (b), the path of an individual polymer may be imaged. Here a **Pn** molecule is seen to run continuously over a step edge and bend back upon itself producing a ‘hairpin bend’ arrangement. The radii of curvature for several such bends have been measured, with the smallest observed radius being 1.3 nm (corresponding to a turn of 180° in 3-4 porphyrin units). Such flexibility is allowed due to the nature of the linkages between the porphyrin cores, with the alternating single and triple bonds between the carbon atoms providing freedom for the backbone of the molecule to bend.

Another feature prevalent in all STM images of **Pn** are the bright contrast regions at the junction where two polymers cross over. Measurements of the apparent height of these cross-over junctions (P_2 in Figure 7.5 (b)) are found to be ~ 0.4 nm, roughly twice the value of the measured height for a **Pn** above the surface (~ 0.2 nm, P_1 in Figure 7.5 (b)). Further examples of these cross-over points can be seen in Figure 7.5 (c) where a region of high molecular coverage is observed. The bottom third of the STM image clearly shows that the bright features where the polymers cross have continuous variation in topographic height, indicating that the polymer chains do not break when crossing. The angle formed between the axes of the two crossing polymers is measured to be $91^\circ \pm 9^\circ$, which implies that there is a preferred orientation for the porphyrin sub-units to adopt at the molecular intersection.

To determine the influence of the chain-chain interactions on the flexibility of **Pn** deposited on the Au(111) surface a statistical analysis of the distance, R , between porphyrin units which are separated by a contour length of L along the chain has been performed. L is chosen to be an integer number, N , of porphyrin sub-units. Figure 7.6 (a) shows histograms of the normalised frequency of R for $N = 5, 7, 9$, and 11. For small values of N we observed a sharply peaked distribution with the average value of the end to end distance, $R_{av} \approx L$ (i.e. **Pn** remains straight for short segments). These data are consistent with previous studies on porphyrin oligomers containing up to four units ($N = 4$) where a sharp peak in the distribution is observed at L with a tail in the distribution to small R [179]. However, for larger values of N the distribution observed in this work broadens and the value of R_{av} deviates significantly from L . This deviation is due

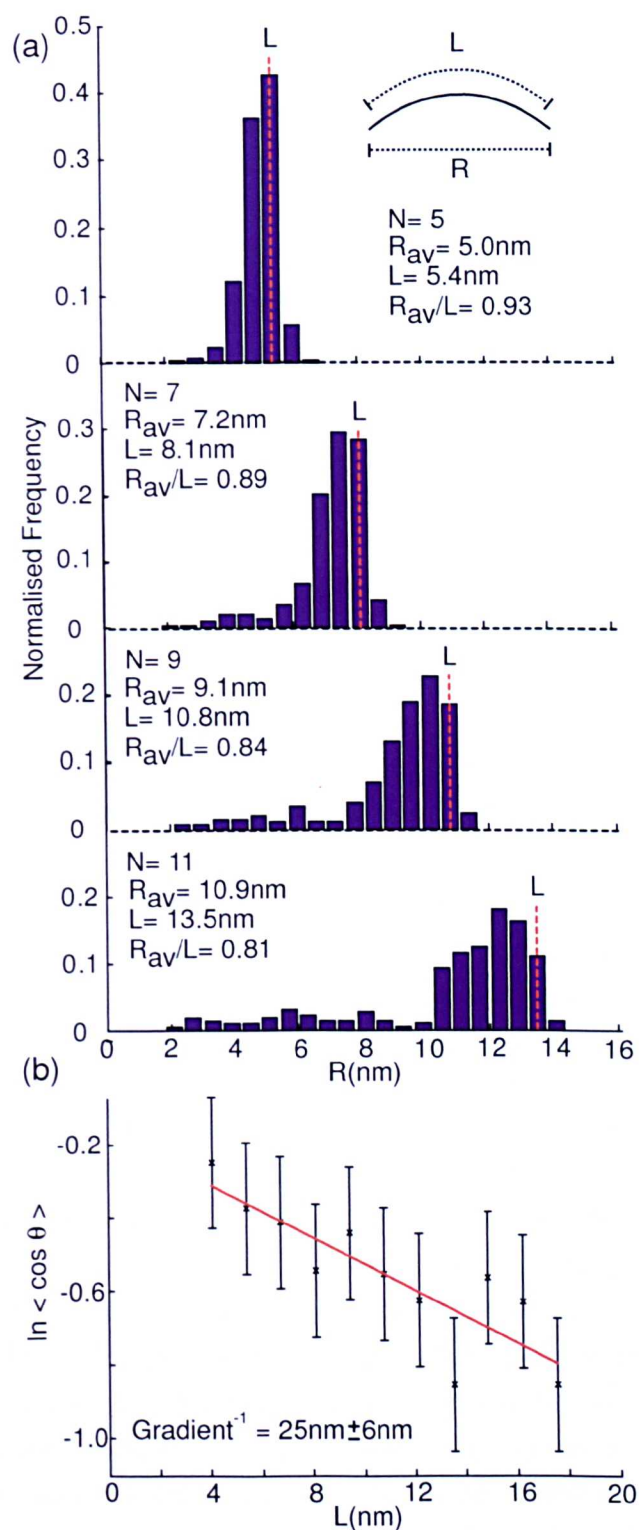


Figure 7.6: (a) Histograms showing the normalised frequency distribution of the end-to-end length, R , for segments of the polymer chain containing 5, 7, 9, and 11 porphyrin monomer units. (b) Plot of $\ln \langle \cos \theta \rangle$ against contour length, L , averaged over several polymer chains.

to the increase in occurrences of $R \ll L$ which is a direct result of the ‘hair-pin’ structures.

A value for the angular correlation length (i.e. the length over which the chain orientation becomes decorrelated), L_c , of **Pn** deposited on to the Au(111)

surface has been determined by measuring the average value of $\cos \theta$, where θ is the angle between vectors tangent to the axis of the polymer measured at two points separated by a contour length of L [184]. The average is taken over all segment pairs with the same contour length separation. It is possible to estimate L_c assuming an exponential dependence:

$$\langle \cos \theta \rangle = e^{-\frac{L}{L_c}} \quad (7.1)$$

The plot of $\ln \langle \cos \theta \rangle$ against L (Figure 7.6 (b)) shows a linear dependence, giving $L_c = 27 \text{ nm} \pm 6 \text{ nm}$. For isolated non-interacting polymers the definition of L_c is equivalent to the persistence length, L_p , which provides a measure of the intrinsic flexibility of a polymer chain [185–187] and has been successfully determined in previous scanning probe studies of polymeric molecules [188,189]. For the densely packed porphyrin polymers discussed here L_c and L_p are not equivalent due to interactions with the surface and between neighbouring chains (for example the interdigitation of alkyl chains). However, it is interesting to note that the value of L_c is significantly greater than the value of persistence length previously measured for analogue oligomers in solution ($L_p \sim 19 \text{ nm}$) [179]. This indicates that polymers adsorbed on surfaces studied here are, on average, straighter than in the solution phase.

This increase is attributed to the planar geometry of the adsorbed molecules: in solution the porphyrins can bend out of plane, whereas on the surface, bending can only occur in the plane of the porphyrins so that deformation is localised in the acetylenic bridges. Inter-chain interactions are also expected to promote parallel alignment of neighbouring chains. Parallel chains of polymers would allow the interaction between the interdigitating alkyl chains to be maximised (as discussed for the oligomers) and minimise the energy cost caused by the bending of the polymer backbone. This finding demonstrates that the anisotropic interactions of the alkyl chains attached to the cores of the porphyrins are the driving force for the self-assembly and long-range ordering of these molecular wires. This is consistent with the STM images which show that sharp bends do not occur in segments of the polymer within quasi-close-packed regions. The images, supported by statistical analysis, show that simple models of polymers, such as the wormlike chain (WLC) [186] model cannot fully account for the observations presented here. In particular the finite frequency of $R \ll L$ in the histograms for large values of L in Figure 7.6 (a) is inconsistent with the WLC model. This disagreement is due to significant inter-chain interactions.

7.6 Summary

The self-assembly of two different porphyrin oligomers and a porphyrin polymer on the Au(111) surface has been demonstrated. These results highlight the impor-

tance of UHV-ESD as a method of facilitating the STM imaging of large complex molecules. The UHV-ESD technique has also been shown to be compatible with these potentially fragile, thermally labile molecules, and provides a non-destructive technique for depositing complex molecules into UHV for study by high resolution STM and synchrotron based techniques. The structures formed are driven by the conformation and interdigitation of the alkyl side chains. All of the structures observed here can be rationalised in terms of the anisotropic nature of the vdW interactions between the alkyl sidegroups of the molecules.

In addition it has been shown that conjugated porphyrin polymers are surprisingly flexible, even when constrained to a two-dimensional surface, and that their conformations and chain-chain crossing geometries are strongly influenced by interchain interactions. The results presented in this chapter (and Chapter 6) demonstrate that complex molecules have the potential to give rise to unexpected, large scale structures due to their shape and functionality. These interactions are not as transparent as the hydrogen-bonding interactions discussed in Chapter 4, and the prototypical molecular systems described here demonstrate that any attempts to design a self-assembled supramolecular structure containing complex three-dimensional molecules must consider a range of intermolecular interactions.

Chapter 8

Conclusion

In this chapter a summary of the findings reported on within this thesis is presented.

8.1 Summary of findings

The work detailed within this thesis has focused on the fundamentals of self-assembly, the interactions between the molecular ‘building blocks’ which ultimately determine the geometric arrangement of the structures formed. A detailed understanding of these nanoscale interactions allows us, in principle, to design structures with predetermined geometries and chemical functionalities, by choosing an appropriate set of starting materials. Several molecules, which possess novel functionalities, have been investigated as part of this work, with particular importance being placed on the intermolecular forces which give rise to the supramolecular assemblies that are formed.

The PTCDI/melamine bimolecular system has been studied, with a range of complex supramolecular structures being observed. These structures have revealed that although a strongly directional hydrogen-bonding interaction exists between the PTCDI and melamine molecules, vdW forces play an important role and can produce a staggering array of complex phases which cannot simply be predicted from a knowledge of the geometry of the hydrogen-bonding interaction. Three new phases of the bi-molecular PTCDI/melamine system have been described in Chapter 4, where ‘melamine-rich’ molecular assemblies have been shown to form on the Au(111) surface producing both kagome lattice structures and networks with square pores. STM and DFT have been utilised to investigate the structures formed, demonstrating that this relatively simple system possesses a complex ‘phase space’, altering the stoichiometric ratio of the molecular constituents and the temperature used to create the networks can lead to a wealth of structures.

The potential to introduce chemical functionality to these supramolecular networks by substituting the PTCDI molecule for the Br₂PTCDI or S₂PTCDI derivative has also been demonstrated. A hexagonal network phase formed from a

mixture of Br₂PTCDI and melamine has been observed to form on the Au(111) surface. However, the addition of these functional sidegroups can lead to an alteration in the structure of the self-assembled networks which form. The S₂PTCDI molecule does not readily participate in the hexagonal phase containing melamine, but is able to form an alternative homo-molecular hexagonal arrangement. This alternative arrangement is driven by a hydrogen-bonding interaction involving the SCH₂CH₂CH₃ side chains of the functionalised molecule. This finding demonstrates the complexities in designing a supramolecular system, where altering the shape of a molecule can effect the intermolecular interactions to such an extent that the molecular arrangement observed is radically different to that of a ‘similar’ molecule.

In order to facilitate the UHV-STM and synchrotron based investigations of complex organic molecules, many of which are thermally labile, the UHV-ESD technique has been developed within the Nottingham Nanoscience group. Chapter 5 detailed results that demonstrated UHV-ESD can be used to deposit C₆₀ for study by STM and XPS, as well as demonstrating that the technique could be used to deposit low coverages of the molecule on a PTCDI/melamine hydrogen-bonded supramolecular network. The results presented in this thesis show that there is a good agreement between the structures formed by thermally deposited C₆₀ and those transferred onto a surface by UHV-ESD. These results represent an important step towards being able to deposit complex molecules with ‘novel’ functionalities on to surfaces held in UHV.

Two examples of complex organic molecules which have been observed to self-assemble on the Au(111) surface have been discussed in Chapters 6 and 7. The SMM Mn₁₂(acetate)₁₆ is found to be compatible with the UHV-ESD process (as determined by NEXAFS measurements of the oxidation states of the Mn atoms within the core of the molecule), and is observed to form complex aggregate structures. The formation of these structures is driven by anisotropic intermolecular interactions, which are a direct consequence of the complex three dimensional shape of the molecule. This prototypical molecular system provides insight into the interactions expected for large molecules adsorbed at surfaces, and demonstrates that moving away from using small planar molecules (such as PTCDI and melamine) as molecular ‘building blocks’ increases the complexity of the molecule-molecule interaction potential. MD simulations have been used to great effect in understanding the interactions which drive the formation of filamentary structures formed by Mn₁₂(acetate)₁₆, revealing that the molecule orientates itself on the surface to maximise the number of CH₃ ligands in contact with the surface. The shape of the molecule also gives rise to the anisotropic nature of the molecule-molecule interactions, with the interdigitation of CH₃ ligands on neighbouring atoms being the most stable state for two interacting molecules. It has also been shown that a degree of lateral organisation can be imposed on the structures formed by Mn₁₂(acetate)₁₆, by using a surface pre-patterned with PTCDI/melamine hexag-

onal network to trap one molecule within each network pore.

Sub-monolayer coverages of porphyrin oligomers and polymers have also been prepared on the Au(111) surface by UHV-ESD. Surprisingly, these large molecules are seen to self-assemble into regular close-packed arrays. In this instance the molecular ordering is mediated by an interdigitation of the alkane chains of neighbouring molecules. The porphyrin polymers are found to be flexible, and the structures that they form also appear to be strongly influenced by molecule-molecule interactions governed by the conformation of the alkyl chains attached to the porphyrin cores of the monomer units.

This work has demonstrated that although the interactions between molecules within self-assembled structures are complex, it is possible to analyse and understand the formation of such structures in terms of the molecule-molecule and molecule-substrate interactions.

Appendix A

Theoretical background to DFT, MM, and MD

In this chapter the concepts underpinning DFT, molecular mechanics (MM), and MD simulations are described. A background to the techniques is presented, as well as a discussion of their computational implementation. Particular attention is given to the implementation of the techniques within the Dmol³ and Forcite programs.

A.1 Background to DFT

DFT is a powerful technique which is based on the principles of quantum mechanics. Within the context of this thesis, DFT has been used to calculate the electronic structure of molecular systems, allowing the HOMO and LUMO of molecules to be simulated in order to better understand how molecular species appear in STM images. DFT also allows the geometric structure corresponding to the energetic ground state of a molecule-molecule junction to be predicted. These calculations enable us to determine whether a particular geometric arrangement of molecules is energetically stable. Fundamentally, all of this information is acquired by solving the Schroedinger equation for the system under study. In many cases, finding this solution or an approximation to it is non-trivial. The first section in this appendix aims to introduce DFT in the context of Hartree-Fock theory and to show the development of DFT into its current form. This appendix is not intended as an exhaustive account of the technique, and further detail can be found in references [190–192].

The Schroedinger equation

The Schroedinger equation in its time independent form gives the relationship between the wave function, Ψ (describing the particles within a system), and the total energy of the system, E .

$$\hat{H}\Psi = E\Psi \quad (\text{A.1})$$

For a many-body system it is not possible to solve the Schroedinger equation exactly, therefore several assumptions and approximations are applied in order to allow a solution to be obtained. The Born-Oppenheimer approximation allows a large system containing many nuclei (and their associated electrons) to be simplified by assuming that the positions of the nuclei are fixed. This assumption is based on a consideration of the mass of the nuclei and the electrons (nuclei are several orders of magnitude more massive than the electrons), for this reason the electronic ‘relaxation’ compared to nuclear motion is instantaneous and hence the motion of the nuclei and electrons can be decoupled (solving the Schroedinger equation for fixed nuclei positions). This allows equation A.1 to be split into nuclear and electronic components.

$$\hat{H}_e\Psi_e = E_e\Psi_e \quad (\text{A.2})$$

$$\hat{H}_n\Psi_n = E_n\Psi_n \quad (\text{A.3})$$

The subscripts e and n refer to electrons and nuclei respectively. The energy of the electronic component may be split into kinetic and potential energy operators, \hat{T} and \hat{V} :

$$\hat{H}_e = \hat{T}_e + \hat{V}_{en} + \hat{V}_{ee} \quad (\text{A.4})$$

$$\hat{H}_n = \hat{V}_{nn} \quad (\text{A.5})$$

The nuclear Hamiltonian contains only an electrostatic term corresponding to the interactions between all of the nuclei within the system, no kinetic term is included due to the arguments inherent to the Born-Oppenheimer approximation. The electronic Hamiltonian includes terms corresponding to the kinetic energy of the electrons, \hat{T}_e , and the potential energy of the electron-electron, \hat{V}_{ee} , and electron-nuclei, \hat{V}_{en} , interactions.

The electronic Hamiltonian for the Born-Oppenheimer approximation of an isolated N -electron system can be written as:

$$\hat{H}_e = \sum_{i=1}^N \left(-\frac{1}{2} \nabla_i^2 \right) + \sum_i V(\mathbf{r}_i) + \sum_{i<j}^N \frac{1}{r_{ij}} \quad (\text{A.6})$$

where the summation is over all electrons in the system, and $V(\mathbf{r}_i)$ is the potential energy of the i^{th} electron in the field of the nuclei. For a given system there are many valid solutions to equation A.1. Each wave function, Ψ_k , that is an eigenfunction of the equation will correspond to an energy eigenvalue, E_k . For each system there will be a ground state Ψ_0 , with an energy E_0 , and it is this

state that we seek to identify in order to find the most stable state of a system. The expectation values for an observable are given by:

$$\langle \hat{A} \rangle = \frac{\int \Psi^* \hat{A} \Psi dx}{\int \Psi^* \Psi dx} = \frac{\langle \Psi | \hat{A} | \Psi \rangle}{\langle \Psi | \Psi \rangle} \quad (\text{A.7})$$

If Ψ is normalised then the expectation value for the observable $\langle \hat{A} \rangle$ is reduced to:

$$\langle \hat{A} \rangle = \int \Psi^* \hat{A} \Psi dx \quad (\text{A.8})$$

For a system in state Ψ , which is not necessarily an eigenfunction of the system, the expectation value for the energy will be given by:

$$E[\Psi] = \langle \hat{H} \rangle = \int \Psi^* \hat{H} \Psi dx \quad (\text{A.9})$$

This energy must be equal to, or greater than, the energy of the ground state, allowing us to impose an upper bound on the energy of the system. For any trial wave function Ψ_{trial} the expectation value for the energy of the system will be:

$$E[\Psi_{trial}] \geq E_0 \quad (\text{A.10})$$

Therefore by minimising $E[\Psi_{trial}]$ with respect to Ψ_{trial} we may obtain the true ground state of the system. This procedure is known as the variation principle, with a formal proof being given in reference [192].

The most complicated system that may be solved analytically by the application of the Born-Oppenheimer approximation is that of the H_2^+ molecule. This is due to the fact that exact solutions to systems which contain more than one electron cannot be written, as the wave function to describe interacting electrons is not known. Another drawback to the current formulation of the problem is that relativistic effects are not incorporated, and the effect of spin interactions are not included. Both of these problems can be overcome to a certain extent by applying the Hartree-Fock approximation.

A.1.1 Hartree-Fock approximation

The Hartree-Fock approximation treats the motion of each electron independently and ignores any interaction between them. This allows the all-electron wave function for a N electron system to be expressed in terms of a sum of the one-electron wave functions. The one-electron wave function, which is in this instance non-relativistic, may be modified to take into account the effect of spin. This is achieved by defining each one-electron wave function to be a product of the spatial waveform and a function which represents spin. The spin positions 'up' and 'down' are represented by the functions α and β ; these two functions are orthonormal

to each other. This combination of the spatial wave function, $\psi(x)$, and the spin component gives rise to a set of one-electron ‘spin-orbitals’ ϕ_i .

From the ‘spin-orbitals’, a many-electron wave function for the system under study may be created. It is not possible to simply sum the set of one-electron spin-orbitals to create the many-electron wave function. As electrons are fermions, the total wave function must be antisymmetric with respect to exchange of electron position. This asymmetry may be ensured by the construction of a Slater determinant, where all the one-electron spin-orbitals are placed within a matrix with the rows containing the electron co-ordinates and the columns containing the ‘spin-orbitals’:

$$\Phi_{SD} = \frac{1}{\sqrt{N!}} \begin{vmatrix} \phi_1(1) & \phi_2(1) & \cdots & \phi_N(1) \\ \phi_1(2) & \phi_2(2) & \cdots & \phi_N(2) \\ \vdots & \vdots & \ddots & \vdots \\ \phi_1(N) & \phi_2(N) \cdots & \phi_N(N) & \end{vmatrix} \quad (\text{A.11})$$

where N is the total number of electrons in the system. For the molecular systems considered within this thesis the columns can be seen as the single-electron wave functions, or molecular orbitals which the electrons occupy, with the rows representing the co-ordinates of the electron occupying that orbital.

In theory it is possible to use a superposition of the Slater determinants as the initial trial electronic wave function. However the Hartree-Fock method assumes that the electronic wave function consists of a single determinant. The electronic energy of the system can then be given by [192]:

$$E_e = \langle \Phi_{SD} | \hat{H}_e | \Phi_{SD} \rangle = \sum_{i=1}^N h_i + \frac{1}{2} \sum_{i,j=1}^N (j_{ij} - k_{ij}) \quad (\text{A.12})$$

where:

$$h_i = \int \phi_i^*(\mathbf{r}_1) \left[-\frac{1}{2} \nabla^2 + V(\mathbf{r}_1) \right] \phi_i(\mathbf{r}_1) d\mathbf{r}_1 \quad (\text{A.13})$$

$$j_{ij} = \iint \phi_i(\mathbf{r}_1) \phi_i^*(\mathbf{r}_1) \frac{1}{r_{12}} \phi_j(\mathbf{r}_2) \phi_j^*(\mathbf{r}_2) d\mathbf{r}_1 d\mathbf{r}_2 \quad (\text{A.14})$$

$$k_{ij} = \iint \phi_i^*(\mathbf{r}_1) \phi_j(\mathbf{r}_1) \frac{1}{r_{12}} \phi_j^*(\mathbf{r}_2) \phi_i(\mathbf{r}_2) d\mathbf{r}_1 d\mathbf{r}_2 \quad (\text{A.15})$$

h_i contains terms which define both the kinetic energy of an electron i and its potential in the field of all nuclei; j_{ik} is the ‘Coulomb integral’ and takes into account the classical electrostatic repulsion between the electrons; and k_{ij} is the ‘exchange integral’ which has no classical analogue. These terms can be written as operators with the whole expression used to define a new Fock operator, \hat{f}_i .

$$\hat{f}_i = \hat{h}_i + \sum_{j=1}^N (\hat{j}_{ij} - \hat{k}_{ij}) \quad (\text{A.16})$$

where \hat{f}_i is the Fock operator for the i^{th} Minimising equation A.12 by applying the variation principle gives rise to the Hartree-Fock equations, which are a pseudo-eigenvalue problem:

$$\hat{f}_i \chi_i = \epsilon_i \chi_i \quad (\text{A.17})$$

where χ_i represents a molecular orbital of the system, and ϵ_i is the energy associated with that molecular orbital. The Hartree-Fock equations must be solved iteratively to obtain the molecular orbitals of the system, and hence the total wave function for the system. Once the orbitals have been found the energy for the system can be calculated. The iterative approach used is known as the self-consistent field (SCF) procedure. The output from the n^{th} iteration is used as the input $(n+1)^{\text{th}}$ iteration, until the difference between energies calculated between successive iterations is less than a convergence value, at which point the solutions are judged to be self-consistent. Once the SCF orbitals have been found, it is possible to calculate the total energy of the system by considering the total electronic energy, as defined by equation A.12, and adding the energy contribution from the nuclei:

$$E_{HF} = E_e + E_n \quad (\text{A.18})$$

Linear combination of atomic orbitals

Methods for solving the Hartree-Fock equations have been proposed by Roothaan [193] and Hall [194]. The solutions involve splitting the molecular orbitals, χ_i , into a set of known functions. This set of known functions is termed the ‘basis set’ and can be viewed as the atomic orbitals of the structure which are combined to give rise to a molecular orbital.

$$\chi_i = \sum_{m=1}^L c_{mi} \nu_m \quad (\text{A.19})$$

where each molecular orbital, χ_i , is constructed from a set of L basis functions (atomic orbitals), ν_m . Substituting equation A.19 into the Hartree-Fock equations results in the solutions being tractable in terms of a set of matrix equations known as the Roothan-Hall equations. The parameters of the basis functions can be altered in order to minimise the energy of the system. Solutions to systems which are found by this type of method are known as Hartree-Fock solutions of the system.

Any type of basis function may in principle be used to produce the orbitals for a system. However, they should have a physical significance to the problem, i.e. the atomic orbital should be centred on the nuclei, and the function should go to zero as the distance from the nuclei becomes large. There is also a computational issue to be considered, for isolated atoms the orbitals are well described

by exponential functions, but such functions are ‘computationally expensive’ and in general Gaussian functions are preferred. A discussion of the different types of basis sets is given towards the end of the DFT section of this appendix.

A.1.2 Limitations of the Hartree-Fock technique

The Hartree-Fock technique has several limitations, most notably its inability to cope with the interactions between electrons. This reliance on using single, non-interacting, wave functions to describe the electrons means that the technique is entirely non-relativistic. The effects of spin may be added ad hoc by enforcing electrons to pair up as opposite spin systems, described by a single wave function. This enforced pairing is known as restricted Hartree-Fock (RHF). If this restriction is not stated, unrestricted Hartree-Fock (UHF), then a separate spatial wave function must be used to describe each electron. UHF has the effect of allowing spin paired electrons to become spatially separate and artificially lower the energy of the system. A by-product of using the UHF method is that the system may exhibit ‘spin contamination’ whereby the calculated electronic ground state is actually a mix of excited states which can lead to discrepancy between predicted and observed molecular structures. For this reason systems with many electrons, for example heavy atoms, are not well suited to be investigated by HF methods.

Hartree-Fock theory relies on the construction of the wave function from a single Slater determinant. However, a single Slater determinant is only an exact description of the wave function for a system of N non-interacting electrons. As all the electrons within the system are treated as non-interacting, there is no correlation between them, resulting in the overestimation of the repulsive coulomb interactions. It is possible to attempt to overcome this problem by mixing Slater determinants, but the mixing itself is not a simple linear combination.

The difference between the true ground state energy of a system and the Hartree-Fock calculated energy is termed the ‘correlation energy’, E_{corr}^{HF} , of the system:

$$E_{corr}^{HF} = E - E_{HF} \quad (\text{A.20})$$

DFT offers an alternative approach to solving the Schrodinger equation by considering the density of an electron gas instead of a wave function. Amongst the benefits offered by DFT is a more thorough treatment of the correlation interaction.

A.2 Density functional theory

Instead of using orbitals to model electron position, DFT uses an electron density to model the distribution of charge within the system under study. This allows the complicated N electron wave function, Ψ , to be replaced with a much simpler

electron density $\rho(\mathbf{r})$. Integrating the electron density over all space should return the total number of electrons within the system:

$$\int \rho(\mathbf{r}) d\mathbf{r} = N \quad (\text{A.21})$$

Modern DFT owes its origins to work by Thomas and Fermi [195] who described electrons as a gas, and showed a relationship between the total kinetic energy of an electron gas and the density of the electron gas. This was one of the first attempts at using density functionals to obtain information about the electronic properties of a system. DFT in its current form is based on the proofs by Hohenberg and Kohn [196] that show there exists an exact energy functional, $E[\rho]$ and that an exact variation principle which may be applied to this functional. The electron density, $\rho(\mathbf{r})$, may be used to determine the electronic properties of the system. That is to say that knowledge of the exact function describing the electron density will allow the calculation of, amongst other things, the ground state energy of the system.

$$E_0 = E[\rho_0(\mathbf{r})] \quad (\text{A.22})$$

Any trial density used will give an energy for the system which is greater than or equal to that of the ground state energy.

$$E_0 \leq E[\rho_{\text{trial}}(\mathbf{r})] \quad (\text{A.23})$$

By minimising equation A.23 a value for the ground state energy of a system can be estimated. By analogy with the Hamiltonian description of the electronic energy of a system the energy functional in DFT may be expressed in terms of the following:

$$E[\rho] = T[\rho] + V_{ne}[\rho] + V_{ee}[\rho] \quad (\text{A.24})$$

where $T[\rho]$ is the kinetic energy of the system and $V_{ne}[\rho]$ is the potential energy of the electron gas as determined by the effect of the nuclear field. The $V_{ee}[\rho]$ term describes the potential energy due to the interaction between electrons. The $V_{ne}[\rho]$ term is system dependant, and can be solved by the Hartree-Fock method described previously. The other two terms require no knowledge about the system and may be universally defined. Unfortunately, the exact form of $T[\rho]$ and $V_{ee}[\rho]$ are unknown. Early methods used to solve the above equation relied on treating the electron-electron potential simply as the coulomb interaction and by expressing the kinetic term by considering an idealised uniform non-interacting electron gas. These methods were unsuccessful as they produced results that predicted no bonding between atoms.

This problem was overcome by Kohn and Sham [197] who split the kinetic energy term into two parts:

$$T[\rho] = T_{ks}[\rho] + (T[\rho] - T_{ks}[\rho]) \quad (\text{A.25})$$

The term $T_{ks}[\rho]$ represents the kinetic energy of a fictitious non-interacting N particle system, and the term in parentheses represents the error due to the interaction between electrons in the real system. This is similar to the approach explained previously in the HF method, with the ground state wave function for this system being described by a single Slater determinant. Instead of the spin-orbitals used for the Slater determinant of the Hatree-Fock method, the orbitals used are Kohn-Sham (KS) orbitals. It is interesting to note that the KS orbitals do not correspond to atomic orbitals, unlike the spin-orbit orbitals, and their actual physical significance is under debate. The KS orbitals, ϕ_i , that form the Slater determinant for this system should reproduce the real electron density:

$$\rho(\mathbf{r}) = \sum_i^N |\phi_i|^2 \quad (\text{A.26})$$

By following the procedure for obtaining the Fock operator, a KS operator can be constructed and the kinetic energy of this system obtained by solving the Schroedinger equation:

$$T_{ks} = -\frac{1}{2} \sum_i^N \int \phi_i^*(r) \nabla^2 \phi_i(r) dr \quad (\text{A.27})$$

It is possible to apply a similar approach in order to split the electron-electron interaction into two separate terms:

$$V_{ee}[\rho] = V_{ks}[\rho] + (V_{ee}[\rho] - V_{ks}[\rho]) \quad (\text{A.28})$$

In this case the exactly solvable term is the $V_{ks}[\rho]$ functional which is identical to the Coulomb-Coulomb interaction considered within the HF method. Again, the term in parentheses represents the error associated with assuming only the classical Coulomb interaction.

The errors caused by assuming a non interacting electron gas and using the coulomb-coulomb interaction to represent the electrostatic potential between electrons are combined into a new term; the exchange correlation function (XC). This function in effect describes the exchange energy of electrons, the correlation energy, and incorporates a kinetic correction. The expression for the energy of the system in terms of the density functionals now becomes:

$$E[\rho] = T_{ks}[\rho] + V_{ne}[\rho] + V_{ks}[\rho] + E_{xc}[\rho] \quad (\text{A.29})$$

The only term not explicitly defined within equation A.29 is the form of the XC, all other terms have previously been formulated explicitly for use in HF theory. The total energy of the system can therefore be expressed as [190]:

$$E[\rho] = -\frac{1}{2} \sum_i \int \phi_i^*(r) \nabla^2 \phi_i(r) dr - \sum_a \int \frac{Z_a \rho(r)}{|R_a - r|} dr + \frac{1}{2} \iint \frac{\rho(r) \rho(r')}{|r - r'|} dr dr' + E_{xc}[\rho] \quad (\text{A.30})$$

Analogous to the HF method we can express the above equation as a Hamiltonian operator acting on the set of Kohn-Sham orbitals, ϕ_i , and it is solvable via a SCF approach as an expansion of these orbitals in terms of a basis set.

Approximate forms of the exchange correlation term

As stated above the only thing missing from our description of the energy of the system is an explicit form of the XC functional. As a general form it may be written as [192]:

$$E_{xc} = \int \rho(r) \epsilon_{xc}[\rho, r] dr \quad (\text{A.31})$$

where ϵ_{xc} is dependant on the form of $\rho(r)$ at all points in space. However, its exact form is not known so an approximation must be suggested. One of the most commonly used forms of the XC is the ‘local density approximation’ (LDA) [198]. The form of the LDA is only dependant on the value of the electron density at each point, r , within the system being studied. This particular function is good for calculations containing systems with slowly varying electron density, but does not accurately describe systems containing molecular species where this is not the case.

$$E_{xc,LDA} = \int \rho(r) \epsilon_{xc}(\rho(r)) dr \quad (\text{A.32})$$

In order to give a more accurate description of XC the gradient of the electronic density may be incorporated into the XC functional. This is the generalised gradient approach (GGA) [199]:

$$E_{xc,GGA} = \int \rho(r) \epsilon_{xc}(\rho(r), \nabla \rho(r), \dots) dr \quad (\text{A.33})$$

For the work reported on here, the Perdew-Burke-Ernzerhof (PBE) functional is used as the form for the XC functional, as it has been shown to accurately model the interactions of a hydrogen bonded system [200].

A.2.1 Basis sets

As discussed previously, both the solutions to the Hatree-Fock and Kohn-Sham equations can be broken down into a set of functions which describe the wave function or density of the system. These functions each represent the molecular orbitals for the system and each of these molecular orbitals is constructed from a set of basis functions representing the atomic orbitals of the system. There are two

main types of basis functions known as Slater type orbitals (STO) and Gaussian type orbitals (GTO). STO [201] have the functional form:

$$\chi_{\zeta,n,l,m}(\mathbf{r}, \theta, \phi) = NY_{l,m}(\theta, \phi)\mathbf{r}^{n-1}e^{-\zeta r} \quad (\text{A.34})$$

where N is a normalisation constant, $Y_{l,m}$ is a spherical harmonic, n , l , and m are the quantum numbers for the atomic orbital, and the final two terms describe how the function falls to zero with increasing distance from the centre of the atom. The STO give a good agreement with the atomic orbitals of hydrogen and are therefore physically realistic. The exponential term is difficult to integrate analytically and for this reason GTO basis sets are more commonly used, as it has been shown that they may be integrated analytically [202].

The most accurate solutions are those which contain the largest number of basis functions. However, there needs to be a compromise between accuracy and speed of calculation. For this reason it is desirable to use the smallest possible number of functions that realistically model the system under study.

The smallest basis set that may be used to describe all of the electrons in a system is known as a minimal (MIN) basis set. In this basis set, only enough functions are included to describe each filled orbital, so for H and He only a single s-orbital is required. The STO-3G basis set is such an example where each atomic orbital that may contain two electrons (s , p_x , p_y , p_z , pd_{xy} , d_{xz} , d_{yz} , ...) is described by a single basis function: With each basis function consisting of a linear combination of three Gaussian peaks, hence 3G. The Gaussian peaks are chosen so that they fit a STO, allowing a physically realistic model of the orbital to be constructed from simple functions. For example, a neon atom described using the STO-3G basis set requires 5 basis functions ($1s$, $2s$, $2p_x$, $2p_y$, and $2p_z$ orbitals). As all of the orbitals constructed have a spherical symmetry, and all of the orbitals are centred on the nucleus, the STO-3G basis set is unable to describe non spherical systems, or systems with a delocalised charge distribution.

The MIN basis set can be improved by including additional orbitals, simply by doubling all the basis functions. Such an approach leads to a double zeta (DZ) basis set, which allows a description of π bonds [190], but may lead to over specifying the number of orbitals required to describe the system. For this reason split valence basis sets are used where only the valence orbitals are doubled. Split valence basis sets, such as 3-21G, address the problem imposed by MIN basis sets of only being able to describe systems with a spherical symmetry. The basis sets are labelled as C-V₁V₂ ... V_NG where C is the number of Gaussian peaks used to model the core levels (as described previously) and the valence orbitals are described by N basis functions, each of which consist of V_{*i*} Gaussian peaks. This allows orbitals with a non spherical symmetry to be described, such as π and δ bonding orbitals. Using the neon atom as an example, basis functions are required for $1s$, $2s$, $2s'$, $2p_{x,y,z}$ and $2p'_{x,y,z}$ orbitals. Therefore there are 9 basis functions in total.

In order to include the directionality of bonds, polarised basis sets are used. The H atom only formally contains s-orbitals but any hydrogen-bonding interactions will be directional, for this reason higher angular momentum p-orbitals are used. Similarly heavier elements, such as carbon, are modelled with d-orbitals to include polarisation. Polarised basis sets offer a way of accounting for the non-nucleocentric distribution of electrons. This is achieved by expressing the orbitals as an expansion, allowing s type orbitals to contain some p character and p type orbitals to contain some d character. Singularly polarised basis sets (such as 6-31G*) included polarised functions for p orbitals whereas doubly polarised basis sets (6-31G**) contain polarised functions for both s and p orbitals.

A.2.2 Limitations of DFT

Although DFT theory offers a better treatment of electron interaction than the HF method, it is not without its limitations. The Kohn-Sham orbitals are not molecular orbitals and their exact physical significance is uncertain. This makes the calculation of ionisation energies and electron affinities based on the calculated KS orbitals difficult and any results should be considered carefully.

One of the biggest drawbacks of DFT is its inability to calculate vdW interactions between atoms. Within the context of molecular self-assembly studied in this work, the vdW forces appear to play a significant role and it is a great failing that such forces are not accounted for in DFT.

A.3 Implementation of DFT

The DFT calculations conducted as part of this thesis used the DMol³ module within the Accelrys Materials Studio suite (v 4.x). The following section describes the choices made for the calculations performed and how the parameters chosen relate to the underlying theory.

Geometry optimisation

The lowest energy configuration for molecules and clusters of molecules are calculated by a 'geometry optimisation' procedure. The position of the atoms within the molecules are allowed to relax to reduce the total energy of the system. At each iteration of the geometry optimisation the potential gradient at each atomic position is determined and the atom is moved so as to minimise the potential. Within Dmol³ a mixture of 'steepest descent', 'conjugate gradient', and 'Newton-Raphson' methods are used to determine the energy minimum from the system under study.

The steepest descent algorithm is relatively simple and allows the system to quickly move towards an energy minimum by finding the 'downhill' direction of

| Value | Coarse | Medium | Fine |
|---|--------------------|--------------------|--------------------|
| Energy (Hartree) | 1×10^{-4} | 2×10^{-5} | 1×10^{-5} |
| Max. force (Hartree \AA^{-1}) | 0.02 | 0.004 | 0.002 |
| Max. displacement (\AA) | 0.05 | 0.005 | 0.005 |

Table A.1: Table showing the convergence tolerance parameters for a Dmol³ geometry optimisation calculation.

the potential gradient, and moving along that direction until the gradient starts to increase [203]. Unfortunately, the steepest descent algorithm does not converge quickly on the energy minimum for the system so the conjugate gradient [204], and Newton-Raphson methods are used once the system is close to the energy minimum.

The convergence tolerance for these calculations can be specified. Each iteration of the geometry optimisation search will bring the structure closer to an energy minima. When the energy difference of the structures between two successive iterations is less than the convergence tolerance, the structure is deemed to have been minimised. Within Dmol³, options are given for Coarse, Medium, and Fine optimisations, shown in table A.1, with the tolerance being specified in terms of the total energy of the system, the maximum force, and the the maximum displacement. The maximum step size may also be set, which defines the maximum distance an individual atom may be moved during an iteration, prohibiting the production of non-physical structures.

Exchange-correlation functional

The type of exchange-correlation potential to be used in the calculation may be specified, using either a GGA or LDA approach. A wide range of functionals may be chosen from, but for the purposes of this work the PBE [205] functional is used.

Treatment of spin

The treatment of the electron spin for the calculations can be performed as ‘spin restricted’ or ‘spin unrestricted’. In spin unrestricted calculations, different orbitals are used to describe the alpha and beta electron spins. The initial pairing of electrons is determined by the formal spin of the molecule.

Self consistent field parameters

As many integrals which need to be calculated as part of the DFT routine cannot be solved analytically, a numerical approach has to be implemented whereby the integrals are evaluated over a grid of points. Dmol³ allows Coarse, Medium and Fine, options to specify the integration accuracy. It has been shown [206] that the

Medium integration accuracy, using a grid of ~ 1000 points is sufficient for most systems.

In order to speed up the SCF convergence, mixing of the charge density and spin density from the previous SCF iteration may be used. A percentage of the previous density is used as a basis for the next iteration. For the calculations conducted as part of this thesis, density mixing of charge 2% and spin 50% were used. The direct inversion in the iterative subspace (DIIS) [207] method is also used to increase the speed at which the SCF converges by estimating an ‘error’ for the density function, and then extrapolating to minimise this ‘error’. This allows the next suggested density functional to be closer to the actual ground state density without having to perform a full SCF iteration between each guess at the density [190].

Basis sets

The basis sets used in Dmol³ are generated numerically, with each function corresponding to an atomic orbital, instead of Gaussian orbitals. The basis functions are given numerically on an atom-centralized spherical-polar mesh. The function consists of a spherical harmonic term and a radial term:

$$\sigma_{basis} = \gamma(\theta, \phi)F(\mathbf{r}) \quad (\text{A.35})$$

The basis sets are confined by a numerical cut-off radius, \mathbf{r}_c , which defines the distance from the centre of an atom at which the density function should go to zero. Dmol³ specifies cut-off values for each element in the periodic table. In this work we use a cut-off distance of 3.7Å which is found to give energies consistent with previous DFT calculations performed on the systems under study, more detail on this is given in appendix B.

A range of basis sets are available for use within Dmol³ ranging from MIN numerical basis sets to doubly polarised numerical (DNP) basis sets. The DNP basis set (used within this work) contains valence orbitals and includes additional polarised d-functions on all non-hydrogen atoms, and polarised p-functions on all hydrogen atoms. This polarisation is especially important for modelling the directional hydrogen-bonding interactions which are studied as part of Chapter 4. DNP is similar to the 6-31G** basis set, but due to the fact the atomic orbitals are physically realistic, they should give rise to more accurate results than a Gaussian basis set [206].

The core-orbitals of atoms may be represented as semi-core pseudo-potentials or effective core potentials. These options treat the core electrons as a simple potential, increasing the speed of the calculation at the cost of its accuracy. For this work an ‘all electron’ approach is taken where all the electrons are treated in the same manner. This is a non-relativistic treatment and as such does not account for the additional shielding effect of the electrons in the core levels of the

atoms.

Orbital calculations

In order to interpret the STM images studied in Chapter 4, the HOMO and LUMO of a molecule can be calculated using DFT. This is simply implemented by taking the molecular orbital corresponding to the highest energy filled state and the lowest energy empty state as calculated using the SCF iterations. A visual representation of the position of the HOMO and the LUMO relative to the chemical structure of the molecule is produced.

A.4 Molecular mechanics simulations

A.4.1 Introduction to molecular mechanics

MM is able to model the structures and estimate the energies of molecular species which are too large to be handled by a DFT approach. Unlike DFT, which calculates the energy of a system from the electron distribution, MM type simulations use a parameterised set of functions which describe the energy of a system in terms of the positions of the atomic nuclei. The parameters for these functions are either obtained empirically or from a higher level of computational theory (such as DFT). In the simplest terms, a MM simulation models a molecule as a set of spheres corresponding to the position of the atoms, and a set of springs which join the chemically bonded atoms together. The parameters in a MM simulation describe the properties of the spheres (e.g. size and mass) and springs (e.g. stiffness and length).

The basis of the MM approach is the observation that different molecules are composed of structurally similar chemical groups. As an example, all C-H bond lengths found in molecules are measured to be between 1.06Å and 1.10Å [190]. The C-H stretch vibration is also observed to have approximately the same value irrespective of the molecular species. These findings imply that the force constants for the bond are always comparable, irrespective of the molecule to which the functional group is attached.

This reductionist interpretation of a molecule can be continued by defining each atom in terms of the functional group that it is part of, as well as its neighbouring atoms. The description of each atom is termed its 'atom type' and allows us to define the properties of an atom in terms of its atomic number and the type of chemical bonding in which it participates. This method allows every chemically distinct atom to be given its own set of parameters, defining its interaction with the neighbouring atoms. Therefore a sp^2 hybridised carbon has a different 'atom type' to a sp^3 hybridised carbon, and an oxygen in an aldehyde group is given a different type to an oxygen in an alcohol group. As the forces between the

atoms are defined by the ‘atom type’, the list of atom types and parameters is often known as the ‘Forcefield’ (FF), with MM simulations often referred to as FF methods.

A.4.2 The Forcefield energy

The energy obtained from a MM simulation is obtained using the FF to describe the interaction between the atoms, and hence is referred to as the Forcefield energy, E_{FF} . This energy may be written as a sum of terms, each one describing a particular interaction.

$$E_{FF} = E_{str} + E_{bend} + E_{tors} + E_{cross} + E_{vdW} + E_{el} \quad (\text{A.36})$$

where E_{str} is the energy function describing the stretching interaction between two chemically bonded atoms, E_{bend} the energy required to alter the angle between three bonded atoms, and E_{tors} the torsional energy involved in rotating around a bond. E_{cross} represents the coupling between the first three terms, and together the first four terms represent the ‘bonded’ interactions between the atoms within the molecule. The final two terms describe the ‘non-bonded’ interactions between the atoms, with E_{vdW} used to represent the vdW interactions, and E_{el} representing the attractive and repulsive electrostatic interactions. A detailed discussion of these forces is given in reference [190], with a summary presented below.

The stretch energy

The stretch energy function is based on the distance between two atoms, A and B . The bond can be thought of as a spring with a force constant K^{AB} , holding the two atoms at an equilibrium separation of R_0^{AB} apart. If the two atoms are moved to a separation of R^{AB} so as to stretch or compress the spring, the energy of the system will be given by:

$$E_{str}(R^{AB} - R_0^{AB}) = K^{AB}(R^{AB} - R_0^{AB})^2 \quad (\text{A.37})$$

This is the form of the harmonic oscillator potential, where the potential is a quadratic function of the displacement from the minima. The harmonic form is the simplest possible description but is sufficient for most equilibrium geometries.

The bending energy

The bending energy is defined as the energy required to produce an angle θ formed by three atoms $A - B - C$, where A and B , and, B and C are bonded together. In the same way as the stretch energy, the bending energy function is written in terms of a departure from an equilibrium angle, θ^{ABC} .

$$E_{bend}(\theta^{ABC} - \theta_0^{ABC}) = K^{ABC}(\theta^{ABC} - \theta_0^{ABC})^2 \quad (\text{A.38})$$

The torsional energy

The torsional energy is the energy required to rotate around the B-C bond in a chain of four bonded atoms, A-B-C-D. Looking along the axis of the B-C bond, the angle between the axes of the A-B and C-D bonds is defined as ω . The torsional energy function takes the form:

$$E_{tors}(\omega) = \sum_{n=1} V_n \cos(n\omega) \quad (\text{A.39})$$

The energy function is periodic in terms of ω as the bond may rotate through 360° and return to the same position, and should therefore have the same energy value at the start and end of the rotation. The $n = 1$ term defines a period of 360° , $n=2$ has a period of 180° , and so on as $360^\circ/n$. This periodicity allows a wide range of bonds with varying rotational freedoms to be modelled.

The cross term energy

The cross term energy incorporates the coupling between the stretching, bending, and torsional energies. The coupling terms represent the fact that it is experimentally observed that altering the bond angle for three bonded atoms, *A-B-C*, will result in a change in the optimum bond separations for *A-B* and *A-C*. Such effects are accounted for by including energy functions of the form:

$$E_{str/bend} = K^{ABC} (\theta^{ABC} - \theta_0^{ABC}) [(R^{AB} - R_0^{AB}) + (R^{BC} - R_0^{BC})] \quad (\text{A.40})$$

Other cross terms considered include stretch/stretch, stretch/torsional, bend/bend, and bend/torsional/bend. The more cross terms included as part of the FF, the more accurate the representation of the physical system being studied.

The van der Waals energy

The E_{vdW} and E_{el} terms contain information about the non-bonding interactions between atoms in the MM simulation. The vdW energy can be considered as the non-bonding energy which arises from non-electrostatic interactions. The vdW interaction is often modelled using a Lennard-Jones potential:

$$E_{vdW}(R) = \epsilon \left[\left(\frac{R_0}{R} \right)^{12} - 2 \left(\frac{R_0}{R} \right)^6 \right] \quad (\text{A.41})$$

where R_0 is the equilibrium separation of the atoms and ϵ is the depth of the energy minimum. The second term in parentheses represents the attractive dipole-dipole (and higher terms) interactions, which is observed to fall as R^{-6} for large separations. The first term in parentheses is repulsive and arises from the Pauli repulsion between electrons and cannot be completely determined from first principles. The

form of this term must be physically realistic and as such is required to go to zero for large R and should go to infinity as R approaches zero. Other models for the repulsive part of the potential replace the R^{-12} term with an exponential to give the Hill potential [208]. However, as the exponential term is ‘computationally expensive’ the majority of FF use the form given in equation A.41.

The electrostatic energy

The electrostatic energy is given by evaluating the coulomb potential over each pair of atoms in the system:

$$E_{el}(R^{AB}) = \frac{Q^A Q^B}{\epsilon R^{AB}} \quad (\text{A.42})$$

The charge on the atoms (Q^A and Q^B) is either defined within the FF parameters, or obtained from a calculation of the electrostatic potential across the molecule using electronic structure methods such as Qeq [209]. As the Coulomb interaction is evaluated over pairs of atoms, many-body effects such as screening are not included. To counter this effect the dielectric constant, ϵ , may be made distance dependant in order to reduce the interaction for larger separations.

A.4.3 Forcefield parametrisation - the Universal Forcefield

The two key factors which determine the accuracy of a FF are the functional forms used to model the energy contributions and the parameters used for these functions. The parameters may be obtained from experimental data, or from higher level computational theory, but in all cases the parameters chosen will be selected to accurately model a specific set of chemical groups. Unfortunately, this means that more ‘exotic’ molecules, which have been less well studied will not have had many of their atomic interactions parameterised.

In an effort to overcome this problem the Universal Forcefield (UFF) [210] was developed by Rappe et al. The UFF derives parameters for the functional forms of the energy terms from atomic constants such as atomic radii and ionisation potentials. This FF enables parameters to be obtained for all structures containing any combination of elements from the periodic table. Due to the complex nature of many of the molecules studied within this thesis, the UFF has been used to ensure that parameters are available for all atomic interactions. In order to confirm the results obtained from such parameters are physically realistic, care must be taken to compare the results obtained from the UFF method with experimental data.

A.4.4 Advantages and limitations of MM methods

The main advantage of MM methods is that they are quick to perform and can be used to model systems which contain large numbers of atoms. Calculations

containing several large molecules and a substrate would contain too many atoms to be handled by a DFT approach, but the use of MM allows the energetics of such systems to be investigated. With the introduction of the UFF, MM calculations can be performed for any structure and allows the study of new ‘exotic’ molecules.

The main limitation of MM is the difficulty involved in obtaining parameters which are an accurate representation of the physical properties of a system. Some of these problems are overcome by the use of other computational techniques to obtain the desired parameters, or by the use of the UFF to predict parameters. Ultimately the accuracy of the simulation can only be judged by comparison with experimental data for the same system that the simulation is trying to model.

A.5 Molecular dynamics simulations

In the previous sections of this appendix the methodologies for obtaining the energy of a given system have been discussed. DFT and MM approaches both calculate the energy of a system given an initial set of atomic co-ordinates, with the minimum energy state for the system being obtained by allowing the structure to relax (geometry optimisation calculation). For relatively simple systems the geometry optimisation calculation should result in the lowest energy structure of the system being obtained. For more complex systems this approach is likely to yield a local energy minima and not the global minimum. One way to solve this problem would be to manually set-up a range of starting geometries and see which produces the lowest energy state. Such a method would be time consuming and many of the initial structures may prove to be physically unrealistic.

MD simulations allow the evolution of a system in time to be modelled, with only physically realistic geometries being formed. From this set of initial geometries for the system the energy minima may be obtained, allowing the potential energy surface of the system to be explored. MD simulations solve the Newtonian laws of motion to describe the evolution of a system by calculating the forces acting on the atoms within the molecule. These forces can be calculated directly from the derivative of the potential energy at the location of a given atom.

A.5.1 Phase space and trajectories

A classical system can be defined by specifying the positions and momenta of all the particles within that system [191]. For a system containing N particles in three-dimensional space, any system can be described by $6N$ co-ordinates.

$$\mathbf{X} = (\mathbf{x}_1, \mathbf{y}_1, \mathbf{z}_1, \mathbf{p}_{x1}, \mathbf{p}_{y1}, \mathbf{p}_{z1}, \mathbf{x}_2, \mathbf{y}_2, \mathbf{z}_2, \mathbf{p}_{x2}, \mathbf{p}_{y2}, \mathbf{p}_{z2}, \dots) \quad (\text{A.43})$$

These co-ordinates may be split into two separate vectors, one describing position, \mathbf{q} , and one describing momentum, \mathbf{p} .

$$\mathbf{q} = (\mathbf{x}_1, \mathbf{y}_1, \mathbf{x}_1, \mathbf{x}_2, \mathbf{y}_2, \mathbf{z}_2, \dots) \quad (\text{A.44})$$

$$\mathbf{p} = (\mathbf{p}_{x1}, \mathbf{p}_{y1}, \mathbf{p}_{z1}, \mathbf{p}_{x2}, \mathbf{p}_{y2}, \mathbf{p}_{z2}, \dots) \quad (\text{A.45})$$

$$\mathbf{X} = (\mathbf{p}, \mathbf{q}) \quad (\text{A.46})$$

From these co-ordinates a phase space point, \mathbf{X} , may be defined. As a system evolves over time, the phase space points will trace out a unique trajectory in phase space. Assuming that no outside forces act on the system, knowledge of one phase point allows the ‘next’ phase point to be calculated using the Newtonian laws of motion. As long as the initial structure is physically realistic, all of the phase points along this trajectory will correspond to real possibilities for the geometric positions of the atoms within the system.

For a system with a set of atomic positions \mathbf{q} at time t_1 , the atomic positions at a time t_2 is given by:

$$\mathbf{q}(t_2) = \mathbf{q}(t_1) + \int_{t_1}^{t_2} \frac{\mathbf{p}(t)}{m} dt \quad (\text{A.47})$$

where $\frac{\mathbf{p}(t)}{m}$ is the velocity of an atom. The relationship between the momenta, \mathbf{p} , at times t_1 and t_2 is given by:

$$\mathbf{p}(t_2) = \mathbf{p}(t_1) + m \int_{t_1}^{t_2} \mathbf{a}(t) dt \quad (\text{A.48})$$

$$\mathbf{a} = \frac{\mathbf{F}}{m} \quad (\text{A.49})$$

With \mathbf{a} being the acceleration as defined by Newton’s 2nd law. The force on an atom can be obtained directly from the derivative of the potential energy with respect to the atomic co-ordinates (as shown in equation A.50).

$$-\frac{\delta V}{\delta \mathbf{q}} = m\mathbf{a} \quad (\text{A.50})$$

This potential energy can be calculated from a MM simulation. For certain systems, such as a simple harmonic oscillator, it is possible to solve equations A.47 and A.48 analytically. In general, the majority of systems cannot be solved analytically and an approximation is required. In the limit where $\Delta t \rightarrow 0$ equations A.47 and A.48 may be modelled using Euler’s approximation as:

$$\mathbf{q}(t + \Delta t) = \mathbf{q}(t) + \frac{\mathbf{p}(t)}{m} \Delta t \quad (\text{A.51})$$

$$\mathbf{p}(t + \Delta t) = \mathbf{p}(t) + m\mathbf{a}(t)\Delta t \quad (\text{A.52})$$

Hence, for any system for which we can calculate the potential, it is possible to simulate its trajectory in phase space, providing that we have a physically realistic

set of initial conditions, and that the time step, Δt , is small. The initial positions of the system may be obtained from a geometry optimisation MM calculation and with the initial momenta of the atoms being assigned randomly using the following relationship between temperature and momentum [191]:

$$\mathbf{T}(t) = \frac{1}{(3N - n)k_B} + \sum_{i=1}^N \frac{|\mathbf{p}_i(t)|^2}{m_i} \quad (\text{A.53})$$

where N is the total number of atoms in the system and n is the number of constrained degrees of freedom. With the momenta being defined relative to the motion of the centre of mass for the whole system.

In reality, Euler’s approximation for solving the equations of motion of the system is unstable, and does not accurately recreate the trajectory of a system for reasonable values of Δt . Therefore a range of ‘integrators’ have been developed, most of which are based on the Verlet algorithm for integrating the equations of motion [211] (the MD simulations performed as part of this work use the Verlet velocity integrator).

A.5.2 Ensembles

Newton’s equations of motion describe the microcanonical ensemble (also known as the NVE ensemble) where the number of particles, the volume of the system, and the total energy of the system are kept constant. The NVE ensemble is generally not an accurate description of real experimental conditions where the system is allowed to exchange heat with the surrounding environment. For such systems the constant number of particles, constant volume, constant temperature (NVT) ensemble is more appropriate. The temperature can be kept constant by simulating the interaction of the system with a heat bath. A treatment of the system using the NVT ensemble can be calculated using Nosé-Hoover dynamics [212].

A.6 Implementation of MM and MD

The MM and MD simulations conducted as part of this thesis used the Forcite module within the Accelrys Materials Studio suite (v 4.x). The choices made for the calculations which have been performed, and how the parameters chosen relate to the underlying theory, is discussed in the following section.

A.6.1 MM calculation options

Geometry optimisation

The lowest energy configurations of molecules and molecular structures are calculated by a geometry optimisation procedure identical to that described for the DFT calculations. Within Forcite, a ‘smart’ algorithm is used which implements

| Value | Coarse | Medium | Fine | Ultra-Fine |
|---|--------|--------|----------------------|----------------------|
| Energy (kcal mol ⁻¹) | 0.002 | 0.001 | 1 x 10 ⁻⁴ | 2 x 10 ⁻⁵ |
| Force (kcal mol ⁻¹ Å ⁻¹) | 2.5 | 0.5 | 0.002 | 0.001 |
| Stress (Gpa) | 2.5 | 0.5 | 0.002 | 0.001 |
| Displacement (Å) | 0.05 | 0.015 | 5 x 10 ⁻⁵ | 1 x 10 ⁻⁵ |

Table A.2: Convergence tolerance parameters for the Forcite geometry optimisation calculation.

a cascade of ‘steepest descent’, ‘conjugate gradient’, and ‘Newton-Raphson’ methods to determine an energy minimum from the system under study. The details of these methods have already been given in section A.3. The convergence tolerances available are shown in table A.2, and are defined in terms of a maximum energy change, maximum force, maximum stress, and maximum displacement between successive iterations of the geometry optimisation.

Forcefield

Several FFs are available to describe the bonding and non-bonding interactions within the system, such as UFF [210], COMPASS [213], and Dreiding [214]. The calculations reported on in this work were performed exclusively using the UFF as it allows for a full parametrisation of all the elements in the periodic table.

Charges

The charges on each atom within the system need to be accurately modelled in order to calculate the electrostatic interactions which contribute to the total energy of the system. Forcite allows the charges to be defined by the user, but some FFs (such as COMPASS) have the atomic charges parameterised within the FF. Within this work the Qeq [209] algorithm, which uses the concept of electronegativity to equalise the charge distribution over all the atoms within the system, is employed to calculate the atomic charges.

Non-bonded interactions

The non-bonded interaction between the atoms can be described by atom based, group based, or Ewald summation methods. The atom based method calculates the pairwise interactions between atoms within a set ‘cut-off’ distance, with the group based approach using a similar technique to calculate the interactions between functional groups. For periodic systems (such as those studied within this thesis) the Ewald summation [215] is a more appropriate description.

A ‘buffer width’ is also set which is used to determine when the list of non-bonded atoms should be re-evaluated. Normally to save time in the calculation, a list is created of all the non-bonded atoms, so the interaction between these atoms are calculated. When the separation between any pair of atoms changes

| Value | Coarse | Medium | Fine | Ultra-Fine |
|--|--------|--------|--------|------------|
| electrostatic/vdW cut-off distance (Å) | 9.5 | 12.5 | 15.5 | 18.5 |
| Ewald accuracy (kcal mol ⁻¹) | 0.01 | 0.001 | 0.0001 | 0.00001 |

Table A.3: Table showing how the Ewald accuracy for calculating the non-bonded contribution to MM energy is related to atomistic cut-off distance.

by at least half the buffer width, the non-bonded atom list is recalculated. For the vdW interactions a repulsive cut-off is specified to define a distance at which the repulsive vdW force between atoms is truncated.

A.6.2 MD calculation options

Ensemble selection

The Forcite MD simulation allows a choice of four different ensembles NVE, NVT, NPH, NPT (N=number of atoms, V=volume, E=total energy, P=pressure, and H=enthalpy) where in each ensemble three conditions are kept constant throughout the simulation. For the NVT ensemble MD calculations may apply the Nosé-Hoover [212] thermostat to keep the temperature constant. The calculations presented within this thesis use the NVE ensemble. The initial momenta of the atoms are defined at random from a temperature dependant Gaussian distribution (with the temperature being defined by the user).

Simulation time

The total simulation time, the length of each time step, and the number of time steps can be specified. As discussed previously a large time step may result in the atoms occupying physically unrealistic positions, to prevent this from occurring an ‘energy deviation’ tolerance may be specified to warn if the change in energy between steps in the MD simulation becomes too large.

Quench dynamics

The Forcite MD simulation allows a ‘quench’ calculation to be performed, where at intervals of a certain number of time steps the atomic co-ordinates of the structure can be used as starting points for geometry optimisation calculations. The local energy minima, and the global energy minimum, for the system can be explored using this technique.

Appendix B

Details of the DFT and MM simulations

This appendix contains the technical details of the DFT and MM calculations which have been discussed throughout this work. Here, the methodologies and parameters of the various calculations are presented.

B.1 DFT calculation details

Within the Nottingham Nanoscience group DFT computational studies have been used to investigate the binding energies (BEs) and structures of molecules involved in hydrogen-bonding interactions [106, 107]. Previous calculations were carried out using the SIESTA package [216, 217]. In this work the Materials studio suite, using the Dmol³ package [218], is used to model the hydrogen-bonding junctions between two or more molecules. In order to ensure that the results produced by the simulations are physically realistic, a series of tests were performed.

Methodology for choosing the DFT calculation parameters

Parameters taken from previous SIESTA calculations were used as a starting point. The cyanuric acid - melamine (CA·M) hydrogen-bond was investigated as experimentally obtained crystallographic data for the dimensions of this structure is available [13]. Figure B.1 (a) shows the structure of the CA·M junction. DFT calculations were performed on the CA·M molecules using the parameters shown in table B.1, with cut-off distances of 2.6 Å and 3.7 Å. The dimensions of the resultant geometry optimised structures were then compared to the crystallographic data (shown in table B.2).

The data shows that there is a good agreement between the crystallographic data and the results of the DFT calculations using a cut-off of 3.7 Å. In order to test the validity of the BEs predicted by DFT, a comparison was made between SIESTA and Dmol³ calculations looking at the PTCDI-PTCDI double hydrogen-

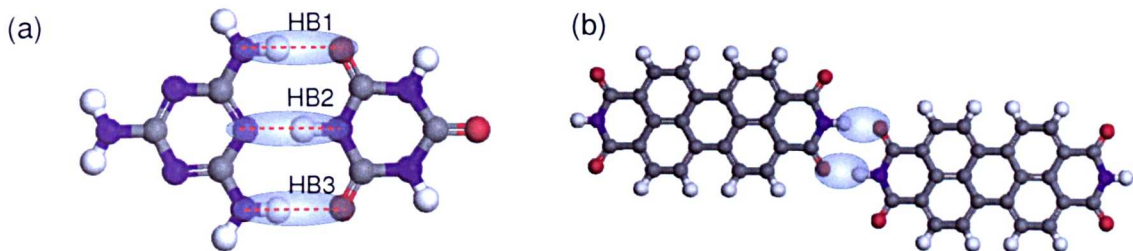


Figure B.1: (a) The cyanuric acid - melamine hydrogen-bonded junction. (b) PTCDI-PTCDI double hydrogen-bond.

| Parameters for DFT test calculations | | |
|--------------------------------------|--|---|
| Functional | GGA Spin Use formal spin as initial | PBE [205] Unrestricted |
| Convergence tolerance (custom) | Energy Max Force Max Displacement Max Iterations Max Step Size | 1×10^{-5} Ha 4×10^{-4} Ha/Å 0.005 Å 400 0.3 Å |
| Basis Set | DNP | |
| Core treatment | All electron relativistic | |
| SCF Tolerance (fine) | SCF Tolerance Max SCF cycles Multipolar expansion | 1×10^{-6} 500 octupole |
| Density Mixing | Charge Spin | 0.02 0.5 |
| Orbital Cut-off (custom) | Scheme Cut-off | Global 2.6/3.7 Å |
| Orbital Occupancy | Use smearing | No |

Table B.1: DFT parameters for the test calculations.

| Calculation/Data | HB1- Distance N-O (Å) | HB2- Distance N-N (Å) | HB3- Distance N-O (Å) |
|------------------|--------------------------|--------------------------|--------------------------|
| Crystallography | 2.94 | 2.85 | 2.98 |
| DFT : 2.6 Å | 2.85 | 2.70 | 2.85 |
| DFT : 3.7 Å | 2.92 | 2.79 | 2.93 |

Table B.2: Comparison of the crystallographic hydrogen-bond distances for the CA·M junction with DFT calculated distances.

| Calculation | Binding energy (eV) |
|-----------------------------------|---------------------|
| Dmol ³ : Cut-off 2.6 Å | 0.794 |
| Dmol ³ : Cut-off 3.7 Å | 0.493 |
| Dmol ³ : Cut-off 5.0 Å | 0.469 |
| SIESTA | 0.487 |

Table B.3: Calculated BEs for two PTCDI molecules in a double hydrogen-bond arrangement using different cut-off values.

bond interaction (shown in Figure B.1 (b)). Table B.3 shows the BEs between two PTCDI molecules calculated using cut-off values of 2.6 Å, 3.7 Å, and 5.0 Å. It can be seen that a value of 3.7 Å for the cut-off is congruent with the BE previously calculated using the SIESTA software.

| Final parameters for DFT calculations | | |
|---------------------------------------|--|---|
| Functional | GGA Spin Use formal spin as initial | PBE [205] Unrestricted |
| Convergence tolerance (Medium) | Energy Max Force Max Displacement Max Iterations Max Step Size | 2×10^{-5} Ha 4×10^{-3} Ha/Å 0.005 Å 500 0.3 Å |
| Basis Set | DNP | |
| Core treatment | All electron | |
| SCF Tolerance (Medium) | SCF Tolerance Max SCF cycles Multipolar expansion | 1×10^{-5} 500 octupole |
| Density Mixing | Charge Spin | 0.02 0.5 |
| Orbital Cut-off (Fine) | Scheme Cut-off | Global 3.7 Å |
| Orbital Occupancy | Use smearing | 0.005 Ha |

Table B.4: Final DFT parameters.

From these preliminary experiments it has been shown that the Dmol³ package accurately predicts the separation of the CA·M hydrogen-bonding interaction, and returns BEs in agreement with those previously calculated by the SIESTA program. From these parameters a change has been made to improve the speed of the calculation, with the treatment of the core electrons altered from a relativistic to a non-relativistic approach. This alteration was found to reduce the time required to perform the simulation while making negligible difference to the accuracy of the results in terms of the hydrogen-bond distance and the BE of the interaction.

The parameters shown in table B.4 were used for the calculations discussed within this thesis.

B.1.1 HOMO, LUMO, and energy DFT calculations for single molecules

The four molecules investigated by DFT within this thesis are melamine, PTCDI, Br₂PTCDI, and S₂PTCDI. The first calculation performed on this selection of molecules is a geometry minimisation to find the structural ground state of the isolated molecules in vacuum. From this calculation, the shape of the HOMO and LUMO may be obtained, and used to determine the appearance of a molecule in an STM image. Figure B.2 shows the HOMO and LUMO for the four molecules, as well as their total energy. The cores of the Br₂PTCDI and S₂PTCDI molecules were constrained to the Z plane so that they would lie flat, as is expected for molecules absorbed on a supporting substrate.

B.1.2 Homo-molecular binding interactions

The BEs for the homo-molecular interactions have been calculated. For melamine only one hydrogen-bonding junction between two molecules has been considered. For PTCDI, and its derivatives, a double hydrogen-bond between two molecules has been modelled, as well as a trimer junction involving three molecules. The BEs for the dimer and trimer junctions are shown in Figures B.3 and B.4 respectively. The *BE* of a hydrogen-bonded junction may be calculated using the following formula:

$$BE = E_{Tot} - (E_{M1} + E_{M2}) \quad (\text{B.1})$$

where E_{Tot} is the total energy of the system, and E_{M1} and E_{M2} are the energies of molecule 1 and molecule 2 in isolation.

B.1.3 Hetero-molecular interactions

The interactions between PTCDI, its derivatives (R₂PTCDI), and melamine have also been investigated. The BEs of these interactions are shown in Figure B.5. In addition to these structures, the BE of a melamine rich hydrogen-bonded vertex has been ascertained (Figure B.6).

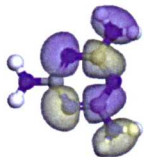
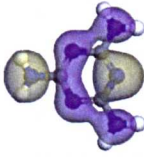
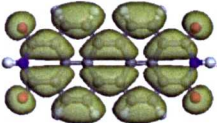
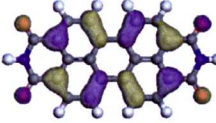
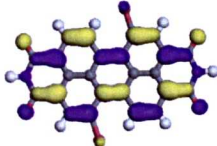
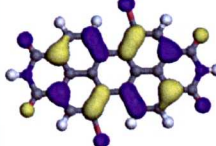
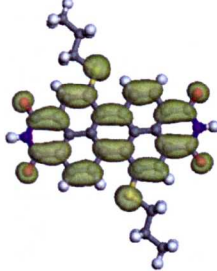
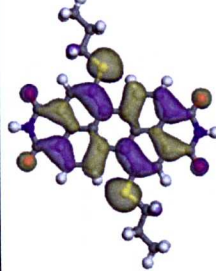
| Molecule | LUMO | HOMO | Energy (eV) |
|-----------------------|---|---|--------------|
| Melamine |  |  | -12140.99715 |
| PTCDI |  |  | -36192.49434 |
| Br ₂ PTCDI |  |  | -176234.0835 |
| S ₂ PTCDI |  |  | -64266.42685 |

Figure B.2: Table showing the LUMO, HOMO, and total energy for melamine, PTCDI, Br₂PTCDI, and S₂PTCDI.

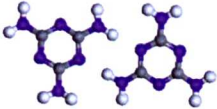
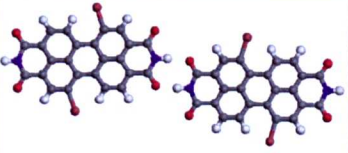
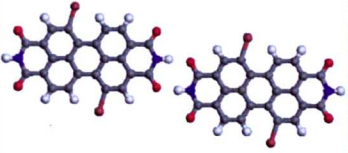
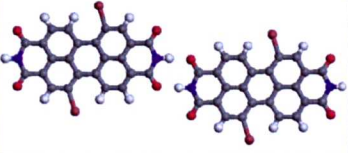
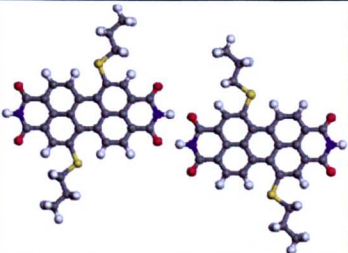
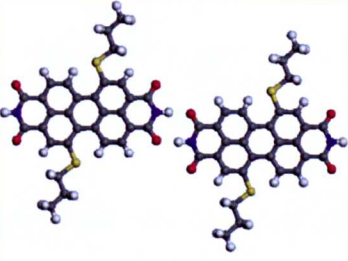
| Molecule | | Total Energy of System (eV) | Binding Energy (eV) |
|----------------------------|---|-----------------------------|---------------------|
| Melamine |  | -24282.5080 | -0.514 |
| PTCDI |  | -72385.46792 | -0.479 |
| Br ₂ PTCDI A |  | -352468.6441 | -0.477 |
| Br ₂ PTCDI B |  | -352468.6393 | -0.472 |
| Br ₂ PTCDI C |  | -352468.6412 | -0.474 |
| S ₂ PTCDI A |  | -128533.3351 | -0.481 |
| S ₂ PTCDI B |  | -128533.3413 | -0.488 |
| S ₂ PTCDI C |  | -128533.33306 | -0.477 |

Figure B.3: Dimer binding energies for homo-molecular pairs.

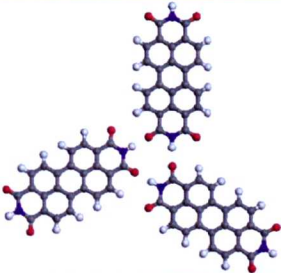
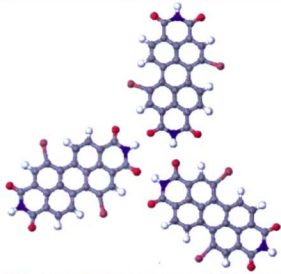
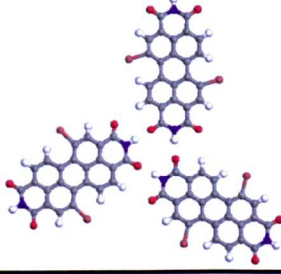
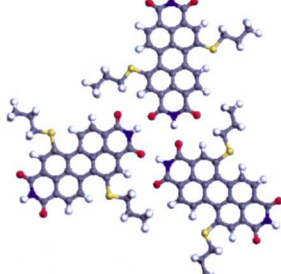
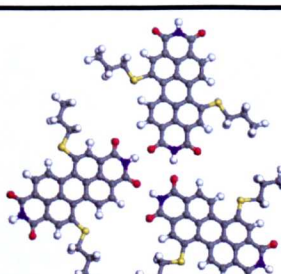
| Molecule | | Total Energy of System (eV) | Binding Energy (eV) |
|-------------------------|---|-----------------------------|---------------------|
| PTCDI |  | -108578.2665 | -0.784 |
| Br ₂ PTCDI A |  | -528702.9762 | -0.726 |
| Br ₂ PTCDI B |  | -528703.0275 | -0.777 |
| S ₂ PTCDI A |  | -192800.144 | -0.863 |
| S ₂ PTCDI B |  | -192799.9838 | -0.703 |

Figure B.4: Trimer binding energies for homo-molecular junctions.

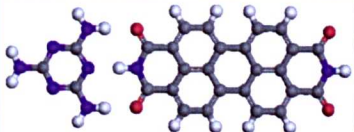
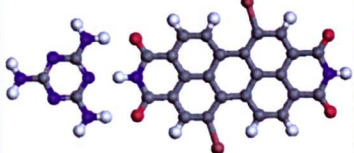
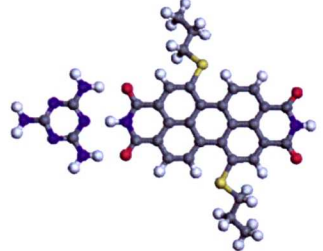
| Molecule | | Total Energy of System (eV) | Binding Energy (eV) |
|-----------------------------|---|-----------------------------|---------------------|
| Mel + PTCDI |  | -48334.28631 | -0.795 |
| Mel + Br ₂ PTCDI |  | -188375.9512 | -0.871 |
| Mel + S ₂ PTCDI |  | -76408.29177 | -0.868 |

Figure B.5: Binding energies for hetero-molecular junctions between melamine - PTCDI.

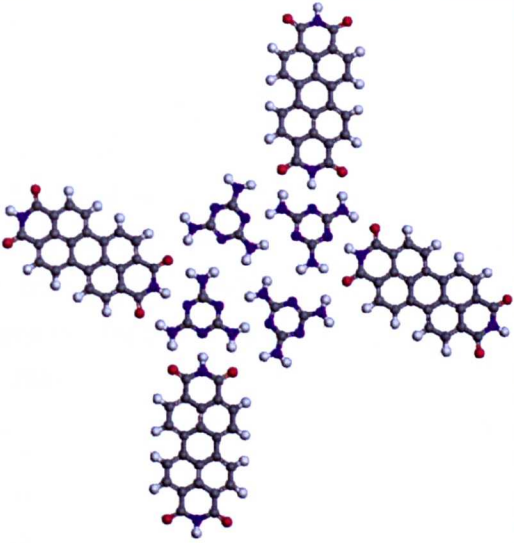
| Melamine rich junction | Total Energy of System (eV) | Binding Energy (eV) |
|---|-----------------------------|---------------------|
|  | -193339.7114 | -5.745 |

Figure B.6: BE of the melamine rich junction.

B.2 MM calculation details for the simulation of $\text{Mn}_{12}(\text{acetate})_{16}$

B.2.1 $\text{Mn}_{12}(\text{acetate})_{16}$ on the Au(111) surface

MM simulations were performed using the Forcite package within Materials Studio 4.3 (Accelrys). Quench calculations were used to obtain the energy minima for a single $\text{Mn}_{12}(\text{acetate})_{16}$ molecule on the Au(111) surface. In a quench calculation a MD simulation is performed and at periodic intervals the geometry from the MD simulation is used as the starting point for a geometry optimisation calculation. This allows a range of starting geometries to be sampled. The simulations were performed using periodic boundary conditions (cell dimensions $A=43.2569 \text{ \AA}$ $B=43.2569 \text{ \AA}$ $C=54.7092 \text{ \AA}$ $\alpha=90^\circ$ $\beta=90^\circ$ $\gamma=120^\circ$) with the molecule being placed in the centre of the cell on top of a 3ML slab of the Au(111) surface, and with the Au atoms of the substrate being constrained throughout the calculations. The formal charges for Mn were set so that the four central atoms had a charge of +4 and the eight outer atoms had a charge of +3. The QEq method was used to distribute the charge across the molecule [209]. The UFF was used to describe the atoms within the molecule, and the atoms within the Au(111) surface, with no changes being made to the automatically assigned force field typings [210]. The calculation parameters are given in table B.5.

After the quench calculation was performed the BE of $\text{Mn}_{12}(\text{acetate})_{16}$ to the Au(111) surface was calculated using the following method:

$$BE_{\text{Mn}_{12}(\text{acetate})_{16}-\text{Au}} = E_{\text{Tot}} - (E_{\text{Mn}_{12}(\text{acetate})_{16}} + E_{\text{Au}}) \quad (\text{B.2})$$

where $BE_{\text{Mn}_{12}(\text{acetate})_{16}-\text{Au}}$ is the BE of $\text{Mn}_{12}(\text{acetate})_{16}$ to the gold substrate, E_{Tot} is the energy of the total system, $E_{\text{Mn}_{12}(\text{acetate})_{16}}$ is the energy of $\text{Mn}_{12}(\text{acetate})_{16}$ in free space, and E_{Au} is the energy of the Au substrate. From this information a graph may be plotted showing the different BEs obtained for structures optimised during the quench simulation (shown in Figure B.7).

As described in the main body of the thesis it is possible to characterise these states in terms of the geometric arrangement of the molecule relative to the surface (state geometries are shown in Figure B.8). The BEs of these states are displayed in table B.6.

| Parameters for MM of $\text{Mn}_{12}(\text{acetate})_{16}$ on Au(111) | | |
|---|-------------------------------------|-----------------|
| Dynamics | Ensemble | NVE |
| | Initial temperature | 298 K |
| | Time step | 1.0 fs |
| | No. of steps | 100,000 |
| | Duration | 100 ps |
| | Initial velocities | Random |
| Quench | Optimise Energy | Every 100 steps |
| Geometry Optimisation | Algorithm | Smart |
| | Convergence tolerance: Energy | 0.001 kcal/mol |
| | Convergence tolerance: Force | 0.005 kcal/mol |
| | Convergence tolerance: Displacement | 0.00005 Å |
| | No. of iterations | 5000 |
| Energy Parameters | Forcefield | Universal |
| | Electrostatic | Elwald |
| | Electrostatic: Accuracy | 0.001 kcal/mol |
| | Electrostatic: Buffer width | 0.5 Å |
| | van der Waals | Elwald |
| | van der Waals: Accuracy | 0.001 kcal/mol |
| | van der Waals: Buffer width | 0.5 Å |
| van der Waals: Repulsion cut-off | 6 Å | |

Table B.5: MM parameters for a quench calculation performed on a single $\text{Mn}_{12}(\text{acetate})_{16}$ molecule on the Au(111) surface.

| State | Energy (eV) |
|-------|------------------|
| M1 | -0.11 ± 0.01 |
| M2 | -0.16 ± 0.01 |
| M3a | -0.22 ± 0.01 |
| M3b | -0.27 ± 0.01 |
| M3c | -0.27 ± 0.02 |
| M4a | -0.26 ± 0.01 |
| M4b | -0.31 ± 0.02 |

Table B.6: Calculated BE of 1 $\text{Mn}_{12}(\text{acetate})_{16}$ molecule to the Au(111) surface for a number of different states obtained from the quench calculation.

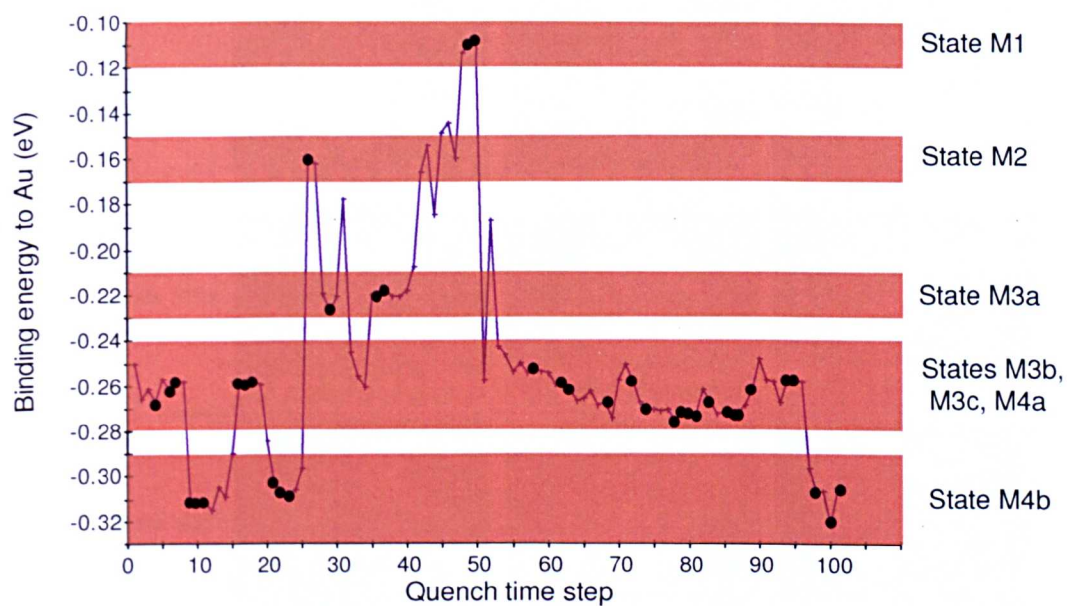


Figure B.7: Graph showing the BEs of $\text{Mn}_{12}(\text{acetate})_{16}$ to the Au(111) surface as determined by the geometry optimisation calculations starting with frames obtained during the course of the quench simulation. The black circles highlight geometry optimisation calculations which have met their convergence criteria.

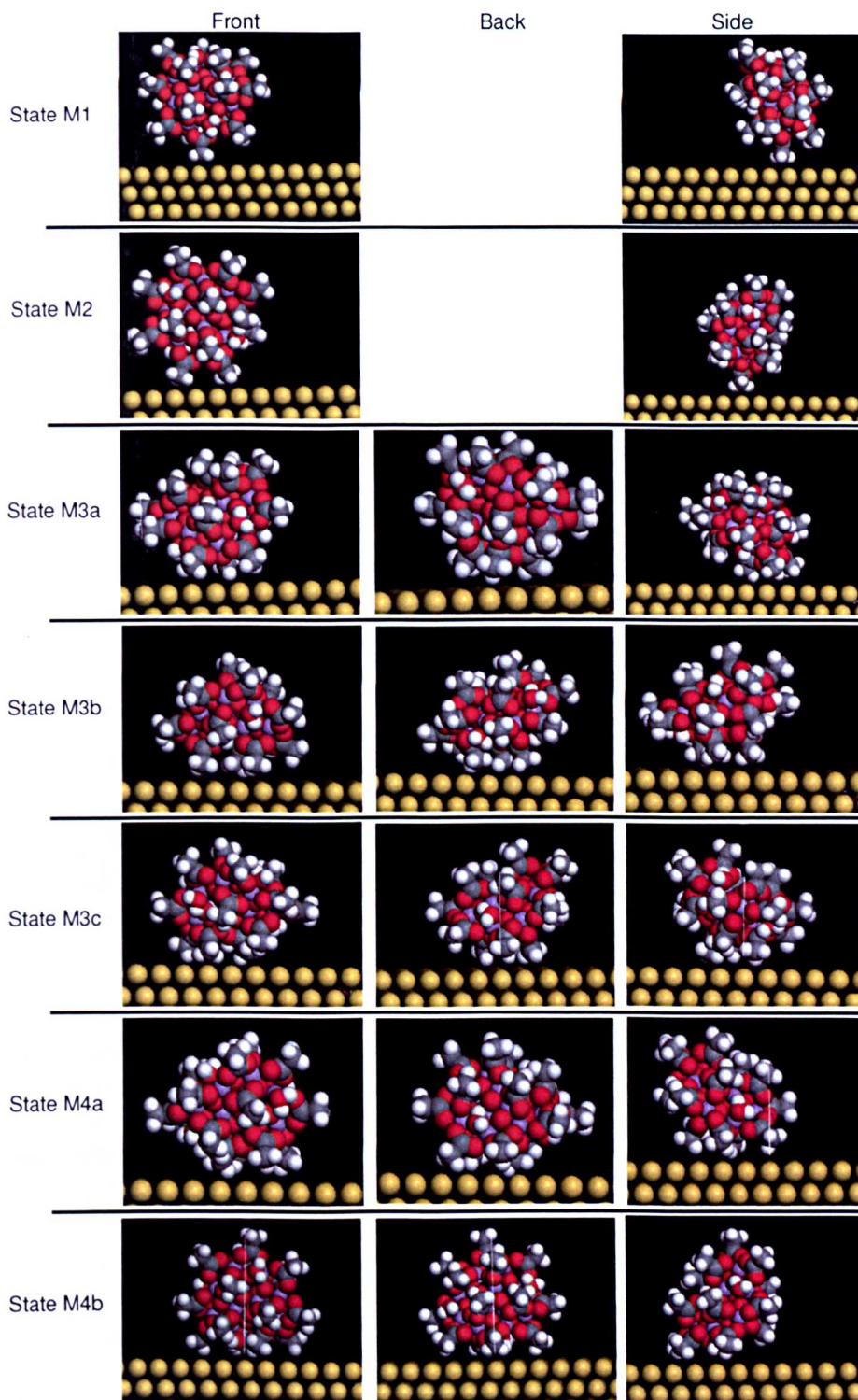


Figure B.8: The energy minima determined by the quench calculation can be grouped by the molecules orientation relative to the surface. The images above show examples of these geometry optimised states. The defining characteristic is the number of CH_3 groups in contact with the Au(111) surface.

B.2.2 Two $\text{Mn}_{12}(\text{acetate})_{16}$ molecules on the Au(111) surface

Quench simulations were carried out as described above for two molecules situated on an Au(111) surface. The BE between the two molecules has been calculated and is shown in Figure B.9. As with the case of an isolated $\text{Mn}_{12}(\text{acetate})_{16}$ adsorbed on the Au(111) surface we are able to identify discrete states for the interaction between two $\text{Mn}_{12}(\text{acetate})_{16}$ molecules. The energies of these states are shown in table B.7. A schematic of the orientations of the two $\text{Mn}_{12}(\text{acetate})_{16}$ molecules for the different states is shown in the main body of this thesis and is reproduced here as Figure B.10.

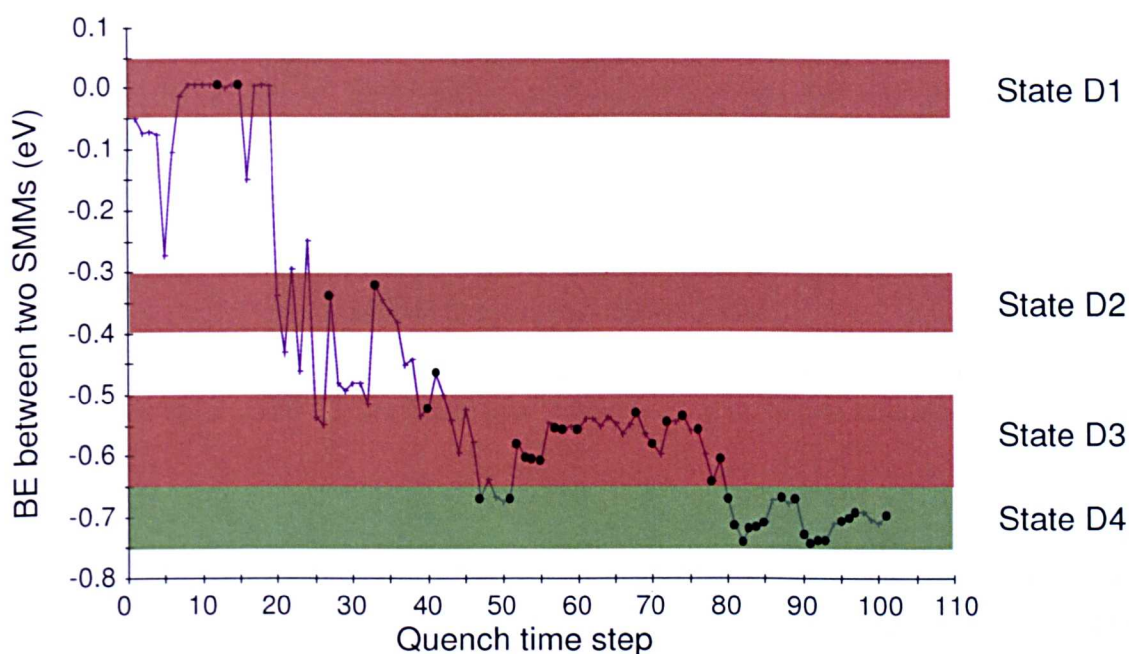


Figure B.9: Graph showing the BE between two $\text{Mn}_{12}(\text{acetate})_{16}$ molecules on the Au(111) surface as determined by the geometry optimisation calculations starting with frames obtained during the course of the quench simulation. The black circles highlight geometry optimisation calculations which have met their convergence criteria.

| State | Energy (eV) |
|-------|------------------|
| D4 | -0.71 ± 0.05 |
| D3 | -0.56 ± 0.1 |
| D2 | -0.33 ± 0.05 |
| D1 | 0 |

Table B.7: Table showing the energy of each state calculated from the quench simulation for the interaction between two $\text{Mn}_{12}(\text{acetate})_{16}$ molecules.

Figure B.10 shows the four states identified by the quench simulation, with state **D1** being a configuration where the $\text{Mn}_{12}(\text{acetate})_{16}$ molecules are not in

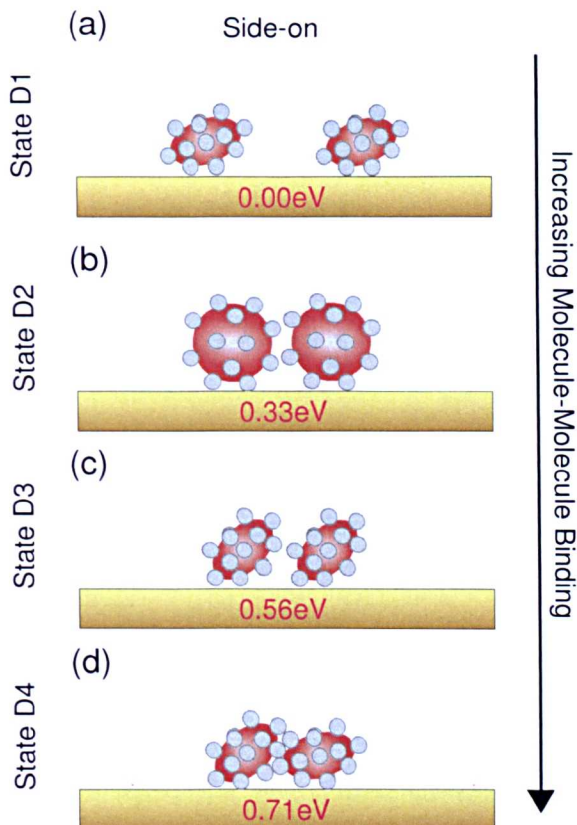


Figure B.10: Schematic showing the orientation of, and the BEs between, two $\text{Mn}_{12}(\text{acetate})_{16}$ molecules on the Au(111) surface which have adopted one of the states identified by the quench simulation.

contact with each other and hence the BE is zero. State **D2** is defined as a conformation where the edges of the molecules are in contact, the BE of this state is determined to be 0.35 eV. The two states with the highest BEs are state **D3** and state **D4** which both adopt a ‘face-to-face’ orientation allowing the surface area in contact to be maximised.

B.2.3 Five $\text{Mn}_{12}(\text{acetate})_{16}$ on the Au(111) surface

In order to reproduce the structures observed using STM after the deposition of $\text{Mn}_{12}(\text{acetate})_{16}$ onto the Au(111) surface, a MD calculation was performed to simulate the motion of five molecules. The calculation parameters used are shown in table B.8.

The simulations were performed using periodic boundary conditions (cell dimensions $A=86.5138 \text{ \AA}$ $B=86.5138 \text{ \AA}$ $C=54.7092 \text{ \AA}$ $\alpha=90^\circ$ $\beta=90^\circ$ $\gamma=120^\circ$) with the molecules being placed in the cell on top of a 3ML slab of the Au(111) surface, and with the Au atoms of the substrate being constrained throughout the calculations.

Figure B.11 demonstrates that, although the five $\text{Mn}_{12}(\text{acetate})_{16}$ are initially well spaced, during the course of the simulation the molecules move together and form a filamentary structure similar to those observed in the STM experiments.

| Parameters for MM of 5 $\text{Mn}_{12}(\text{acetate})_{16}$ molecules on Au(111) | | |
|---|-------------------------------------|----------------|
| Dynamics | Ensemble | NVE |
| | Initial temperature | 298 K |
| | Time step | 1.0 fs |
| | No. of steps | 500,000 |
| | Duration | 500 ps |
| | Initial velocities | Random |
| Geometry Optimisation | Algorithm | Smart |
| | Convergence tolerance: Energy | 0.001 kcal/mol |
| | Convergence tolerance: Force | 0.005 kcal/mol |
| | Convergence tolerance: Displacement | 0.00005 Å |
| | No. of iterations | 5000 |
| Energy Parameters | Forcefield | Universal |
| | Electrostatic | Elwald |
| | Electrostatic: Accuracy | 0.001 kcal/mol |
| | Electrostatic: Buffer width | 0.5 Å |
| | van der Waals | Elwald |
| | van der Waals: Accuracy | 0.001 kcal/mol |
| | van der Waals: Buffer width | 0.5 Å |
| | van der Waals: Repulsion cutoff | 6 Å |

Table B.8: MM parameters for a MD calculation performed on five $\text{Mn}_{12}(\text{acetate})_{16}$ molecules on the Au(111) surface.

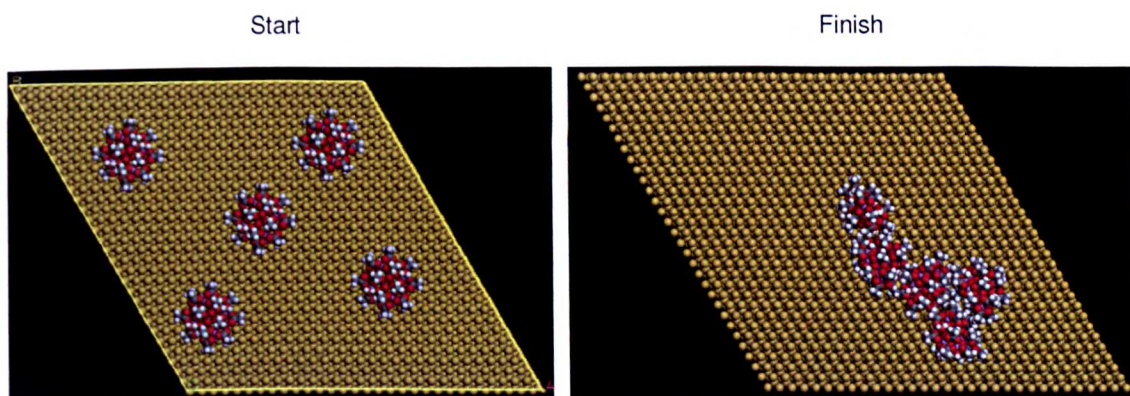


Figure B.11: Start and end frames from a MD simulation of five $\text{Mn}_{12}(\text{acetate})_{16}$ on an Au(111) substrate.

B.2.4 Note on the magnitude of the calculated BEs

In order to compare the magnitude of the BEs predicted by the MM calculations to experimental results, a model system comprising of a linear alkane chain deposited onto an Au(111) surface has been investigated. Linear alkane chains containing 1 to 10 carbon atoms were simulated on an Au(111) slab consisting of three layers of atoms, with the BE of each system being determined by a geometry optimisation calculation (using the same parameters as for the $\text{Mn}_{12}(\text{acetate})_{16}$ calculations). The BEs of these calculations may then be directly compared to experimental data [219] as displayed in table B.9. Table B.9 shows that the BE predicted by the Universal force-field consistently underestimates the experimental value by a factor of ~ 3 . It is therefore expected that the values determined above for the BE of a $\text{Mn}_{12}(\text{acetate})_{16}$ to the Au(111) surface, and between pairs of $\text{Mn}_{12}(\text{acetate})_{16}$ molecules, are a factor of three less than the actual value.

| Molecule | No. of carbon atoms in alkyl chain | Experimentally determined BE [219] (kJ/mol) | BE determined by MM using the Universal Forcefield (kJ/mol) |
|----------|------------------------------------|---|---|
| Methane | 1 | 14.5 | 5.0 |
| Ethane | 2 | 24.1 | 6.4 |
| Propane | 4 | 40.5 | - |
| Hexane | 6 | 55.9 | 16.1 |
| Heptane | 7 | 62.7 | 23.1 |
| Octane | 8 | 69.7 | 25.9 |
| Nonane | 9 | 75.2 | 28.2 |
| Decane | 10 | 80.1 | 29.0 |

Table B.9: Table comparing the BE of several alkane chains to the Au(111) surface, as determined by experiment and MM (Universal) calculations.

List of abbreviations and acronyms

| | |
|--|---|
| AFM | Atomic force microscopy |
| BDA | 4,4'-biphenyl dicarboxylic acid |
| BE | Binding energy |
| Br ₂ PTCDI | dibromo-PTCDI |
| CA·M | Cyanuric acid-melamine |
| CRM | Charged residual model |
| DATP | 4,4'-Diamino- <i>p</i> -terphenyl |
| DFT | Density functional theory |
| FCC | Face centered cubic |
| HCP | Hexagonal close-packed |
| HOMO | Highest occupied molecular orbital |
| HOPG | Highly orientated pyrolytic graphite |
| HV | High voltage |
| IEM | Ion evaporation model |
| K-cell | Knudsen cell |
| LCAO | Linear combination of atomic orbitals |
| LDOS | Local density of states |
| LINAC | Linear accelerator |
| LL | Fast entry load lock |
| LUMO | Lowest unoccupied molecular orbital |
| MD | Molecular dynamics |
| Melamine | 1,3,5-triazine-2,4,6-triamine |
| ML | Monolayers |
| MM | Molecular mechanics |
| Mn ₁₂ (acetate) ₁₆ | Mn ₁₂ O ₁₂ (O ₂ CCH ₃) ₁₆ (H ₂ O) ₄ |
| NEXAFS | X-ray adsorption fine structure |
| NTCDI | Naphthalenetetracarboxylic diimide |
| P4 | Porphyrin tetramer |
| P6 | Porphyrin hexamer |
| PES | Photoelectron spectroscopy |
| PI | Proportional, integral |
| P _{<i>n</i>} | Porphyrin polymer |
| PP | Protoporphyrin |
| PTCDA | Perylenetetracarboxylic dianhydride |
| PTCDI | 3,4:9,10-perylenetetracarboxylic diimide |
| RGA | Residual gas analyser |

| | |
|----------------------|--|
| SCM | Scanning capacitance microscopy |
| SMM | Single molecule magnet |
| S ₂ PTCDI | di(propylthioether)-PTCDI |
| SPM | Scanning probe microscopy |
| STM | Scanning tunnelling microscope |
| TMA | Trimisic acid |
| TMLA | 1,2,4-benzenetricarboxylic acid (trimellitic acid) |
| TMP | Turbo-molecular pump |
| TPTC | <i>p</i> -terphenyl-3,5,3',5'-tetracarboxylic acid |
| TSP | Titanium sublimation pump |
| UHV | Ultra-high vacuum |
| UHV-ESD | Ultra-high vacuum electrospray deposition |
| vdW | van der Waals |
| WLC | Wormlike chain |
| XPS | X-ray photoemission spectroscopy |

Bibliography

- [1] RP Feynman. There's plenty of room at the bottom. *Engineering and Science*, 23(5):22–36, 1960.
- [2] DM Eigler and EK Schweizer. Positioning single atoms with a scanning tunneling microscope. *Nature*, 344(6266):524–526, April 1990.
- [3] KE Drexler. *The engines of creation*. Doubleday, 1986.
- [4] MF Crommie, CP Lutz, DM Eigler, and EJ Heller. Waves on a metal-surface and quantum corrals. *Surf. Rev. Lett.*, 2(1):127–137, February 1995.
- [5] KE Drexler. Nanorex, inc. - molecular machinery gallery. <http://nanoengineer-1.com/content/index.php>.
- [6] Y He, T Ye, M Su, C Zhang, AE Ribbe, W Jiang, and C Mao. Hierarchical self-assembly of DNA into symmetric supramolecular polyhedra. *Nature*, 452(7184):198–201, 2008.
- [7] JM Lehn. Supramolecular chemistry - scope and perspectives molecules, supermolecules, and molecular devices. *Angew. Chem. Int. Ed.*, 27(1):89–112, January 1988.
- [8] JR Nitschke and JM Lehn. Self-organization by selection: Generation of a metallosupramolecular grid architecture by selection of components in a dynamic library of ligands. *Proc. Natl. Acad. Sci.*, 100(21):11970–11974, October 2003.
- [9] V Berl, I Huc, RG Khoury, MJ Krische, and JM Lehn. Interconversion of single and double helices formed from synthetic molecular strands. *Nature*, 407(6805):720–723, October 2000.
- [10] RH Grubbs. Olefin-metathesis catalysts for the preparation of molecules and materials (Nobel lecture 2005). *Adv. Synth. Catal.*, 349(1-2):34–40, January 2007.
- [11] J Israelachvili. *Intermolecular and surface forces*. Academic Press, 2nd edition, 1991.

- [12] P Atkins and J de Paula. *Physical Chemistry*. Oxford University Press, 7th edition, 2002.
- [13] A Ranganathan, VR Pedireddi, and CNR Rao. Hydrothermal synthesis of organic channel structures: 1 : 1 hydrogen-bonded adducts of melamine with cyanuric and trithiocyanuric acids. *J. Am. Chem. Soc.*, 121(8):1752–1753, March 1999.
- [14] LMA Perdigao, NR Champness, and PH Beton. Surface self-assembly of the cyanuric acid-melamine hydrogen bonded network. *Chem. Commun.*, (5):538–540, February 2006.
- [15] FH Allen, WDS Motherwell, PR Raithby, GP Shields, and R Taylor. Systematic analysis of the probabilities of formation of bimolecular hydrogen-bonded ring motifs in organic crystal structures. *New J. Chem.*, 23(1):25–34, January 1999.
- [16] PA Staniec, LMA Perdigao, BL Rogers, NR Champness, and PH Beton. Honeycomb networks and chiral superstructures formed by cyanuric acid and melamine on Au(111). *J. Phys. Chem. C*, 111(2):886–893, January 2007.
- [17] N Zhu, T Osada, and T Komeda. Supramolecular assembly of biphenyl dicarboxylic acid on au(111). *Surf. Sci.*, 601(8):1789–1794, 2007.
- [18] S Stepanow, N Lin, F Vidal, A Landa, M Ruben, JV Barth, and K Kern. Programming supramolecular assembly and chirality in two-dimensional dicarboxylate networks on a Cu(100) surface. *Nano Lett.*, 5(5):901–904, 2005.
- [19] JA Theobald, NS Oxtoby, MA Phillips, NR Champness, and PH Beton. Controlling molecular deposition and layer structure with supramolecular surface assemblies. *Nature*, 424(6952):1029–1031, August 2003.
- [20] JC Swarbrick, J Ma, JA Theobald, NS Oxtoby, JN O’Shea, NR Champness, and PH Beton. Square, hexagonal, and row phases of PTCDA and PTCDI on Ag-Si(111) $\sqrt{3} \times \sqrt{3}$ R 30°. *J. Phys. Chem. B*, 109(24):12167–12174, June 2005.
- [21] S Jensen and CJ Baddeley. Formation of PTCDI-Based metal organic structures on a Au(111) surface modified by 2-D Ni clusters. *J. Phys. Chem. C*, 112(39):15439–15448, 2008.
- [22] ME Canas-Ventura, W Xiao, D Wasserfallen, K Mullen, H Brune, JV Barth, and R Fasel. Self-assembly of periodic bicomponent wires and ribbons. *Angew. Chem. Int. Ed.*, 46(11):1814–1818, 2007.

- [23] F Silly, AQ Shaw, MR Castell, and GAD Briggs. A chiral pinwheel supramolecular network driven by the assembly of PTCDI and melamine. *Chem. Commun.*, (16):1907, 2008.
- [24] LMA Perdigao, EW Perkins, J Ma, PA Staniec, BL Rogers, NR Champness, and PH Beton. Bimolecular networks and supramolecular traps on Au(111). *J. Phys. Chem. B*, 110(25):12539–12542, June 2006.
- [25] PA Staniec, LMA Perdigao, A Saywell, NR Champness, and PH Beton. Hierarchical organisation on a two-dimensional supramolecular network. *ChemPhysChem*, 8(15):2177–2181, October 2007.
- [26] M Lackinger, S Griessl, T Markert, F Jamitzky, and WM Heckl. Self-assembly of benzene-dicarboxylic acid isomers at the liquid solid interface: Steric aspects of hydrogen bonding. *J. Phys. Chem. B*, 108(36):13652–13655, September 2004.
- [27] MO Blunt, JC Russell, MD Gimenez-Lopez, JP Garrahan, X Lin, M Schroder, NR Champness, and PH Beton. Random tiling and topological defects in a Two-Dimensional molecular network. *Science*, 322(5904):1077–1081, November 2008.
- [28] S De Feyter, A Gesquiere, M Klapper, K Mullen, and FC De Schryver. Toward two-dimensional supramolecular control of hydrogen-bonded arrays: The case of isophthalic acids. *Nano Lett.*, 3(11):1485–1488, November 2003.
- [29] DL Keeling, NS Oxtoby, C Wilson, MJ Humphry, NR Champness, and PH Beton. Assembly and processing of hydrogen bond induced supramolecular nanostructures. *Nano Lett.*, 3(1):9–12, 2003.
- [30] G Pawin, KL Wong, KY Kwon, and L Bartels. A homomolecular porous network at a Cu(111) surface. *Science*, 313(5789):961–962, 2006.
- [31] LMA Perdigao, A Saywell, GN Fontes, PA Staniec, G Goretzki, AG Phillips, NR Champness, and PH Beton. Functionalized supramolecular nanoporous arrays for surface templating. *Chem. Eur. J.*, 14(25):7600–7607, 2008.
- [32] UK Weber, VM Burlakov, LMA Perdigao, RHJ Fawcett, PH Beton, NR Champness, JH Jefferson, GAD Briggs, and DG Pettifor. Role of interaction anisotropy in the formation and stability of molecular templates. *Phys. Rev. Letts.*, 100(15):156101, April 2008.
- [33] JB Taylor and PH Beton. Kinetic instabilities in the growth of one dimensional molecular nanostructures. *Phys. Rev. Letts.*, 97(23):236102, December 2006.

- [34] A Langner, SL Tait, N Lin, C Rajadurai, M Ruben, and K Kern. Self-recognition and self-selection in multicomponent supramolecular coordination networks on surfaces. *Proc. Natl. Acad. Sci.*, 104(46):17927–17930, November 2007.
- [35] A Dmitriev, H Spillmann, N Lin, JV Barth, and K Kern. Modular assembly of two-dimensional metal-organic coordination networks at a metal surface. *Angew. Chem. Int. Ed.*, 42(23):2670–2673, 2003.
- [36] U Schlickum, R Decker, F Klappenberger, G Zoppellaro, S Klyatskaya, M Ruben, I Silanes, A Arnau, K Kern, H Brune, and JV Barth. Metal-organic honeycomb nanomeshes with tunable cavity size. *Nano Lett.*, 7(12):3813–3817, December 2007.
- [37] A Cnossen, D Pijper, T Kudernac, MM Pollard, N Katsonis, and BL Feringa. A trimer of ultrafast nanomotors: synthesis, photochemistry and self-assembly on graphite. *Chem. Eur. J.*, 15(12):2768–2772, 2009.
- [38] CL Claypool, F Faglioni, WA Goddard, HB Gray, NS Lewis, and RA Marcus. Source of image contrast in STM images of functionalized alkanes on graphite: A systematic functional group approach. *J. Phys. Chem. B*, 101(31):5978–5995, July 1997.
- [39] S Furukawa, H Uji-i, K Tahara, T Ichikawa, M Sonoda, FC De Schryver, Y Tobe, and S De Feyter. Molecular geometry directed kagome and honeycomb networks: Toward two-dimensional crystal engineering. *J. Am. Chem. Soc.*, 128(11):3502–3503, March 2006.
- [40] K Tahara, S Furukawa, H Uji-I, T Uchino, T Ichikawa, J Zhang, W Mamdough, M Sonoda, FC De Schryver, S De Feyter, and Y Tobe. Two-dimensional porous molecular networks of dehydrobenzo[12]annulene derivatives via alkyl chain interdigitation. *J. Am. Chem. Soc.*, 128(51):16613–16625, December 2006.
- [41] S Lei, M Surin, K Tahara, J Adisoejoso, R Lazzaroni, Y Tobe, and S De Feyter. Programmable hierarchical three-component 2D assembly at a liquid-solid interface: Recognition, selection, and transformation. *Nano Lett.*, 8(8):2541–2546, August 2008.
- [42] YH Wei, K Kannappan, GW Flynn, and MB Zimmt. Scanning tunneling microscopy of prochiral anthracene derivatives on graphite: Chain length effects on monolayer morphology. *J. Am. Chem. Soc.*, 126(16):5318–5322, April 2004.

- [43] L Grill, M Dyer, L Lafferentz, M Persson, MV Peters, and S Hecht. Nano-architectures by covalent assembly of molecular building blocks. *Nature Nanotech.*, 2(11):687–691, November 2007.
- [44] S Weigelt, C Busse, C Bombis, MM Knudsen, KV Gothelf, T Strunskus, C Woll, M Dahlbom, B Hammer, E Laegsgaard, F Besenbacher, and TR Linderoth. Covalent interlinking of an aldehyde and an amine on a Au(111) surface in ultrahigh vacuum. *Angew. Chem. Int. Ed.*, 46(48):9227–9230, 2007.
- [45] M Treier, NV Richardson, and R Fasel. Fabrication of surface-supported low-dimensional polyimide networks. *J. Am. Chem. Soc.*, 130(43):14054–14055, October 2008.
- [46] M Matena, T Riehm, M Stohr, TA Jung, and LH Gade. Transforming surface coordination polymers into covalent surface polymers: Linked polycondensed aromatics through oligomerization of n-heterocyclic carbene intermediates. *Angew. Chem. Int. Ed.*, 47(13):2414–2417, 2008.
- [47] S Griessl, M Lackinger, M Edelwirth, M Hietschold, and WM Heckl. Self-assembled two-dimensional molecular host-guest architectures from trimesic acid. *Single Molecules*, 3(1):25–31, 2002.
- [48] R Madueno, MT Raisanen, C Silien, and M Buck. Functionalizing hydrogen-bonded surface networks with self-assembled monolayers. *Nature*, 454(7204):618–621, July 2008.
- [49] LMA Perdigao, PA Staniec, NR Champness, and PH Beton. Entrapment of decanethiol in a hydrogen-bonded bimolecular template. *Langmuir*, 25(4):2278–2281, February 2009.
- [50] S Stepanow, M Lingenfelder, A Dmitriev, H Spillmann, E Delvigne, N Lin, XB Deng, CZ Cai, JV Barth, and K Kern. Steering molecular organization and host-guest interactions using two-dimensional nanoporous coordination systems. *Nature Mater.*, 3(4):229–233, April 2004.
- [51] H Spillmann, A Kiebele, M Stohr, TA Jung, D Bonifazi, FY Cheng, and F Diederich. A two-dimensional porphyrin-based porous network featuring communicating cavities for the templated complexation of fullerenes. *Adv. Mater.*, 18(3):275–279, February 2006.
- [52] M Li, K Deng, SB Lei, YL Yang, TS Wang, YT Shen, CR Wang, QD Zeng, and C Wang. Site-selective fabrication of two-dimensional fullerene arrays by using a supramolecular template at the liquid-solid interface. *Angew. Chem. Int. Ed.*, 47(35):6717–6721, 2008.

- [53] G Binning and H Rohrer. Scanning tunnelling microscopy. *IBM J. Res. Dev.*, 30(4):355–369, July 1986.
- [54] FJ Giessibl. Advances in atomic force microscopy. *Rev. Mod. Phys.*, 75(3):949–983, July 2003.
- [55] CD Bugg and PJ King. Scanning capacitance microscopy. *J. Phys. E Sci. Instrum.*, 21(2):147–151, 1988.
- [56] AP French and EF Taylor. *An introduction to quantum physics*. Nelson Thornes, 2001.
- [57] J Bardeen. Tunnelling from a many-particle point of view. *Phys. Rev. Letts.*, 6(2):57–59, 1961.
- [58] R Wiesendanger. *Scanning probe microscopy and spectroscopy: Methods and applications*. Cambridge University Press, 1994.
- [59] J Tersoff and DR Hamann. Theory of the scanning tunnelling microscope. *Phys. Rev. B*, 31(2):805–813, 1985.
- [60] DP Woodruff and TA Delchar. *Modern Techniques of surface science*. 2nd edition, 1994.
- [61] CJ Chen. Origin of atomic resolution on metal-surface in scanning tunneling microscopy. *Phys. Rev. Letts.*, 65(4):448–451, July 1990.
- [62] SJ van der Molen and P Liljeroth. Charge transport through molecular switches. *J. Phys-Condens. Mat.*, 22(13):133001, April 2010.
- [63] K Glockler, C Seidel, A Soukopp, M Sokolowski, E Umbach, M Bohringer, R Berndt, and WD Schneider. Highly ordered structures and submolecular scanning tunnelling microscopy contrast of PTCDA and DM-PBDCI monolayers on Ag(111) and Ag(110). *Surf. Sci.*, 405(1):1–20, May 1998.
- [64] DW Pohl. Dynamic piezoelectric transition devices. *Rev. Sci. Instrum.*, 58(1):54–57, January 1987.
- [65] CN Woodburn, AW McKinnon, DA Roberts, ME Taylor, and ME Welland. A one-dimensional piezoelectric-driven inertial micropositioner with vertical capabilities. *Meas. Sci. Technol.*, 4(4):535–537, April 1993.
- [66] PA Staniec. *Networks and structures of adsorbed molecules stabilised by hydrogen bonding*. University of Nottingham, Thesis, (PhD), 2007.
- [67] JF Jorgensen, K Carneiro, LL Madsen, and K Conradsen. Hysteresis correction of scanning tunnelling microscope images. *J. Vac. Sci. Technol. B*, 12(3):1702–1704, June 1994.

- [68] D Briggs and MP Seah. *Practical surface analysis*, volume 1. John Wiley and Sons, 2nd edition, 1994.
- [69] MP Seah and WA Dench. Quantitative electron spectroscopy of surfaces: A standard data base for electron inelastic mean free paths in solids. *Surface and Interface Analysis*, 1(1):2–11, 1979.
- [70] BV Crist. *Handbook of Monochromatic XPS spectra*, volume 1-3. John Wiley and Sons, 2000.
- [71] K Siegbahn. Electron-spectroscopy for atoms, molecules, and condensed matter. *Rev. Mod. Phys.*, 54(3):709–728, 1982.
- [72] T Koopmans. *Physica*, 1:104–113, 1934.
- [73] CJ Satterley, LMA Perdigo, A Saywell, G Magnano, A Rienzo, LC Mayor, VR Dhanak, PH Beton, and JN O’Shea. Electropray deposition of fullerenes in ultra-high vacuum: in situ scanning tunneling microscopy and photoemission spectroscopy. *Nanotechnology*, 18(45):455304, November 2007.
- [74] MA Phillips. *C₆₀ and its derivatives at Si surfaces: experimental and theoretical studies of electronic structures*. University of Nottingham, Thesis, (PhD), 2004.
- [75] J Stohr and DA Outka. Determination of molecular orientations on surfaces from the angular-dependance of near-edge X-ray-adsorbition fine-structure spectra. *Phys. Rev. B*, 36(15):7891–7905, November 1987.
- [76] D Attwood. *Soft X-rays and extreme ultraviolet radiation - Principles and applications*. Cambridge University Press, Cambridge, 2007.
- [77] R Nyholm, S Svensson, J Nordgren, and A Flodstrom. A soft-X-ray monochromator for the max synchrotron radiation facility. *Nucl. Instr. and Meth. A*, 246(1-3):267–271, May 1986.
- [78] A Chambers. *Basic vacuum technology*. Taylor & Francis, 2nd edition, 1998.
- [79] R Zhang and DG Ivey. Preparation of sharp polycrystalline tungsten tips for scanning tunneling microscopy imaging. *J. Vac. Sci. Tech. B*, 14(1):1–10, February 1996.
- [80] T Zambelli, P Jiang, J Lagoute, SE Grillo, S Gauthier, A Gourdon, and C Joachim. Deformation of a 3.7-nm long molecular wire at a metallic step edge. *Phys. Rev. B*, 66(7):075410, August 2002.
- [81] L Grill. Large molecules on surfaces: deposition and intramolecular STM manipulation by directional forces. *J. Phys.: Condens. Matter*, 22(8):084023, March 2010.

- [82] JB Fenn. Ion formation from charged droplets - roles of geometry, energy, and time. *J. Am. Soc. Mass Spectrom.*, 4(7):524–535, July 1993.
- [83] CM Whitehouse, RN Dreyer, M Yamashita, and JB Fenn. Electrospray interface for liquid chromatographs and mass spectrometers. *Anal. Chem.*, 57(3):675–679, 1985.
- [84] SJ Gaskell. Electrospray: Principles and practice. *J. Mass Spectrom.*, 32(7):677–688, July 1997.
- [85] JN O’Shea, JB Taylor, JC Swarbrick, G Magnano, LC Mayor, and K Schulte. Electrospray deposition of carbon nanotubes in vacuum. *Nanotechnology*, 18(3):035707, January 2007.
- [86] LC Mayor, J Ben Taylor, G Magnano, A Rienzo, CJ Satterley, JN O’Shea, and J Schnadt. Photoemission, resonant photoemission, and X-ray absorption of a Ru(II) complex adsorbed on rutile TiO₂ (110) prepared by in situ electrospray deposition. *J. Chem. Phys.*, 129(11), September 2008.
- [87] LC Mayor, A Saywell, G Magnano, CJ Satterley, J Schnadt, and JN O’Shea. Adsorption of a Ru(II) dye complex on the Au(111) surface: Photoemission and scanning tunneling microscopy. *J. Chem. Phys.*, 130(16):164704, April 2009.
- [88] A Rienzo, LC Mayor, G Magnano, CJ Satterley, E Ataman, J Schnadt, K Schulte, and JN O’Shea. X-ray adsorbtion and photoemission spectroscopy of zinc-protophyrin adsorbed on rutile TiO₂(110) prepared by in situ electrospray deposition. *J. Chem. Phys.*, (132):084703, 2010.
- [89] S Rauschenbach, FL Stadler, E Lunedei, N Malinowski, S Koltsov, G Costantini, and K Kern. Electrospray ion beam deposition of clusters and biomolecules. *Small*, 2(4):540–547, April 2006.
- [90] JE Lyon, AJ Cascio, MM Beerbom, R Schlaf, Y Zhu, and SA Jenekhe. Photoemission study of the poly(3-hexylthiophene)/Au interface. *Appl. Phys. Lett.*, 88(22):222109, May 2006.
- [91] P Kebarle and L Tang. From ions in solution to ions in the gas phase - the mechanism of electrospray mass spectrometry. *Anal. Chem.*, 65(22):A972–A986, November 1993.
- [92] LB Loeb, AF Kip, and GG Hudson. Pulses in negative point-to-plane corona. *Phys. Rev.*, 60(10):714–722, November 1941.
- [93] RB Cole. Some tenets pertaining to electrospray ionization mass spectrometry. *J. Mass Spectrom.*, 35(7):763–772, July 2000.

- [94] AM GananCalvo. Cone-jet analytical extension of Taylor's electrostatic solution and the asymptotic universal scaling laws in electrospraying. *Phys. Rev. Letts.*, 79(2):217–220, July 1997.
- [95] JF de la Mora, J Navascues, F Fernandez, and J Rosell-Llompart. Generation of submicrob monodisperse aerosols in electrosprays. *J. Aerosol Sci.*, 21(1):S673–S676, 1990.
- [96] Lord Rayleigh. On the equilibrium of liquid conducting masses charged with electricity. *Philos. Mag.*, 14(87):184–186, 1882.
- [97] A Gomez and KQ Tang. Charge and fission of droplets in electrostatic sprays. *Phys. Fluids*, 6(1):404–414, January 1994.
- [98] M Dole, LL Mack, and RL Hines. Molecular beams of macroions. *J. Chem. Phys.*, 49(5):2240–2249, 1968.
- [99] JV Iribarne and BA Thomson. Evaporation of small ions from charged droplets. *J. Chem. Phys.*, 64(6):2287–2294, 1976.
- [100] H Pauly. *Atom, molecule, and cluster beams I: Basic theory, production and detection of thermal energy beams*, volume 1. Springer, Berlin, 2000.
- [101] IM Hanson. *Creation of novel interfaces using electrospray mass spectrometry and size-selected clusters*. University of Birmingham, Thesis, (PhD), 2007.
- [102] R Campargue. Progress in overexpanded supersonic jets and skimmed molecular-beams in free-jet zones of silence. *J. Phys. Chem.*, 88(20):4466–4474, 1984.
- [103] JV Barth, H Brune, G Ertl, and RJ Behm. Scanning tunneling microscopy observations on the reconstructed Au(111) surface - atomic-structure, long-range superstructure, rotational domains, and surface-defects. *Phys. Rev. B*, 42(15):9307–9318, November 1990.
- [104] P Kowalczyk, W Kozlowski, Z Klusek, W Olejniczak, and PK Datta. STM studies of the reconstructed Au(111) thin-film at elevated temperatures. *Appl. Surf. Sci.*, 253(10):4715–4720, March 2007.
- [105] K Morgenstern, J Kibsgaard, JV Lauritsen, E Laegsgaard, and F Besenbacher. Cobalt growth on two related close-packed noble metal surfaces. *Surf. Sci.*, 601(9):1967–1972, May 2007.
- [106] LMA Perdigo, GN Fontes, BL Rogers, NS Oxtoby, G Goretzki, NR Champness, and PH Beton. Coadsorbed NTCDI-melamine mixed phases on Ag-Si(111). *Phys. Rev. B*, 76(24):245402, December 2007.

- [107] J Ma, BL Rogers, MJ Humphry, DJ Ring, G Goretzki, NR Champness, and PH Beton. Dianhydride-amine hydrogen bonded perylene tetracarboxylic dianhydride and tetraaminobenzene rows. *J. Phys. Chem. B*, 110(25):12207–12210, June 2006.
- [108] EI Altman and RJ Colton. Nucleation, growth, and structure of fullerene films on Au(111). *Surf. Sci.*, 279(1-2):49–67, December 1992.
- [109] AJ Maxwell, PA Bruhwiler, A Nilsson, N Martensson, and P Rudolf. Photoemission, autoionization, and X-ray-absorption spectroscopy of ultrathin-film C₆₀ on Au(111). *Phys. Rev. B*, 49(15):10717–10725, April 1994.
- [110] TJ Marks and MA Ratner. Design, synthesis, and properties of molecule-based assemblies with large 2nd-order optical nonlinearities. *Angew. Chem. Int. Ed.*, 34(2):155–173, February 1995.
- [111] C Joachim, JK Gimzewski, and A Aviram. Electronics using hybrid-molecular and mono-molecular devices. *Nature*, 408(6812):541–548, November 2000.
- [112] JV Barth, G Costantini, and K Kern. Engineering atomic and molecular nanostructures at surfaces. *Nature*, 437(7059):671–679, September 2005.
- [113] JY Lee, BH Hong, WY Kim, SK Min, Y Kim, MV Jouravlev, R Bose, KS Kim, IC Hwang, LJ Kaufman, CW Wong, P Kim, and KS Kim. Near-field focusing and magnification through self-assembled nanoscale spherical lenses. *Nature*, 460(7254):498–501, July 2009.
- [114] JI Martin, J Nogues, K Liu, JL Vicent, and IK Schuller. Ordered magnetic nanostructures: fabrication and properties. *J. Magn. Magn. Mater.*, 256(1-3):449–501, January 2003.
- [115] ZH Nie and E Kumacheva. Patterning surfaces with functional polymers. *Nature Mater.*, 7(4):277–290, March 2008.
- [116] F Kulzer and M Orrit. Single-molecule optics. *Annu. Rev. Phys. Chem.*, 55:585–611, 2004.
- [117] APHJ Schenning and EW Meijer. Supramolecular electronics; nanowires from self-assembled pi-conjugated systems. *Chem. Commun.*, (26):3245–3258, 2005.
- [118] JAAW Elemans, SB Lei, and S De Feyter. Molecular and supramolecular networks on surfaces: From two-dimensional crystal engineering to reactivity. *Angew. Chem. Int. Ed.*, 48(40):7298–7332, 2009.

- [119] L Bartels. Tailoring molecular layers at metal surfaces. *Nature Chem.*, 2(2):87–95, February 2010.
- [120] V Palermo and P Samori. Molecular self-assembly across multiple length scales. *Angew. Chem. Int. Ed.*, 46(24):4428–4432, 2007.
- [121] SJH Griessl, M Lackinger, F Jamitzky, T Markert, M Hietschold, and WA Heckl. Incorporation and manipulation of coronene in an organic template structure. *Langmuir*, 20(21):9403–9407, October 2004.
- [122] F Rosei, M Schunack, Y Naitoh, P Jiang, A Gourdon, E Laegsgaard, I Stensgaard, C Joachim, and F Besenbacher. Properties of large organic molecules on metal surfaces. *Prog. Surf. Sci.*, 71(5-8):95–146, June 2003.
- [123] R Sessoli, D Gatteschi, A Caneschi, and MA Novak. Magnetic bistability in a metal-ion cluster. *Nature*, 365(6442):141–143, September 1993.
- [124] MA Novak, R Sessoli, A Caneschi, and D Gatteschi. Magnetic-properties of a Mn cluster organic-compound. *J. Magn. Magn. Mater.*, 146(1-2):211–213, April 1995.
- [125] JR Friedman, MP Sarachik, J Tejada, and R Ziolo. Macroscopic measurement of resonant magnetization tunneling in high-spin molecules. *Phys. Rev. Letts.*, 76(20):3830–3833, May 1996.
- [126] D Gatteschi and R Sessoli. Quantum tunneling of magnetization and related phenomena in molecular materials. *Angew. Chem. Int. Ed.*, 42(3):268–297, 2003.
- [127] MN Leuenberger and D Loss. Quantum computing in molecular magnets. *Nature*, 410(6830):789–793, April 2001.
- [128] F Meier, J Levy, and D Loss. Quantum computing with spin cluster qubits. *Phys. Rev. Letts.*, 90(4):047901, January 2003.
- [129] R Sessoli, HL Tsai, AR Schake, SY Wang, JB Vincent, K Folting, D Gatteschi, G Christou, and DN Hendrickson. High-spin molecules - $[\text{Mn}_{12}\text{O}_{12}(\text{O}_2\text{CR})_{16}(\text{H}_2\text{O})_4]$. *J. Am. Chem. Soc.*, 115(5):1804–1816, March 1993.
- [130] S Phark, ZG Khim, BJ Kim, BJ Suh, S Yoon, J Kim, JM Lim, and Y Do. Atomic force microscopy study of $\text{Mn}_{12}\text{O}_{12}(\text{O}_2\text{CC}_4\text{H}_3\text{S})_{16}(\text{H}_2\text{O})_4$ single-molecule magnet adsorbed on Au surface. *Jpn. J. Appl. Phys. 1*, 43(12):8273–8277, December 2004.
- [131] A Naitabdi, JP Bucher, P Gerbier, P Rabu, and M Drillon. Self-assembly and magnetism of Mn-12 nanomagnets on native and functionalized gold surfaces. *Adv. Mater.*, 17(13):1612–1616, July 2005.

- [132] SMJ Aubin, ZM Sun, HJ Eppley, RM Rumberger, IA Guzei, K Foltz, PK Gantzel, AL Rheingold, G Christou, and DN Hendrickson. Single-molecule magnets: Jahn-Teller isomerism and the origin of two magnetization relaxation processes in Mn-12 complexes. *Polyhedron*, 20(11-14):1139–1145, May 2001.
- [133] A Cornia, AC Fabretti, M Pacchioni, L Zobbi, D Bonacchi, A Caneschi, D Gatteschi, R Biagi, U Del Pennino, V De Renzi, L Gurevich, and HSJ Van der Zant. Direct observation of single-molecule magnets organized on gold surfaces. *Angew. Chem. Int. Ed.*, 42(14):1645–1648, 2003.
- [134] L Zobbi, M Mannini, M Pacchioni, G Chastanet, D Bonacchi, C Zanardi, R Biagi, U Del Pennino, D Gatteschi, A Cornia, and R Sessoli. Isolated single-molecule magnets on native gold. *Chem. Commun.*, (12):1640–1642, 2005.
- [135] V Corradini, U del Pennino, R Biagi, V De Renzi, A Gambardella, GC Gazdadi, A Candini, L Zobbi, and A Cornia. Self-assembling of Mn12 molecular nanomagnets on FIB-patterned Au dot matrix. *Surf. Sci.*, 601(13):2618–2622, July 2007.
- [136] SH Phark, ZG Khim, JM Lim, J Kim, and S Yoon. Study on the films of a single-molecule magnet Mn12 modified by the selective insertion of a sulfur-terminated ligand. *J. Magn. Magn. Mater.*, 310(2):E483–E485, March 2007.
- [137] F Pineider, M Mannini, R Sessoli, A Caneschi, D Barreca, L Armelao, A Cornia, E Tondello, and D Gatteschi. Solvent effects on the adsorption and self-organization of Mn-12 on Au(111). *Langmuir*, 23(23):11836–11843, November 2007.
- [138] E Coronado, A Forment-Aliaga, FM Romero, V Corradini, R Biagi, V De Renzi, A Gambardella, and U del Pennino. Isolated Mn-12 single-molecule magnets grafted on gold surfaces via electrostatic interactions. *Inorg. Chem.*, 44(22):7693–7695, October 2005.
- [139] RV Martinez, F Garcia, R Garcia, E Coronado, A Forment-Aliaga, FM Romero, and S Tatay. Nanoscale deposition of single-molecule magnets onto SiO₂ patterns. *Adv. Mater.*, 19(2):291, January 2007.
- [140] RW Saalfrank, A Scheurer, I Bernt, FW Heinemann, AV Postnikov, V Schunemann, AX Trautwein, MS Alam, H Rupp, and P Muller. The Fe-III[Fe-III(L-1)₂]₃ star-type single-molecule magnet. *Dalton T.*, (23):2865–2874, 2006.

- [141] J Means, V Meenakshi, RVA Srivastava, W Teizer, A Kolomenskii, HA Schuessler, H Zhao, and KR Dunbar. Films of Mn-12-acetate deposited by low-energy laser ablation. *J. Magn. Magn. Mater.*, 284:215–219, December 2004.
- [142] V Meenakshi, W Teizer, DG Naugle, H Zhao, and KR Dunbar. Films of Mn-12-acetate by pulsed laser evaporation. *Solid State Commun.*, 132(7):471–476, November 2004.
- [143] R Moroni, R Buzio, A Chincarini, U Valbusa, FB de Mongeot, L Bogani, A Caneschi, R Sessoli, L Cavigli, and M Gurioli. Optically addressable single molecule magnet behaviour of vacuum-sprayed ultrathin films. *J. Mater. Chem.*, 18(48):5999–5999, 2008.
- [144] L Vitali, S Fabris, AM Conte, S Brink, M Ruben, S Baroni, and K Kern. Electronic structure of surface-supported bis(phthalocyaninato) terbium(III) single molecular magnets. *Nano Lett.*, 8(10):3364–3368, October 2008.
- [145] AL Barra, A Caneschi, D Gatteschi, DP Goldberg, and R Sessoli. Slow magnetic relaxation of $[\text{Et}_3\text{NH}]_2[\text{Mn}(\text{CH}_3\text{CN})_4(\text{H}_2\text{O})_2]$ $[\text{Mn}_{10}\text{O}_4(\text{biphen})_4\text{Br}_{12}]$ (biphen=2,2'-biphenoxide) at very low temperature. *J. Solid State Chem.*, 145(2):484–487, July 1999.
- [146] A Saywell, G Magnano, CJ Satterley, LMA Perdigo, NR Champness, PH Beton, and JN O'Shea. Electrospray deposition of C_{60} on a hydrogen-bonded supramolecular network. *J. Phys. Chem. C*, 112(20):7706–7709, May 2008.
- [147] H Suzuki, T Yamada, T Kamikado, Y Okuno, and S Mashiko. Deposition of thermally unstable molecules with the spray-jet technique on Au(111) surface. *J. Phys. Chem. B*, 109(27):13296–13300, July 2005.
- [148] S Rauschenbach, R Vogelgesang, N Malinowski, JW Gerlach, M Benyoucef, G Costantini, ZT Deng, N Thontasen, and K Kern. Electrospray ion beam deposition: Soft-landing and fragmentation of functional molecules at solid surfaces. *ACS Nano*, 3(10):2901–2910, October 2009.
- [149] H Tanaka and T Kawai. Partial sequencing of a single DNA molecule with a scanning tunnelling microscope. *Nature Nanotech.*, 4(8):518–522, August 2009.
- [150] R Otero, M Lukas, REA Kelly, W Xu, E Laegsgaard, I Stensgaard, LN Kantorovich, and F Besenbacher. Elementary structural motifs in a random network of cytosine adsorbed on a gold(111) surface. *Science*, 319(5861):312–315, January 2008.

- [151] M Marschall, J Reichert, A Weber-Bargioni, K Seufert, W Auwärter, S Klyatskaya, G Zoppellaro, M Ruben, and JV Barth. Random two-dimensional string networks based on divergent coordination assembly. *Nature Chem.*, 2(2):131–137, February 2010.
- [152] M Cavallini, M Facchini, C Albonetti, and F Biscarini. Single molecule magnets: from thin films to nano-patterns. *Phys. Chem. Chem. Phys.*, 10(6):784–793, 2008.
- [153] S Voss, M Fonin, U Rudiger, M Burgert, U Groth, and YS Dedkov. Electronic structure of Mn-12 derivatives on the clean and functionalized Au surface. *Phys. Rev. B*, 75(4):045102, January 2007.
- [154] P Ghigna, A Campana, A Lascialfari, A Caneschi, D Gatteschi, A Tagliaferri, and F Borgatti. X-ray magnetic-circular-dichroism spectra on the superparamagnetic transition-metal ion clusters Mn-12 and Fe-8. *Phys. Rev. B*, 64(13):132413, October 2001.
- [155] S Voss, M Fonin, L Burova, M Burgert, YS Dedkov, AB Preobrajenski, E Goering, U Groth, AR Kaul, and U Ruediger. Investigation of the stability of Mn-12 single molecule magnets. *Appl. Phys. A*, 94(3):491–495, March 2009.
- [156] J Adisojoso, K Tahara, S Okuhata, S Lei, Y Tobe, and S De Feyter. Two-Dimensional crystal engineering: A Four-Component architecture at a Liquid-Solid interface. *Angew. Chem. Int. Ed.*, 48(40):7353–7357, 2009.
- [157] RH Friend, RW Gymer, AB Holmes, JH Burroughes, RN Marks, C Taliani, DDC Bradley, DA Dos Santos, JL Bredas, M Logdlund, and WR Salaneck. Electroluminescence in conjugated polymers. *Nature*, 397(6715):121–128, January 1999.
- [158] M Granstrom, K Petritsch, AC Arias, A Lux, MR Andersson, and RH Friend. Laminated fabrication of polymeric photovoltaic diodes. *Nature*, 395(6699):257–260, September 1998.
- [159] H Sirringhaus, N Tessler, and RH Friend. Integrated optoelectronic devices based on conjugated polymers. *Science*, 280(5370):1741–1744, June 1998.
- [160] SJ Tans, MH Devoret, HJ Dai, A Thess, RE Smalley, LJ Geerligs, and C Dekker. Individual single-wall carbon nanotubes as quantum wires. *Nature*, 386(6624):474–477, April 1997.
- [161] S Frank, P Poncharal, ZL Wang, and WA de Heer. Carbon nanotube quantum resistors. *Science*, 280(5370):1744–1746, June 1998.

- [162] AJ Heeger. Nobel lecture: Semiconducting and metallic polymers: The fourth generation of polymeric materials. *Rev. Mod. Phys.*, 73(3):681–700, July 2001.
- [163] HL Anderson, SJ Martin, and DDC Bradley. Synthesis and 3rd-order nonlinear-optical properties of a conjugated porphyrin polymer. *Angew. Chem. Int. Ed.*, 33(6):655–657, March 1994.
- [164] MH Chang, M Hoffmann, HL Anderson, and LM Herz. Dynamics of excited-state conformational relaxation and electronic delocalization in conjugated porphyrin oligomers. *J. Am. Chem. Soc.*, 130(31):10171–10178, August 2008.
- [165] VSY Lin, SG Dimagno, and MJ Therien. Highly conjugated, acetylenyl bridged porphyrins - new models for light-harvesting antenna systems. *Science*, 264(5162):1105–1111, May 1994.
- [166] G Sedghi, K Sawada, LJ Esdaile, M Hoffmann, HL Anderson, D Bethell, W Haiss, SJ Higgins, and RJ Nichols. Single molecule conductance of porphyrin wires with ultralow attenuation. *J. Am. Chem. Soc.*, 130(27):8582–8583, July 2008.
- [167] MU Winters, E Dahlstedt, HE Blades, CJ Wilson, MJ Frampton, HL Anderson, and B Albinsson. Probing the efficiency of electron transfer through porphyrin-based molecular wires. *J. Am. Chem. Soc.*, 129(14):4291–4297, April 2007.
- [168] K Susumu, PR Frail, PJ Angiolillo, and MJ Therien. Conjugated chromophore arrays with unusually large hole polaron delocalization lengths. *J. Am. Chem. Soc.*, 128(26):8380–8381, July 2006.
- [169] F Schreiber. Structure and growth of self-assembling monolayers. *Prog. Surf. Sci.*, 65(5-8):151–256, December 2000.
- [170] HM Zhang, ZX Xie, BW Mao, and X Xu. Self-assembly of normal alkanes on the Au(111) surfaces. *Chem. Eur. J.*, 10(6):1415–1422, March 2004.
- [171] LC Giancarlo, HB Fang, SM Rubin, AA Bront, and GW Flynn. Influence of the substrate on order and image contrast for physisorbed, self-assembled molecular monolayers: STM studies of functionalized hydrocarbons on graphite and MoS₂. *J. Phys. Chem. B*, 102(50):10255–10263, December 1998.
- [172] JP Rabe and S Buchholz. Commensurability and mobility in 2-dimensional molecular-patterns on graphite. *Science*, 253(5018):424–427, July 1991.

- [173] YH Wei, WJ Tong, C Wise, XL Wei, K Armbrust, and M Zimmt. Dipolar control of monolayer morphology: Spontaneous SAM patterning. *J. Am. Chem. Soc.*, 128(41):13362–13363, October 2006.
- [174] D Bleger, D Kreher, F Mathevet, AJ Attias, G Schull, A Huard, L Douillard, C Fiorini-Debuischert, and F Charra. Surface noncovalent bonding for rational design of hierarchical molecular self-assemblies. *Angew. Chem. Int. Ed.*, 46(39):7404–7407, 2007.
- [175] X Zhang, CJ Yan, GB Pan, RQ Zhang, and LJ Wan. Effect of C-H ... F and O-H ... O hydrogen bonding in forming self-assembled monolayers of BF₂-substituted beta-dicarbonyl derivatives on HOPG: STM investigation. *J. Phys. Chem. C*, 111(37):13851–13854, September 2007.
- [176] W Mamdough, H Uji-i, JS Ladislaw, AE Dulcey, V Percec, FC De Schryver, and S De Feyter. Solvent controlled self-assembly at the liquid-solid interface revealed by STM. *J. Am. Chem. Soc.*, 128(1):317–325, January 2006.
- [177] SS Li, HJ Yan, LJ Wan, HB Yang, BH Northrop, and PJ Stang. Control of supramolecular rectangle self-assembly with a molecular template. *J. Am. Chem. Soc.*, 129(30):9268, August 2007.
- [178] DX Wu, K Deng, QD Zeng, and C Wang. Selective effect of guest molecule length and hydrogen bonding on the supramolecular host structure. *J. Phys. Chem. B*, 109(47):22296–22300, December 2005.
- [179] JE Lovett, M Hoffmann, A Cnossen, ATJ Shutter, HJ Hogben, JE Warren, SI Pascu, CWM Kay, CR Timmel, and HL Anderson. Probing flexibility in porphyrin based molecular wires using double electron electron resonance. *J. Am. Chem. Soc.*, 131:13852–13859, 2009.
- [180] T Kudernac, SB Lei, JAAW Elemans, and S De Feyter. Two-dimensional supramolecular self-assembly: nanoporous networks on surfaces. *Chem. Soc. Revs.*, 38(2):402–421, 2009.
- [181] JC Moore. Gel permeation chromatography i. a new method for molecular weight distributions of high polymers. *J. Polym. Sci. Pol. Chem.*, 2(2):835–843, 1964.
- [182] M Brun, R Demadrille, P Rannou, A Pron, JP Travers, and B Grevin. Multiscale scanning tunneling microscopy study of self-assembly phenomena in two-dimensional polycrystals of pi-conjugated polymers: The case of regioregular poly (dioctylbithiophene-alt-fluore-none). *Adv. Mater.*, 16(23-24):2087–2092, December 2004.

- [183] E Mena-Osteritz, A Meyer, BMW Langeveld-Voss, RAJ Janssen, EW Meijer, and P Bauerle. Two-dimensional crystals of poly(3-alkylthiophene): Direct visualization of polymer folds in submolecular resolution. *Angew. Chem. Int. Ed.*, 39(15):2680–2684, 2000.
- [184] M Ullner and CE Woodward. Orientational correlation function and persistence lengths of flexible polyelectrolytes. *Macromolecules*, 35(4):1437–1445, February 2002.
- [185] LD Landau and EM Lifshitz. *Statistical Physics*. Pergamon, London, 1958.
- [186] J Wilhelm and E Frey. Radial distribution function of semiflexible polymers. *Phys. Rev. Letts.*, 77(12):2581–2584, September 1996.
- [187] GS Manning. Polymer persistence length characterised as a critical length for instability caused by a fluctuating twist. *Phys. Rev. A*, 34(1):668–670, July 1986.
- [188] P Samori, C Ecker, I Gossel, PAJ de Witte, JJLM Cornelissen, GA Metselaar, MBJ Otten, AE Rowan, RJM Nolte, and JP Rabe. High shape persistence in single polymer chains rigidified with lateral hydrogen bonded networks. *Macromolecules*, 35(13):5290–5294, June 2002.
- [189] C Rivetti, M Guthold, and C Bustamante. Scanning force microscopy of DNA deposited onto mica: Equilibration versus kinetic trapping studied by statistical polymer chain analysis. *J. Mol. Biol.*, 264(5):919–932, December 1996.
- [190] F Jensen. *Introduction to computational chemistry*. John Wiley & sons Ltd, Chichester, 1999.
- [191] CJ Cramer. *Essentials of computational chemistry: Theories and Models*. John Wiley & sons Ltd, Chichester, second edition edition, 2004.
- [192] RG Parr and W Yang. *Density-Functional theory of atoms and molecules*. Oxford University Press, 1989.
- [193] CCJ Roothaan. New developments in molecular orbital theory. *Rev. Mod. Phys.*, 23(2):69–89, 1951.
- [194] GG Hall. The molecular orbital theory of chemical valency 8. A method of calculating ionization potentials. *Proc. R. Soc. A*, 205(1083):541–552, 1951.
- [195] LH Thomas. The calculation of atomic fields. *Proc. Cam. Phil. Soc.*, 23:542–548, July 1927.
- [196] P Hohenberg and W Kohn. Inhomogeneous electron gas. *Phys. Rev. B*, 136(3B):B864–&, 1964.

- [197] W Kohn and LJ Sham. Self-consistent equations including exchange and correlation effects. *Phys. Rev.*, 140(4A):1133–1138, 1965.
- [198] PAM Dirac. Note on exchange phenomena in the thomas atom. *Proc. Cam. Phil. Soc.*, 26:376–385, July 1930.
- [199] AD Becke. Density-functional exchange-energy approximation with correct asymptotic-behavior. *Phys. Rev. A*, 38(6):3098–3100, September 1988.
- [200] NA Benedek, IK Snook, K Latham, and I Yarovsky. Application of numerical basis sets to hydrogen bonded systems: A density functional theory study. *J. Chem. Phys.*, 122(14), April 2005.
- [201] JC Slater. Atomic shielding constants. *Phys. Rev.*, 36(1):0057–0064, July 1930.
- [202] SF Boys. Electronic wave functions 1. A general method of calculation for the stationary states of any molecular system. *Proc. R. Soc. A*, 200(1063):542–554, 1950.
- [203] M Levitt and S Lifson. Refinement of protein conformations using a macromolecular energy minimization procedure. *J. Mol. Biol.*, 46(2):269–279, 1969.
- [204] R Fletcher and CM Reeves. Function minimization by conjugate gradients. *Computer Journal*, 7(2):149–154, 1964.
- [205] JP Perdew, K Burke, and M Ernzerhof. Generalized gradient approximation made simple. *Phys. Rev. Letts.*, 77(18):3865–3868, October 1996.
- [206] B Delley. An all-electron numerical-method for solving the local density functional for polyatomic-molecules. *J. Chem. Phys.*, 92(1):508–517, January 1990.
- [207] D Cremer and Z He. Sixth-order Moller-Plesset perturbation theory - on the convergence of the MPn series. *J. Phys. Chem. A*, 100(15):6173–6188, April 1996.
- [208] TL Hill. Physical interaction of electrons with dielectric media. *J. Chem. Phys.*, 16(4):394–399, 1948.
- [209] AK Rappe and WA Goddard. Charge equilibration for molecular-dynamics simulations. *J. Phys. Chem.*, 95(8):3358–3363, April 1991.
- [210] AK Rappe, CJ Casewit, KS Colwell, WA Goddard, and WM Skiff. UFF, a full periodic-table force-field for molecular mechanics and molecular-dynamics simulations. *J. Am. Chem. Soc.*, 114(25):10024–10035, December 1992.

- [211] L Verlet. Computer experiments on classical fluids i. thermodynamical properties of Lennard-Jones molecules. *Phys. Rev.*, 159(1):98–103, 1967.
- [212] WG Hoover. Canonical dynamics - equilibrium phase-space distributions. *Phys. Rev. A*, 31(3):1695–1697, 1985.
- [213] H Sun. COMPASS: an ab initio force-field optimized for condensed-phase applications - overview with details on alkane and benzene compounds. *J. Phys. Chem. B*, 102(38):7338–7364, September 1998.
- [214] SL Mayo, BD Olafson, and WA Goddard. Dreiding - a generic force-field for molecular simulations. *J. Phys. Chem.*, 94(26):8897–8909, December 1990.
- [215] N Karasawa and WA Goddard. Force-fields, structures, and properties of poly(vinylidene fluoride) crystals. *Macromolecules*, 25(26):7268–7281, December 1992.
- [216] P Ordejon, E Artacho, and JM Soler. Self-consistent order-N density-functional calculations for very large systems. *Phys. Rev. B*, 53(16):10441–10444, April 1996.
- [217] JM Soler, E Artacho, JD Gale, A Garcia, J Junquera, P Ordejon, and D Sanchez-Portal. The SIESTA method for ab initio order-N materials simulation. *J. Phys.: Condens. Matter*, 14(11):2745–2779, March 2002.
- [218] B Delley. From molecules to solids with the DMol³ approach. *J. Chem. Phys.*, 113(18):7756–7764, November 2000.
- [219] SM Wetterer, DJ Lavrich, T Cummings, SL Bernasek, and G Scoles. Energetics and kinetics of the physisorption of hydrocarbons on Au(111). *J. Phys. Chem. B*, 102(46):9266–9275, November 1998.

List of Figures

| | | |
|------|--|----|
| 1.1 | Three perspectives of nanoscale physics | 2 |
| 2.1 | Examples of supramolecular chemistry. | 6 |
| 2.2 | Bonding motif of the cyanuric acid - melamine (CA·M) molecular network. | 7 |
| 2.3 | CA·M molecular network structure, formed on the Au(111) and Ag/Si(111) surface. | 9 |
| 2.4 | Structures formed on the HOPG surface driven by hydrogen-bond interactions between molecules with carboxylic acid functionalities. | 11 |
| 2.5 | Homomolecular interactions leading to porous and close-packed structures. | 13 |
| 2.6 | STM images showing networks formed by metal co-ordination involving Fe atoms, di-pyridine, and di-carboxylic ligands. | 14 |
| 2.7 | STM images of structures stabilised by vdW interactions between alkyl chains. | 16 |
| 2.8 | STM images of the covalently bound structures formed from reactive proto-porphyrin derivatives deposited on the Au(111) surface. | 17 |
| 2.9 | Hexagonal porous networks formed from chemically functionalised molecules | 19 |
| 2.10 | Examples of the entrapment of molecular species within a porous self-assembled network. | 20 |
| 3.1 | Schematic representation of a one-dimensional rectangular potential barrier. | 23 |
| 3.2 | Schematic showing the reciprocal nature of the interacting orbitals of the tip and the surface. | 25 |
| 3.3 | Schematic showing how electrons may tunnel between the filled and empty states of the tip and sample. | 26 |
| 3.4 | Energy level diagram showing how the presence of molecular orbitals may effect quantum tunnelling. | 28 |
| 3.5 | Diagram showing the different imaging modes of STM. | 29 |
| 3.6 | Diagram demonstrating the effect of different feedback parameters. | 30 |
| 3.7 | Schematic showing the motion of a slipstick inertial motor. | 31 |
| 3.8 | Illustration of the motion of the piezoelectric scan-tube. | 32 |

| | | |
|------|--|----|
| 3.9 | Schematic of the electron energy levels for an organic molecule. Core- and valence-levels are shown. | 34 |
| 3.10 | Universal curve showing how the inelastic mean free path of electrons varies with their kinetic energy. | 35 |
| 3.11 | XPS spectra illustrating the ‘initial state effects’ on BE. | 37 |
| 3.12 | Schematic depicting shake-up and shake-off of electrons as a result of the removal of a core-electron. | 38 |
| 3.13 | Schematic showing how the removal of an electron from a high angular momentum orbital will result in a splitting of energy levels. | 39 |
| 3.14 | Schematic showing the re-arrangement of electrons due to X-ray absorption processes | 40 |
| 3.15 | Schematic showing the predicted NEXAFS spectra for single atoms and diatomic pairs. | 41 |
| 3.16 | Schematic showing the angular dependence of the NEXAFS technique. | 42 |
| 3.17 | Image of the Nottingham STM/UHV chamber. | 45 |
| 3.18 | Diagram showing the set up for electrochemical tip etching. | 47 |
| 3.19 | Diagram showing the formation of an electrospray event whereby a solvent containing C ₆₀ is converted from a liquid into a plume of droplets. | 49 |
| 3.20 | Schematic representation of the IEM and CRM pathways for the formation of gas-phase ions. | 50 |
| 3.21 | The electrospray experimental set-up. | 52 |
| 3.22 | Schematic showing the free-jet expansion. | 53 |
| 3.23 | Schematic showing the herringbone reconstruction of the Au(111) surface. | 55 |
| 3.24 | STM images showing the Au(111) herringbone reconstruction. | 56 |
| 4.1 | Chemical structures, dimer bonding arrangements, and homomolecular close-packing of PTCDI and melamine. | 59 |
| 4.2 | HOMO and LUMO orbital structures for PTCDI and melamine. | 60 |
| 4.3 | Mixed phase structure formed by PTCDI and melamine. | 61 |
| 4.4 | Structures of the hexagonal and parallelogram phases of the PTCDI/melamine hydrogen-bonded networks formed on the Au(111) surface. | 63 |
| 4.5 | Structures of the square and super-hexagonal melamine-rich phases. | 65 |
| 4.6 | Structure of the melamine-rich hydrogen-bonded junction. | 66 |
| 4.7 | Flow diagram demonstrating the methodology for forming the various PTCDI/melamine hydrogen-bonded network phases on the Au(111) surface. | 68 |
| 4.8 | Schematic showing the conditions required to form the various PTCDI/melamine structures. | 69 |

| | | |
|------|--|-----|
| 4.9 | Adding chemical functionality to a PTCDI/melamine hexagonal network by using R ₂ PTCDI as molecular building block. | 70 |
| 4.10 | Structure of the homo-molecular hexagonal network formed by S ₂ PTCDI on the Ag/Si(111) surface. | 71 |
| 4.11 | Schematic showing two possible arrangements of the trimer node for hydrogen-bonded S ₂ PTCDI molecules. | 71 |
| 4.12 | Schematic showing the structures used to determine the DFT calculated binding energies for homo-molecular and hetero-molecular interactions of R ₂ PTCDI and melamine | 72 |
| 4.13 | The HOMO and LUMO for Br ₂ PTCDI. | 74 |
| 4.14 | STM images showing the method used to produce the Br ₂ PTCDI/melamine hexagonal network on the Au(111) surface. | 74 |
| 4.15 | STM images showing chains of the hexagonal network, formed from S ₂ PTCDI molecules, running along the herringbone reconstruction of the Au(111) surface. DFT calculation showing the HOMO and LUMO of the molecule are also shown. | 76 |
| 4.16 | STM images showing a high coverage of S ₂ PTCDI adsorbed on the Au(111) surface. | 77 |
| 4.17 | STM images showing a small region of the S ₂ PTCDI/melamine hexagonal structure. | 78 |
| 5.1 | Schematic of the electrospray apparatus. | 81 |
| 5.2 | STM images of an Au(111) surface after electrospray deposition of C ₆₀ | 82 |
| 5.3 | STM images of an Au(111) surface after electrospray of blank solvent. | 82 |
| 5.4 | STM images of an Au(111) surface after UHV-ESD of multilayer C ₆₀ coverage. | 83 |
| 5.5 | C 1s spectra for 3.5 ML and 1 ML of C ₆₀ on Au(111). | 84 |
| 5.6 | Structural models of PTCDI, melamine, C ₆₀ , and of the hexagonal and parallelogram hydrogen-bonded networks. | 85 |
| 5.7 | STM images showing the network structures formed on the Au(111) substrate prior to UHV-ESD of C ₆₀ | 86 |
| 5.8 | STM images of the surface after UHV-ESD of C ₆₀ | 88 |
| 5.9 | STM images showing the similarities between electrosprayed and sublimed C ₆₀ | 90 |
| 5.10 | STM images showing an area of network that has been re-ordered. | 91 |
| 6.1 | Chemical structure of Mn ₁₂ (acetate) ₁₆ | 94 |
| 6.2 | Schematic of the modified UHV-ESD set-up | 96 |
| 6.3 | STM images of the Au(111) surface after UHV-ESD of Mn ₁₂ (acetate) ₁₆ | 98 |
| 6.4 | Schematic showing the bonding states (corresponding to local energy minima obtained by a MD quench simulation) available to a single Mn ₁₂ (acetate) ₁₆ molecule adsorbed on the Au(111) surface | 100 |

| | | |
|------|---|-----|
| 6.5 | Schematic showing the bonding states (corresponding to local energy minima obtained by a MD quench simulation) available to a pairs of $\text{Mn}_{12}(\text{acetate})_{16}$ molecules adsorbed on the Au(111) surface. | 102 |
| 6.6 | NEXAFS spectra measured at the Mn $2p$ adsorption edge (Mn L-edge) for a range of coverages (0.2 ML - 2.5 ML) of the $\text{Mn}_{12}(\text{acetate})_{16}$ deposited on the Au(111) surface. | 104 |
| 6.7 | $\text{Mn}_{12}(\text{acetate})_{16}$ adsorbed on a supramolecular network. | 106 |
| 7.1 | Chemical structures of the porphyrin oligomers P4 ($N = 4$) and P6 ($N = 6$) and porphyrin polymer Pn ($N \approx 30-50$) | 109 |
| 7.2 | STM images of close-packed domains of P6 adsorbed on the Au(111) surface after UHV-ESD. | 112 |
| 7.3 | STM image and structural model for the close-packed arrangement of P4 | 113 |
| 7.4 | Angle resolved N $1s$ NEXAFS spectra, N $1s$, and Zn $2p$ core-level spectra for P4 | 114 |
| 7.5 | STM image of the porphyrin polymer Pn after UHV-ESD on the Au(111) surface. | 115 |
| 7.6 | Analysis of the persistence length, L_P , of the porphyrin polymer Pn . | 117 |
| B.1 | Structure of two hydrogen-bonded junctions. | 146 |
| B.2 | Table showing the LUMO, HOMO, and total energy for melamine, PTCDI, Br_2PTCDI , and S_2PTCDI | 149 |
| B.3 | Dimer binding energies for homo-molecular pairs. | 150 |
| B.4 | Trimer binding energies for homo-molecular junctions. | 151 |
| B.5 | Binding energies for hetero-molecular junctions between melamine - PTCDI. | 152 |
| B.6 | BE of the melamine rich junction. | 152 |
| B.7 | Graph showing the BEs of $\text{Mn}_{12}(\text{acetate})_{16}$ to the Au(111) surface. | 155 |
| B.8 | The energy minima determined by the quench calculation can be grouped by the molecules orientation relative to the surface. | 156 |
| B.9 | Graph showing the BE between two $\text{Mn}_{12}(\text{acetate})_{16}$ molecules on the Au(111) surface. | 157 |
| B.10 | Schematic showing the orientation of, and the BEs between, two $\text{Mn}_{12}(\text{acetate})_{16}$ molecules on the Au(111) surface which have adopted one of the states identified by the quench simulation. | 158 |
| B.11 | Start and end frames from a MD simulation of five $\text{Mn}_{12}(\text{acetate})_{16}$ on an Au(111) substrate. | 159 |

List of Tables

| | | |
|-----|--|-----|
| 4.1 | Binding energies for various R ₂ PTCDI interactions. | 73 |
| A.1 | Table showing the convergence tolerance parameters for a Dmol ³ geometry optimisation calculation. | 134 |
| A.2 | Convergence tolerance parameters for the Forcite geometry optimisation calculation. | 143 |
| A.3 | Table showing how the Ewald accuracy for calculating the non-bonded contribution to MM energy is related to atomistic cut-off distance. | 144 |
| B.1 | DFT parameters for the test calculations. | 146 |
| B.2 | Comparison of the crystallographic hydrogen-bond distances for the CA-M junction with DFT calculated distances. | 146 |
| B.3 | Calculated BEs for two PTCDI molecules in a double hydrogen-bond arrangement using different cut-off values. | 147 |
| B.4 | Final DFT parameters. | 147 |
| B.5 | MM parameters for a quench calculation performed on a single Mn ₁₂ (acetate) ₁₆ molecule on the Au(111) surface. | 154 |
| B.6 | Calculated BE of 1 Mn ₁₂ (acetate) ₁₆ molecule to the Au(111) surface for a number of different states obtained from the quench calculation. | 154 |
| B.7 | Table showing the energy of each state calculated from the quench simulation for the interaction between two Mn ₁₂ (acetate) ₁₆ molecules. | 157 |
| B.8 | MM parameters for a MD calculation performed on five Mn ₁₂ (acetate) ₁₆ molecules on the Au(111) surface. | 159 |
| B.9 | Table comparing the BE of several alkane chains to the Au(111) surface, as determined by experiment and MM calculations. | 160 |